

Early Detection of Disease Biomarkers in Exhaled Breath through Nanomaterials-Based Sensors: A Comprehensive Investigation

Submitted in partial fulfillment of the requirements
of the degree of

Doctor of Philosophy

by

Aref Aasi

Advisor:

Professor Balaji Panchapakesan



School of Mechanical Engineering

WORCESTER POLYTECHNIC INSTITUTE

April 2023

ACKNOWLEDGMENTS

In August 2019, I was lucky enough to begin my doctoral program at the Worcester Polytechnic Institute (WPI). First and foremost, I would like to express my gratitude to WPI for giving me this opportunity to study, thrive, and be engaged in a professional place. The last four years didn't fly without difficulties, but it was rewarding, and I obtained both personal and professional growth. I am deeply indebted to my family, friends, professors, and colleagues for support during my Ph.D. program. I exclusively express my sincere appreciation to my advisor, Prof. Balaji Panchapakesan for his insightful guidance in carrying out my dissertation research. I am thankful for their support, and patience, it has been an honor working and collaborating within the Small Systems Laboratory group. I would like also to thank Prof. Jamal Yagoobi as the Department's head for their comments and encouragements. Additionally, I had the privilege of working in the lab with Dr. Sadegh Mehdi Aghaei, and I would like to thank for his advice and support during my research. I would like to acknowledge Mr. Javahersaz, who has encouraged me through my life toward greatness. I greatly cherish my amazing and diligent parents Ali Akbar, and Tahereh, and my brother Dr. Erfan Aasi for encouraging me in all of my pursuits and inspiring me to follow my dreams. Finally, this thesis is only a small part of research from a wide range of studies that have been done, and it is just the beginning of my journey.

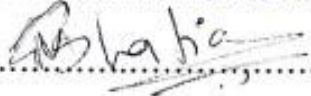
DEDICATION

This dissertation is dedicated to my beloved father Ali Akbar, my beloved mother Tahereh, my love, and especially my uncle, who has always supported me in pursuing my dreams and education. Their unwavering love and encouragement have been the driving force behind my success. I also dedicate this work to my mentors, whose guidance and expertise have been invaluable throughout my academic journey. Finally, I dedicate this dissertation to all those who strive for knowledge and innovation, as we work together to make the world a better place.

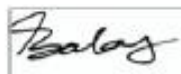
THESIS APPROVAL

This thesis entitled **Early Detection of Disease Biomarkers in Exhaled Breath through Nanomaterials-Based Sensors: A Comprehensive Investigation** by **Aref Aasi** is approved for the degree of **Doctor of Philosophy**.

Examiners:

Professor Adam Clayton Powell 
Professor Ahmet Can Sabuncu 
Professor Mehul Bhatia 

Advisor:

Professor Balaji Panchapakesan 

ME Graduate Committee Representative:

Professor Yihao Zheng 

Date: April 7, 2023

Place: ME-HL 102

ABSTRACT

Although small compounds can also be extremely powerful cancer biomarkers, early illness detection, particularly cancer detection, mostly focuses on the precise recognition of large-sized molecules, such as proteins or DNA. Clinical trials have shown the potential of breath analysis for detecting various serious illnesses including cancer.

The non-invasive and early identification of physiological diseases using gas analysis of exhaled breath has gained popularity. The identification and monitoring of diseases may benefit greatly from the development of gas sensing of volatile organic compounds (VOCs) and inorganic gases in exhaled breath. These substances can give insight into a person's metabolic state and numerous medical disorders, including cancer. For instance, studies have shown that breath analysis can identify particular VOCs linked to various cancers, including lung, breast, liver, and colorectal cancers. Moreover, breath analysis has demonstrated potential in the diagnosis of multiple sclerosis, Parkinson's disease, and other neurodegenerative disorders.

The use of nanomaterial-based sensors has shown great potential for the development of highly selective, sensitive, and cost-effective sensors for breath analysis. These sensors can detect and quantify specific biomarkers present in exhaled breath samples that are indicative of different physiological disorders. Hence, the principal objectives of this project are to comprehensively investigate the biosensing capabilities of diverse families of nanomaterials toward specific disease biomarkers.

We studied the sensing capability of a Carbon Nanotube (CNT)-based sensor toward toluene as a well-known lung cancer biomarker and tuned its properties. Later, liver cancer biomarkers (octenol, decane, and hexanal) detection were explored employing the CNT sensor. The results disclosed that the targets were physisorbed on the bare single-walled CNT, however, their adsorption was enhanced by surface modifications, and they were chemisorbed on the modified sensor substrate.

Then, in search of new disease biomarkers, we looked at other popular nanomaterials including black phosphorene and transition metal dichalcogenides (MoS₂, WS₂). For instance, the MoS₂ biosensor was used to study the detection of biomarkers for colorectal cancer, such as

benzaldehyde and indole. The outcomes demonstrated that the sensor could effectively capture biomarker molecules after increasing the sensor's sensing capabilities.

Next, the sensing behavior of novel nanomaterials such as BC₆N, and PdPS/Se toward organic and inorganic molecules were scrutinized. For example, the body releases inorganic compounds such as Ammonia (NH₃) through the breath and urine during the metabolism of proteins. Nonetheless, elevated levels of NH₃ in the breath can be a sign of renal disease.

Finally, point of care (POC) diagnostics were developed based on the single-walled CNTs. An experimental test setup were assembled, along with these chips and devices for this purpose. Their ability to sense molecules was investigated, with formaldehyde serving as a key indicator for lung cancer. It was divulged that the sensitivity of fabricated field-effect transistor (FET) SWCNT toward formaldehyde in presence of humidity (mimicking human breath) can be improved after its surface functionalization.

All in all, biomarkers play an important role in clinical practice, and cancer research, and the development of new biomarkers and technologies for their detection and analysis has the potential to improve cancer diagnosis and treatment outcomes. Ergo, our findings will enable us to comprehend nanomaterial-based biosensors and platforms more fully and identify the disease biomarkers. It might also pave the way for a novel approach to early disease diagnosis and especially cancer monitoring.

TABLE OF CONTENTS

ACKNOWLEDGMENTS	I
DEDICATION	II
ABSTRACT	I
TABLE OF CONTENTS	III
LIST OF FIGURES	VI
LIST OF TABLES	XI
ABBREVIATIONS	XII
CHAPTER 1	1
INTRODUCTION	1
1.1 MOTIVATION	1
1.2 GENERAL STATEMENT OF PROBLEM AREA	3
1.3 RESEARCH OBJECTIVES	5
1.4 ORGANIZATION OF THIS DISSERTATION	6
2. CHAPTER 2	8
2.1 CARBON NANOTUBES (CNTs)	8
2.2 PHOSPHORUS	15
2.3 TRANSITION METAL DICHALCOGENIDES (TMDs)	17
2.4 DISEASE BIOMARKERS- CANCER BIOMARKERS:	20
2.5 GAS SENSING	22
3. CHAPTER 3	25
SWCNT- BASED PLATFORM FOR EARLY DETECTION OF LUNG CANCER	25
3.1 OVERVIEW	26
3.2 COMPUTATIONAL METHOD	28

3.3 FIRST-PRINCIPLES CALCULATIONS USING DENSITY FUNCTIONAL THEORY:	29
SUMMARY	48
4. CHAPTER 4	50
SWCNT- BASED PLATFORM FOR EARLY DETECTION OF LIVER CANCER	50
4.1 OVERVIEW	50
4.2 COMPUTATIONAL METHOD	52
4.3 FIRST-PRINCIPLES CALCULATIONS USING DENSITY FUNCTIONAL THEORY:	54
SUMMARY	64
5. CHAPTER 5	65
PHOSPHORENE-BASED PLATFORM FOR DETECTION OF ALCOHOLS	65
5.1 OVERVIEW	65
5.2 COMPUTATIONAL METHOD	68
5.3 FIRST-PRINCIPLES CALCULATIONS USING DENSITY FUNCTIONAL THEORY:	69
SUMMARY	87
6. CHAPTER 6	88
6.1 DETECTION OF COLORECTAL CANCER BIOMARKERS- MoS_2	88
6.2 OVERVIEW	88
6.3 COMPUTATIONAL METHOD	90
6.4 FIRST-PRINCIPLES CALCULATIONS USING DENSITY FUNCTIONAL THEORY:	91
SUMMARY	101
7. CHAPTER 7	102
7.1 OVERVIEW	102
7.2 COMPUTATIONAL METHOD	104
7.3 FIRST-PRINCIPLES CALCULATIONS USING DENSITY FUNCTIONAL THEORY:	106
SUMMARY	131
8. CHAPTER 8	133
PHOSPHOCHALCOGENIDE, (PdPSe, AND PdDPS)-INORGANIC GAS MOLECULES	133
8.1 OVERVIEW	134
8.2 COMPUTATIONAL METHOD	135
8.3 FIRST-PRINCIPLES CALCULATIONS USING DENSITY FUNCTIONAL THEORY:	138
SUMMARY	150

9. CHAPTER 9	151
9.1 OVERVIEW	151
9.2 EXPERIMENTAL METHOD.....	155
9.3 COMPUTATIONAL METHOD	160
9.4 EXPERIMENTAL RESULTS.....	160
9.5 FIRST-PRINCIPLES CALCULATIONS USING DENSITY FUNCTIONAL THEORY:.....	173
SUMMARY.....	183
10. CHAPTER 10	186
REFERENCES.....	189

LIST OF FIGURES

Figure 1-1. Graphical abstract.	7
Figure 2-1. The foundation of all carbon allotropes is graphene. It can be rolled into 1D nanotubes (middle) or layered into 3D graphite (right), and 0D fullerene (left). Figure taken from Reference [47] with permission.....	8
Figure 2-2. (a) The carbon atoms' hexagonal configuration in CNT and graphene. The conventional unit cell vectors a_G (m) and b_G (n) are shown, together with the unit cell (shaded) having two carbon atoms. Additionally, two distinct lattice vectors (2,1) (1,0) are shown. (b) Diagram of the perpendicular to the plane of the sheets in-plane σ bonds and π orbitals [53].	10
Figure 2-3. According to their chirality and dimension, distinct types of nanotubes have diverse structures: a) metallic armchair CNT, b) metallic zigzag CNT, c) semiconductive zigzag CNT, and d) semiconductive chiral CNT [52].	11
Figure 2-4. Graphene's relation to dispersion Where the conduction and valence bands collide, there are six high-symmetry K-points called Dirac points. The shape transforms into a cone known as the Dirac cone very near these spots [66].	13
Figure 2-5. Carbon nanotubes' electronic band structure. Dirac cone with authorized k_C wave vectors in (a), dispersion relation with one of the K-points and the Dirac cone in (b), and a slice of the dispersion relation for a certain allowed wave vector, $k_C \neq 0$, displaying the conduction and valence bands as well as the bandgap in (c) [67].	13
Figure 2-6. A semiconducting carbon nanotube's DOS for a number of its subbands is represented graphically, highlighting a discrete bandgap in the band diagram [68].	15
Figure 2-7. The composition of black P crystals [73].	16
Figure 2-8. Photoluminescence spectra for single-layer phosphorene and bulk BP samples on a 300 nm Si/ SiO ₂ substrate, exhibiting a strong signal at 1.45 eV, and an AFM image of a single-layer phosphorene crystal with the reported thickness of 0.85 nm from exfoliation process [72].	17
Figure 2-9. Layered transition metal dichalcogenides material's crystalline structure shown schematically [74].	18
Figure 2-10. (a) MoS ₂ device optical image with Au electrodes. (b, c) SEM pictures of the MoS ₂ layer at various magnifications and scale bars (10 and 2 μ m, respectively) [78].	19
Figure 2-11. The MoS ₂ -based FET with Ti/Au electrodes and a back-gate is shown in (a) a schematic and (b) an optical picture. The MoS ₂ flake is indicated by the dotted triangle in (c). Following exposure to (a) 400 ppb of NO ₂ and (d) 500 ppm of NH ₃ , the device's conductance changes. The device was activated at $V_G = 30$ V in (c), and it was deactivated at $V_G = 0$ in (d) (d). Changes in the device's conductance that occur in real time as a result of time spent being exposed to (e) NO ₂ and (f) NH ₃ at various concentrations [79].	20
Figure 2-12. Diagrams illustrating the charge transfer mechanisms occurring in a monolayer of MoS ₂ when (a) NO ₂ and (b) NH ₃ molecules are present [77].	23
Figure 2-13. (a) A chemiresistive gas sensor schematic depiction. pictures of the (b) blank sensor and (c) coated sensors with the sensing substance [89].	24
Figure 3-1. (a) Optimized structure of a pristine (8,0) SWCNT and (b) its corresponding energy band structure, showing semiconducting behavior with an energy bandgap of 0.643 eV. The dotted line indicates the Fermi level, which is set to zero. Different adsorption sites on a SWCNT (Ho: hollow, A: axial, Z: zigzag, and T:	

top). (c) The optimized molecular structure of toluene (C ₇ H ₈). (d) The most stable adsorption configuration of toluene on pristine SWCNT. Distances are given in the unit of Å.	30
Figure 3-2. (a) The electronic total charge density, (b) energy band structure, and (c) total DOS curve for toluene adsorption on pristine (8,0) SWCNT. The black solid line and red dashed line in the band structure represent spin-up and spin-down bands, respectively. The Fermi level is set to zero.	32
Figure 3-3. The optimized structures of a single (a) Pt, (b) Pd, (c) Rh, and (d) Ru decorated (8,0) SWCNT. The bond lengths, the diameters, and the binding distances between the metal atom and the nanotube are also given in the unit of Å. The sticks between atoms are only for visualization.	35
Figure 3-4. Energy band structures of (a) Pt-SWCNT, (b) Pd-SWCNT, (c) Rh-SWCNT, and (d) Ru-SWCNT systems. The black solid line and red dashed line represent spin-up and spin-down bands, respectively. The dotted blue line indicates the Fermi level, which is set to zero.	37
Figure 3-5. Total DOS curves for pristine SWCNT and (a) Pt-SWCNT, (b) Pd-SWCNT, (c) Rh-SWCNT, and (d) Ru-SWCNT systems. PDOS of the s and p orbitals of C atoms in SWCNT and s and d orbitals of metal atoms are also presented. The positive and negative values denote the spin-up and spin-down channels, respectively. The dashed lines indicate the Fermi level, which are set to zero.	38
Figure 3-6. The most stable adsorption configurations for Toluene on (a) Pt-SWCNT, (b) Pd-SWCNT, (c) Rh-SWCNT, and (d) Ru-SWCNT systems. The bond lengths, the diameters, and the binding distances between the metal atom and the nanotube are also given in the unit of Å. The sticks between atoms are only for visualization.	41
Figure 3-7. The electronic total charge densities for the adsorption of toluene on (a) Pt-SWCNT, (b) Pd-SWCNT, (c) Rh-SWCNT, and (d) Ru-SWCNT systems. The sticks between atoms are only for visualization.	43
Figure 3-8. Energy band structure of toluene adsorption on (a) Pt-SWCNT, (b) Pd-SWCNT, (c) Rh-SWCNT, and (d) Ru-SWCNT systems. The black solid line and red dashed line represent spin-up and spin-down bands, respectively. The dotted blue line indicates the Fermi level, which is set to zero.	44
Figure 3-9. Total DOS curves for toluene adsorption on (a) Pt-SWCNT, (b) Pd-SWCNT, (c) Rh-SWCNT, and (d) Ru-SWCNT systems. PDOS of the s and p orbitals of C atoms and s orbital of H atoms in Toluene and s and d orbitals of metal atoms are also presented. The positive and negative values denote the spin-up and spin-down channels, respectively. The dashed lines indicate the Fermi level, which are set to zero.	46
Figure 4-1. (a) Relaxed structure of a pristine SWCNT along with various adsorption locations on the SWCNT (Ho: hollow, A: axial, Z: zigzag, and T: top), (b) its energy band structure, the dotted line indicates the Fermi level, which is set to zero. (c) The relaxed molecular structure of octenol, decane, and hexanal in two views are illustrated.	55
Figure 4-2. The possible adsorption sites on the SWCNT.	56
Figure 4-3. The relaxed atomic structures of a) Octenol, b) Decane, and c) Hexanal adsorption on pristine SWCNT surface along with their electronic band structures.	57
Figure 4-4. The most relaxed configuration of a) Pt-decorated SWCNT, b) its band structure, and along with c) its DOS calculations.	60
Figure 4-5. The most stable structures of Pt-decorated SWCNT toward octenol, decane, and hexanal molecules. The distances between the different atoms are shown.	61
Figure 4-6. Electronic band structure, and DOS plots for Pt-decorated SWCNT exposed to (a) octenol, (b) decane, and (c) hexanal molecules. Fermi level with blue dotted line is set to zero.	62

Figure 4-7. The total charge densities of a) octenol, b) decane, c) hexanal on Pt-decorated SWCNT systems.	63
Figure 5-1. (a) Illustration of monolayer phosphorene sheet as well as its primitive unit cell, Brillouin zone with the high-symmetry points, and different possible adsorption sites (b) electronic band structure of the phosphorene unit cell.	69
Figure 5-2. The energetically preferable adsorption configurations of gas molecules upon the pristine phosphorene surface.....	71
Figure 5-3. The obtained electronic band structures for gas molecules on pristine phosphorene (P). The Fermi level was fixed to be zero.	72
Figure 5-4. (a) Illustration of Pt-decorated phosphorene sheet, (b) band structure, and (c) DOS of the pristine phosphorene (P) and Pt-decorated phosphorene (Pt-P).	75
Figure 5-5. The most relaxed structures for adsorption of gas molecules on the Pt-decorated phosphorene surface. (Pt: green, P: orange, C: gray, O: red, H: white).....	77
Figure 5-6. The electronic band structures for gas molecules-Pt-decorated phosphorene (Pt-P). The Fermi level was fixed to be zero (the dotted green line).	78
Figure 5-7. Total PDOS curves of gas molecules-Pt-decorated phosphorene (Pt-P) sheet. The dashed line means the Fermi level, which was set to be zero.	80
Figure 5-8. Illustrations of two probe devices, I–V characteristics calculations for pristine phosphorene (P), and Pt-decorated phosphorene (Pt-P) in a, b) armchair, and c, d) zigzag directions.	82
Figure 5-9. The sensitivity of adsorption of the studied gases for pristine (P) and Pt-decorated phosphorene (Pt-P) sheets for both (a) Armchair (b) Zigzag directions.	83
Figure 5-10. The most stable configuration of different number of Pt on the phosphorene. (a) 2 atoms of Pt. (b) 3 atoms of Pt. (c) 4 atoms of Pt.....	85
Figure 5-11. The most favorable adsorption of methanol upon different number of Pt- decorated phosphorene. (a) 2 atoms of Pt. (b) 3 atoms of Pt. (c) 4 atoms of Pt.	86
Figure 7-1. (a) Top and side view of the optimized structure of a pristine BC ₆ N sheet and its hexagonal unit cell containing six C atoms, one B atom, and one N atom. Bond lengths are given in the unit of Å. (b) The corresponding band structure for a pristine BC ₆ N sheet semiconducting behavior with an energy bandgap of 1.228 eV at the K-point. The dotted green line indicates the Fermi level, which is set to zero.	107
Figure 7-2. The most stable adsorption configurations (top and side view) for (a) acetone, (b) ethanol, (c) methanol, (d) formaldehyde, (e) toluene, (f) carbon dioxide, and (f) water molecules on pristine BC ₆ N sheet.....	109
Figure 7-3. The relaxed structures of co-adsorbed gas molecules on pristine BC ₆ N sheet.....	111
Figure 7-4. The co-adsorption energies of gas molecules on pristine BC ₆ N sheet.	111
Figure 7-5. Energy band structures of (a) acetone, (b) ethanol, (c) methanol, (d) formaldehyde, (e) toluene, (f) carbon dioxide, and (f) water molecules on pristine BC ₆ N sheet. The dotted green line indicates the Fermi level, which is set to zero.....	115
Figure 7-6. The most stable adsorption configurations (top and side view) for defective BC ₆ N sheet with one (a) C vacant adjacent to N atom, (b) C vacant adjacent to B atom, (c) N vacant, and (d) B vacant.	117

Figure 7-7. The most stable adsorption configurations (top and side view) for (a) acetone, (b) ethanol, (c) methanol, (d) formaldehyde, (e) toluene, (f) carbon dioxide, and (f) water molecules on defective BC ₆ N sheet.	120
Figure 7-8. The co-adsorption energies of gas molecules on defective BC ₆ N sheet.	121
Figure 7-9. The relaxed structures of co-adsorbed gas molecules on defected BC ₆ N sheet.	122
Figure 7-10. Energy band structures of (a) acetone, (b) ethanol, (c) methanol, (d) formaldehyde, (e) toluene, (f) carbon dioxide, and (f) water molecules on defective BC ₆ N sheet. The dotted green line indicates the Fermi level, which is set to zero.	123
Figure 7-11. Total DOS curves for (a) acetone, (b) ethanol, (c) methanol, (d) formaldehyde, (e) toluene, (f) carbon dioxide, and (f) water molecules on defective BC ₆ N sheet. The dotted green line indicates the Fermi level, which is set to zero. The dashed lines indicate the Fermi level, which are set to zero.	124
Figure 7-12. (a) Schematic structural model of a gas sensor based on defective BC ₆ N with two electrodes. I–V characteristics of BC ₆ N sensor after (b) acetone, (c) ethanol, (d) methanol, (e) formaldehyde, (f) toluene, (g) carbon dioxide, and (h) water molecules adsorption.	130
Figure 7-13. (a) Sensitivity of pristine and defective BC ₆ N sensor toward acetone, ethanol, methanol, formaldehyde, toluene, carbon dioxide, and water gas molecules. (b) The selectivity of pristine and defective BC ₆ N sensor for ethanol detection.	131
Figure 8-1. (a) Bonds between Pd, P, and S atoms. (b) Schematic of PdPSe-based gas device (c) Electronic Band structure of PdPS unit cell by PBE, and HSE calculations. (d) Bonds between Pd, P, and Se atoms. (e) Schematic of PdPSe-based gas device (f) Electronic Band structure of PdPSe unit cell by PBE, and HSE calculations.	137
Figure 8-2. Phonon band structure for (a) PdPS, and (b) PdPSe monolayers.	139
Figure 8-3. (a) Optimized structure of PdPS-based gas device in both view (side and top) along with possible adsorption sites on the surface (b) DOS of the PdPS monolayer (c) Optimized structure of PdPSe-based gas device in both view (side and top) along with possible adsorption sites on the surface (d) DOS of the PdPSe monolayer.	140
Figure 8-4. The most stable adsorption configurations (top and side view) for CO, CO ₂ , NH ₃ , NO, and NO ₂ gas molecules adsorption on the PdPS along with their corresponding electronic band structure.	143
Figure 8-5. The most stable adsorption configurations (top and side view) for CO, CO ₂ , NH ₃ , NO, and NO ₂ gas molecules adsorption on the PdPSe along with their corresponding electronic band structure.	144
Figure 8-6. Density of states (DOS) for adsorption of (a) CO, (b) CO ₂ , (c) NH ₃ , (d) NO, and (e) NO ₂ gas molecules upon PdPS monolayer.	147
Figure 8-7. Density of states (DOS) for adsorption of (a) CO, (b) CO ₂ , (c) NH ₃ , (d) NO, and (e) NO ₂ gas molecules upon PdPSe monolayer.	148
Figure 8-8. Quantum conductance of (a) PdPS-, (b) PdPSe-based device prior to and post adsorption of the gas molecules.	149
Figure 9-1. (a) Conceptual illustration of a back-gated metal-decorated CNT FET. (b) Flowchart of device fabrication. (c) Photograph of an entire wafer consisting of 147 sensors. (d) Photograph of a single device and optical microscopy image of its interdigitated electrodes. (e) Raman spectroscopy of carbon nanotubes; a small D band, large G band and pronounced 2D band suggest the carbon nanotube structure. (f) SEM image of nanotubes; the inset is an AFM image of a nanotube film.	158

Figure 9-2. Schematic diagram of gas sensing setup.....	159
Figure 9-3. (a) Source-drain current of a back-gated CNT FET as a function of gate voltage measured in dry air (initial), after exposure in 80% humid air for 5 min, recovery with N ₂ for 10 min, recovery in dry air at 150°C for 2.5 min, and recovery in dry air at 150°C for 5 min. (b) The difference between source-drain current presented in (a) and the source-drain current measured in dry air (initial) versus gate voltage. (c) The normalized source-drain current change of the back-gated CNT FET in N ₂ and humid air (RH = 80%) at different gate voltages. The inset shows source-drain current change at V _G = 0, -5, and -10 V. (d) Dynamic sensing transient of a back-gated CNT FET for 300 ppm formaldehyde in DI water at room temperate. D, H, and HF represent drift, humid air, and formaldehyde in humid air, respectively. The V _{ds} were set to 1 V.....	164
Figure 9-4. The I _{sd} - V _G characteristics for a back-gated (a) bare, (b) Ni-decorated, (c) Pd-decorated. (d) Pt-decorated, and (e) ITO-decorated CNT FETs at V _{sd} = 1V. Hysteresis (V _{Hysteresis}) was measured at (I _{sd,max} + I _{sd,min})/2 between the forward (FW) and reverse (RV) sweeps. (f) Hysteresis and area of hysteresis loop for different back-gated CNT FETs.....	166
Figure 9-5. (a) Conductance change and (b) sensitivity of back-gated Bare, Ni-, Pd-, Pt-, ITO-decorated CNT FETs to 300 ppm formaldehyde at RH=80% and room temperate. Experiments were done at V _g = -5 V and V _{ds} = 1 V.	167
Figure 9-6. Dynamic sensing transients of back-gated Pt-decorated CNT FET for 3 ppb - 300 ppm formaldehyde at RH=80% and room temperate. Experiments were done at V _g = -5 V and V _{ds} = 1 V.....	168
Figure 9-7. (a) The sensitivity of the back-gated Pt-decorated CNT FET as a function of formaldehyde concentration at RH=80% and room temperate. The insets show a zoom on 0.003 – 0.03 ppm, 0.3 – 30 ppm, and 30 – 300 ppm regions. (b) The dynamic response-recovery curve of the back-gated Pt-decorated for 300 ppm formaldehyde at RH=80% and room temperate. The response and recovery curves were modeled by an exponential fit (dashed lines) (c) Dynamic response-recovery curve of the back-gated Pt-decorated for 300 ppm formaldehyde. The first recovery (blue region) was done at RH=80% and T = 70°C. The second recovery (green region) was made in a dry atmosphere at T = 70°C. The response and recovery curves were modeled by an exponential fit (dashed lines). Experiments were done at V _g = -5 V and V _{ds} = 1 V.	169
Figure 9-8. The dynamic response-recovery curve of the back-gated Pt-decorated for 3 ppb formaldehyde at RH=80% and room temperate. The response and recovery curves were modeled by an exponential fit (dashed lines).	172
Figure 9-9. (a) The optimized structures of pristine CNT, CNT-formaldehyde, CNT-water, CNT-methanediol and their corresponding energy band structures. (b) The optimized structures of Pt- CNT, Pt-CNT-formaldehyde, Pt-CNT-water, Pt-CNT-methanediol and their corresponding energy band structures. The bond lengths and the binding distances are also given in the unit of Å. The sticks between atoms are only for visualization. The dotted blue line indicates the Fermi level, which is set to zero.....	176
Figure 9-10. Total DOS curves for (a) pristine CNT, (b) Pt-CNT-formaldehyde (F), (c) Pt-CNT-water (W), and (d) Pt-CNT-methanediol (M). The dashed lines indicate the Fermi level, which are set to zero.	181
Figure 9-11. The experimental sensitivities of the back-gated Pt-decorated SWCNT FET to 80% humidity and formaldehyde in 80% humidity vs the DFT sensitivities of the Pt-decorated SWCNT to individual formaldehyde, water, and methanediol molecule.	184

LIST OF TABLES

Table 3-1. Bond distances (d) and angles (\angle) of the toluene molecule before and after interaction with pristine and metal decorated SWCNT.	32
Table 3-2. The calculated adsorption energy (E_{ad}), binding distance between the metal atom and the nanotube (D), magnetic moment (m), charge transfer (Q), Fermi level (EF), energy bandgap (E_g) for spin-up (-down) channel. The negative values of charge indicate a charge transfer from metal to the nanotube. a: Ca atom and b: Cb atom in Figure 3-1 (a).	39
Table 3-3. The calculated adsorption energy (E_{ad}), binding distance (D) which is the distance between C1-C6 of the toluene and the metal in the metal-decorated CNT structure (the underlined distance is the shortest distance) or the shortest distance between the toluene molecule and the nanotube in the pristine CNT structure, magnetic moment (m), charge transfer (Q), energy bandgap (E_g), sensitivity (S), and recovery time (τ) at 498 K. The negative values of charge indicate a charge transfer from molecule to the nanotube. T: Toluene.	42
Table 4-1. The energy bandgap of (m,0) zigzag SWCNTs (E_g), where m is the chiral index of the SWCNT.	55
Table 4-2. The calculated adsorption energy (E_{ad}), interaction distance (D), which is the distance between the molecule and SWCNT, charge transfer (Q), energy bandgap (E_g), and recovery time (τ).....	58
Table 5-1. Calculated absorption energy (E_{ad}), minimum distance of interaction (D), where is the minimum distance between the gas and phosphorene surface, net total charge transfer (Q), (The negative values of charge imply that the molecule gives charges to the sheet), energy bandgap (E_g), and recovery time (τ).	74
Table 5-2. The adsorption energy of the different number of Platinum on the pristine Phosphorene surface.	84
Table 5-3. The adsorption energy of Methanol on the the different number of Pt- decorated Phosphorene surface... ..	85
Table 6-1. The calculated adsorption energy (E_{ad}), interaction distance (D), which is the distance between the molecule and the MoS2 sheet, net charge transfer (Q), (the negative values of charge indicate a charge transfer from the molecule to the surface, and vice versa), energy bandgap (E_g), and recovery time (τ).....	98
Table 7-1. The calculated adsorption energy (E_{ad}), interaction distance (D), which is the distance between the molecule and BC ₆ N sheet, charge transfer (Q), energy bandgap (E_g), and recovery time (τ). The negative values of charge indicate a charge transfer from the molecule to the nanotube.....	114
Table 7-2. The sensitivity (%) of the sensor based on defective BC ₆ N with two electrodes toward acetone, ethanol, methanol, formaldehyde, toluene, carbon dioxide, and water molecules at bias voltages of 1.0, 1.2, and 1.4 V. Negative (positive) sensitivity means that the current of the sensor dropped (enhanced) after interaction with the gas molecule.	127
Table 7-3. Theoretically reviewed 2D materials for VOCs sensing.	128
Table 8-1. The calculated adsorption energy (E_{ad}), interaction distance (D), which is the distance between the molecule and the PdPS/ PdPSe sheets, charge transfer (Q), the negative values of charge indicate a charge transfer from the molecule to the nanotube, energy bandgap (E_g), and recovery time (τ).	145
Table 9-1. The calculated adsorption energy (E_{ad}), binding distance which is the shortest atom to atom distance between molecule and the nanotube (D), the charge transfer (Q) on the molecule or Pt, energy bandgap (E_g), and sensitivity (S). The negative values of charge indicate a charge transfer from the molecule to the nanotube.	179

Abbreviations

CNT	Carbon nanotubes
SWCNT	Single-walled carbon nanotubes
VOCs	Volatile organic compounds
FET	Field Effect Transistors
POC	Point-of-care
IVD	IN-VITRO DIAGNOSTICS
VOCs	Volatile organic compounds
LC	Lung cancer
CRC	Colorectal cancer
BC	Breast cancer
BP	Black phosphorene
BC ₆ N	Borocarbonitride
PdPX	Phosphochalcogenides
TMDs	Transition metal dichalcogenides
DFT	Density functional theory
ATK	Atomistix toolKit
NEGF	Nonequilibrium green's function
vdW	van der Waals

Chapter 1

INTRODUCTION

1.1 Motivation

Nanotechnology, a developed technology based on quantum mechanics, molecular biology, material science, microelectronics, and computer technology, is a scientific way to synthesize new materials on nanoscales. The ideas and concepts behind nanoscience and nanotechnology started in December 1959 with a talk called “There’s Plenty of Room at the Bottom” by physicist Richard Feynman at an annual meeting of American Physical Society at the California Institute of Technology, long before the term nanotechnology was used. Over a decade later, Prof. Tanggulachi firstly defined this newly emerged subject as nanotechnology [1].

The National Nanotechnology Initiative (NNI) in the United States describes Nanotechnology as “a science, engineering, and technology conducted at the nanoscale (1 to 100 nm), where unique phenomena enable novel applications in a wide range of fields, from chemistry, physics and biology, to medicine, engineering and electronics” [2].

The field of nanotechnology has recently focused more on gas sensing technology. The discipline has rapidly grown as demand for highly sensitive and selective sensors has increased, with applications spanning, health, public safety, agriculture, and industry.

Gas sensing is essential for managing chemical processes, preventing air pollution and health risks, contaminating devices, and making medical diagnoses. The creation of novel systems for gas sensing with high sensitivity, selectivity, stability, and quick reaction and recovery has taken a lot of work [3, 4]. In theory, gas sensors function by converting detectable signals from gas adsorption. Due to their outstanding performance and inexpensive cost, conductance-based gas sensors have earned a lot of interest.

Nanotechnology-based gas sensors for the detection of diseases through exhaled breath are devices that detect and analyze the chemical composition of exhaled breath to identify specific biomarkers that indicate the presence of certain diseases. These sensors use advanced technology to detect even trace amounts of gases and volatile organic compounds (VOCs) in breath samples,

which can help diagnose diseases such as lung cancer, asthma, and chronic obstructive pulmonary disease (COPD) at an early stage. The use of gas sensors for disease detection through exhaled breath offers a non-invasive and cost-effective alternative to traditional diagnostic methods, making it an attractive option for healthcare providers and patients alike.

The potential of new materials, and the development of semiconductors as sensing components have also fueled the development of the sensing industry [5, 6]. Semiconductors are the foundation of modern solid-state and electronic devices [7]. The number of transistors per square inch on integrated circuits doubles annually, according to an observation known as Moore's law [8]. The size of the devices has continually dropped at a rate similar to that predicted by Moore's law due to a variety of advancements in semiconducting materials, their characteristics, and the procedures used to fabricate them [9]. The performance and efficiency of these devices have greatly increased as a result of their reduction in size.

The market for point-of-care (POC) and in vitro diagnostic (IVD) devices for the detection of diseases through exhaled breath is growing rapidly, driven by the increasing prevalence of chronic diseases and the need for non-invasive and accurate diagnostic tools. The global market for breath analyzers is expected to reach \$1.4 billion by 2024, with a CAGR of 24.6% from 2019 to 2024, and the U.S. breath analyzers market is anticipated to expand at a CAGR of 15.4% from 2022 to 2030. These growth projections highlight the importance and potential of developing new and innovative gas sensor technologies for disease detection through exhaled breath. So, one of the motivations behind this dissertation comes from the market, where there is a rising daily desire for new technological products especially in POC and IVD devices.

Due to their widespread use and high sensitivities, metal oxide-based gas sensors have been the subject of much research in recent years [10]. However, a very high operating temperature would be used in order to provide a strong response to the targeted gases. This compromises the practical applications of these devices because it increases power consumption and poses thermal safety issues [11]. Another motivation behind this dissertation is to make new gas-sensing materials with extremely high surface-to-volume ratios and robust surface activities is a remarkably simple and effective method for creating gas sensors that operate at low or room temperature.

Nowadays, two-dimensional (2D) nanomaterials, a class of single-atom thick materials could now solve the obstacles. They can create high-mobility, low-power, large-area, flexible, and

inexpensive electronic devices and have a number of advantages for further miniaturizing nano-electronic devices [12-15]. They are resilient to the effects of quantum confinement due to their inherent thinness. Additionally, 2D materials do not have problems with dangling bonds or surface roughness. Consequently, because of their outstanding qualities, 2D nanomaterial-based nano-electronic devices have the potential to transform the global market.

Due to their exceptional semiconducting performance and distinctive, thickness-dependent physical and chemical features, such as extremely high surface activity and huge surface-to-volume ratios, 2D layered nanomaterials have attracted a lot of attention [16-19]. Furthermore, field-effect transistors (FETs) with low power requirements and good thermal safety may be made with ease from 2D layered nanomaterials. These benefits set 2D layered nanomaterials apart from traditional metal oxides and provide them with a bright future in the creation of ultrahigh sensitivity and power-efficient sensor platforms.

Last but not least motivation for this dissertation is to help in early diagnosis of serious diseases such as lung cancer, liver cancer, colorectal cancer and Alzheimer [20]. Since ancient times, physicians have known the relationship between a person's smell and corresponding disease state. Breath analysis dates back to ancient Greeks, who used exhaled breath for diagnosis of different diseases. For example, a sweet, fruity odor can be a sign of complications from diabetic ketoacidosis, a sewer smell of breath can be an indication of lung disease and bacterial proliferation and a fishy smell can be indications of liver ailments [21, 22]. For these reasons, improved diagnostic methods are necessary.

1.2 General Statement of Problem Area

The discovery and development of disease biomarkers have revolutionized the diagnosis and treatment of many diseases. The ability to identify diseases using human breath has been made possible by modern nanotechnology, which has allowed the development of gas sensors that can detect and monitor a variety of diseases from human breath. The use of advanced materials and technologies for the detection of volatile organic compounds (VOCs) in human breath such as semiconductor gas sensors can achieve simultaneous recognition for many analytes, improving the accuracy of diagnosis when used in conjunction with pattern-recognition technology. The analysis of volatile organic compounds in exhaled breath samples provides a new frontier in medical diagnostics due to their noninvasive nature and possible cost-effectiveness.

Among the possible one-dimensional materials in gas detectors, Carbon nanotubes (CNTs) have exhibited emerging advances especially for fabricating field-effect transistor (FET)-type gas sensors [23, 24]. The single wall carbon nanotube (SWCNT) is a great candidate for gas sensing applications thanks to its small size, high surface-volume ratio, excellent charge transfer, fast response, high sensitivity, high adsorption capacity and low operational temperature.

Inspired by the triumphs of graphene, other 2D nanomaterials, such as transition metal dichalcogenides (TMDs), MoS₂, MXenes, silicene, borocarbide, and borophene, to name a few, have become the center of intense research for the development of advanced gas sensing devices [25-27]. Due to the significant direct band gap that is caused by spin-orbit coupling in phosphorene, and TMDs, these materials have garnered a lot of attention. For example, unlike semimetallic graphene, phosphorene has a semiconductor character with a high carrier mobility of up to 1000 cm² V⁻¹ s⁻¹ at room temperature, making it a promising candidate for nanoelectronic and gas sensing applications [28, 29]. Thickness-dependent band gap, significant in-plane anisotropy, and high carrier mobility are some of phosphorene's most noteworthy characteristics [30].

Besides, in MoS₂'s monolayer, numerous studies have shown that the band gap, energy levels, and electronic structure properties can be well tuned (e.g., range from 1.0 to 2.0 eV) [31] by a variety of physical and chemical parameters [32], such as chemical doping [33], chemical modification [34], defect engineering [35], strain engineering [36], foreign species intercalation [37], and heterostructure construction [38].

Graphene has a limited sensitivity to the adsorption of gas molecules, however this sensitivity can be increased by adding dopants or structural flaws [39-42]. Excitingly in phosphorene monolayer, each phosphorus atom establishes bonds with three nearby phosphorus atoms in a puckered honeycomb configuration [43, 44]. As a result of their buckled structure, phosphorene and TMDs are anticipated to have a significantly higher chemical reactivity for molecules adsorption than graphene, making them suitable materials for gas molecule detection.

Contrarily, due to the much lesser impact of gas molecule adsorption on the electrical properties of semiconducting materials than on metallic materials, conductance-based nanoscale gas sensors are more sensitive than those based on metallic materials. This issue might be resolved by the semiconducting armchair ribbons of 2D materials.

1.3 Research Objectives

This dissertation uses first-principles simulations and experiments to investigate the electrical, magnetic, and gas sensing capabilities of CNTs particularly SWCNT nanomaterials, common and novel 2D materials.

Initially, due to the attractive features of FET-based gas sensors such as small size, easy integration, mass-production capability, and low-cost manufacturing, we have developed a FET-type SWCNT. Later, we used computational methods and employed first-principles methods based on density functional theory (DFT) to investigate the adsorption behavior of a gas molecules on a SWCNT-based gas sensor. We will concentrate on the following aspects for SWCNT:

- 1) The potential and well-known analytes present in exhaled breath which could be related to diseases were extracted and categorized.
- 2) The theoretical First principle method based on DFT was carried out for different biomarkers as well as various nanomaterials.
- 3) A thin film of high-purity semiconducting SWCNTs network was used to fabricate a back-gated Pt-decorated SWCNT FET sensors.
- 4) The sensing capability of the fabricated SWCNT FET to aldehydes at a sub-ppb level such as formaldehyde was assessed.
- 5) The theoretical DFT method was implemented for the system and results were compared with the actual experimental results.

Moreover, in the quest for finding the gas sensor substrate based on 2D nanomaterials other than graphene, different nanomaterials such as phosphorene, TMDs (MoS_2 , WS_2), and other novel materials and graphene-like materials such as BC_6N were investigated. We will focus on the following viewpoints for 2D materials:

- 6) Inspecting the most stable adsorption configurations, adsorption sites, adsorption energies, charge transfer, quantum conductance modulation, and electronic properties of all studied gas molecules on the adsorbents.
- 7) Exploring new materials that have lately been introduced and applied.

- 8) The effects of functionalization, decoration, and defects on the sensitivity of adsorbents.

1.4 Organization of This Dissertation

The rest of this dissertation is organized into the following sections:

A literature review on SWCNTs, common allotrope of phosphorus (black phosphorene), TMDs (MoS_2 , and WS_2), novel 2D materials such as borocarbonitride (BC_6N), and PdPS/Se materials is given in Chapter 2. In Chapter 3, the study focuses on the SWCNT-based sensor's ability for detection of volatile organic compounds (VOCs) using DFT and nonequilibrium Green's function (NEGF) methods. Several VOCs, such as acetone, ethanol, formaldehyde, methanol, toluene, benzaldehyde, decane, and hexanal, along with CO_2 and H_2O molecules, were considered as the target gases. In this chapter, its sensing behavior to detect toluene, which is an important biomarker for certain diseases, particularly lung cancer is scrutinized. Chapter 4 of this dissertation focuses on the potential capability of SWCNT to detect biomarkers of liver cancer, such as 1-Octen-3-ol (octenol), decane, and hexanal compounds. The methodology used to investigate the SWCNT's sensing properties towards these compounds.

Chapter 5 is dedicated to the black phosphorene (BP) as a 2D material, we have investigated the potential application of BP-based sensor for detection of VOCs using DFT. Furthermore, the capacity of MoS_2 , and WS_2 as a subfamily of TMDs, for the detection of specific VOCs related to colorectal, and breast cancers was examined using the theoretical method in Chapter 6. Chapter 7 relates the gas sensing competence of novel 2D materials such as BC_6N using first principle calculations. In chapter 8, the adsorption of gas molecules (NO , NO_2 , NH_3 , CO , and CO_2) on novel 2D phosphochalcogenides PdPX ($X = \text{S}, \text{Se}$) nanosheets are examined. Finally, chapter 9 presents an experimental and theoretical study of SWCNT-based sensors for formaldehyde as an important biomarker in exhaled breath of lung cancer patients. The SWCNT-based device fabrication, and

test rig are described in this chapter. The summary, conclusion and outlook have been shown in Chapter 10.

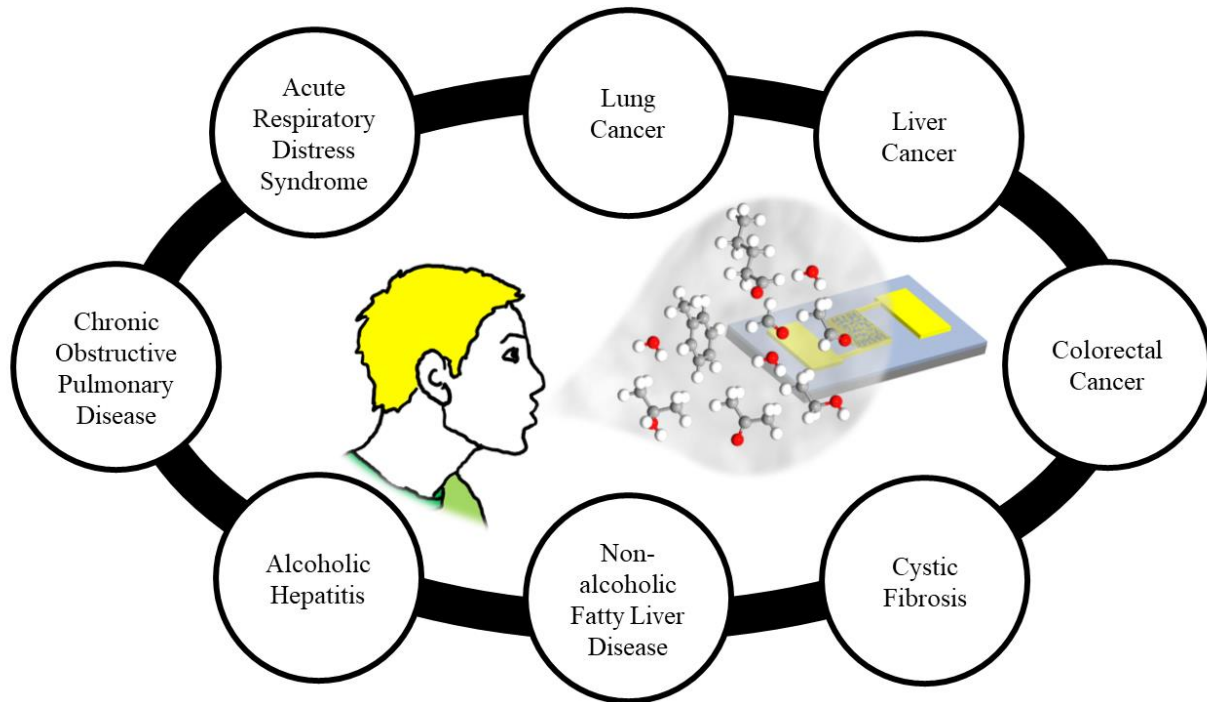


Figure 1-1. Graphical abstract.

2. Chapter 2

Background and State of the Art

2.1 Carbon nanotubes (CNTs)

Graphene is a planar monolayer of carbon atoms arranged in a 2D honeycomb crystal structure. Graphene is an allotrope of carbon and the fundamental component of all other allotropes of carbon [45]. As demonstrated in Figure 2-1, graphene layers can be stacked to create 3D graphite, rolled to create 1D carbon nanotubes (CNT), or wrapped to create 0D fullerene [46].

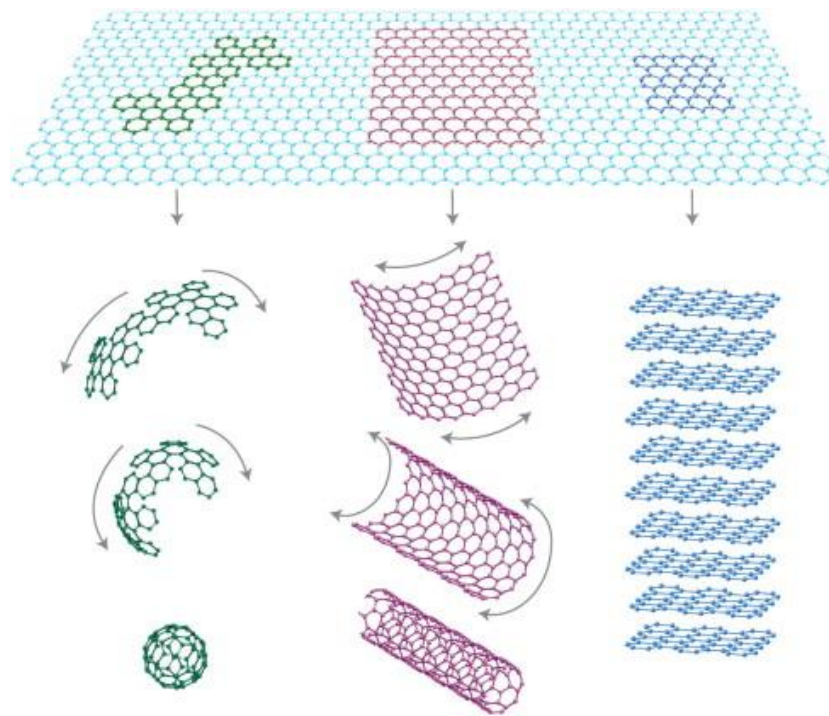


Figure 2-1. The foundation of all carbon allotropes is graphene. It can be rolled into 1D nanotubes (middle) or layered into 3D graphite (right), and 0D fullerene (left). Figure taken from Reference [47] with permission.

CNTs are made up of one or more sheets of carbon atoms that are shaped like cylinders. As a by-product of arc-discharge experiments where it was noticed that fine carbon-like fibers formed on the discharge cathode, carbon nanotubes were first identified and characterized by Iijima in 1991 [48]. It was quickly discovered that carbon nanotubes have remarkable mechanical, electrical, thermal, and optical properties. The chirality of graphene is described as the rolling up of the material, and it has a chiral vector \vec{C}_h that is inversely correlated with the size of the CNTs.

Depending on how they were created, single wall carbon nanotubes (SWCNT) can range in length from a few micrometers to 0.4–2.6 nm [49, 50]. The multi-wall carbon nanotube (MWCNT), another type of CNT, is made up of multilayer cylinders with an interlayer spacing of 2.7 to 4.2 [51], depending on the cylinders' diameter and quantity. MWCNTs have a diameter between 10 and 20 nm [52].

As seen in Figure 2-2, a sheet of covalently connected graphene has carbon atoms arranged in hexagonal patterns. A weaker van der Waals bond stacks the layers of graphene to produce graphite. The beginning and conclusion of a (m,n) lattice vector on the graphene plane serve as indices of CNT when they combine to form the tube (Figure 2-2 (a)). The lattice vector affects the chirality, diameter, and other characteristics of CNTs. CNTs with an index of (m,m) have armchair chirality, and tubes with an index of (m,0) have zigzag chirality [52].

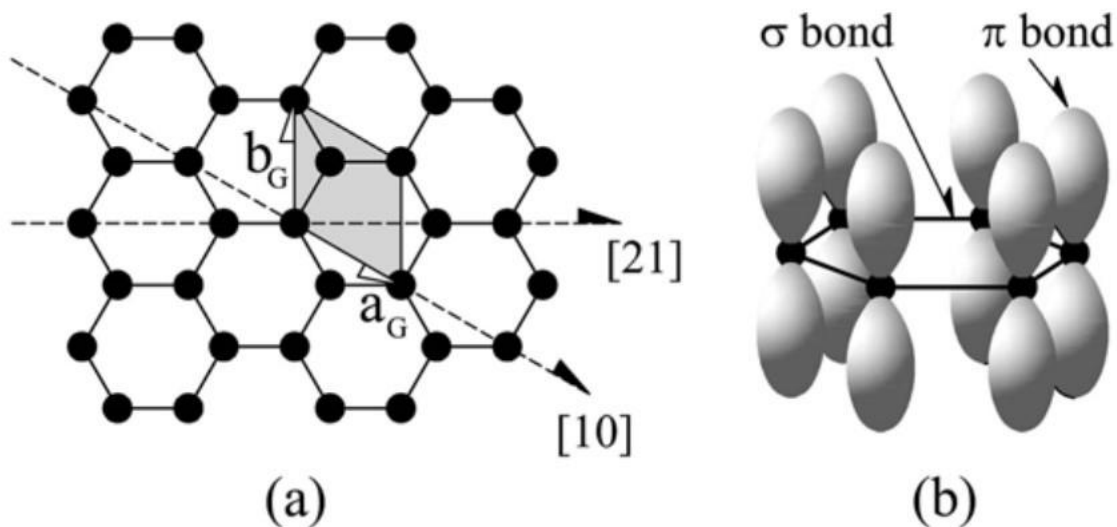


Figure 2-2. (a) The carbon atoms' hexagonal configuration in CNT and graphene. The conventional unit cell vectors a_G (m) and b_G (n) are shown, together with the unit cell (shaded) having two carbon atoms. Additionally, two distinct lattice vectors (2,1) (1,0) are shown. (b) Diagram of the perpendicular to the plane of the sheets in-plane σ bonds and π orbitals [53].

The chemical and electrical characteristics of CNTs are governed by their chirality and diameter. Figure 2-3 demonstrates how various lattice structures result in various CNTs. Figure 2-3 (a) shows a chair-sized nanotube (10,10). The initial Brillouin zone of a graphene sheet is depicted in the hexagon's bottom panel in reciprocal space, and the vertical lines indicate the electronic states of the nanotube.

The center-line of this particular nanotube crosses two hexagonal corners, creating a metallic nanotube [52]. Figure 2-3 (b) and (c) depict zigzag chirality in two distinct CNTs with lattice indices of (12,0) and (14,0). Although the electronic states in Figure 2-3 (b)'s bottom panel straddle the hexagonal corners, a minor band gap may form because of the nanotube's curvature. The corner points of the hexagonal carbon atom in Figure 2-3 (c) are not covered by the states on the vertical lines. This nanotube is hence semiconducting. Since the corners of the carbon hexagonal are not positioned along the vertical lines of the electronic state, Figure 2-3 (d), a chiral CNT with a (7, 16) lattice, is also a semiconducting CNT [52].

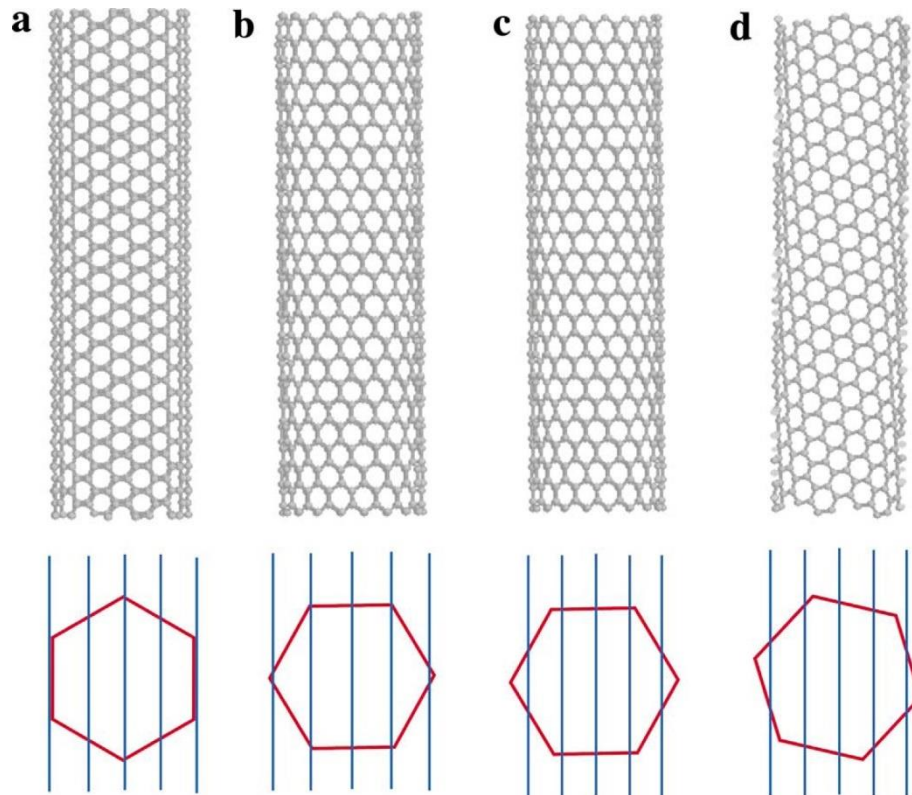


Figure 2-3. According to their chirality and dimension, distinct types of nanotubes have diverse structures: a) metallic armchair CNT, b) metallic zigzag CNT, c) semiconductive zigzag CNT, and d) semiconductive chiral CNT [52].

The ideal and pure structure of a CNT is formed of unbroken covalent carbon-carbon bonds, which gives CNTs their strength. SWCNT's Young's modulus has been calculated to be 1.25 TPa [54]. MWCNTs have demonstrated up to 63 GPa of tensile strength and 12% of elongation [55]. NASA scientists only recently began considering the possibility of building a CNT-based space elevator to the moon [56]. Naturally, it is still difficult to correctly combine CNTs so that they may be used at their maximum strength at the macroscale.

CNTs and other 2D nanostructured materials are both often synthesized today using the chemical vapor deposition (CVD) technique [57-60]. More control over the solid-state CNTs' shape, growth direction, and other characteristics is possible with CVD. By heating a catalyst to high temperatures (500–1000 °C) in a tube furnace

while a hydrocarbon gas is flowing through the tube reactor, CNTs are created during CVD. The tabular form of carbon results from the dissociation of hydrocarbon molecules catalyzed by the transition metal catalyst and the dissolution and saturation of carbon atoms in the metal nanoparticle.

The ability to create CNTs with regulated diameter size, orientation, and even chirality is a benefit of the CVD technique. Aligned CNTs can be made into a variety of shapes by CVD, including horizontal films [61], vertical forest [62, 63], cylindrical pillars [62], and sheets [62]. These shapes can be employed for a variety of applications, such as imaging and probing [64], microelectronics [65], and sensors [61].

The physical structure of the graphene lattice is what gives carbon nanotubes their electrical structure. With the enforced boundary conditions stated in the preceding section, the electronic properties are thus obtained from the graphene's dispersion relation, which connects the energy to the permitted wave vectors. Using the tight binding method, the 2D Schrödinger equation is solved to get the dispersion relation.

The dispersion relation of graphene is depicted in Figure 2-4. Where the valence and conduction bands converge, there are six high symmetry locations called Dirac points, also known as K-points. The dispersion relation takes the form of a cone that is known as the Dirac cone when it is close to the Dirac points. Figure 2-5 illustrates how the band structure of a CNT resembles a slice of the Dirac cone as a result of the boundary requirements imposed by the development of a carbon nanotube.

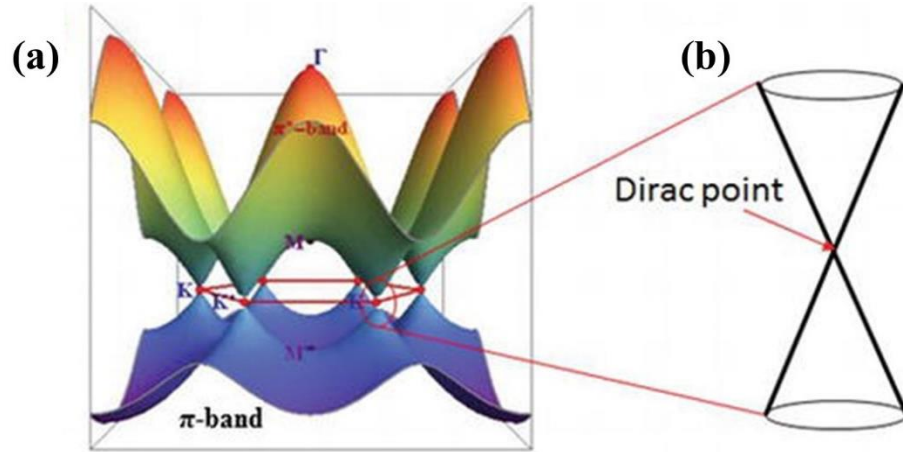


Figure 2-4. Graphene's relation to dispersion Where the conduction and valence bands collide, there are six high-symmetry K-points called Dirac points. The shape transforms into a cone known as the Dirac cone very near these spots [66].

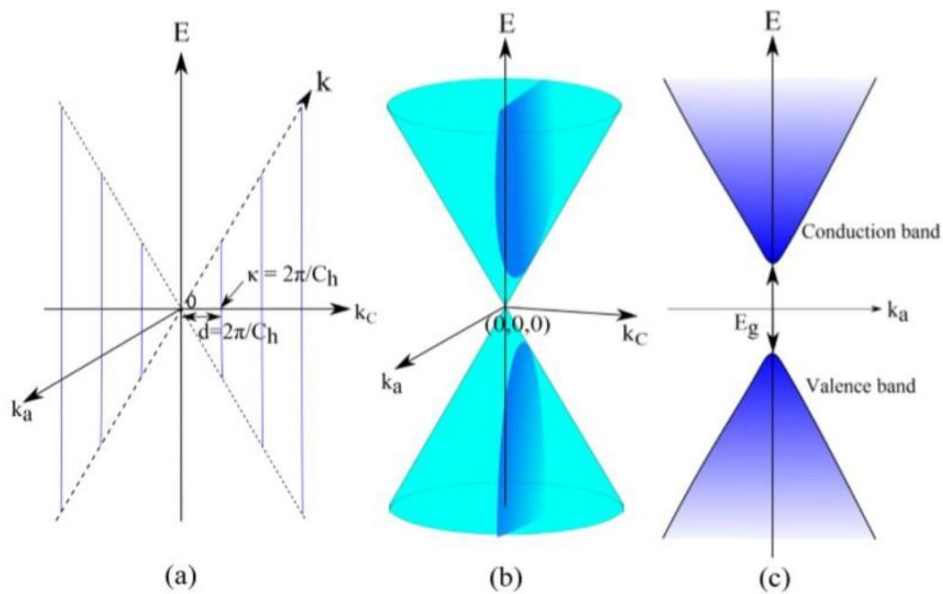


Figure 2-5. Carbon nanotubes' electronic band structure. Dirac cone with authorized \vec{k}_C wave vectors in (a), dispersion relation with one of the K-points and the Dirac cone in (b), and a slice of the dispersion relation for a certain allowed wave vector, $\vec{k}_C \neq 0$, displaying the conduction and valence bands as well as the bandgap in (c) [67].

Thus, for a given \vec{K}_c , a slice of the Dirac cone is produced, and depending on whether it contains the zero point at which the conduction and valence bands intersect, metallic CNTs can be produced, or semiconducting CNTs with a bandgap can be produced. The diameter of the carbon nanotube, which determines the type and bandgap energy of a CNT, is what matters structurally in this situation. For CNTs, the dispersion relation is given by:

$$E(\vec{K})_{linear}^{\pm} = \pm hv_f |\vec{K} - \vec{k}| = \pm \left(\frac{\sqrt{3}}{2} \right) a V_{pp\pi} |\vec{K} - \vec{k}| \quad (1)$$

Where denotes the initial Brillouin zone's offset of $\vec{K} = \vec{K}_c + \vec{K}_a$ from its origin, v_f denotes the Fermi velocity corresponding to the Fermi energy, $V_{pp\pi}$ denotes the nearest neighbor interaction energy, and a denotes the graphene lattice spacing. The quantity of quantum states per unit of energy is contained in the density of states (DOS). The DOS for a specific sub-band, $E_a(k)$, in a CNT, a 1D solid, is given by:

$$D_a(E) = \frac{1}{\pi} \frac{dk}{dE_a} \quad (2)$$

One adds together all of the sub-bands E_a in order to get the overall density of states. Figure 2-6 depicts the appearance of various sub-bands and the related DOS. The charge carrier density, group velocity, and finally the current through the CNT may all be found out from the DOS.

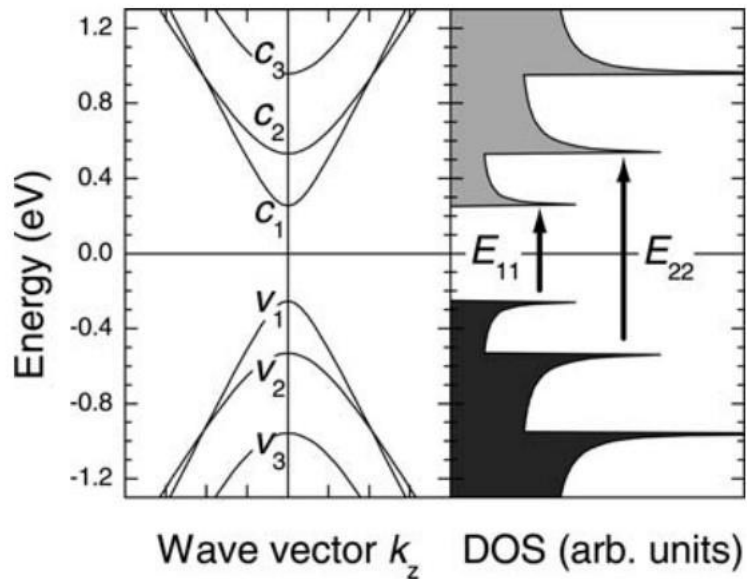


Figure 2-6. A semiconducting carbon nanotube's DOS for a number of its subbands is represented graphically, highlighting a discrete bandgap in the band diagram [68].

2.2 Phosphorus

The allotropes of phosphorus, such as blue phosphorus (blue P), green phosphorus (green P), and black phosphorus (black P), are notable for their diversity. [69-72]. The elemental 2D substance after graphene, called Black P, was successfully isolated in 2014 with the proven field-effect functionality [73, 74]. Similar to bulk graphite, black P is a layered substance in which individual atomic layers are stacked on top of one another by van der Waals interactions. Each phosphorus atom in a layer forms a puckered honeycomb structure by covalently bonding to three nearby phosphorus atoms as depicted in Figure 2-7. Phosphorene is the name for monolayer black P, and it is the most thermodynamically stable allotrope.

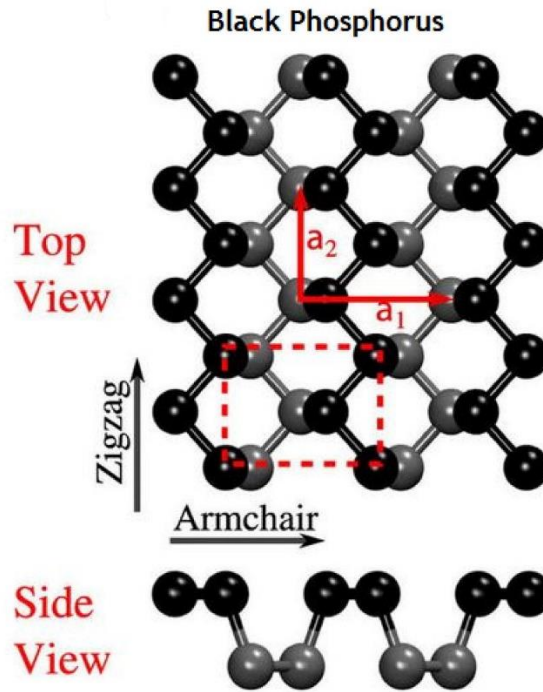


Figure 2-7. The composition of black P crystals [75].

It was reported that by using an adhesive tape and micromechanical cleavage, atomically thin phosphorene flakes can be separated from their parent bulk crystal (BP), which is readily accessible in the market [73, 74]. According to photoluminescence spectra, the band gap of phosphorene is 1.45 eV after being transferred onto the Si/SiO₂ substrates (see Figure 2-8).

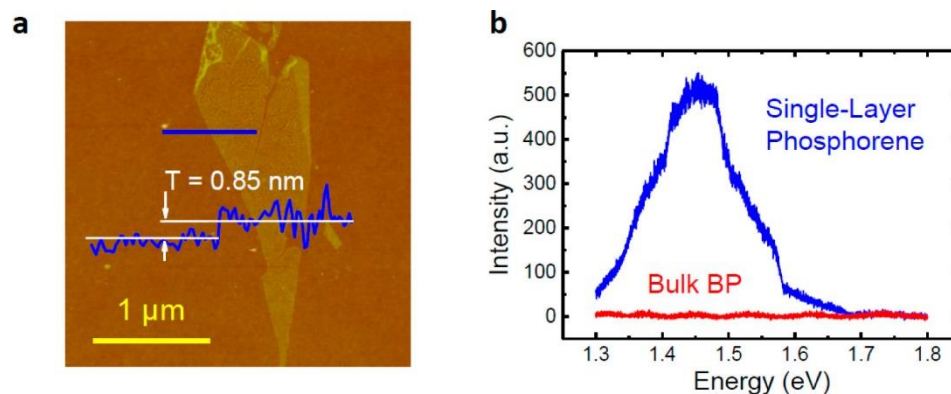


Figure 2-8. Photoluminescence spectra for single-layer phosphorene and bulk BP samples on a 300 nm Si/ SiO₂ substrate, exhibiting a strong signal at 1.45 eV, and an AFM image of a single-layer phosphorene crystal with the reported thickness of 0.85 nm from exfoliation process [74].

2.3 Transition metal dichalcogenides (TMDs)

A single layer of TMDs is composed of metal atoms sandwiched between chalcogen atoms. Through covalent bonding, the metal is joined to the nearby chalcogens. In addition, weak van der Waals forces of attraction hold such layers together in a stack (Figure 2-9).

Transition Metal Dichalcogenides (TMDC) - MX₂
M = Transition metal
X = Chalcogen

1																	18
H	2											13	14	15	16	17	He
Li	Be											B	C	N	O	F	Ne
Na	Mg	3	4	5	6	7	8	9	10	11	12	Al	Si	P	S	Cl	Ar
K	Ca	Sc	Ti	V	Cr	Mn	Fe	Co	Ni	Cu	Zn	Ga	Ge	As	Se	Br	Kr
Rb	Sr	Y	Zr	Nb	Mo	Tc	Ru	Rh	Pd	Ag	Cd	In	Sn	Sb	Te	I	Xe
Cs	Ba	Lu	Hf	Ta	W	Re	Os	Ir	Pt	Au	Hg	Tl	Pb	Bi	Po	At	Rn
Fr	Ra	Lr	Rf	Db	Sg	Bh	Hs	Mt	Ds	Rg	Cn	Uut	Fl	Uup	Lv	Uus	Uuo

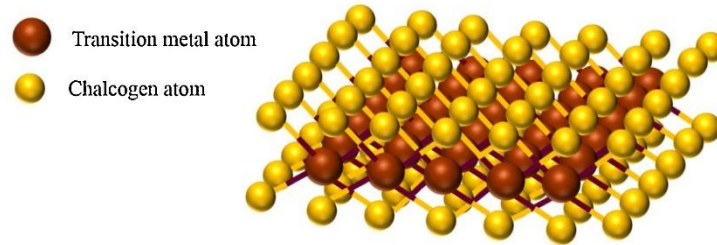


Figure 2-9. Layered transition metal dichalcogenides material's crystalline structure shown schematically [76].

They can be made using a variety of methods, such as liquid exfoliation, micromechanical exfoliation, and CVD [77, 78]. MoS₂, and WS₂, are excellent examples of TMDs for chemical sensing among disulfides. An n-type semiconductor among these TMD 2-D stacked materials is MoS₂ [25]. Cho et al. [79] used in situ photoluminescence to clarify the charge transfer-based gas sensing mechanism in atomically layered MoS₂.

An optical view of the MoS₂ gas sensor with two patterned Au electrodes and a 10 μm by 10 μm gap is shown in Figure 2-10 (a). SEM imaging of a MoS₂ layer creating the device channel with the usual morphology of a one atomic layer network of merging triangular MoS₂ crystals is shown in Figure 2-10 (b), and (c).

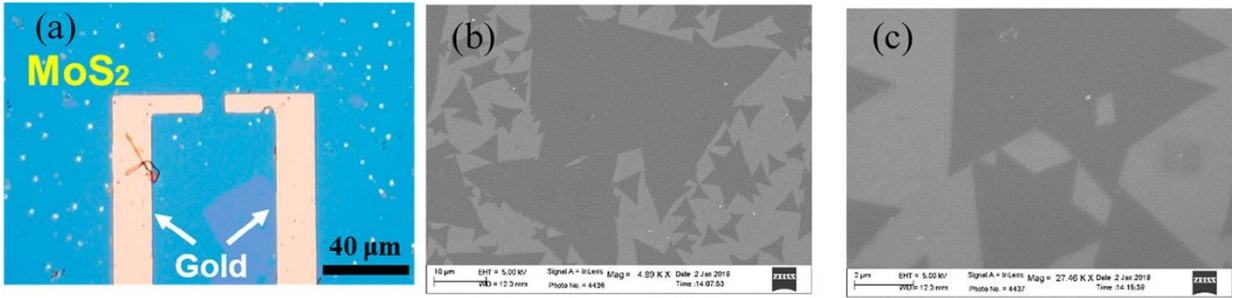


Figure 2-10. (a) MoS₂ device optical image with Au electrodes. (b, c) SEM pictures of the MoS₂ layer at various magnifications and scale bars (10 and 2 μm, respectively) [80].

A schematic of the MoS₂ FET-based sensor for NO₂ and NH₃ detection is shown in Figure 2-11 [81]. Figure 2-11 (b) displays the optical picture of the device with Ti/Au electrodes and a MoS₂ channel. Reactive gas molecules are adsorbed on the surface of the MoS₂ upon exposure, changing the concentration of charge carriers. The current variations could be measured to keep track of this alternation. When exposed to 400 parts per billion (ppb) of NO₂ and 500 parts per million (ppm) of NH₃, the device's IDS-VDS is plotted in Figure 2-11 (c) and (d).

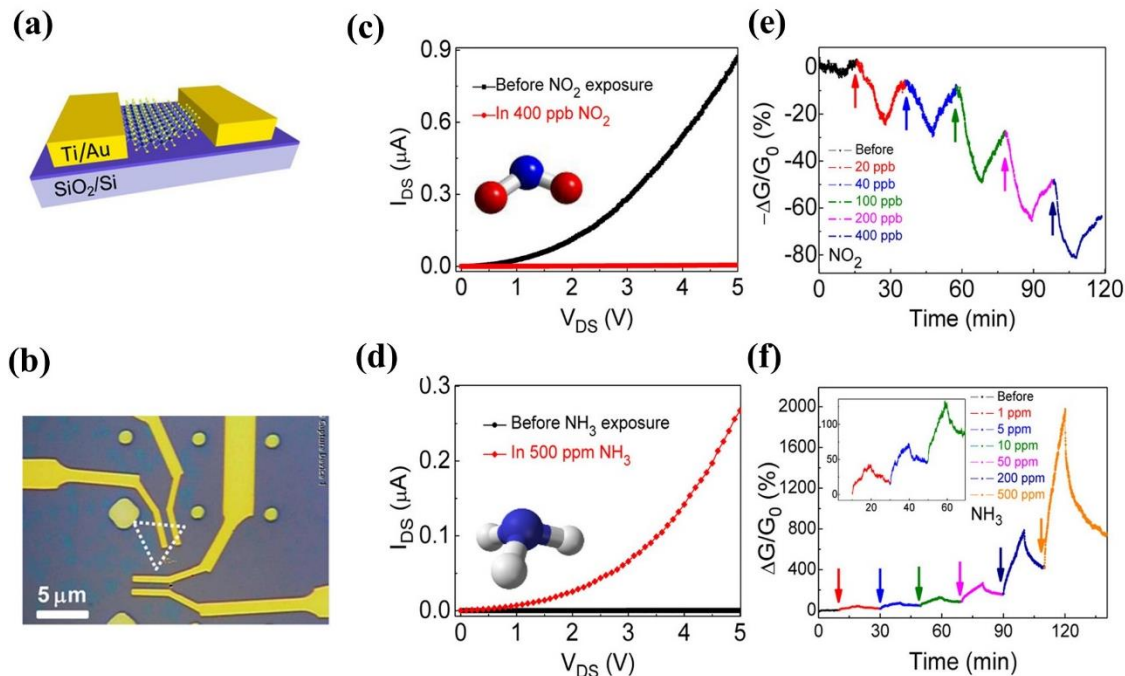


Figure 2-11. The MoS₂-based FET with Ti/Au electrodes and a back-gate is shown in (a) a schematic and (b) an optical picture. The MoS₂ flake is indicated by the dotted triangle in (c). Following exposure to (a) 400 ppb of NO₂ and (d) 500 ppm of NH₃, the device's conductance changes. The device was activated at $V_G = 30$ V in (c), and it was deactivated at $V_G = 0$ in (d) (d). Changes in the device's conductance that occur in real time as a result of time spent being exposed to (e) NO₂ and (f) NH₃ at various concentrations [81].

2.4 Disease Biomarkers- Cancer Biomarkers:

Disease biomarkers are biological molecules or other measurable indicators that can be used to detect the presence or progression of a disease. These markers can be found in various biological samples, such as blood, urine, or tissues. The discovery of disease biomarkers has revolutionized the diagnosis and treatment of many diseases, including cancer, cardiovascular disease, and neurological disorders.

Biomarkers can be classified into several categories based on their characteristics and functions. Some of the most common categories of biomarkers include:

- 1- Diagnostic biomarkers: These biomarkers are used to detect the presence of a disease or condition. For example, PSA (prostate-specific antigen) is a biomarker that is used to screen for prostate cancer.
- 2- Prognostic biomarkers: These biomarkers are used to predict the outcome of a disease or condition. For example, the presence of certain genetic mutations in breast cancer can indicate a poor prognosis.
- 3- Predictive biomarkers: These biomarkers are used to predict how a patient will respond to a particular treatment. For example, the presence of a certain protein in lung cancer can indicate whether the patient is likely to respond to a particular chemotherapy regimen.
- 4- Pharmacodynamic biomarkers: These biomarkers are used to monitor the effect of a drug on a disease or condition. For example, changes in blood pressure can be used as a pharmacodynamic biomarker to monitor the effectiveness of a drug for hypertension.
- 5- Safety biomarkers: These biomarkers are used to monitor the safety of a drug or treatment. For example, changes in liver function tests can indicate potential liver toxicity from a drug.

The discovery and development of disease biomarkers is a rapidly evolving field, and new biomarkers are constantly being discovered and validated. Biomarkers have the potential to improve the accuracy of diagnosis, provide earlier detection of diseases, and improve treatment outcomes.

The ability to identify diseases using human breath has long been known. Modern nanotechnology has allowed for the development of gas sensors that can now detect, forecast, and monitor a variety of diseases from human breath. From diabetes to cancer, it is critical to treat a disease in its early stages to improve patient outcomes and save treatment costs [82].

The analysis of volatile organic compounds in exhaled breath samples provides a new frontier in medical diagnostics due to its noninvasive nature and possible cost-effectiveness. Many studies have shown that as a result of the aberrant metabolic processes occurring in cancer tissues, individuals with lung [83], breast [84, 85], liver [86], and colorectal cancer [87] all exhale various patterns of VOCs.

Hence, gas-sensing detection of human breath provides early diagnosis that is quick, affordable, and non-invasive. Due to its straightforward design and exceptional sensitivity,

semiconductor gas sensors are among the best components for sensor integration. It is simple to create an array arrangement that achieves simultaneous recognition for many analytes, improving the accuracy of diagnosis when used in conjunction with pattern-recognition technology.

2.5 Gas Sensing

Mechanism for Gas Sensing in 2D Layered Nanomaterials.

Charge transfer between adsorbates and adsorbents serves as the foundation for the sensing mechanism of 2D materials [77, 79, 81]. The adsorption of the gas species on the surface of the sensing materials causes a change in the sensors' resistance when they are exposed to reactive gases. Due to the desorption of gas species from the sensing materials, the resistance of the sensors returns when exposed to air or an inert environment.

The interactions of gas molecules (NO_2 and NH_3) with CVD-grown monolayer MoS_2 serve as an illustration of this mechanism (n-type semiconductor). Figure 2-12 illustrates how an unpaired electron of the N atom in NO_2 acts as a strong oxidant and seeks to suck electrons away from the MoS_2 upon adsorption [79]. Reduced carrier concentration and thus reduced electrical conductivity are caused by this charge transfer. Conversely, NH_3 functions as an electron donor since it has a single electron pair. As a result, the electrons move from the NH_3 to the MoS_2 conduction band, increasing the carrier concentration and improving the electrical conductivity of MoS_2 .

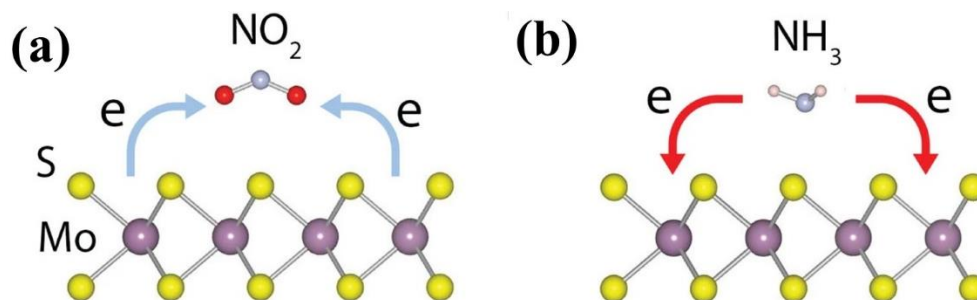


Figure 2-12. Diagrams illustrating the charge transfer mechanisms occurring in a monolayer of MoS₂ when (a) NO₂ and (b) NH₃ molecules are present [79].

Configurations of Gas-sensing Devices

The chemiresistor-type gas sensor belongs to the category of chemical sensors in which chemical interactions with analytes cause changes in the sensing material's resistance. The key benefits of this kind of sensor are straightforward manufacturing, simple operation, and direct measurements [88-90]. Figure 2-13 shows the conventional design of a chemiresistive gas sensor. This sensor was created by dropping a dispersed solution comprising the detecting components onto a ceramic plate that had previously been screen printed with heater layers made of RuO₂ and an Au electrode layer [91].

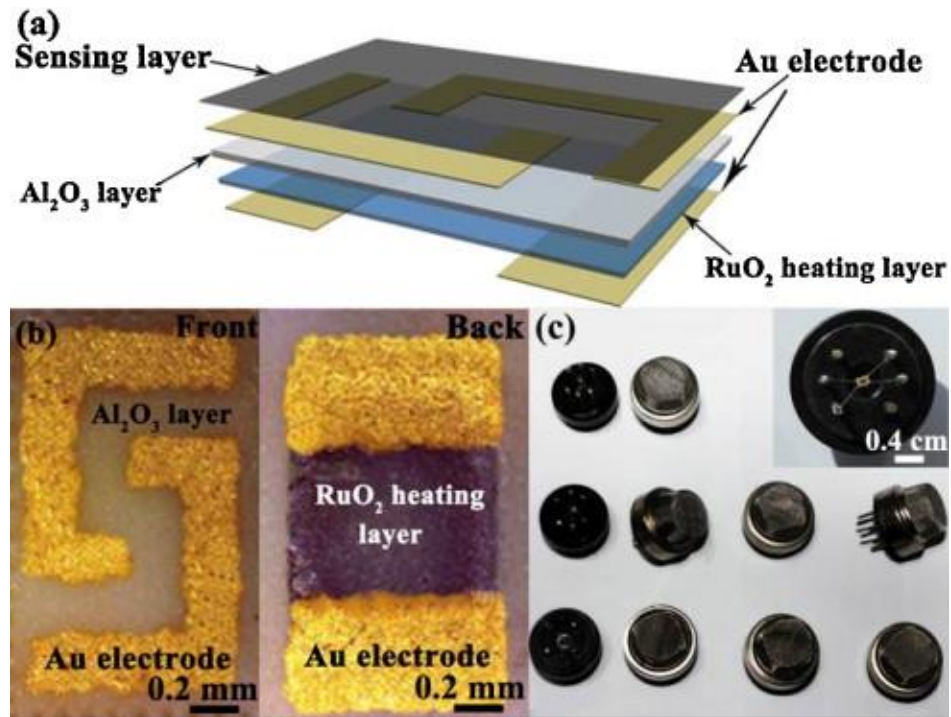


Figure 2-13. (a) A chemiresistive gas sensor schematic depiction. pictures of the (b) blank sensor and (c) coated sensors with the sensing substance [91].

FET is a significant class of electronic gas sensor [92]. When exposed to gas molecules, a FET-based sensor's drain current (I_{DS}), which is controlled by the gate voltage (V_G), can be regulated effectively. The effectiveness of a FET-based gas sensor is determined by the on/off current ratio. Higher sensitivity is typically offered by on/off current ratios that are higher [93]. As a result of their exceptional semiconducting qualities and substantial lateral size, a variety of 2D nanomaterials have demonstrated the potential to be used as channel materials for FET-based gas sensors [94-97].

3. Chapter 3

Theoretical Study on CNT Sensor

SWCNT- based Platform for Early Detection of Lung Cancer

In this study, single-wall carbon nanotubes (SWCNTs) decorated by platinum-group transition metals (Pt, Pd, Rh, or Ru) were introduced as promising nanosensors for the detection of toluene, an important biomarker in the exhaled breath of the lung cancer patients. First-principle calculations based on density functional theory (DFT) was employed to scrutinize the impact of an individual toluene gas molecule on the structural, electronic, and magnetic properties of pristine and metal decorated SWCNTs. It was discovered that toluene is physisorbed on the pristine SWCNT through the interaction of the π orbitals of the carbon atoms in the toluene and the nanotube. Decoration of the SWCNT with metal atoms enhances the adsorption energies significantly by means of strong overlapping between d orbital of the metal atoms and p orbital of C atoms in the benzene ring of toluene. The order of absolute values of adsorption energies for metal-CNT-Toluene (T) systems is $E_{\text{Ru-CNT-T}} > E_{\text{Rh-CNT-T}} > E_{\text{Pt-CNT-T}} > E_{\text{Pd-CNT-T}}$. Our spin-polarized calculations indicated that the Rh-SWCNT, Ru-SWCNT, and Rh-SWCNT-Toluene systems exhibit magnetic properties. Interestingly, a semiconducting behavior for spin-up channel and a metallic behavior for spin-down channel was observed in the Ru-SWCNT system. Our investigations showed that toluene is strongly chemisorbed on Rh- and Ru-SWCNT systems *via* strong covalent bonds with the superior response (-96.98% and -99.98% , respectively), suggesting their potential for breath analysis and environmental applications. Further, the strength of toluene chemisorption on Pt- and Pd-SWCNTs was found to be moderate with significant reversibility at small time scales. The Pd-SWCNT offered an excellent response of 61.60% (2.25 times higher than that Pt-SWCNT's response) and a fast recovery time of 2 ms, potentially, manifesting its suitability for determination of low concentration toluene. Our findings propose the metal decorated SWCNT molecular sensors for the detection of toluene in the exhaled breath of the lung cancer patients and large scale toluene removal from the environment.

3.1 Overview

Since ancient times, physicians have known the relationship between a person's smell and disease state. Breath analysis dates back to ancient Greeks, who used exhaled breath for diagnosis of different diseases [98]. That brings us to the important question, *can we smell cancer?* Studies have indicated many cancer raises polyamine levels, that do have a distinct odor in breath and urine [99-101]. The polyamine metabolic pathway is a recognized drug target for cancer prevention, owing to the polyamine levels and cancer cell proliferation [102, 103]. A 2008 study by Horvath et al. demonstrated that canine's could be trained for smelling ovarian cancer with 100% sensitivity and 97.5% specificity [104]. Similarly, McCulloch et al., demonstrated that house-hold dogs could be trained to identify early stage lung (sensitivity 0.99, specificity 0.99) and breast cancers (sensitivity 0.88, specificity 0.98) from human breath. Thus, identifying cancer biomarkers from human breath continues to be an important fascination as well as an area of research for potential diagnostic early screening of cancer.

As it is widely known, early diagnosis of cancers is vital for reducing the patient's mortality rate [105]. A non-invasive approach for the detection of the cancers in the early stage is the analysis of volatile organic compounds (VOCs) biomarkers in the exhaled breath of the patients [106, 107]. Lung cancer is the leading cause of cancer death in both men and women with a 5-year survival rate at 56% for localized lung cancer and 5% for metastasized lung cancers [108]. Only 16% of lung cancers are detected at an early stage [108]. Toluene (C_7H_8), an organic aromatic compound (present in paints, paint thinners, finger nail polish, lacquers, adhesives, and rubbers), is considered as an essential lung cancer biomarker [83]. The concentration of toluene in the human breath is in the range of 10 to 100 ppb, considerably higher in the breath of patients with lung cancer in comparison with healthy non-smokers [109-111]. Besides that, acute exposure to toluene can lead to a central nervous system disturbance, liver, and kidney damage [112]. The average concentration of toluene for the indoor air levels is around 21 ppb [113], and its 8-hour time-weighted average (TWA) exposure limit is 100 ppm recommended by occupational safety and health administration (OSHA) [114]. Hence, very low-level detection of toluene is of great importance for cancer diagnosis and air quality monitoring. Various nanostructures based on metal oxides such as TiO_2 [115], SnO_2 [116, 117], WO_3 [118], and Fe_2O_3 [119] have been introduced as potential platforms for toluene detection. Nevertheless, since the metal oxide gas sensors typically work at high temperature, developing high precision sensors for toluene detection that operate at

room temperature is still high in demand owing to cost efficiency, low power consumption, and device miniaturization.

The carbon nanotube (CNT) is a great candidate for gas sensing applications thanks to its small size, high surface-volume ratio, excellent charge transfer, fast response, high sensitivity, and low operational temperature [120-127]. Nonetheless, pristine CNTs have several practical drawbacks such as low sensitivity toward various gases, lack of selectivity, and long recovery time that should be overcome in order to realize an applicable gas sensor [128, 129]. Woods *et al.* employed density functional theory (DFT) to assess the adsorption process of the benzene derivatives (aniline, toluene, and nitrobenzene) on single-wall CNTs (SWCNTs). The adsorption processes were obtained to be in the range of physisorption [130]. They discovered that the dominant adsorption mechanism of the molecules above on the nanotube is the weak non-covalent interaction between the CNT and the benzene ring [130, 131]. Functionalization of pristine CNTs with transition metals was found to be an effective technique to enhance the sensor's sensitivity and specificity owing to the strong catalytic performance upon gas interaction [132-145]. The high sensitivity of transition metals [146-152] and large surface area to volume ratio of CNT imply that the metal-CNT composite has a great synergy for the detection of VOCs. Moreover, compared to pure transition metal adsorbent, carbon composite materials offer a lower cost. Satishkumar *et al.* reported the synthesis of metal nanoparticles-SWCNT for the first time [132], and its gas sensing application was first theoretically investigated by Zhao *et al.* [134]. It was revealed that the metal clusters serve as the reactive sites for capturing the foreign molecules that cannot be trapped by the C atoms in the pristine CNTs [134]. Kwon *et al.* reported the fabrication and characterization of a high-efficiency gas sensor based on multi-wall CNTs (MWCNTs)-Pt composite [141]. They measured a sensor response of 3.91 at a concentration of 1 ppm toluene gas. Leghrib *et al.* developed a highly sensitive sensor based on metal nanoclusters (Rh, Pd, Ni, or Au) decorated MWCNTs for detection of benzene at room temperature [137]. They discovered that a microarray sensor based on benzene-sensitive and benzene-insensitive metal-decorated MWCNTs is capable of the selective detection of benzene at trace level (below 50 ppb). Bohli *et al.* inspected the selectivity and sensitivity of the Au nanoparticle-decorated MWCNTs functionalized with a long-chain thiol self-assembled monolayer 1-hexadecanethiol (HDT) [144]. Based on their findings, the presence of the self-assembled layer on Au-MWCNT enhances the sensitivity (17 times) of the sensor and improves its selectivity. Wan *et al.* analyzed the sensing mechanism of Rh-SWCNT

toward benzene and aniline as two kinds of typical gases in the exhaled sample of lung cancer patients using DFT [145]. They found that Rh-SWCNT has a superior sensitivity toward the benzene and aniline while showing insensitivity upon CO₂ interaction [145].

However, to the best of our knowledge, no study so far has comprehensively addressed the sensing capability of metal decorated SWCNTs with respect to toluene as one of the emerging lung cancer biomarkers. Here, we utilized first-principles methods based on DFT to investigate the adsorption behavior of a toluene molecule on a SWCNT decorated by platinum-group metals (Pt, Pd, Rh, or Ru). The most stable adsorption configurations, adsorption energies, charge transfer, electronic, and magnetic properties of the toluene on the metal-nanotube were studied. Our results divulge the promising future of metal-decorated CNT sensors in the development of high-performance room temperature breath analyzer nanosensors for early detection of lung cancer.

3.2 Computational Method

First-principles calculations based on DFT method was employed for this study, performed in the Atomistix ToolKit (ATK) software package [153-155]. Spin-polarized DFT with the Generalized Gradient Approximation of Perdew-Burke-Ernzerhof (GGA-PBE) exchange-correlation functional with the Hartwigsen, Goedecker, Hutter (HGH) pseudopotentials with tier 3 was adopted. In order to consider the long-range van der Waals (vdW) interactions [156], the Grimme vdW correction (PBE-D2) [157] was used. The electronic temperature was 300°K, and the energy mesh cut-off was set to 150 Ry.

A zigzag (8,0) SWCNT, composed of 96 C atoms, was considered in a periodically repeated supercell with lattice constants of $a = b = 30 \text{ \AA}$, large enough to avoid the spurious image-image interactions, and $c = 12.82 \text{ \AA}$. The average C-C bond length is 1.42 \AA , and the diameter of the nanotube is 6.40 \AA . In order to study the metal-SWCNT structure, a metal atom was added to the SWCNT supercell. Using the conjugate gradient method, the structures were fully relaxed such that the force on each atom is less than 0.01 eV/\AA . The Brillouin zone was sampled with a $1 \times 1 \times 11$ Monkhorst-Pack k -point grid during geometry optimization. The k -point grid was then increased to $1 \times 1 \times 101$ for electronic structure calculations to achieve more accurate results for electronic structure calculations.

The adsorption energy of a toluene gas molecule on the pristine SWCNT or metal-SWCNT was calculated by:

$$E_{\text{ad}} = E_{\text{Toluene+X}} - (E_{\text{Toluene}} + E_{\text{X}}) \quad (3)$$

where X is SWCNT or metal-SWCNT. $E_{\text{Toluene+X}}$, E_{X} , and E_{Toluene} are the total energies of the toluene-nanotube complex, nanotube, and the isolated toluene, respectively. A negative E_{ad} states that the adsorption process of toluene is exothermic, and the more negative value relates to a stronger interaction between the adsorbate and nanotube. Moreover, the charge transfer (Q_{T}) upon adsorption of the toluene on the nanotube was obtained using Mulliken population analysis from counting the charge difference between the adsorbed and the isolated toluene molecule. A negative Q_{T} indicates a charge transfer from toluene to the nanotube, whereas a positive Q_{T} shows that toluene withdraws electrons from nanotube.

3.3 First-principles calculations using density functional theory:

3.3.1 The Structure of pristine SWCNT

The accuracy of the employed computational method was first verified by structural optimization of the pristine (8,0) SWCNT (see Figure 3-1 (a)) and calculating its energy band structure (see Figure 3-1 (b)). Our calculations manifested that the pristine (8,0) SWCNT is a semiconductor with a direct bandgap of 0.643 eV at Γ -point, C-C bond length of 1.42 Å, and diameter of 6.40 Å, in good agreement with the literature [143].

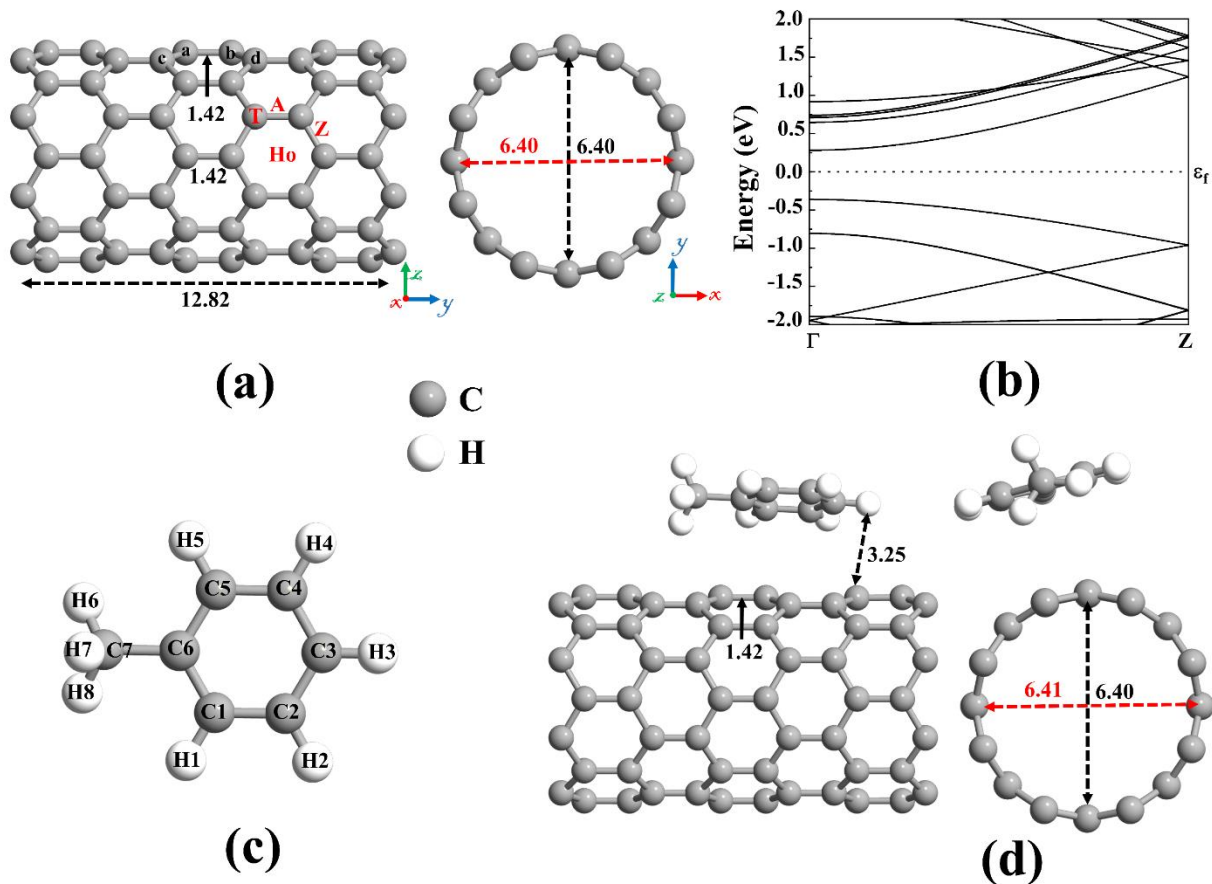


Figure 3-1. (a) Optimized structure of a pristine (8,0) SWCNT and (b) its corresponding energy band structure, showing semiconducting behavior with an energy bandgap of 0.643 eV. The dotted line indicates the Fermi level, which is set to zero. Different adsorption sites on a SWCNT (Ho: hollow, A: axial, Z: zigzag, and T: top). (c) The optimized molecular structure of toluene (C_7H_8). (d) The most stable adsorption configuration of toluene on pristine SWCNT. Distances are given in the unit of Å.

3.3.2 Analysis of SWCNT-Toluene System

Benzene (C_6H_6), as the simplest aromatic hydrocarbon, consists of six carbon atoms bonded in a planar hexagon ring. A carbon atom has four valence electrons to share. It uses three electrons in the sp^2 hybrid orbitals to create σ bonds with two adjacent carbons and one hydrogen atom. The fourth valence electron in the unhybridized p orbital of each carbon atom is shared with two neighboring carbon atoms, forming π bonds perpendicular to the molecular plane. Toluene (C_7H_8) can be produced by replacing one H atom of benzene with a methyl CH_3 functional group. The optimized molecular structure of toluene is shown in Figure 3-1 (c) and its bond lengths and bond angles before and after interaction with an adsorbent are listed in Table 3-1. The toluene

molecule has six aromatic C:C bonds, one single C-C bond, and eight H-C bonds. The full relaxation of the geometry of isolated C_7H_8 gives C:C ~ 1.393 Å, C-C ~ 1.490 Å and C-H ~ 1.095 Å, in agreement with the experimental data (C-C ~ 1.395 Å, C-C ~ 1.513 Å and C-H ~ 1.086 Å) [158].

The adsorption behavior of an individual toluene molecule on the pristine SWCNT was first discussed. Various adsorption configurations can be considered as input geometries. The hexagon carbon ring of the toluene can be placed above C atom (T site), C-C bond (A and Z sites), and the center of C hexagon (Ho site) of SWCNT, see Figure 3-1 (a), where the molecular axis of toluene is aligned parallel with respect to the nanotube's surface. The toluene molecule can also be placed perpendicular to the SWCNT's surface with methyl group pointing to or pointing away from the surface. Comparing the adsorption energies of different adsorption configuration, the parallel alignment of the carbon ring of the toluene on top of the C atom of the nanotube was discovered to be energetically more favorable, as shown in Figure 3-1 (d). The distance minimum atom-atom distance between toluene and the SWCNT (H-C) was found to be 3.25 Å. The small adsorption energy of -0.571 eV, along with a small charge transfer of $0.022 e$ from toluene to the nanotube, suggesting that the toluene molecule is physisorbed on the surface. Since CNT also has π orbitals transverse to its axis, one can consider the toluene-SWCNT system as two π - π interacting systems. As a result, the interactions between toluene and SWCNT are relatively weak, governed by vdW forces. Figure 3-2 (a) presents the electronic total charge density of the toluene adsorption on pristine SWCNT. Clearly, there is no orbital overlap between the molecule and the nanotube, confirming the occurrence of toluene physisorption on the nanotube. The SWCNT and the toluene structures are kept almost unchanged after the interaction. Therefore, no significant changes in the electronic and magnetic properties of the nanotube after interaction with the toluene is expected. Figure 3-2 (b) provides the band structure of the SWCNT-Toluene system. Like pristine nanotube, SWCNT-Toluene does not manifest magnetic behavior. There is a little reduction in the energy bandgap of pristine SWNT (0.643 eV) after adsorption of toluene (0.638 eV), consistent with very small charge transfer between the molecule and the nanotube. As can be seen in Figure 3-2 (c), toluene has a negligible impact on the total DOS near the Fermi level. The toluene's highest occupied molecular orbital (HOMO) is deep in the valence band, and its lowest unoccupied molecular orbital (LUMO) is positioned high in the conduction band of the SWCNT. Hence,

toluene adsorption preserves the semiconducting nature of the SWCNT. These results are consistent with the previous finding [130].

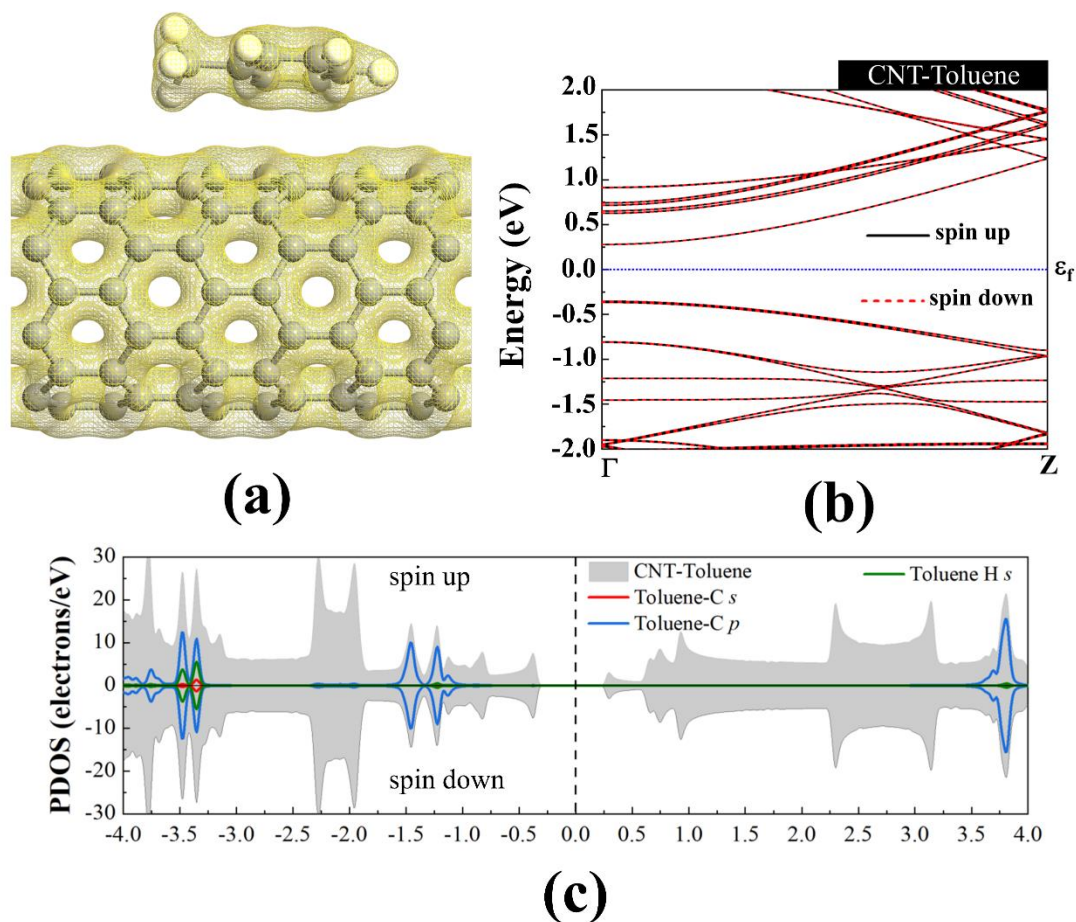


Figure 3-2. (a) The electronic total charge density, (b) energy band structure, and (c) total DOS curve for toluene adsorption on pristine (8,0) SWCNT. The black solid line and red dashed line in the band structure represent spin-up and spin-down bands, respectively. The Fermi level is set to zero.

Table 3-1. Bond distances (d) and angles (\angle) of the toluene molecule before and after interaction with pristine and metal decorated SWCNT.

Description	Toluene - Isolated	Toluene - SWCNT	Toluene-Pt-SWCNT	Toluene - Pd-SWCNT	Toluene - Rh-SWCNT	Toluene - Ru-SWCNT
d C1:C2	1.39	1.40	1.44	1.43	1.42	1.41
d C2:C3	1.39	1.41	1.42	1.41	1.43	1.44
d C3:C4	1.39	1.41	1.40	1.40	1.42	1.43
d C4:C5	1.39	1.40	1.41	1.41	1.42	1.43
d C5:C6	1.40	1.41	1.41	1.41	1.44	1.44

d C6:C1	1.40	1.41	1.44	1.43	1.43	1.45
d C6-C7	1.49	1.51	1.51	1.51	1.51	1.50
d C1-H1	1.10	1.10	1.10	1.10	1.09	1.09
d C2-H2	1.09	1.10	1.10	1.10	1.09	1.09
d C3-H3	1.09	1.10	1.10	1.10	1.09	1.09
d C4-H4	1.09	1.10	1.10	1.10	1.09	1.10
d C5-H5	1.10	1.10	1.10	1.10	1.09	1.09
d C7-H6	1.10	1.11	1.11	1.11	1.10	1.11
d C7-H7	1.10	1.11	1.11	1.11	1.10	1.11
d C7-H8	1.10	1.110	1.11	1.11	1.11	1.10
∠C5-C6-C1	119.47	119.39	118.35	118.36	118.77	119.38
∠C6-C1-C2	120.18	120.96	119.73	120.11	120.18	120.47
∠C1-C2-C3	120.15	120.10	119.7	119.94	120.46	119.28
∠C2-C3-C4	119.87	119.45	119.87	119.74	119.82	120.66
∠H1-C1-C6	119.82	119.21	119.02	119.44	119.47	118.77
∠H2-C2-C1	119.89	119.70	119.65	119.41	120.24	120.41
∠H7-C7-C6	110.37	110.16	110.56	111.15	110.28	109.99
∠H8-C7-H7	107.51	107.56	107.12	107.44	108.77	108.73

distances (d) in Å, angles (∠) in degrees

3.3.3 Analysis of Metal-decorated SWCNT System

The decoration of the SWCNT with platinum-group metals (Pt, Pd, Rh, or Ru) is the next topic of our study. As described in Figure 3-1 (a), four possible sites (Ho, T, A, and Z) were considered for individual atom adsorption. After structural optimization and adsorption energy calculations, the most favorable adsorption configurations were selected for further studies and presented in Figure 3-3. It was found that all the metal atoms tend to be adsorbed on the T site (axial C-C bond). The adsorption energy, the binding distance between the metal atom and the nanotube, the total magnetic moment, charge transfer, Fermi level, energy bandgap for spin-up and -down channels for selected metal decorated SWCNTs are tabulated in Table 3-2. The metal atoms are located between two C atoms (C_a and C_b as labeled in Figure 3-1) of the SWCNT, where Pt-C distances are 2.12 and 2.13 Å, Pd-C distances are 2.23 and 2.23 Å, Rh-C distances are 2.09 and 2.08 Å and the Ru-C distances are 2.09 and 2.08 Å. The C atoms connected to metal atoms are distorted, showing the appearance of sp^3 hybridization. As a result, the diameter of the CNT is elongated in the decoration orientation and contracted in the perpendicular direction. The values of diameter for the Pt-SWCNT, Pd-SWCNT, Rh-SWCNT, and Ru-SWCNT are 6.45 (6.38), 6.43

(6.39), 6.45 (6.37), 6.46 (6.37) Å in the direction of the adsorbed metal (perpendicular to the adsorption site), respectively. Further, the creation of metal-C bonds deteriorates the strength of C_a-C_b bonds, causing these bonds to get enlarged. The C-C bond length in the pristine SWCNT is elongated from 1.42 Å to 1.48, 1.46, 1.47, and 1.47 Å after decorating with Pt, Pd, Rh, and Ru atoms, respectively.

The Pt, Pd, Rh, and Ru adsorption energies on SWCNT were calculated to be -2.572, -1.535, -2.628, and -2.665 eV, respectively. These values are in good agreement with the reported data in the literature [139, 159-161]. Upon interaction of transition metals with C atoms of SWCNT, a donation (electron transfer from the bonding π (HOMO) states of the nanotube to unoccupied orbitals of metal) and a back donation (electron transfer from the occupied orbitals of metal to anti-bonding π^* (LUMO) states of the nanotube) occur [162]. The values of electronegativity of C, Pt, Pd, Rh, and Ru are 2.55, 2.28, 2.20, 2.28, and 2.20, respectively. Ergo, the C atoms surrounding a metal atom attract electrons from the metal thanks to their higher electronegativity, resulting in the accumulation of positive charges on the metal atom. The interactions between the Pt, Pd, Rh, and Ru atoms and SWCNT caused a charge transfer of 0.159, 0.125, 0.312, and 0.376 e from the metals to the nanotube, respectively. Hence, the net charge transfer for metal and SWCNT interaction is a back donation. It can be deduced that the charge transfer has a direct relationship with adsorption energy while it has an inverse relationship with binding distance. Additionally, as can be seen in Table 3-2, the Fermi energy level (E_F) is shifted to higher energies, indicating that the nanotube gains electrons after complexation with metal atoms. The Fermi level of the pristine (8,0) SWCNT resides at -4.86 eV, whereas the Fermi levels of Pt-SWCNT, Pd-SWCNT, Rh-SWCNT, and Ru-SWCNT are located at -4.80, -4.81, -4.78, and -4.77 eV, respectively.

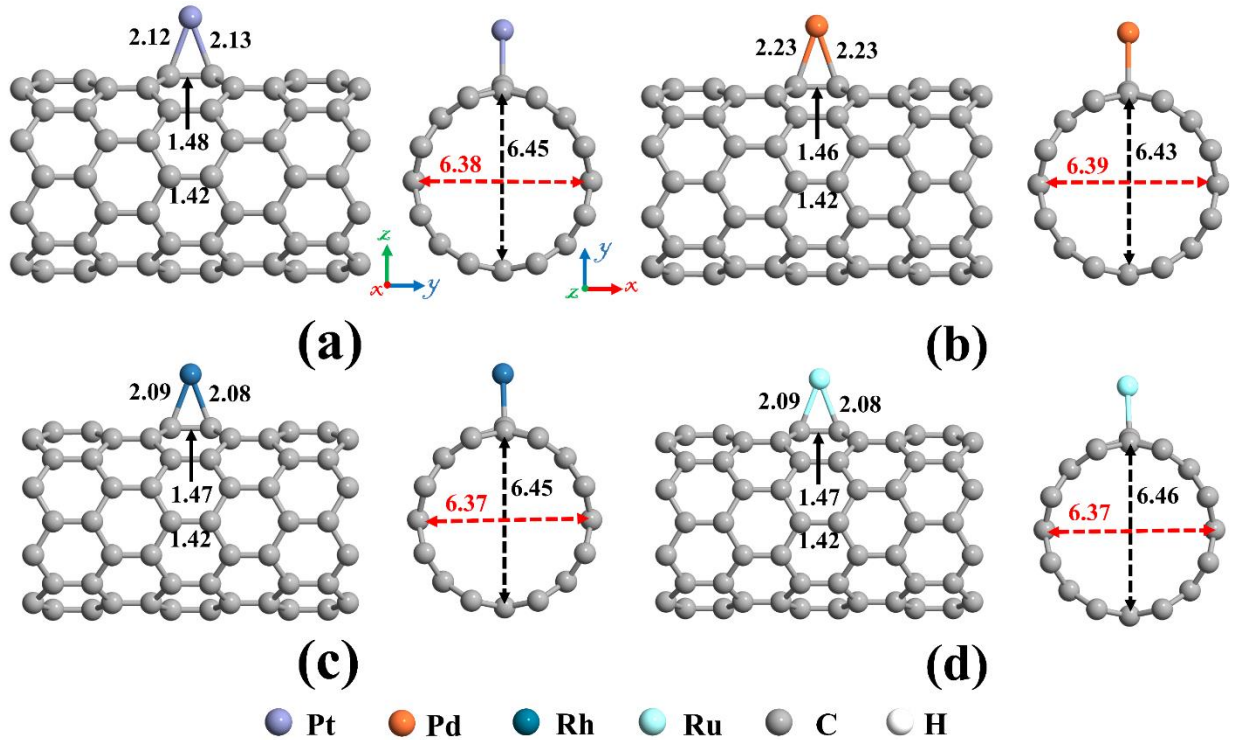


Figure 3-3. The optimized structures of a single (a) Pt, (b) Pd, (c) Rh, and (d) Ru decorated (8,0) SWCNT. The bond lengths, the diameters, and the binding distances between the metal atom and the nanotube are also given in the unit of Å. The sticks between atoms are only for visualization.

The electronic and magnetic properties of the SWCNT undergo significant changes upon interaction with metal atoms. Energy band structures of the metal decorated SWCNT systems are presented in Figure 3-4. While pristine (8,0) SWCNT shows a non-magnetic ground state, transition metal decorated (8,0) SWCNT has a magnetic ground state, giving rise to the total magnetic moment from $2.0 \mu_B$ for Ru, $0.9 \mu_B$ for Rh, and zero for Pd and Pt. In the case of Pt and Pd, the energy bandgap reduces to 0.591 and 0.630 eV, respectively, from 0.643 eV in the pristine SWCNT derived from adsorbate states. The valence band and conduction band do not start at the same energy level in the Rh-SWCNT system, confirming its magnetic behavior. Our spin-polarized calculations showed that Rh-SWCNT is a semiconductor with a direct bandgap of 0.632 eV for spin-up channel and indirect bandgap of 0.117 eV for the spin-down channel. The significant reduction of the bandgap for the spin-down channel corresponds to two novel induced states by Rh atom around the Fermi level. In the case of Ru, a bandgap of 0.628 eV and zero bandgap are obtained for the spin-up and spin-down channels, respectively. Three novel states are appeared near Fermi level for the spin-down channel, two fully occupied almost flat bands and

one band that crosses the Fermi level, indicating the metallization of the nanotube. The half-metallic behavior of Ru-SWCNT shows its potential for spintronics application.

The PDOS of the systems is provided in Figure 3-5. One can see that the PDOS curves of spin-up and -down channels are symmetric in Pt-SWCNT and Pd-SWCNT systems, while they are asymmetric in Rh-SWCNT and Ru-SWCNT. The induction of Rh and Ru impurity states that carry magnetic moments is the main cause for this observation. The orbital hybridization between d -orbital of the metal atom and p -orbital of C atoms (π^* states) has the main contribution to the total DOS of the complex system around the Fermi level. One can notice that the Pt d and C p peaks in the Pt-SWCNT systems are located closer to the Fermi level in comparison with those in the Pd-SWCNT system, confirming the more reduction in the bandgap of SWCNT after interaction with Pt atom. In the case of Rh and Ru, the intensities of the peaks near the Fermi level increased, and they are pronounced in the spin-down channel. Comparing Figure 3-1 (b) and Figure 3-4, one can say that the valence and conduction band edges at Z-point are flattened after the decoration of SWCNT with metal atoms. This can be attributed to the localized states in the interaction area caused by metal atoms.

The origin of the various strengths of the metal bonds can be described by Brewer-Engel valence-bond theory [162]. Although all the valence electrons have a contribution to the bonding in the transition metals, the electrons of s and p orbitals of the transition metals define the long-range structure, and the electrons of the d orbital determine the short-range bonding, consequently the strength of a bond [163]. The transition metals studied here have the following electron configurations: Pt ($[\text{Xe}] 4f^{14} 5d^9 6s^1$), Pd ($[\text{Kr}] 4d^{10}$), Rh ($[\text{Kr}] 4d^8 5s^1$), and Ru ($[\text{Kr}] 4d^7 5s^1$). Pd and Pt atoms have ten valence electrons, and their d -bands are nearly full. However, the orbital diffusiveness for the $5d$ orbitals of Pt is greater than that for the $4d$ orbital of Pd. For this reason, the orbital overlap between π electron cloud of C atoms and d orbital of the Pt atom is stronger than the Pd atom. Rh and Ru atoms have 9 and 8 valence electrons, signifying that their d orbitals have more tendency for hybridization with the π electron cloud of C atoms. These results support our previous findings.

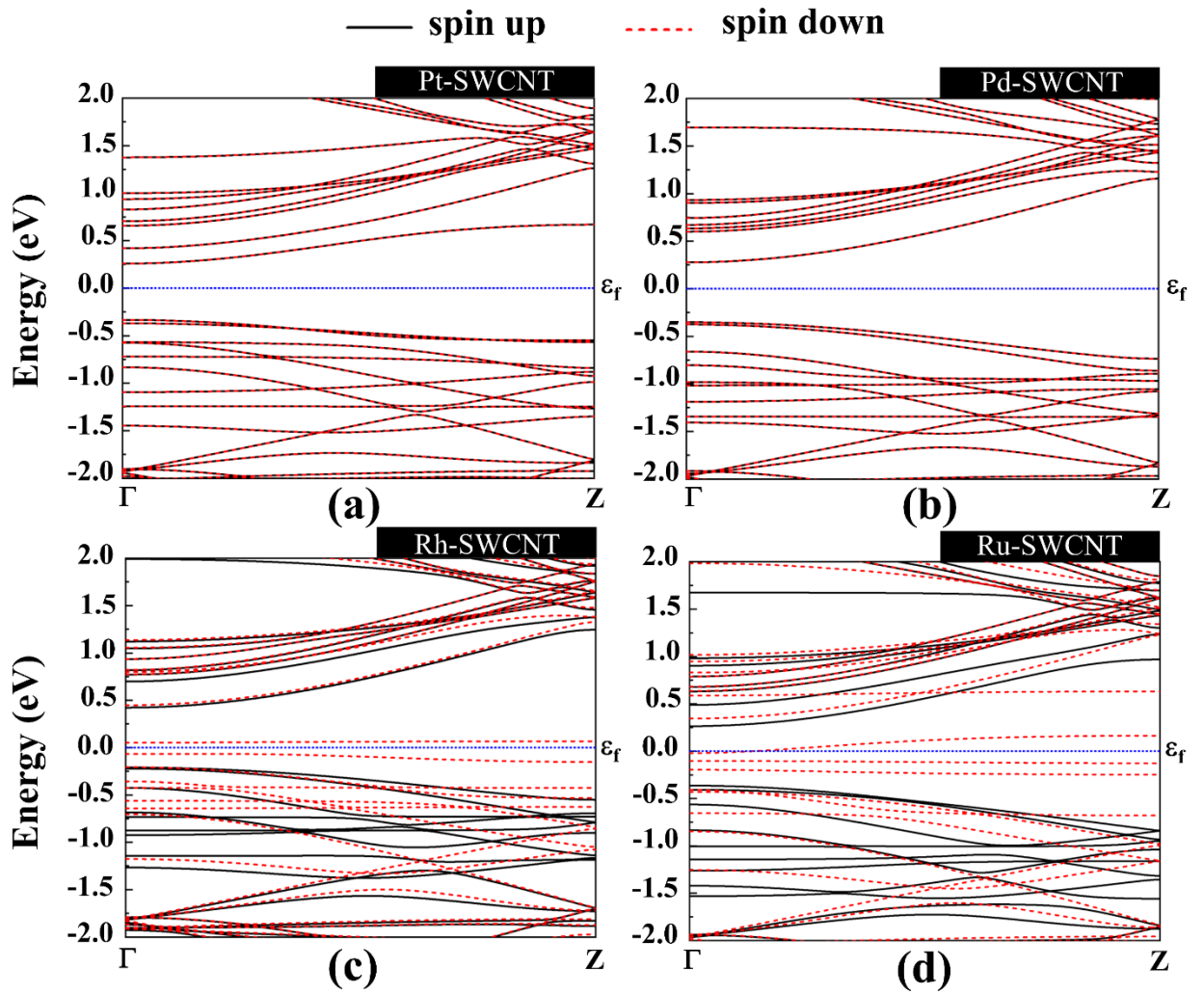


Figure 3-4. Energy band structures of (a) Pt-SWCNT, (b) Pd-SWCNT, (c) Rh-SWCNT, and (d) Ru-SWCNT systems. The black solid line and red dashed line represent spin-up and spin-down bands, respectively. The dotted blue line indicates the Fermi level, which is set to zero.

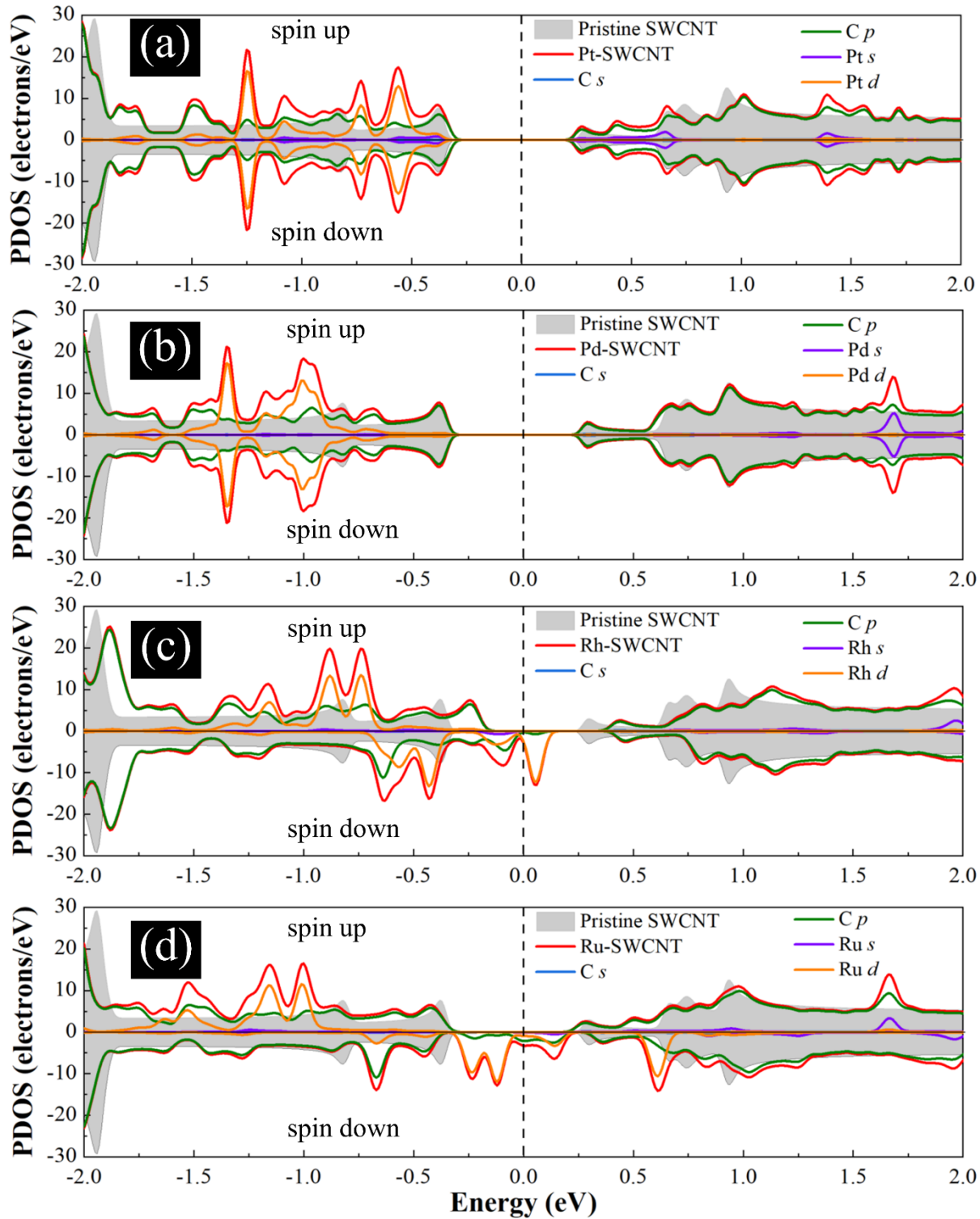


Figure 3-5. Total DOS curves for pristine SWCNT and (a) Pt-SWCNT, (b) Pd-SWCNT, (c) Rh-SWCNT, and (d) Ru-SWCNT systems. PDOS of the s and p orbitals of C atoms in SWCNT and s and d orbitals of metal atoms are also presented. The positive and negative values denote the spin-up and spin-down channels, respectively. The dashed lines indicate the Fermi level, which are set to zero.

Table 3-2. The calculated adsorption energy (E_{ad}), binding distance between the metal atom and the nanotube (D), magnetic moment (m), charge transfer (Q), Fermi level (E_f), energy bandgap (E_g) for spin-up (-down) channel. The negative values of charge indicate a charge transfer from metal to the nanotube. a: Ca atom and b: Cb atom in Figure 3-1 (a).

System	E_{ad} (eV)	D (Å)	m (μ_B)	Q (e)	E_f (eV)	E_g (eV)
SWCNT	-	-	0.00	-	-4.86	0.643 (0.643)
Pt-SWCNT	-2.572 (-2.604 ^[139] , -2.7 ^[160])	2.12 (a) and 2.13 (b)	0.00	-0.159	-4.80	0.591 (0.591)
Pd-SWCNT	-1.535 (-1.615 ^[139] , -1.7 ^[160])	2.23 (a) and 2.23 (b)	0.00	-0.125	-4.81	0.630 (0.630)
Rh-SWCNT	-2.628 (-2.67 ^[161])	2.09 (a) and 2.08 (b)	0.90	-0.312	-4.78	0.632 (0.117)*
Ru-SWCNT	-2.665 (-2.133 ^[159])	2.09 (a) and 2.08 (b)	2.00	-0.376	-4.77	0.628 (0.000)*

*Indirect bandgap

3.3.4 Adsorption of Toluene on Metal-decorated SWCNT

Finally, the toluene adsorption on metal decorated SWCNTs was studied, and the most stable structures are depicted in Figure 3-6. Toluene molecule is adsorbed on metal decorated SWCNT in a configuration with the molecular axis parallel to the surface and with large deformation. It is reported that benzene is chemisorbed in a flat arrangement on four Pt-group metals (Ru, Rh, Pd, and Pt) [164]. As mentioned before, upon the interaction of metal atoms with SWCNT, the metal atoms are positively charged, whereas the SWCNT becomes rich in electrons. Henceforth, metal atoms can act as capturing centers for the toluene that cannot be trapped by the p orbital of C atom in the pristine SWCNT. Due to interaction with the toluene, the distances between metal atoms and C atoms of the CNT are elongated, indicating that the interactions between them get weakened. The distance between Pt, Pd, Rh, and Ru atoms and C_a (C_b) (as labeled in Figure 3-1 (a)) of CNT are changed from 2.12 (2.13), 2.23 (2.23), 2.09 (2.08), and 2.09 (2.08) Å to 2.14 (2.18), 2.22 (2.24), 2.23 (2.08), and 2.17 (2.15) Å, respectively, after interaction with toluene molecule. Furthermore, the Rh and Ru atoms are slightly moved toward the hollow position (the center of the hexagon ring). The Rh- C_c (Ru- C_c) and Rh- C_d (Ru- C_d) distances are 2.78 (2.34) Å and 2.39 (2.30) Å, accordingly. The C atoms of the nanotube in the interaction area are protruded owing to the sp^3 hybridization. It caused the diameter of the CNT got enlarged in the decoration direction and shortened in the perpendicular direction. The values of diameter for the Pt-SWCNT, Pd-SWCNT, Rh-SWCNT, and Ru-SWCNT systems after interaction with toluene are

6.52 (6.31), 6.47 (6.34), 6.54 (6.27), 6.52 (6.27) Å in the orientation of the adsorbed metal (perpendicular to the adsorption orientation), respectively. It should be added that the C_a-C_b is slightly reinforced after interaction of the metal decorated CNT with toluene since the strength of metal-C bonds got deteriorated. The C_a-C_b bond length in the Pt-, Pd-, Rh-, and Ru- SWCNT changed from 1.48, 1.46, 1.47, 1.47 Å to 1.46, 1.45, 1.45, 1.43 Å upon toluene adsorption, respectively.

The toluene structure also undergoes a structural change upon adsorption on different metal decorated SWCNT systems (See Table 3-1). Table 3-3 also presents the adsorption energy, binding distance, magnetic moment, charge transfer, Fermi level, energy bandgap, sensitivity, and recovery time of toluene-metal-SWCNT systems. In the case of Pt-SWCT, the distances between Pt atom and C₁-C₆ atoms of toluene are 2.22, 2.41, 3.14, 3.59, 3.44, and 2.80 Å, respectively. Therefore, the C₁ atom of toluene is more impacted compared to others in response to its strong interaction with Pt atom. As can be seen in Table 3-1, the C₁:C₂ and C₆:C₁ bonds in toluene after interaction with Pt-SWCNT got elongated by 3.6% and 2.85%, respectively, compared to isolated toluene. For Pd-SWCNT, the distances between Pd atom and C₁-C₆ atoms of toluene are 2.30, 2.57, 3.22, 3.58, 3.36, and 2.75 Å, respectively, representing that the Pd-C₁ is the minimum binding distance. It was found that upon the interaction of toluene with Pd-SWCNT, its C₁:C₂ and C₆:C₁ bonds get stretched by 2.8% and 2.1%, respectively, in comparison with isolated toluene. Moreover, the H₇-C₇-C₆ bond angle of the toluene is increased from 110.37° to 111.15°. In the case of Rh-SWCNT, the distances between Rh atom and C₁-C₆ atoms of toluene are 2.42, 2.39, 2.37, 2.37, 2.34, and 2.36 Å, respectively, showing that the minimum binding distance is between Rh and C₅ atom (2.34 Å). The C₅:C₆ bond is enlarged by 2.8%, and H₂-C₂-C₁ (H₈-C₇-H₇) bond angle of the toluene increased from 119.89° (107.51°) to 120.24° (108.77°) compared to isolated toluene. Finally, for Ru-SWCNT, the distances between Ru atom and C₁-C₆ atoms of toluene are 2.29, 2.29, 2.22, 2.26, 2.27, and 2.23 Å, respectively. All the C₁-C₆ atoms are affected by Ru atom, and the interactions between Ru and C₃ and C₆ are more noticeable. The C₂:C₃ and C₆:C₁ bonds are elongated by 3.6% in comparison with isolated toluene. The H₂-C₂-C₁ (H₈-C₇-H₇) bond angle increased from 119.89° (107.5°) to 120.4° (108.73°), while the H₁-C₁-C₆ bond angle decreased from 119.82° (110.37°) to 118.77° (109.99°). To sum up, although toluene molecule is adsorbed in parallel to the metal-SWCNT systems, it is slightly tilted in Pt-SWCNT (C₁ and C₂ are located closer to the Pt) and Pd-

SWCNT (C_1 is located closer to Pd), and it is a little bent in Rh-SWCNT (C_1 - C_6 atoms are lightly shifted toward Rh) and significantly bent in Ru-SWCNT (all C_1 - C_6 atom are moved toward Ru).

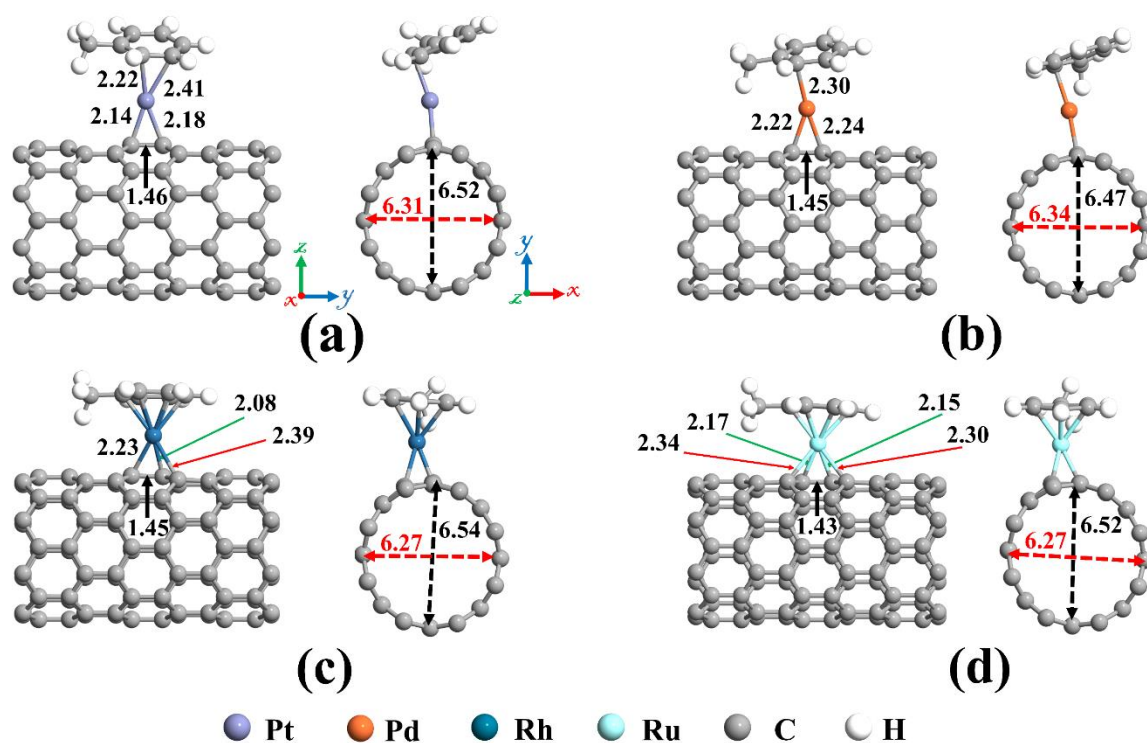


Figure 3-6. The most stable adsorption configurations for Toluene on (a) Pt-SWCNT, (b) Pd-SWCNT, (c) Rh-SWCNT, and (d) Ru-SWCNT systems. The bond lengths, the diameters, and the binding distances between the metal atom and the nanotube are also given in the unit of Å. The sticks between atoms are only for visualization.

The adsorption energies were calculated to be -1.655 , -1.306 , -2.165 , and -4.087 eV for toluene adsorption on Pt-, Pd-, Rh-, and Ru-decorated SWCNT systems, respectively. The total charge transfer from toluene to Pt-, Pd-, Rh-, and Ru-SWCNTs were also found to be 0.068, 0.056, 0.162, and 0.178 e , accordingly. The electrons are transferred from the toluene to the C atoms of SWCNT in the interaction area through metal atoms. The charge transfer from toluene to pristine SWCNT and metal-SWCNT can be confirmed by evaluating the Fermi levels shift. As can be seen in Table 3-1 and Table 3-2, the Fermi levels of pristine, Pt-, Pd-, Rh-, and Ru-SWCNT systems are shifted to higher energies by 0.06, 0.20, 0.12, 0.34, and 0.44 eV after toluene adsorption, in good agreement with the obtained values for charge transfer. The higher adsorption energy and larger charge transfer are, the shorter binding distances would be. The average distances between Pt, Pd,

Rh, and Ru atoms to C₁-C₆ atoms of toluene are 2.93, 2.96, 2.37, and 2.26 Å, respectively. One can conclude that the order of absolute values of adsorption energies for metal-CNT-T systems ($E_{\text{Ru-CNT-T}} > E_{\text{Rh-CNT-T}} > E_{\text{Pt-CNT-T}} > E_{\text{Pd-CNT-T}}$) have a direct relationship with the order of charge transfer ($Q_{\text{Ru-CNT-T}} > Q_{\text{Rh-CNT-T}} > Q_{\text{Pt-CNT-T}} > Q_{\text{Pd-CNT-T}}$) and an inverse relationship with average binding distances ($D_{\text{Ru-CNT-T}} < D_{\text{Rh-CNT-T}} < D_{\text{Pt-CNT-T}} < D_{\text{Pd-CNT-T}}$). The above results lead to the conclusion that a toluene molecule can be chemisorbed on the metal-SWCNTs with different adsorption properties.

Table 3-3. The calculated adsorption energy (E_{ad}), binding distance (D) which is the distance between C₁-C₆ of the toluene and the metal in the metal-decorated CNT structure (the underlined distance is the shortest distance) or the shortest distance between the toluene molecule and the nanotube in the pristine CNT structure, magnetic moment (m), charge transfer (Q), energy bandgap (E_{g}), sensitivity (S), and recovery time (τ) at 498 K. The negative values of charge indicate a charge transfer from molecule to the nanotube. T: Toluene.

System	E_{ad} (eV)	D (Å)	m (μ_{B})	Q (e)	E_{f} (eV)	E_{g} (eV)	S (%)	τ (sec)
CNT-T	-0.571	<u>3.25</u>	0.00	-0.022	-4.80	0.638 (0.638)	+10.52	7.4×10^{-10}
Pt-CNT-T	-1.655	<u>2.22</u> -2.41-3.14-3.59-3.44- 2.80 (avg: 2.93)	0.00	-0.068	-4.60	0.607 (0.607)	-27.30	6.9×10^1
Pd-CNT-T	-1.306	<u>2.30</u> -2.57-3.22-3.58-3.36- 2.75 (avg: 2.96)	0.00	-0.056	-4.69	0.606 (0.606)	+61.60	2.0×10^{-2}
Rh-CNT-T	-2.165	2.42-2.39-2.37-2.37- <u>2.34</u> - 2.36 (avg: 2.37)	0.62	-0.162	-4.44	0.375* (0.292)*	-96.98	1.0×10^7
Ru-CNT-T	-4.087	2.29-2.29- <u>2.22</u> -2.26-2.27- 2.23 (avg: 2.26)	0.00	-0.178	-4.33	0.450 (0.450)	-99.98	2.8×10^{26}

*Indirect bandgap

To gain more insight into the adsorption toluene on metal decorated SWCNTs, their electronic total charge densities were calculated and presented in Figure 3-7. In the case of Pt-SWCNT-Toluene system, a strong orbital overlap is observed between Pt and C₁ atom of toluene. Moreover, a weak orbital hybridization is formed between Pt and C₂ atom. For Pd-CNT-T, a moderate orbital mixing between Pt and C₁ atom is noticeable. In the case of Rh-CNT-T, Rh atom has moderate and weak orbital overlap with C₁-C₆ atoms of toluene. Finally, the orbitals of the Ru atom are strongly and moderately mixed with C₁-C₆ atoms of toluene in the Ru-CNT-T system. It can be deduced that more orbital mixing will result in a larger charge transfer and higher adsorption energy, as discovered before.

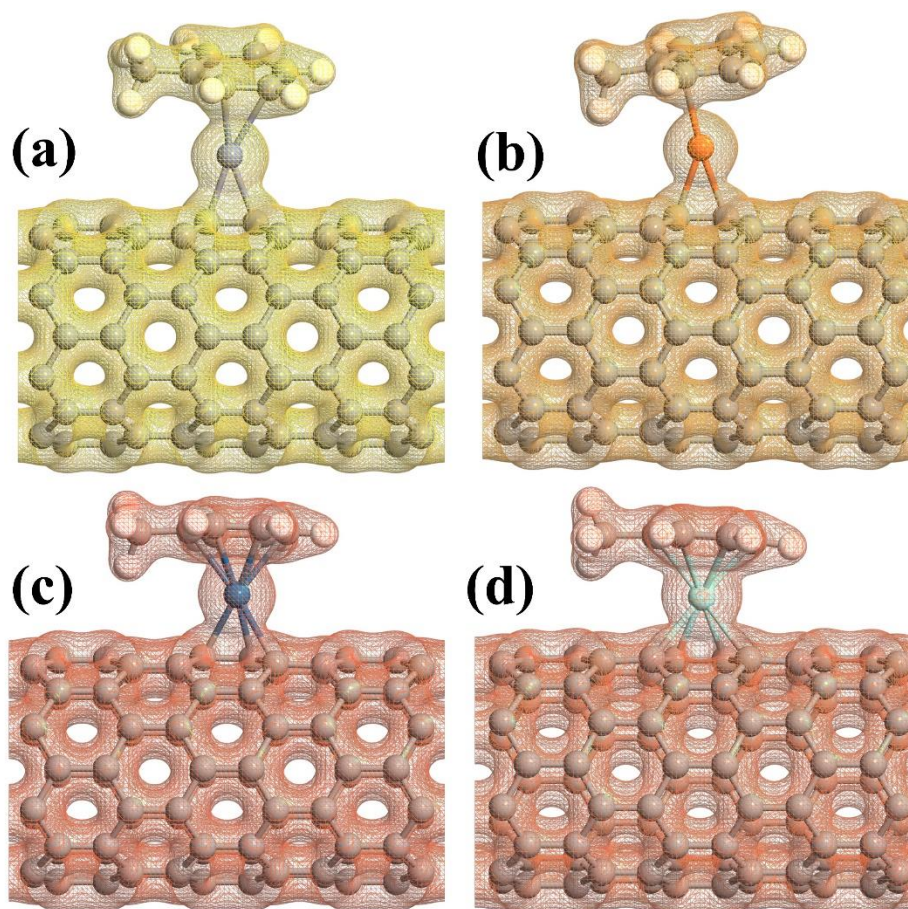


Figure 3-7. The electronic total charge densities for the adsorption of toluene on (a) Pt-SWCNT, (b) Pd-SWCNT, (c) Rh-SWCNT, and (d) Ru-SWCNT systems. The sticks between atoms are only for visualization.

The orbital hybridization and the charge transfer from toluene to metal-SWCNTs cause significant changes to the magnetic and electronic properties of the nanotubes. Figure 3-8 presents the energy band structure of metal-SWCNTs after toluene adsorption. The energy bandgap of Pt-SWCNT (Pd-SWCNT) increases (decreases) from 0.591 (0.630) eV to 0.607 (0.606) eV after interaction with toluene, indicating that the conductivity of the system drops (increases). The Pt- and Pd-CNT-T systems show no magnetic properties. For Ru-SWCNT, toluene increases (decreases) the energy bandgap for spin-up (-down) channel from 0.628 (0.000) eV to 0.450 eV. As can be seen in Figure 3-8 (d), toluene adsorption quenches the magnetism of Ru-SWCNT due to the saturation of Rh atom with C atoms of toluene. For toluene adsorption on Rh-SWCNT, the

energy band structure curves for spin-up and -down channels are not symmetric. Its total magnetic moment is decreased from 0.90 to 0.62 μ_B after toluene adsorption. The energy bandgap of Rh-SWCNT drops (rises) from 0.632 (0.117) eV to 0.375 (0.292) eV upon toluene adsorption.

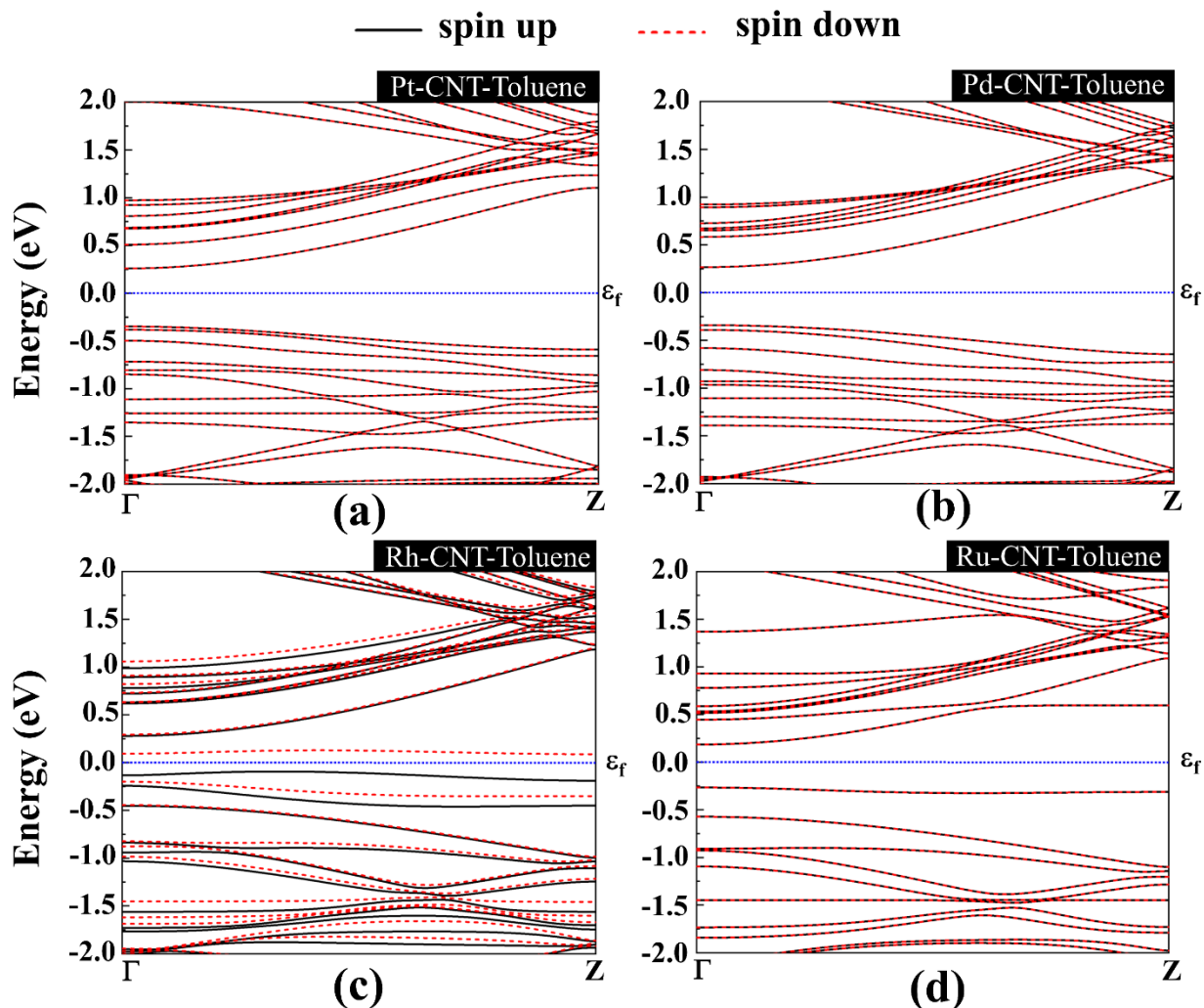


Figure 3-8. Energy band structure of toluene adsorption on (a) Pt-SWCNT, (b) Pd-SWCNT, (c) Rh-SWCNT, and (d) Ru-SWCNT systems. The black solid line and red dashed line represent spin-up and spin-down bands, respectively. The dotted blue line indicates the Fermi level, which is set to zero.

Figure 3-9 describes the PDOS curves of metal-SWCNT-Toluene systems. The asymmetry in DOS curves for spin-up and spin-down channels is only observed for the Rh-SWCNT-Toluene system, confirming its magnetic behavior. As discussed in section 3.3, the hybridization between Pt 5*d*, Pd 4*d*, Rh 4*d*, and Ru 4*d* and C 2*p* orbitals of SWCNT happens when the SWCNT and metal

atoms interact. A similar binding mechanism is expected for the metal-CNT-toluene system, where the metal atom is sandwiched between two π systems. Comparing Figure 3-5 and Figure 3-9, the d orbitals of metal atoms are significantly broadened after interaction with toluene. If the DOS of two orbitals lie in the same energy range, then there is an orbital hybridization. For this reason, the number of overlapping peaks between d orbital of metal and p orbital of C atom of toluene close to Fermi level (in the energy range of -2 to 2 eV) were counted. In the case of Pt-CNT-Toluene, two overlapping peaks are presented at -1.09 and -1.26 eV. One overlapping point was also found for Pd-CNT-T, which is located at -1.11 eV. The larger number of overlapping peaks for Pt-CNT-T in comparison with Pd-CNT-T suggests that the orbital hybridization is stronger in the former system. Besides, for both systems, the hybridization of d orbital of metal and p of C orbital hybridization can be seen deep in the valence band in the energy range of -3.25 to -2.25 eV, where the p orbital of C is more pronounced. The PDOS of the Rh-CNT-T system demonstrates four overlapping peaks for the spin-up channel and four overlapping peaks for the spin-down channel. The overlapping peaks for spin-up (-down) are positioned at -0.12 ($+0.1$), -0.45 (-0.34), -0.92 (-0.85), and -1.8 (-1.60) eV. An overlapping peak of the spin-down channel is situated in the conduction band. The orbitals are also overlapped deep in the conduction band in the energy range of 2.15 eV to 2.55 eV, where the C p is more highlighted compared to lower energies. Likewise, Ru-CNT-T indicates seven overlapping points at 1.38 , 0.59 , -1.90 , -1.70 , -1.40 , -0.90 , and -0.30 eV, where two peaks are in the conduction band. Similarly, the overlap of these orbitals happens deep in the conduction band in the energy range of 2.10 to 3.15 eV, where the C p is more marked compared to lower energies. The sharp peak located at -1.45 eV in the PDOS of Ru d orbital corresponds to the flat band in the band structure of Ru-CNT-T, check Figure 3-8 (d).

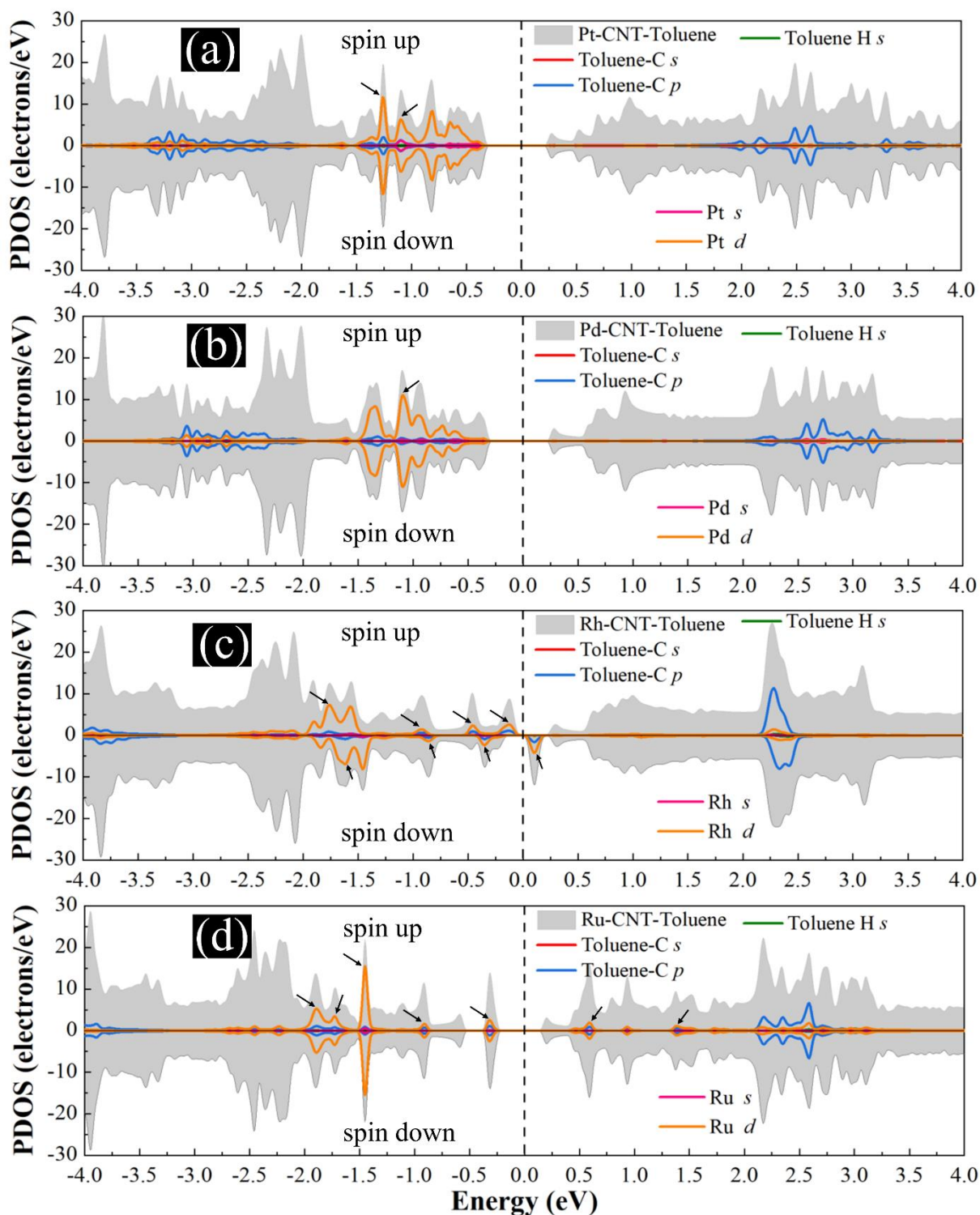


Figure 3-9. Total DOS curves for toluene adsorption on (a) Pt-SWCNT, (b) Pd-SWCNT, (c) Rh-SWCNT, and (d) Ru-SWCNT systems. PDOS of the s and p orbitals of C atoms and s orbital of H atoms in Toluene and s and d orbitals of metal atoms are also presented. The positive and negative values denote the spin-up and spin-down channels, respectively. The dashed lines indicate the Fermi level, which are set to zero.

3.3.5 Gas Sensing Evaluation of Metal-decorated SWCNT

In order to develop a reliable sensor for toluene detection, two crucial challenges should be addressed, namely high sensitivity in low concentration and short recovery time. Table 3-3 lists the sensitivity and recovery of the considered systems. Sensitivity (S) is the variation of the conductivity (σ) for the nanosensors with and without gas is expressed as [165]:

$$S = \frac{\sigma_{\text{gas}} - \sigma_{\text{pure}}}{\sigma_{\text{pure}}} \times 100 \quad (4)$$

Here σ_{gas} and σ_{pure} are the conductivity of the toluene adsorbed system and isolated system, respectively. The electrical conductivity of a material can be determined as [165]:

$$\sigma \propto \exp(-E_g / 2k_B T) \quad (5)$$

Here E_g is the bandgap, T is the temperature, and k_B is the Boltzmann constant. It can be deduced that the tuning of the bandgap that alters the electrical conductivity plays a vital role in the sensitivity of a sensor. A small drop (rise) in the energy bandgap dramatically enhances (reduces) the electrical conductivity. Pristine SWCNT shows +10.52% sensitivity toward toluene due to its low adsorption energy. It was also found that the sensitivities of Pt-SWCNT and Pd-SWCNT systems for toluene detection are -27.30% and +61.60%, respectively. The situation with Rh-SWCNT and Ru-SWCNT can be complicated owing to their magnetic ground states. For the spin-up channel, the sensitivity for toluene detection by Rh-SWCNT and Ru-SWCNT systems are +169.71% and +34.16%, respectively. Further, excellent sensitivities of -96.98% and -99.98% were found for Rh-SWCNT and Ru-SWCNT systems for the spin-down channel.

The recovery time (τ) can be expressed using the conventional transition state theory as follows [40]:

$$\tau = \nu_0^{-1} \exp(-E_{\text{ad}} / k_B T) \quad (6)$$

Here ν_0 is the attempt frequency. It is expected that at a constant temperature, small adsorption energies result in a fast desorption process of the toluene gas. It can also be concluded that at constant adsorption energy, the recovery time can be shortened by enhancing the temperature. Due to the high adsorption energies of toluene on metal decorated CNTs, a short

recovery cannot be obtained at room temperature. For this reason, it is assumed that the sensors are recovered by annealing at 498°K in UV irradiation. The obtained recovery times for toluene desorption from Pt-, Pd-, Rh-, and Ru-CNT systems are 7.4×10^{-10} , 69, 0.02, 10^7 , and 2.8×10^{26} sec, respectively.

In short, despite the superior sensitivity, Rh-SWCNT and Ru-SWCNT systems are not promising candidates for toluene detection ascribable to their lack of reversibility originated from the strong chemical reaction between the toluene and the metal atom. However, they may still be used as a single use/disposable sensor for breath analysis. On the other hand, they may be potential platforms for the removal of toluene from the environment, thanks to their high adsorption energies. However, Pt- and Pd-SWCNT systems offer moderate adsorption energies for toluene detection, resulting in shorter recovery times for their sensors. The sensitivity of the Pt-SWCNT sensor (-27.30%) may be adequate to detect the toluene at sub-ppm concentrations. Interestingly, the sensitivity of the Pd-SWCNT ($+61.60\%$) is 2.25 greater than that of Pt-SWCNT, indicating the potential of Pd-SWCNT for toluene detection at low concentrations and fast recovery (milliseconds). Thus, Pd-SWCNT can be proposed as a superior material for breath analysis of lung cancer.

Summary

Detection of disease states from human breath has been the subject of fascination to human beings since the time of ancient Greeks. Today, it is possible to train canine's or use modern materials and technologies as sensors for detection of VOC's from human breath. We employed first-principle calculations to explore the adsorption geometry, adsorption energy, charge transfer, electronic, and magnetic properties of pristine and metal decorated SWCNTs with toluene, an important lung cancer biomarker in exhaled breath of patients. Our results revealed that although a toluene molecule is only physisorbed on pristine SWCNT *via* VdW forces ($E_{ad} = -0.571$ eV), a significant improvement on its adsorption energy is found by utilizing transition metal (Pt, Pd, Rh, or Ru) decorated SWCNT system as the adsorbent. The chemical adsorption processes occurred by the interaction of metal atom on the SWNT sensors and C atoms in toluene. The *d* orbital of metal atom interacts with *p* orbital of C atom of toluene as the perpendicular orientation of these orbitals makes it easier for them to overlap. The adsorption energies of toluene on Pt-, Pd-, Rh-, and Ru-SWCNT systems were found to be -2.572 , -1.535 , -2.628 , and -2.665 eV, respectively,

suggesting higher negative interaction energies leads to stronger chemi-adsorption. Rh- and Ru-SWCNT systems offer outstanding responses to toluene (-96.98% and -99.98% , respectively), but the weak recovery suggests its use as single use disposable breath analyzers for detecting very low levels of toluene in human breath. Pt- and Pd-SWCNT systems can detect toluene with sensitivity -27.12% and $+61.60\%$, respectively. Toluene is moderately chemisorbed on these systems, offering a short recovery time of 69 sec and 2 ms, thus enabling their adoption for lung cancer breath analysis. Based on our results, metal decorated SWCNTs are promising candidates to detect an individual toluene molecule, opening new doors for the early screening of lung cancer from human breath or sensors for personal safety monitoring in variety of environments.

4. Chapter 4

Theoretical Study on CNT Sensor

SWCNT- based Platform for Early Detection of Liver Cancer

Regarding the serious threat of liver cancer owing to the concealment and hard detection of liver tumors at an early stage, primary diagnosis becomes quite crucial to guarantee human health. So, in this work platinum-decorated single-walled carbon nanotubes (SWCNTs) were proposed as superior nanodevice for the detection of 1-Octen-3-ol (octenol), decane, and hexanal as liver cancer biomarkers in the exhaled breath of the patients. Herein, density functional theory (DFT) calculations have been utilized to scrutinize the structural and electronic properties of pristine and Pt-decorated SWCNTs. Obtained results showed that the gas molecules were weakly physisorbed on the pristine SWCNT with negligible charge transfer and large interaction distances. Contrariwise, after the decoration of the SWCNT with Pt metal atom, significant charges are transferred, and energy adsorption increased. The results disclosed that the energy adsorption has been enhanced, for example, energy adsorption increased two times for decane and hexanal molecules (-1.06 , and -1.07 eV) upon adsorption on Pt-decorated SWCNT. Moreover, substantial charges with amount of 0.238, 0.245, and 0.223 e were transferred from octenol, decane, and hexanal to the surface, respectively. So, investigations revealed that these compounds are strongly chemisorbed on Pt-SWCNT with small interaction distances and along with the short recovery time of 1.7, 83.4, and 123 sec at room temperature toward octenol, decane, and hexanal, respectively which make it a compelling nanodevice. Considering the findings, Pt-SWCNT is an excellent substrate for the sense of liver cancer biomarkers with desired recovery time and the results demonstrate its feasibility for potential application in the near future in the field of liver cancer diagnosis.

4.1 Overview

Liver cancer is the third most common cause of cancer death throughout-the-world as reported by WHO [166], it occurs when the normal cells in the liver become abnormal and those abnormal cells grow rapidly [167]. The treatment of cancer including liver cancer is a long and

difficult process and based on the stage its survival years may change. So, the early diagnosis of the disease is of great importance [168, 169]. There are several methods to diagnose cancers but unfortunately, most of them are costly and unsuitable for widespread screening [170]. However, exhaled breath analysis as a non-invasive technique and diagnostic tool for various diseases, therapeutic monitoring, and metabolic status has gained tremendous interest in recent years [72, 171-173].

Exhaled breath contains more than 3,500 components, the majority of which are volatile organic compounds (VOCs) [174-176]. These compounds (VOCs) in exhaled breath carry the fingerprints of metabolic and biophysical processes happening in human body [177]. It has been revealed that VOC concentration profiles and/or VOC composition vary between patients with and without certain disorders [178]. So, research on human exhaled breath analysis, due to its potential possibility of the facile and swift diagnosis of diseases such as cancers, has obtained great attention [179, 180]. For example, acetone, ethanol, formaldehyde, and toluene have been reported to be related to lung cancer, diabetic ketoacidosis, Alzheimer's [181-183]. Moreover, studies revealed that the other VOC gases from exhaled breath, such as octenol (1-Octen-3-ol), hexanal, and decane are liver cancer biomarkers [86, 184, 185]. In this regard, detecting octenol, hexanal, and decane species by gas sensors would be effective and workable for the diagnosis of liver cancer.

It is worth mentioning that gas and molecules detection has been investigated by many scientists with help of different nanomaterials [186-188], for instance, adsorption of sulfadimethoxine and tetracycline molecules on β -antimonene nanotube [189], interaction of styrene on single and double-walled square-octagon phosphorene nanotubes has been explored [190], and adsorption of aldrin and dieldrin molecules on blue phosphorene was studied [191].

Due to carbon nanotube's (CNTs) unique properties including their high surface-to-volume rate, excellent sensing behaviors like a quick response, good sensitivity, low cost, and hollow structure, they have attracted a lot of attention [121-123, 127, 145, 192, 193]. For example, there has been works regarding functionalization of CNTs to enhance the efficacy of anticancer drugs, and the interactions between functionalized nanotube and drug molecule were governed by van der Waals (vdW) energy [194]. On the other hand, CNT-type devices can be used as a platform for gas detection. In fact, gas molecules upon adsorption may act as electron donors or acceptors and consequently change the density of charge carriers of the CNT. [195, 196]. Due to these properties, CNT-based gas sensors experienced rapid advancement and development in recent

years [197]. For example, utilization of CNT for detection of NO, and CO as dangerous components for environment and health have been investigated [139, 198, 199]. Single-walled carbon nanotube (SWCNTs) can be used to fabricate extremely highly sensitive sensor and celerity with the purpose of detecting trace gas. In another study, ammonia sensing as a toxic and flammable gas, upon SWCNT was investigated [200].

Furthermore, adsorption of other gas molecules such as NO₂, CO₂, SO₂, and H₂S were explored over SWCNT-based gas device [201-203]. In spite of the potential fascinating characteristics of SWCNT, several reports have shown that the weak interaction and insufficient charge transfer between the gas molecules and pristine SWCNT sheet, the pristine SWCNT fails to detect some gas molecules. To enhance detection and sensing of SWCNT toward target gas molecules, decoration of SWCNT with transition metal (TM), especially (Pt or Pd) was proposed.

Given these facts, it was reported that Pd-decorated SWCNT could be a good platform for methane detection, the adsorption energy results revealed that after modifying the nanotube with Pd, it exhibits good sensitivity and has a stronger interaction with the methane [204]. Recently our group comprehensively studied the toluene sensing as lung cancer biomarker upon TM decorated SWCNT, and it was noted that Pt, and Pd platforms are more efficient than pristine SWCNT for toluene detection [20].

Nonetheless, to the best of our knowledge, calculations related to octenol, decane, and hexanal adsorptions on pristine, and Pt-decorated SWCNTs have not been reported. Geometrical structures, adsorption energies, and electronic properties have been thoroughly studied in this work with first-principles methods based on DFT. We have employed DFT to investigate interaction behavior of the molecules upon pristine/TM-decorated SWCNT. Our calculations can provide fundamental adsorption and sensing mechanism of such platform and help the development of high-performance room temperature breath analyzer biosensor for early detection of liver cancer.

4.2 Computational Method

In this theoretical work, first-principles computations based on DFT method was used and carried out in the Atomistix ToolKit (ATK) software package [153, 154]. The generalized-gradient approximation (GGA) as formulated by Perdew-Burke-Ernzerhof (GGA-PBE) was employed to calculate the exchange-correlation functional with the Hartwigsen, Goedecker, Hutter (HGH)

pseudopotentials with tier 3 [205]. The Grimme vdW correction (PBE-D2) was adopted to deal with the long-range van der Waals (vdW) interactions [157]. The kinetic energy cut-off and electronic temperature were set to 150 Ry, and 300 K, respectively.

An (8,0) zigzag SWCNT was studied. The supercell is periodically repeated and contains 96 C atoms with conditions as $a = b = 30 \text{ \AA}$, and $c=12.82 \text{ \AA}$ aiming at preventing the spurious image-image interactions. All the structures had been relaxed until the convergence tolerances of force and stress on each atom were selected to be less than 0.01, and 0.001 eV/Å, respectively. The primitive Brillouin zone k-point was sampled performed in $1 \times 1 \times 11$ Monkhorst-Pack mesh for geometry optimization and $1 \times 1 \times 101$ k-points for electronic calculations.

For the purpose of evaluation of the adsorption stability and interaction between the gas molecules and the pristine/metal-decorated-SWCNT, their adsorption energy (E_{ad}) was defined as:

$$E_{ad} = E_{Y+Molecule} - (E_Y + E_{Molecule}) \quad (7)$$

Here Y is the SWCNT or the metal decorated-SWCNT. $E_{Y+Molecule}$, E_Y , and $E_{Molecule}$ are the total energies of the molecule-nanotube complex, nanotube, and the isolated molecule, accordingly. In the above-defined equation, negative adsorption energy represents that the interaction is exothermic and energetically favorable. In addition, the structural stability of pristine and Pt decorated SWCNT is calculated in terms of its formation energy [14, 206-208]:

$$E_{form} = \left(\frac{1}{n}\right)[E_Y - n(E_C)] \quad (8)$$

where n has the meaning of the number of carbon atoms in the SWCNT and E_C denotes the energy of the isolated carbon atom. For pristine, and Pt-decorated SWCNT, the formation energy is observed as -6.706 , and -6.658 eV/carbon atom, respectively. The negative values of E_{form} demonstrating the geometrical stability of the structures.

Also, the adsorption energies for all interactions were obtained by considering the basis set superposition error (BSSE) by using counterpoise (cp) correction.

$$\Delta E_{ad,cp} = E_{ad} - E_{BSSE} \quad (9)$$

where $\Delta E_{ad,cp}$ is corrected counterpoise energy, E_{BSSE} is the energy of basis set superposition error. Furthermore, the charge transfer (Q) characterizes the change of the carried charge amount by gas molecules after adsorption and can be analyzed employing Mulliken population analysis by measuring the charge difference among them. It is worth mentioning that the positive value indicates the transfer of a corresponding number of electrons from the gas molecule to the surface, while the negative one represents the converse electron transferring path.

4.3 First-principles calculations using density functional theory:

After relaxation, C–C bond distances are 1.42 Å and the diameter is 6.37 Å for pristine (8,0) SWCNT (Figure 1a). The accuracy of the calculations by optimizing the structure and computing the energy band structure was verified. The results disclosed that the pristine SWCNT at Γ -point has a direct bandgap of 0.643 eV, which makes it a semiconductor [143, 161]. Moreover, energy bandgap for other (m,0) zigzag SWCNTs, where m stands for chirality of SWCNTs were calculated and exhibited in Table 4-1.

It is worth to mention that a carbon atom has four valence electrons. In each carbon atom in the nanotube, σ bonds are created with three adjacent carbon atoms using carbon's three electrons in the sp^2 hybrid orbitals. Also, π bonds transverse to the tube's axis are formed by the fourth valence electron in the unhybridized p orbital of each carbon atom is shared with two neighboring carbon atoms. The optimized molecules, octenol ($C_8H_{16}O$), decane ($C_{10}H_{22}$), and hexanal ($C_6H_{12}O$) are shown in Figure 4-1.

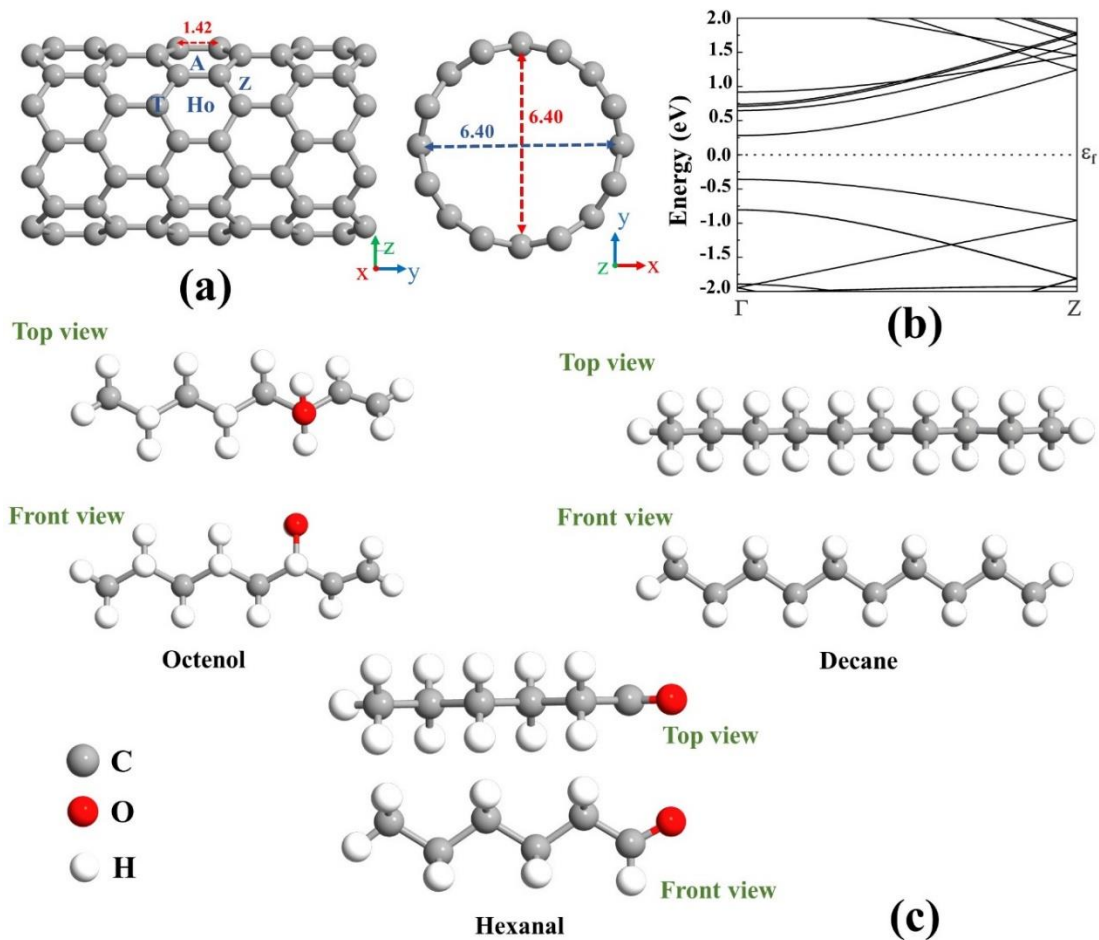


Figure 4-1. (a) Relaxed structure of a pristine SWCNT along with various adsorption locations on the SWCNT (Ho: hollow, A: axial, Z: zigzag, and T: top), (b) its energy band structure, the dotted line indicates the Fermi level, which is set to zero. (c) The relaxed molecular structure of octenol, decane, and hexanal in two views are illustrated.

Table 4-1. The energy bandgap of (m,0) zigzag SWCNTs (E_g), where m is the chiral index of the SWCNT.

(eV) \ m	9	10	11	12	13	14	15
E_g	0.093	0.76	0.94	0.078	0.63	0.73	0.028

Since the molecules tend to be adsorbed in numerous configurations, possible adsorption situations were considered. As can see from Figure 4-1, molecules can be positioned above the C-C bond (A and Z locations), C atom (T location), and the middle of the C hexagon (Ho location)

of SWCNT. These possible adsorption sites as exhibited well in Figure 4-2 were determined through optimizing all atomic positions [209]. At these sites, different molecular orientations (perpendicular or parallel to the axis of the nanotube) were studied.

The strength of adsorption was assessed by calculating adsorption energies between analytes and sensing materials. The more negative adsorption energy, the more exothermic adsorption, and the stronger the interaction. The most favorable adsorption geometries and their band structures were illustrated in Figure 4-3.

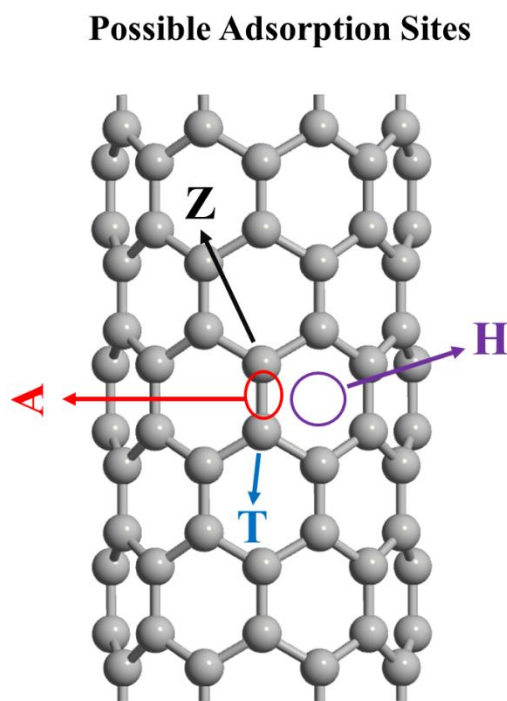


Figure 4-2. The possible adsorption sites on the SWCNT.

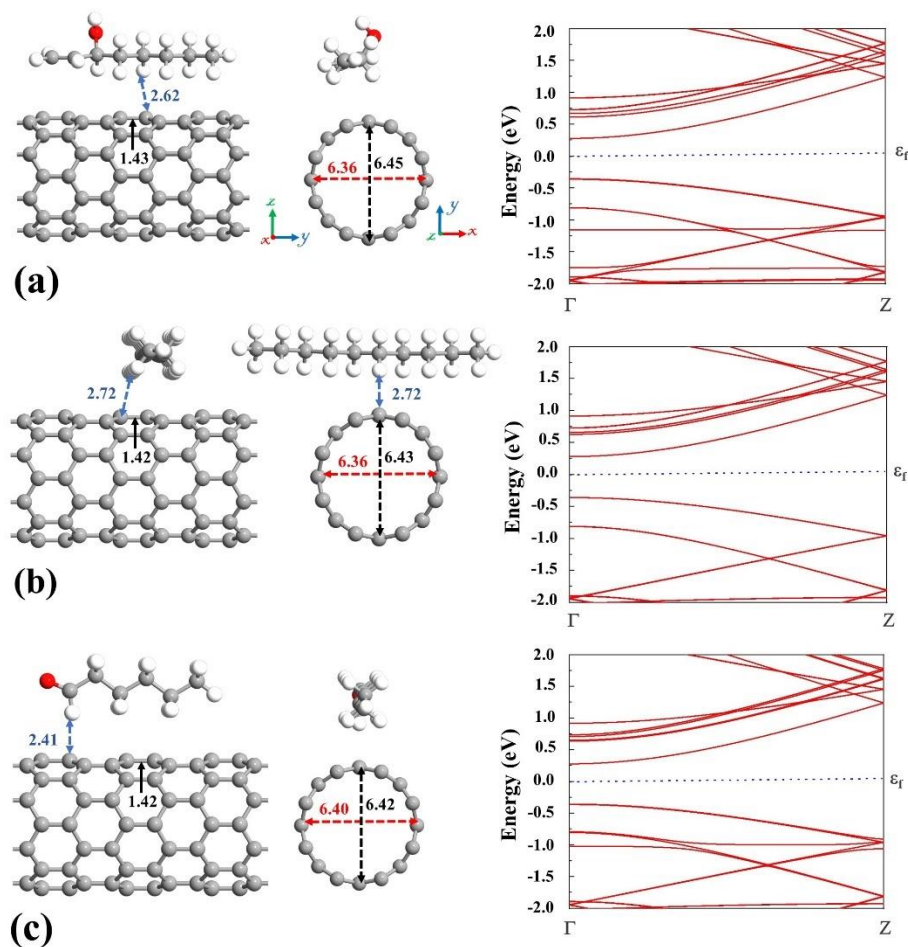


Figure 4-3. The relaxed atomic structures of a) Octenol, b) Decane, and c) Hexanal adsorption on pristine SWCNT surface along with their electronic band structures.

The horizontal alignment of the molecules on top of the C atom of the nanotube was revealed to be energetically more desirable, as depicted in Figure 4-3. Upon exposure the interaction distance was calculated for the structures. The minimum atom–atom distance (interaction distance) between gas molecules and the CNT surface (C-H) was estimated to be 2.62, 2.72, and 2.41 Å, after octenol, decane, and hexanal adsorption, respectively.

The atomic radii of C, O, and H atoms are 0.67, 0.48, and 0.53 Å, respectively [210]. So, the sum of atomic radii of H and C is 1.2 Å. Therefore, the interaction distances between the SWCNT and the molecules are much larger than the sums of corresponding atomic radii, indicating that gas molecules are weakly adsorbed on the surface. The adsorption energies of octenol, decane, and hexanal molecules on pristine SWCNT are -0.76 , -0.56 , and -0.53 eV, respectively,

indicating that the interactions between these molecules and SWCNT are weak (see Table 4-2). In addition, the C-C bonds and distances were not changed considerably approving the weak adsorption of the molecules upon pristine SWCNT.

Moreover, the band gap of pristine SWCNT (0.643 eV) is decreased slightly for octenol (0.633 eV), decane (0.40 eV), and hexanal (0.635 eV). The charge transfer upon adsorption of the gas molecules on the pristine SWCNT is studied from the differences in the charge concentrations before and after adsorption. From calculations, net total charge of -0.019 , -0.013 , and $-0.024 e$ was obtained after adsorption of octenol, decane, and hexanal, respectively. These slight amounts of charge transfer agree well with the low adsorption energies of the molecules on the bare SWCNT and indicating that electrons were transferred from molecules to the SWCNT surface. All data and calculations are tabulated in Table 4-2.

Table 4-2. The calculated adsorption energy (E_{ad}), interaction distance (D), which is the distance between the molecule and SWCNT, charge transfer (Q), energy bandgap (E_g), and recovery time (τ).

System	E_{ad} (eV)	Q (e)	D (Å)	E_g (eV)	τ (sec)	τ (sec)	τ (sec)
					@ T=298 K (Visible light)	@ T=298 K (UV light)	@ T=348 K (UV light)
Pristine CNT	-	-	-	0.643	-	-	-
Pristine CNT-Octenol	-0.76	-0.019	2.62	0.633	7.06	7.06×10^{-4}	4.47×10^{-10}
Pristine CNT-Decane	-0.56	-0.013	2.72	0.64	0.0029	2.93×10^{-7}	1.98×10^{-11}
Pristine CNT-Hexanal	-0.53	-0.024	2.41	0.635	9.13×10^{-4}	9.13×10^{-8}	98.54
Pt-CNT	-2.05	-	-	0.591	-	-	-
Pt-CNT-Octenol	-0.96	-0.238	1.82	0.598	$1.7 \times 10^{+4}$	1.7	79.16×10^{-4}
Pt-CNT-Decane	-1.06	-0.245	1.79	0.6	$8.34 \times 10^{+5}$	83.4	0.22
Pt-CNT-Hexanal	-1.07	-0.223	1.78	0.618	$1.23 \times 10^{+6}$	123	0.31

To assess the performance of a gas sensor, one vital indicator recovery time should be explored [211]. The recovery time (τ) can be defined employing the conventional transition state theory as follows:

$$\tau = A^{-1} \exp(-E_{ad}/K_B T) \quad (10)$$

Here, T is the temperature, and K_B is the Boltzmann constant. A is the attempt frequency, which is the vibration frequency of single bonds between the molecule and the surface. It is known that at a constant temperature, small adsorption energies result in a fast desorption process of the

gas molecules. The recovery times obtained at room temperature ($T = 298 \text{ K}$) and under visible light ($\nu_0 = 10^{12} \text{ Hz}$) were 7.06, 0.0029, and $9.13 \times 10^{-4} \text{ s}$, for octenol, decane, and hexanal, respectively. A good gas sensor should satisfy reasonable short recovery time, the recovery time could be around several to several hundred seconds which would be acceptable for sensing application.

Ergo, adsorptions between considered gas molecules and pristine SWCNT are relatively weak, and it may well be argued that they are physisorbed upon interaction with the pristine SWCNT. So, to enhance the adsorption and interaction, the surface of SWCNT was decorated with Pt atoms. After optimization upon different potential sites on the SWCNT, the most relaxed Pt-decorated SWCNT was achieved with an adsorption energy of -2.05 eV , which creates two bonds with a minimum distance of 2.12 \AA with the C atoms of CNT (Figure 3-2).

Due to the strong adsorption of Pt atom upon SWCNT ($E_{\text{ad}} = -2.05 \text{ eV}$), and a large charge transfer ($0.101 e$), a conspicuous deformation in SWCNT was observed in accordance with previous works [139, 143, 160, 212]. Thereby, the diameter of the CNT is stretched in the decoration orientation and shrank in the perpendicular direction. Besides, the formation of metal-C bonds degrades the strength of C-C bonds, making these bonds to get enlarged from 1.42 (pristine) to 1.48 \AA (after decoration). The most stable structure, electronic band structure, and density of states (DOS) for the Pt-decorated SWCNT are depicted in Figure 4-4.

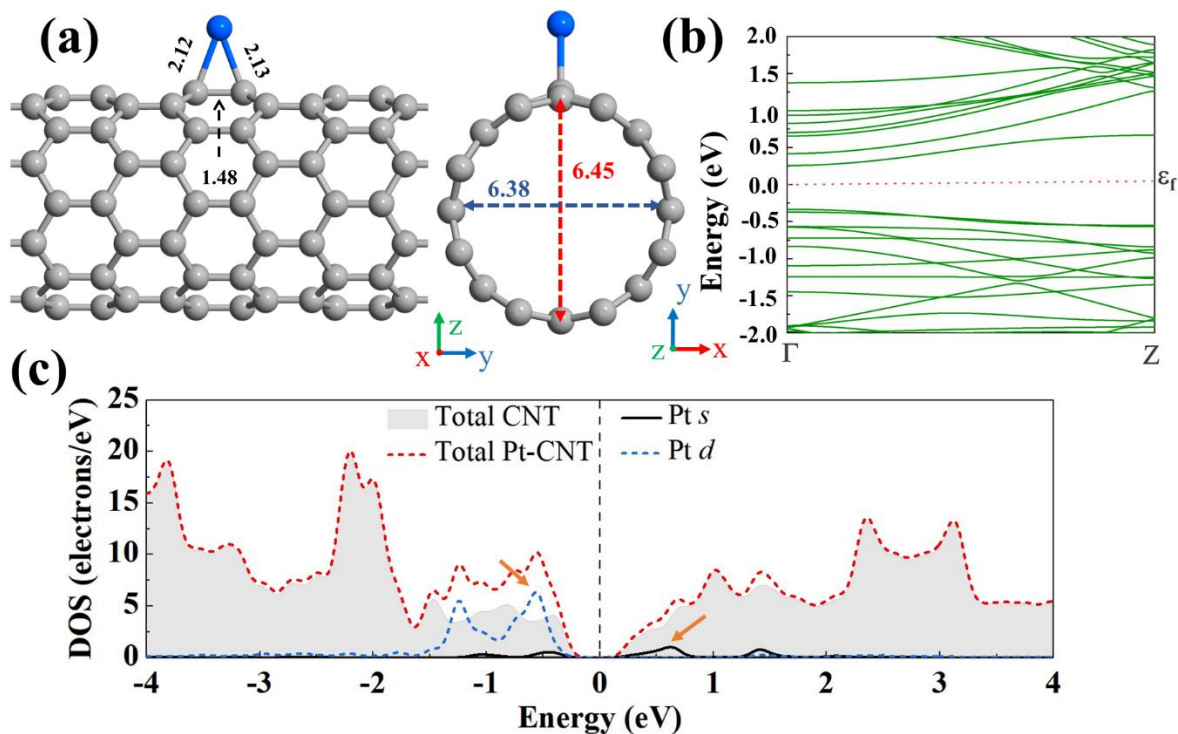


Figure 4-4. The most relaxed configuration of a) Pt-decorated SWCNT, b) its band structure, and along with c) its DOS calculations.

The metal atom is located between two C atoms of the SWCNT, where Pt-C distances are 2.12 and 2.13 Å. Since the sum of covalent radii of Pt (1.77 Å) and C (0.67 Å) is 2.44 Å and is larger than the obtained minimum distance, it can be assumed that the chemical bonds created between C and Pt atoms. As can be seen from Figure 4-4, the Pt-SWCNT is a direct bandgap semiconductor ($E_g = 0.591$ eV). Additionally, new peaks appeared in DOS of SWCNT after decoration by Pt atom at the energy range of -1.0 to 0 eV and 0 to 1 eV, attributed to the d and s orbitals of the metal atom, respectively.

Next, the most energetically preferable adsorption configurations for the studied analytes on the Pt-decorated SWCNT are displayed in Figure 4-5. The gas molecules were positioned on top of the Pt atom with various molecular orientations.

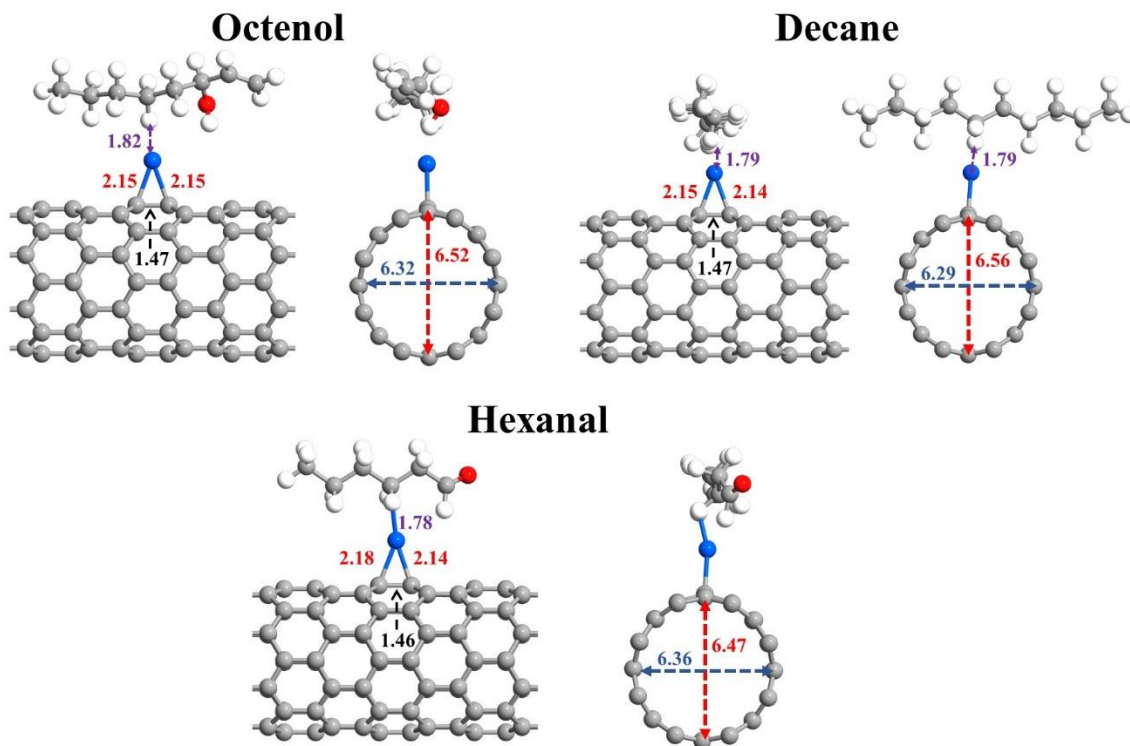


Figure 4-5. The most stable structures of Pt-decorated SWCNT toward octenol, decane, and hexanal molecules. The distances between the different atoms are shown.

It was discovered that upon exposure to the Pt-decorated SWCNT, the studied molecules adopt a horizontal orientation with respect to the surface with its H atom toward Pt atom. The minimum distance between H and Pt was found to be 1.82, 1.79, and 1.78 Å for octenol, decane, and hexanal, respectively. The sum of covalent radii of the H-Pt bond is 2.3 Å, which can confer those minimum distances are smaller than the sum of covalent radii representing strong adsorption.

Moreover, from adsorption energy calculations as described in Table 4-2, E_{ad} of -0.96 , -1.06 , and -1.07 eV was procured for adsorption of octenol, decane, and hexanal on the Pt-decorated SWCNT. It is apparent that the adsorption of all analytes has been intensified after decorating the SWCNT with Pt metal, for example, the adsorption energy of octenol has been incremented from -0.76 eV (on pristine) to -0.96 eV (on Pt-decorated SWCNT), and also the adsorption energy of decane, and hexanal increased two times. From calculation of BSSE adsorption energies, over adsorption of octenol, decane, and hexanal molecules on pristine SWCNT, adsorption of -0.82 , -0.64 , and -0.57 eV was found, respectively. Also, after octenol, decane, and hexanal adsorption upon Pt-decorated SWCNT, energy of -1.05 , -1.09 , and -1.12 eV was achieved, respectively.

Conspicuously from Figure 4-5 can be observe that the values of the diameter of the Pt-SWCNT for the octenol, decane, and hexanal are 6.52 (6.32), 6.56 (6.29), and 6.47 (6.36) Å in the direction of the adsorbed metal (perpendicular to the adsorption site), respectively. Due to the strong adsorption of the molecules upon Pt atom, the C-Pt bond lengths were altered from 2.12 (2.13) to 2.15 (2.15), 2.15 (2.14), and 2.18 (2.14) Å for octenol, decane, and hexanal, respectively.

To shed light on the adsorption mechanism of Pt-SWCNT towards the molecules, the electronic band structures, and DOS calculations were collected and are exhibited in Figure 4-6.

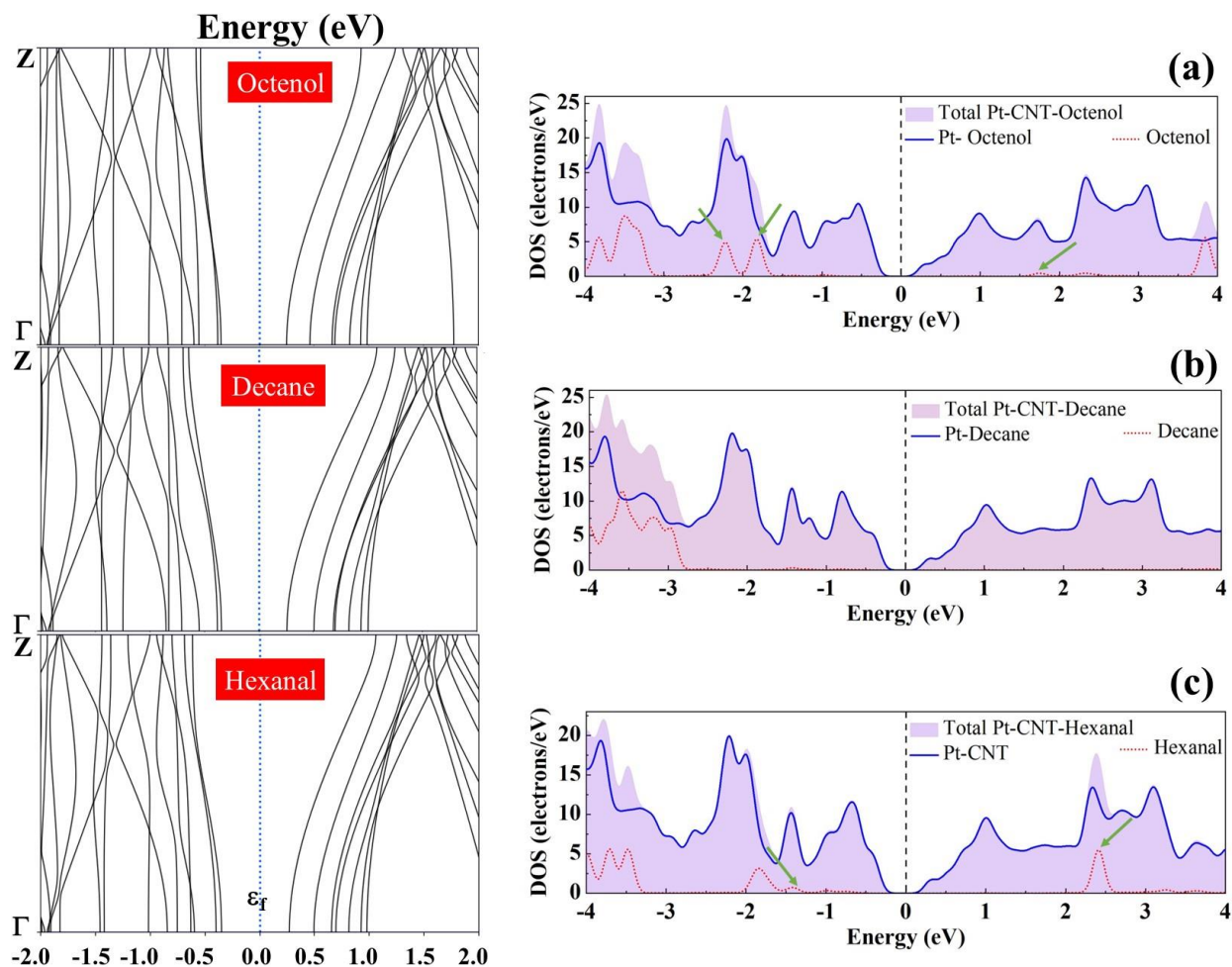


Figure 4-6. Electronic band structure, and DOS plots for Pt-decorated SWCNT exposed to (a) octenol, (b) decane, and (c) hexanal molecules. Fermi level with blue dotted line is set to zero.

Upon adsorption of octenol, decane, and hexanal molecules on the Pt-SWCNT, the energy band gap of 0.598, 0.6, and 0.618 eV were obtained. It means that the energy bandgap of the Pt-

decorated SWCNT (0.591 eV) was slightly increased after interaction with the molecules. It can be noticed from DOS calculations that there are numbers of overlapping peaks (as some highlighted by arrows) between molecules and the Pt atom. For instance, after octenol adsorption, overlapping peaks appeared in the energy range of -1.5 to -2.5 eV, and 1.5 to 2 eV. In the case of hexanal, there are discernible peaks in the range of 2 to 2.5 eV and in the vicinity of the Fermi level from -1 to -1.5 eV. However, there are some peaks after decane adsorption in the range of -2.5 to -3.5 eV, which are not close to the Fermi level. The larger number of overlapping peaks could suggest that the orbital hybridization is stronger in the system.

In order to acquire more information, the electronic total densities were obtained and exhibited in Figure 4-7. It was found that all the gas molecules donate electrons to the surface, a significant net charge of 0.238, 0.245, and 0.223 e was achieved for octenol, decane, and hexanal, respectively. These large amounts of charge transfer agree well with the high adsorption energies of the molecules on the Pt-decorated SWCNT.

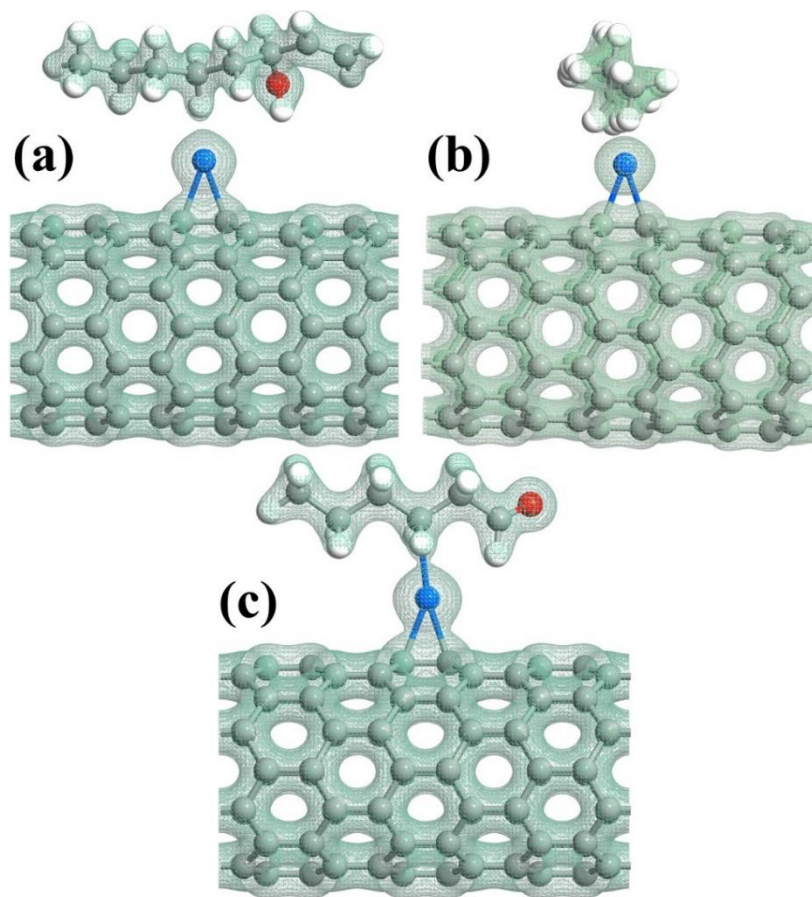


Figure 4-7. The total charge densities of a) octenol, b) decane, c) hexanal on Pt-decorated SWCNT systems.

Finally, based the recovery time findings, the octenol on Pt-SWCNT has the shortest recovery time followed by decane, and hexanal at room temperature. As an example, the recovery time of Pt-SWCNT gas sensor after octenol, decane, and hexanal adsorption could be ~ 1.7 , 83.4, and 123 s by annealing at 25° C in UV irradiation ($\nu_0 = 10^{16}$ Hz), see Table 4-2.

To sum up, it was manifested that the Pt-decorated SWCNT has good detection toward liver cancer biomarkers from exhaled breath. It was divulged that these compounds (octenol, decane, and hexanal) has a weak adsorption on the pristine SWCNT. However, after decorating of the SWCNT with Pt atom, its detection to the molecules greatly improved. It was found that Pt-SWCNT has a large adsorption energy of -0.96 , -1.06 , and -1.07 eV toward octenol, decane, and hexanal, respectively along with large total charges that was emitted from the molecules to the surface, which confirm the chemical adsorption that happened between them. Overall, it could be supposed that Pt-SWCNT gas sensor has a great potential for liver cancer biomarkers detection through exhaled breath at room temperature.

Summary

This study proposes a novel sensing material CNT-based to detect the possible liver cancer patients through an exhaled breath. In summary, we applied first-principle calculations based on DFT to investigate the adsorption geometry, adsorption energy, charge transfer, electronic band structure, and DOS of pristine and Pt-decorated SWCNT with liver cancer biomarkers (octenol, decane, and hexanal) adsorption. Our results manifested that Pt-decorated SWCNT has a remarkable capability for detection of octenol, decane, and hexanal in comparison with the pristine SWCNT, resulting in chemisorption. Calculated results predict that after adsorption of octenol, decane, and hexanal, upon Pt-SWCNT adsorption energy of -0.96 , -1.06 , and -1.07 eV with noticeable amounts of electron charges 0.238, 0.245, and 0.223 e observed, respectively. Also, the recovery time of 1.7, 83.4, and 123. s at room temperature under UV light was achieved, which is a key parameter for gas sensors to be reused. Thus, the findings of the present study will lay a road in the development of nanosensors based on CNT material for liver cancer detection.

5. Chapter 5

Theoretical Study on Phosphorene

Phosphorene-based Platform for Detection of Alcohols

Inspired by prior advancements and the growing utilization of two-dimensional (2D) based gas sensors, this work presents the potential of black phosphorene for sensing volatile organic compounds (VOCs) gas molecules. First-principles density functional theory (DFT) combined with non-equilibrium Green's function (NEGF) calculations were employed to evaluate the VOCs sensing performance of suspended pristine and Pt-decorated phosphorene materials. Several VOCs, such as acetone, ethanol, formaldehyde, methanol, and toluene, along with CO₂ and H₂O molecules, were considered as the target gases. The results indicated that although the electronic properties of the pristine phosphorene were slightly affected by the VOCs adsorption, the decoration of the phosphorene sheet with Pt atoms drastically increased its alcohol's sensitivity. The sensor based on Pt-decorated phosphorene was found to be sensitive and selective toward methanol between considered other gas molecules with a gas response of 41.10%. A short recovery time of 0.17 sec at room temperature under UV light obtained theoretically and it confirmed the potential application of Pt-phosphorene-based sensor for alcohol detection at room temperature.

5.1 Overview

Single gas molecules detection is pivotal to many areas, including medical diagnosis and environmental monitoring. Nanomaterials such as metal oxide nanoparticles have drawn tremendous attention for gas molecule adsorption owing to their exceptionally high surface-to-volume ratio [213]. In spite of high sensitivity and fast response, the high operating temperature of metal oxide nanoparticles-based gas sensors accelerated the development of low-power alternatives. Since the debut of graphene, [214] the world's first two-dimensional (2D) nanomaterial, many reports demonstrated the promising applications of graphene and its derivatives for gas sensing because of the high carrier mobility, high thermal stability, low electrical noise, and low operating temperature [215-217].

Research on nanostructure hybrid materials for gas sensing has been gaining momentum in recent years. Especially, noble metal decorated novel structures were found to be remarkably

sensitive and selective owing to the synergistic effect of the compound configuration [218, 219]. For example, adsorption of toxic gases NO_2 and H_2S on transition metal (e.g., Pt and Pd)-decorated graphene was investigated, [220] and it was found that metal decoration obviously enhance the interactions between graphene and gas molecules. It was found that the adsorption energy and charge transfer were 7–10 fold and 3–10 times higher than that of pristine graphene, respectively, and Pt-decorated graphene was more sensitive to H_2S . Gas sensing characteristics of the MoS_2 and Au-functionalized MoS_2 toward organic compounds was investigated experimentally and theoretically. [221] It was revealed that MoS_2 -Au sensor showed higher sensitivity to the gas molecules at room temperature compared to that of the pristine MoS_2 sensor.

Inspired by the triumphs of graphene, other 2D nanomaterials such as transition metal dichalcogenides (TMDs), MoS_2 , MXenes, silicene, borocarbide, borophene, to name a few, have become the center of intense research for the development of advanced gas sensing devices [5, 25, 222-225]. As a strong competitor to graphene, phosphorene (monolayer black phosphorus) was first introduced in 2014 [74]. Few-layer black phosphorus was successfully synthesized by exfoliation techniques and showed a bandgap varying from 0.3 to 1.5 eV depending on the number of stacked layers [226]. Unlike semimetallic graphene, phosphorene has a semiconductor character with high carrier mobility up to $1,000 \text{ cm}^2 \text{ V}^{-1} \text{ s}^{-1}$ at room temperature, making it a promising candidate for the nanoelectronics field and gas sensing applications [28, 29]. Using first-principle calculations, it was predicted that phosphorene as a gas sensor outperforms other 2D counterparts such as graphene and MoS_2 [44]. It was revealed that the sensor is more sensitive to nitrogen-based gas molecules such as NO and NO_2 in comparison with carbon-based molecules such as CO and CO_2 [44]. The first FET-based gas sensor based on multi-layer phosphorene was fabricated in 2015 and found to be very sensitive to NO_2 concentration down to 5 ppb [227]. The superior molecular adsorption energy, less out-of-plane electrical conductance, higher surface-to-volume ratio, larger surface area, excellent mechanical flexibility, high operating frequencies, and ambipolar behavior make phosphorene rival or surpass other 2D materials for gas sensing applications [228].

Most studies of phosphorene-based gas sensors focus on the detection of toxic inorganic compounds. However, volatile organic compounds (VOCs) are an important class of atmospheric pollutants which can cause health effect. They include alcohols, aldehydes, ketones, aromatics, *etc.*, and are emitted by numerous daily-use household products such as furniture polish, paint, sanitizer, floor lacquers, to name a few. These organic chemicals are also present in exhaled human

breath and can serve as a potential biomarker for biomedical applications [229, 230]. Human breath contains about 870 VOCs which are linked to various diseases such as lung, colorectal, diabetic ketoacidosis, and kidney cancer [20, 231, 232]. Moreover, inhaling alcohol for a long time can cause severe damages to the human body such as methanol poisoning that can cause organ failure, blindness, or even death if it recognized too late [233]. Developing a reliable, sensitive, and inexpensive alcohol gas detection system has attracted extensive attention not only in medical and clinical applications but also in food, brewing, and fuel industries [234]. Hence, there have been increasing high demands to develop efficient sensors for VOCs especially alcohol detection.

The adsorption behavior of typical VOCs such as ethanol, propionaldehyde, acetone, toluene, and hexane on phosphorene was investigated [235]. The interaction of VOCs with phosphorene was found to be stronger than with MoS₂ [235]. However, the VOCs bind weakly to the phosphorene, making it challenging to detect them. It was reported that compression strain is a possible solution to enhance the sensibility of phosphorene to VOCs [235].

Different approaches were employed to improve the gas sensitivity of phosphorene. Suspended phosphorene-based gas sensor presented a 23% higher response to 200 ppm NO₂ with two-times faster recovery rate in comparison with phosphorene supported on a conventional substrate [236]. The introduction of vacancy defects and substitutional impurities such as Ti, Si, Mn, and Fe can drastically improve the H₂S and SO₂ sensing of phosphorene [237]. It was demonstrated that decoration of phosphorene with Alkali and Alkaline earth metals causes a significant enhancement of the nitrogen-based gas molecules adsorption energies, which is necessary for gas removal [238].

Here, we aim to enhance the VOCs sensing characteristics of phosphorene through metal functionalization. To this end, density functional theory (DFT) calculations were employed to investigate the interactions of suspended Pt-decorated phosphorene sensors with different gas molecules such as acetone, ethanol, formaldehyde, methanol, toluene, CO₂, and H₂O. Taking many concerns into consideration, the sensors' performance in terms of sensitivity, selectivity, and recovery time was analyzed. Our findings provide new insights into the development of high-performance phosphorene-based nanosensors for medical diagnosis and environmental monitoring applications.

5.2 Computational Method

The results were carried out in Atomistix ToolKit (ATK) package using first principles DFT method combined with non-equilibrium Green's function formalism (NEGF) [153, 154, 239]. The generalized gradient approximation (GGA) of Perdew-Burke-Ernzerhof (PBE) was utilized for exchange and correlation functions treatment. To describe the Van der Waals (vdW) interactions, the DFT-D2 method of Grimme was operated [156, 157]. The energy of adsorption for molecules upon pristine or Pt-decorated phosphorene based on vdW corrected were calculated by:

$$E_{ad} = E_{P-P/Pt-P+molecule} - E_{P-P/Pt-P} - E_{molecule} \quad (11)$$

Where $E_{P-P/Pt-P+molecule}$, $E_{P-P/Pt-P}$, and $E_{molecule}$ are the whole energies for the pristine or Pt-decorated phosphorene-gas molecule system, pristine or Pt-decorated phosphorene, and the single molecule, respectively. For these calculations, the basis set of Fritz-Haber-Institute (FHI) pseudopotentials with double- ζ polarized were employed. The kinetic energy cut-off was set to 90 Hartree. A large vacuum with a sufficient size of 20 Å in z direction where the supercell is not periodic was considered to decouple the slabs. All configurations were optimized using the limited-memory Broyden-Fletcher-Goldfarb-Shanno (LBFGS) quasi-Newton method till the convergence criteria of 0.01 eV/Å for force and 0.001 eV/Å³ for stress acting on the atoms. For sampling Brillouin zones (BZ), $5 \times 5 \times 1$ and $11 \times 11 \times 1$ k -points were used for geometry optimization and electronic calculations, respectively.

Moreover, charge transfer (Q_T) between the pristine or decorated-phosphorene surface and molecules was obtained. In order to get more accurate results for charge transfer a good description of virtual states far above the Fermi level seems necessary. For this reason, the Hartwigsen, Goedecker, Hutter (HGH) pseudopotentials were used with Tier 4 basis set instead of Fritz-Haber-Institute (FHI) with double- polarized basis set. It is worth mentioning, a negative Q_T suggests that charges transfer from the gas molecule to the pristine or decorated phosphorene, while a positive Q_T denotes a reverse charge transferring path.

The calculations of electron transport were performed by GGA-PBE and NEGF approaches. In a device with two metal electrodes configuration, the passing current through the device at a finite bias voltage (V_b) was obtained from the Landauer-Büttiker equation:

$$I = \frac{2e}{h} \int_{\mu_L}^{\mu_R} T(E, V_b) [f_R(E, V_b) - f_L(E, V_b)] dE \quad (12)$$

Here μ_L and μ_R are the chemical potentials of the left and right electrodes, respectively. T and f are transmission functions and Fermi-Dirac distribution at energy E and V_b . E_f is the Fermi energy, the average value of chemical potentials of the left and right electrodes, which is usually fixed to zero. The bias energy window is $\mu_L = E_f - eV_b/2$ and $\mu_R = E_f + eV_b/2$. Additionally, $1 \times 3 \times 50$ k -points was used for electronic transport calculations.

5.3 First-principles calculations using density functional theory:

We first studied the structural properties of a suspended pristine phosphorene. The most stable structure of phosphorene and its unit cell's band structure is presented in Figure 5-1. It was confirmed that phosphorene is a semiconductor with a direct bandgap of 0.882 eV bandgap at the Γ point where both the valence band maximum (VBM) and the conduction band minimum (CBM) are located. The lattice constants for a monolayer of phosphorene were found to be $a = 3.32 \text{ \AA}$ and $b = 4.41 \text{ \AA}$. These results are in great agreement with the literature [240].

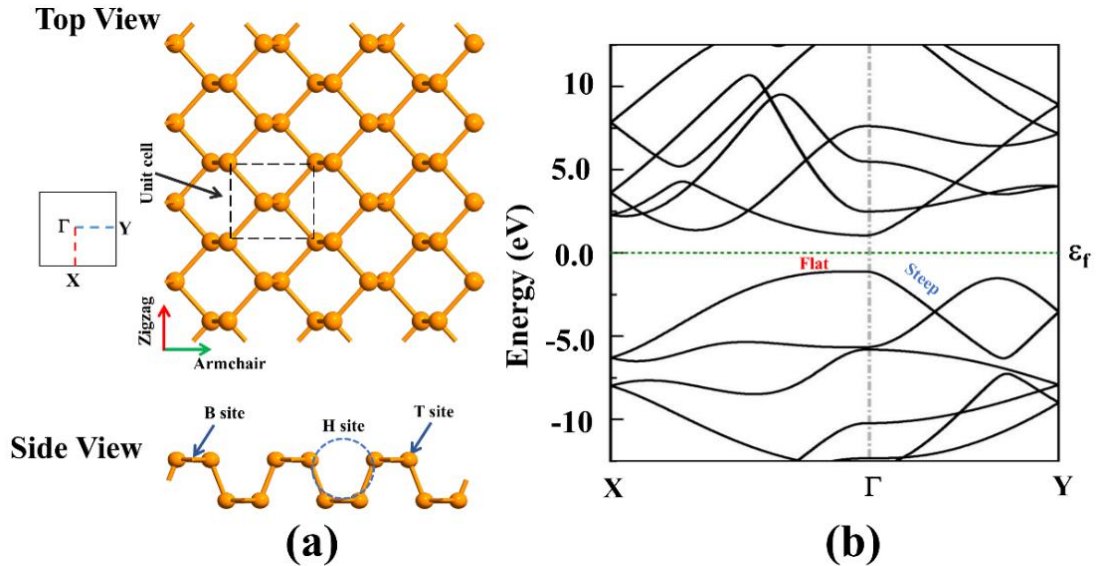


Figure 5-1. (a) Illustration of monolayer phosphorene sheet as well as its primitive unit cell, Brillouin zone with the high-symmetry points, and different possible adsorption sites (b) electronic band structure of the phosphorene unit cell.

In order to obtain the preferential adsorption sites of the VOCs on the pristine phosphorene sheet, the gas molecules were positioned at a distance of 2 Å above different locations of the sheet with diverse molecular orientations. Three possible adsorption locations, including B (above P-P bond), H (above hollow hexagon), and T sites (top of P atom), were analyzed, as shown in Figure 1(a). The molecular axes were considered perpendicular and parallel to the surface of phosphorene. All possible adsorption configurations were relaxed, and their adsorption energies were calculated. The negative adsorption energy is exhibitive of the exothermic process; thus, the most stable structure has the most negative adsorption energy. The most preferable adsorption configurations are depicted in Figure 5-2.

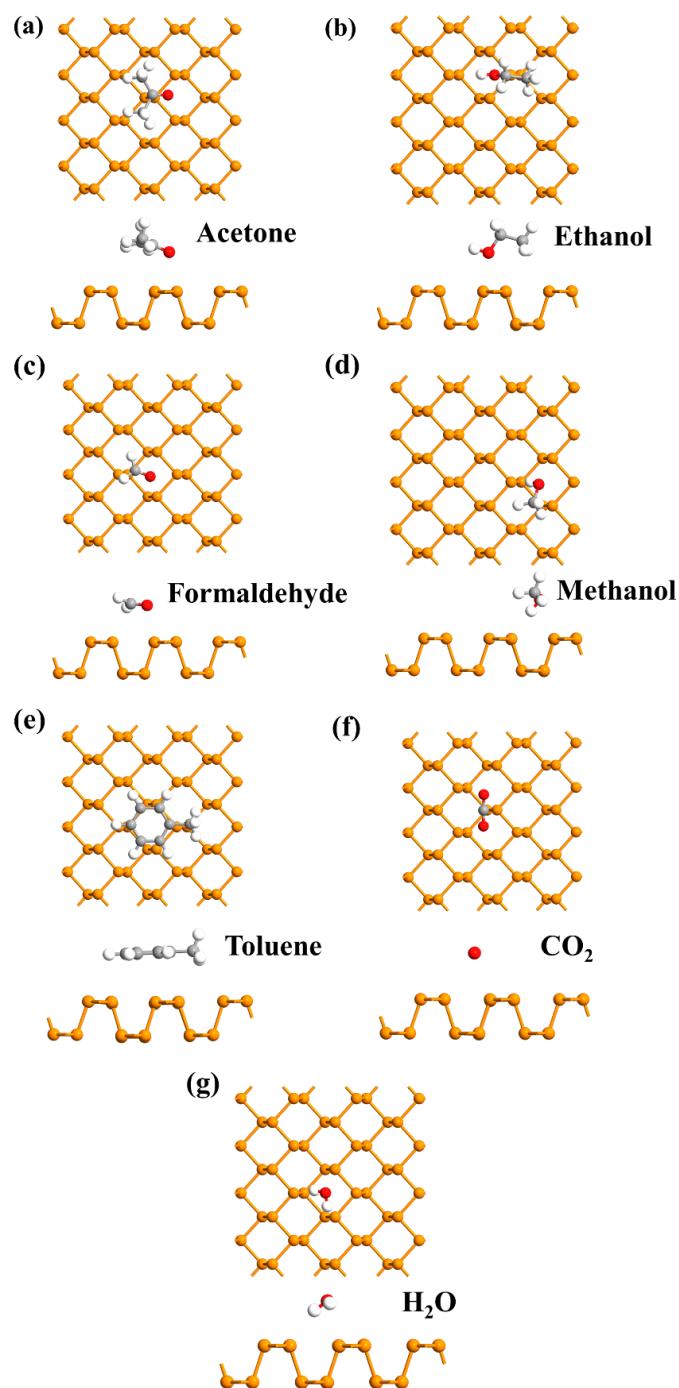


Figure 5-2. The energetically preferable adsorption configurations of gas molecules upon the pristine phosphorene surface.

The calculated adsorption energies of pristine phosphorene toward acetone, ethanol, formaldehyde, methanol, toluene, CO₂, and H₂O were obtained to be -0.74 , -0.73 , -0.66 , -0.67 ,

-1.16, -0.44, and -0.54 eV, respectively. A small charge of 0.042, 0.043, 0.032, 0.035, 0.051 e was transferred from acetone, ethanol, and formaldehyde, methanol, and toluene to the phosphorene, respectively. While CO₂, and H₂O withdraw a small charge of 0.012, and 0.021 e from the surface, respectively. It was revealed that all molecules were adsorbed physically on the pristine phosphorene, except toluene which was strongly physisorbed. Electronic band structures of the aforementioned structures were provided in Figure 5-3. It was noticed that after the adsorption of the gases on the phosphorene, the electronic band structures remained almost unchanged. The energy bandgap of pristine phosphorene (0.882 eV) upon gas molecules adsorption was slightly changed (<40 meV). The energy bandgaps for acetone-, ethanol-, formaldehyde-, methanol-, toluene-, CO₂-, and H₂O-phosphorene were calculated to be 0.882, 0.894, 0.9, 0.882, 0.844, 0.879, 0.885 eV, respectively.

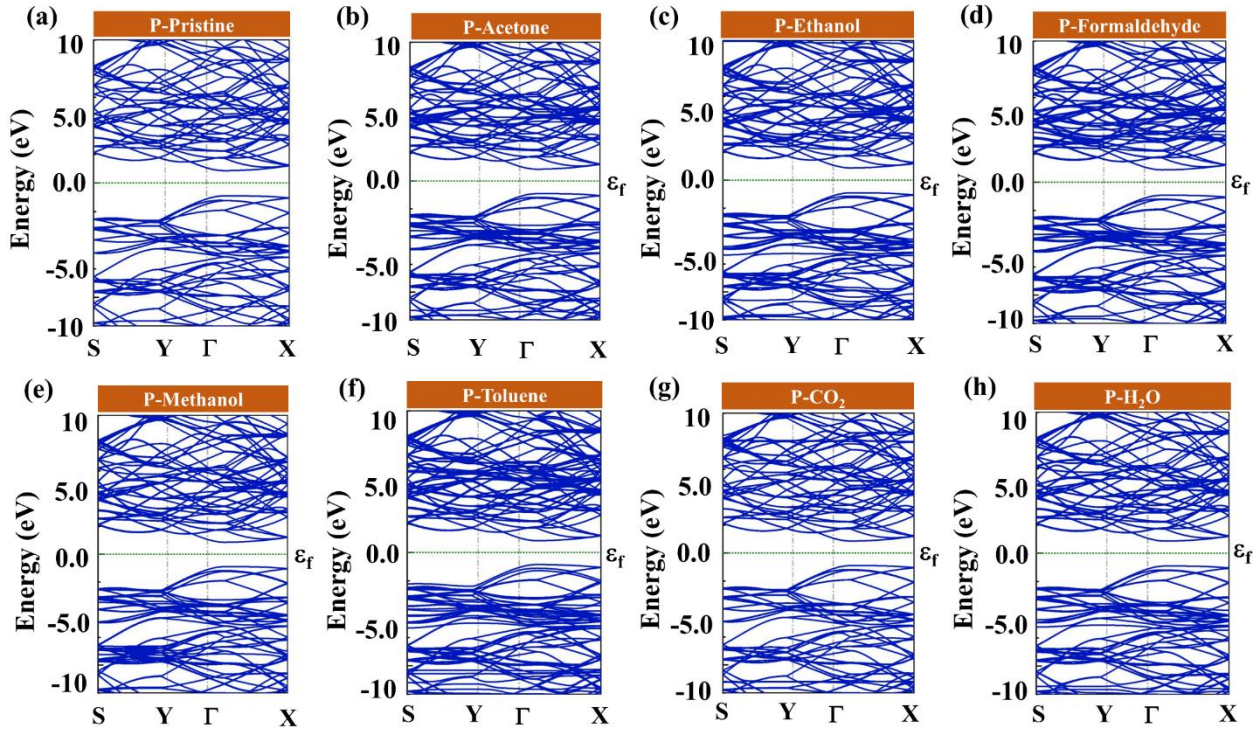


Figure 5-3. The obtained electronic band structures for gas molecules on pristine phosphorene (P). The Fermi level was fixed to be zero.

Because of the physical adsorption of the molecules upon the pristine phosphorene, large interaction distances were obtained. The minimum distance of 2.94 (O-P), 2.87 (O-P), 2.99 (O-P), 2.35 (H-P), 3.16 (H-P), 3.18 (C-P), and 2.57 (H-P) Å was found for acetone, ethanol, formaldehyde, methanol, toluene, CO₂, and H₂O molecules with phosphorene sheet, respectively.

The C, O, H, and P atoms have covalent radii of 0.77, 0.73, 0.37, and 1.07 Å, respectively [210]. So, the sums of corresponding covalent radii are 1.8, 1.8, 1.8, 1.44, 1.44, 1.84, and 1.44 Å, respectively. Since the minimum distances between the phosphorene surface and the gases are larger than the sums of covalent radii, it can be concluded that considered molecules were adsorbed physically adsorbed on the pristine phosphorene, supporting the adsorption energies calculations. The adsorption energies, minimum interaction distances, energy bandgaps, and the net charge transfer of the above configurations were presented in Table 5-1.

As an important factor for evaluation of a sensor's performance, recovery time (τ) can be determined based on the conventional transition state theory [211]:

$$\tau = \nu_0^{-1} \exp(-E_{ad} / k_B T) \quad (13)$$

Here T is the temperature, ν_0 is the attempt frequency, and K_B is the constant of Boltzmann. The recovery time of the pristine phosphorene-based sensor for the considered gases was listed in Table 5-1. A room temperature ($T = 300$ K) and under visible light ($\nu_0 = 10^{12}$ Hz), the recovery times were obtained 2.67, 1.81, 0.12, 0.18, 3.03×10^{-7} , 2.45×10^{-5} , and 0.001 sec, for acetone, ethanol, formaldehyde, methanol, toluene, CO_2 , and H_2O , respectively. Except for toluene, the obtained recovery times are well within the detectable range. The recovery time for toluene can be reduced substantially to 3.03×10^{-3} sec with the assistance of UV radiation.

Table 5-1. Calculated absorption energy (E_{ad}), minimum distance of interaction (D), where is the minimum distance between the gas and phosphorene surface, net total charge transfer (Q), (The negative values of charge imply that the molecule gives charges to the sheet), energy bandgap (E_g), and recovery time (τ).

System	E_{ad} (eV)	D (Å)	Q (e)	E_g (eV)	τ (sec) @ T=300 K (visible light)	τ (sec) @ T=300 K (UV light)
Pristine P	-	-	-	0.882	-	-
Pristine P-Acetone	-0.74	2.94	-0.042	0.882	2.67	2.67×10^{-4}
Pristine P-Ethanol	-0.73	2.87	-0.043	0.894	1.81	1.82×10^{-4}
Pristine P- Formaldehyde	-0.66	2.99	-0.032	0.900	0.12	1.21×10^{-5}
Pristine P-Methanol	-0.67	2.35	-0.035	0.882	0.18	1.78×10^{-5}
Pristine P-Toluene	-1.16	3.16	-0.051	0.844	$3.03 \times 10^{+7}$	$3.03 \times 10^{+3}$
Pristine P-CO ₂	-0.44	3.18	+0.012	0.879	2.45×10^{-5}	2.45×10^{-9}
Pristine P-H ₂ O	-0.54	2.57	+0.021	0.885	0.001	1.17×10^{-7}
Pt-P	-5.84	2.24	-	0.897	-	-
Pt-P-Acetone	-1.47	2.13	-0.123	0.967	$4.86 \times 10^{+12}$	$4.86 \times 10^{+8}$
Pt-P-Ethanol	-1.14	2.35	-0.198	0.754	$1.39 \times 10^{+7}$	$1.39 \times 10^{+3}$
Pt-P-Formaldehyde	-1.48	2.13	-0.112	0.977	$7.16 \times 10^{+12}$	$7.16 \times 10^{+8}$
Pt-P-Methanol	-0.908	2.37	-0.242	0.821	$1.77 \times 10^{+3}$	0.17
Pt-P-Toluene	-1.64	2.21	-0.142	0.878	$3.48 \times 10^{+15}$	$3.48 \times 10^{+11}$
Pt-P-CO ₂	-0.48	2.72	-0.055	0.876	1.15×10^{-4}	1.15×10^{-8}
Pt-P-H ₂ O	-0.83	2.47	-0.084	0.864	86.9	0.008

Due to the weak binding of VOCs to the pristine phosphorene, in an attempt to enhance the interactions, the surface of phosphorene was decorated by the Pt atom. The optimized structure of Pt-decorated phosphorene in company with its electronic band structure and density of states (DOS) is illustrated in Figure 5-4. The adsorption energy of Pt on the phosphorene surface was obtained to be -5.84 eV, and it creates three bonds with a minimum distance of 2.24 Å with P atoms of phosphorene. So, the stability of Pt-decorated phosphorene can be confirmed by comparing with previous works [240-242]. Since this distance is smaller than the sum of covalent radii (2.75 Å) of Pt (1.77 Å) and P (0.98 Å), it can be deduced that the chemical bonds appeared between Pt and P atoms. Although the electronic band structure of the phosphorene was affected by Pt decoration, it was observed that the energy bandgap value was slightly increased from 0.882 eV (pristine phosphorene) to 0.897 eV for Pt-decorated phosphorene. Three peaks attributed to d orbitals of Pt and their hybridization with P atom of phosphorene altered the DOS of the pristine phosphorene in the energy range of -3.5 to -0.5 eV.

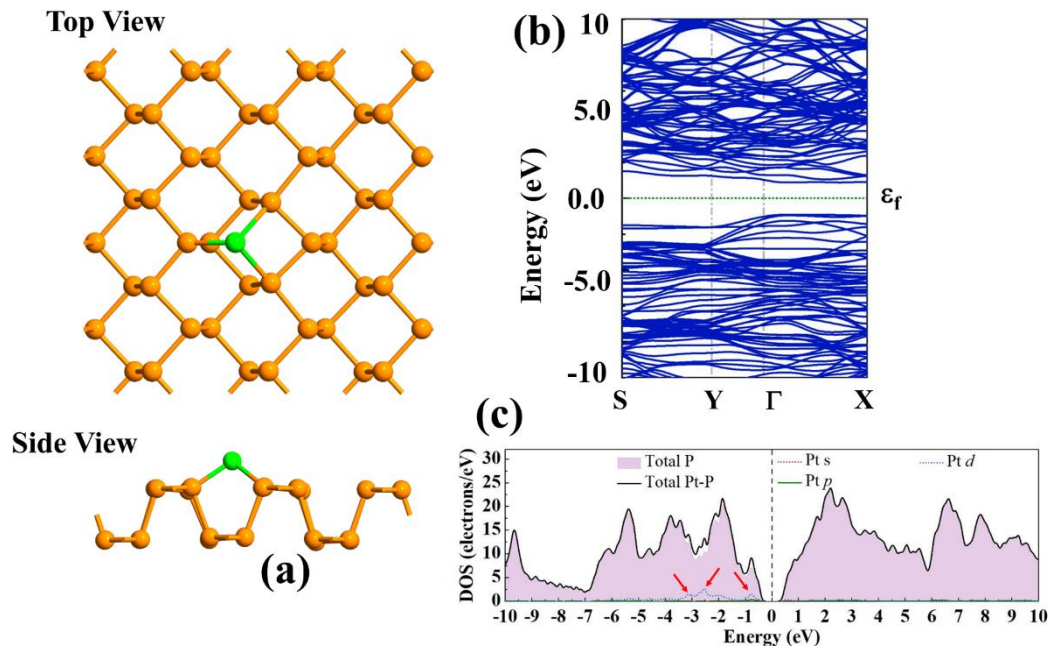


Figure 5-4. (a) Illustration of Pt-decorated phosphorene sheet, (b) band structure, and (c) DOS of the pristine phosphorene (P) and Pt-decorated phosphorene (Pt-P).

The most energetically preferable adsorption configurations for different VOCs on the Pt-decorated phosphorene were displayed in Figure 5-5. The gas molecules were positioned on top of the metal atom (Pt) with various molecular orientations. It was found out that upon exposure to the Pt-decorated phosphorene, acetone adopts a horizontal orientation respecting the surface of the sheet and creates two bonds through its O and C atoms with the Pt. The minimum distance between O and Pt was found to be 2.13 Å. The adsorption of ethanol upon the Pt-decorated phosphorene showed similar behavior to acetone; however, it does not create any bond, and its H atom points to the Pt with a minimum distance of 2.35 Å. Like acetone, formaldehyde adsorbs horizontally on the Pt-phosphorene sheet and forms two bonds (O-Pt and C-Pt), where its minimum distance was found to be 2.13 Å. Similar to ethanol, methanol was adsorbed with a minimum distance of (H-Pt) 2.37 Å. Toluene prefers a parallel orientation respecting the surface of the sheet, and it creates a bond through its C atom with Pt, with a minimum distance of 2.21 Å. Finally, the CO₂ and H₂O molecules adopt a tilted parallel orientation respecting the plane with a minimum distance (O-Pt) of 2.72 Å and (O-Pt) 2.47 Å, respectively. The sums of covalent radii (minimum distance) of O-Pt, H-Pt, C-Pt, O-Pt, C-Pt, O-Pt, O-Pt bonds in acetone-, ethanol-, formaldehyde-, methanol-, toluene-, CO₂-, and H₂O- are 2.50 (2.13), 2.10 (2.35), 2.54 (2.13), 2.10 (2.37), 2.54 (2.21), 2.50

(2.72), and 2.50 (2.47), respectively. Hence, the minimum distances between the Pt-phosphorene surface and the ethanol, methanol, CO₂, and H₂O (acetone, formaldehyde, and toluene) are larger (smaller) than the sums of covalent radii. It can be concluded that ethanol, methanol, CO₂, and H₂O were physisorbed on the Pt-phosphorene, while acetone, formaldehyde, and toluene are chemisorbed.

The energies of adsorption for acetone, ethanol, formaldehyde, methanol, toluene, CO₂, and H₂O with Pt-decorated phosphorene were calculated to be -1.47, -1.14, -1.48, -0.908, -1.64, -0.48, and -0.83 eV, respectively. Compared to the pristine phosphorene, the adsorption energies were augmented 1.98, 1.56, 2.24, 1.35, 1.41, 1.09, and 1.53 times, respectively. It can be deduced that ethanol, methanol, and HO₂ are strongly physisorbed on the Pt-decorated phosphorene, while CO₂ was weakly physisorbed on the sheet. Moreover, acetone, formaldehyde, and toluene molecules are chemically adsorbed on Pt-decorated phosphorene. A total net charge of 0.123, 0.198, 0.112, 0.242, 0.142, 0.055, and 0.084 *e* was found for acetone, ethanol, formaldehyde, methanol, toluene, CO₂, and H₂O, respectively. All gas molecules act as electron donors except for acetone and methanol, which withdraw electrons from the surface. The minimum distances, total net charge, and adsorption energies were tabulated in Table 5-1.

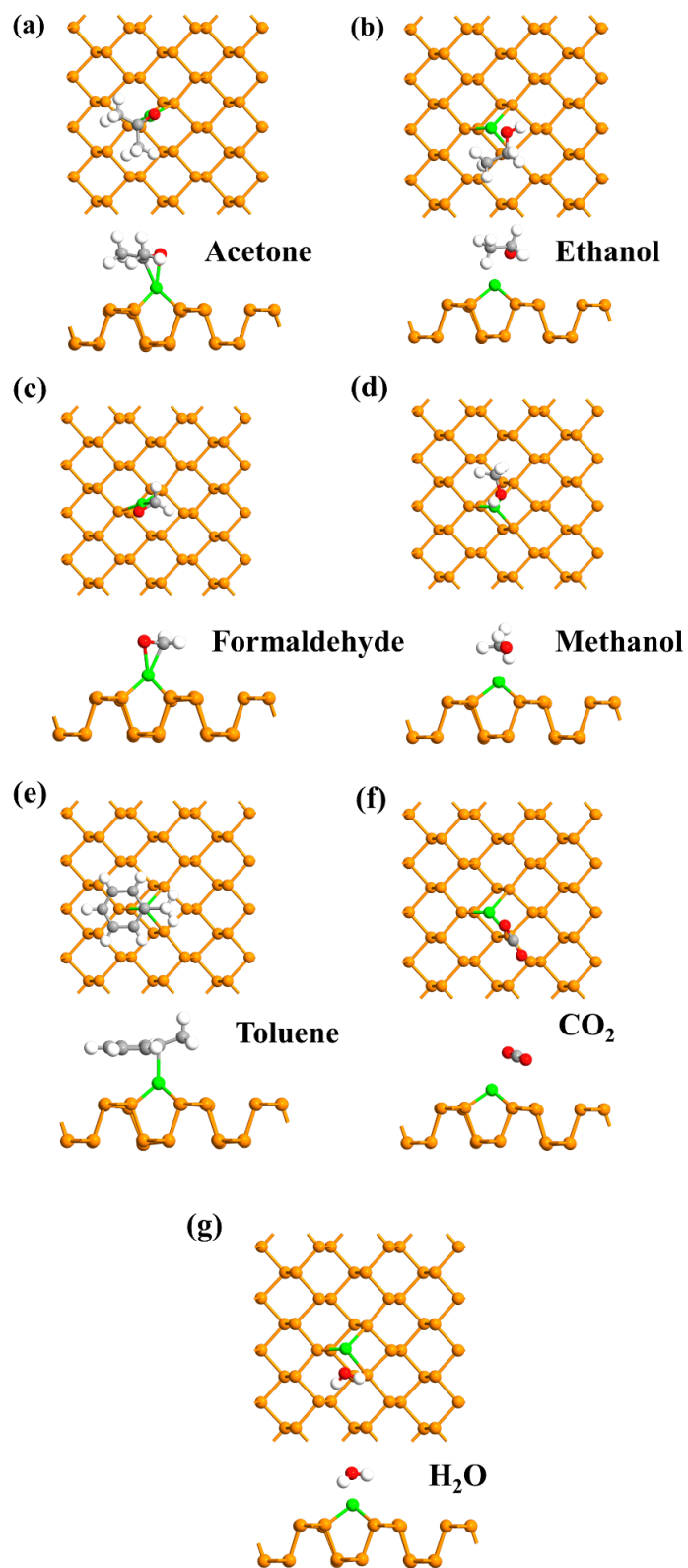


Figure 5-5. The most relaxed structures for adsorption of gas molecules on the Pt-decorated phosphorene surface. (Pt: green, P: orange, C: gray, O: red, H: white).

In order to acquire more information about the adsorption behavior of gases on the Pt-decorated phosphorene, the electronic band structures of the adsorption configurations were calculated and illustrated in Figure 5-6. The achieved energy bandgaps for acetone, ethanol, formaldehyde, methanol, toluene, CO₂, and H₂O were 0.967, 0.754, 0.977, 0.821, 0.878, 0.876, and 0.864 eV, respectively. It means that the energy bandgap of Pt-decorated phosphorene was changed 70, 143, 80, 76, 19, 21, and 33 meV after adsorption of acetone, ethanol, formaldehyde, methanol, toluene, CO₂, and H₂O, respectively, implying that toluene, CO₂, and H₂O adsorption on the sheet has a trivial impact on the electronic band structure near the Fermi level.

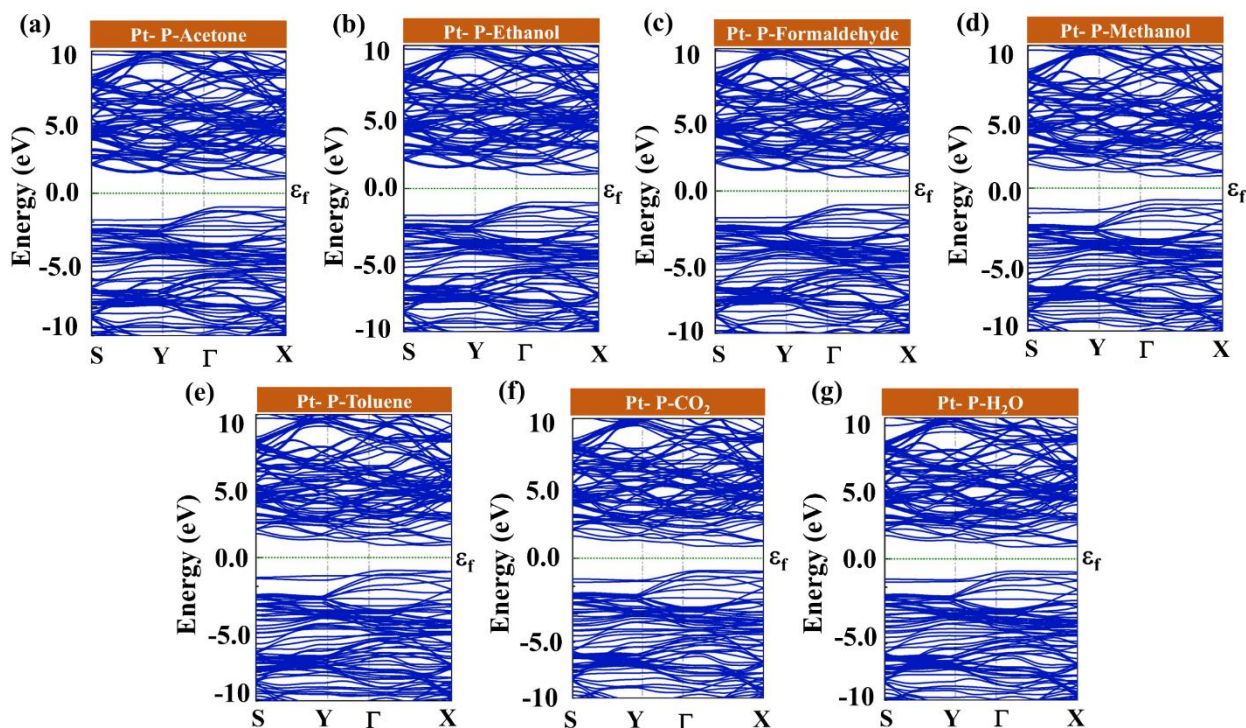


Figure 5-6. The electronic band structures for gas molecules-Pt-decorated phosphorene (Pt-P). The Fermi level was fixed to be zero (the dotted green line).

Moreover, the projected DOS (PDOS) of the gases on the Pt-decorated phosphorene were illustrated in Figure 5-7 to elucidate the adsorption mechanism. For acetone, formaldehyde, and toluene, in the energy range of -3.0 to 0.0 eV, the peak of Pt *d* orbitals and the DOS of the molecules lie in the same energy, as highlighted with blue arrows. This orbital hybridization near the Fermi level can be attributed to the chemisorption process and high adsorption energies. For

ethanol and methanol, no overlapping was noticed around Fermi Level, confirming the physisorption process. However, an orbital overlap can be observed around energy of -4.0 eV.

To assess the performance of the Pt-phosphorene gas sensor, recovery times (τ) for VOCs were calculated. Acetone, ethanol, formaldehyde, methanol, toluene, CO_2 , and H_2O can be desorbed from the surface in visible light and at room temperature after $4.86 \times 10^{+12}$, $1.39 \times 10^{+7}$, $7.16 \times 10^{+12}$, $1.77 \times 10^{+3}$, $3.48 \times 10^{+15}$, 1.15×10^{-4} , and 86.9 sec, respectively. Due to the strong physisorption or chemisorption of the VOCs, the achieved recovery times are too high for practical applications. It was stated that exposure to UV light could facilitate the recovery process by diminishing the desorption-barrier [243]. The obtained τ for desorption at room temperature and under UV exposure was found to be $4.86 \times 10^{+8}$, $1.39 \times 10^{+3}$, $7.16 \times 10^{+8}$, 0.17 , and $3.48 \times 10^{+11}$ sec, for acetone, ethanol, formaldehyde, methanol, and toluene, respectively. Hence, the Pt-phosphorene gas sensor has a good potential to be used for alcohol detection with a reasonable recovery time, especially methanol.

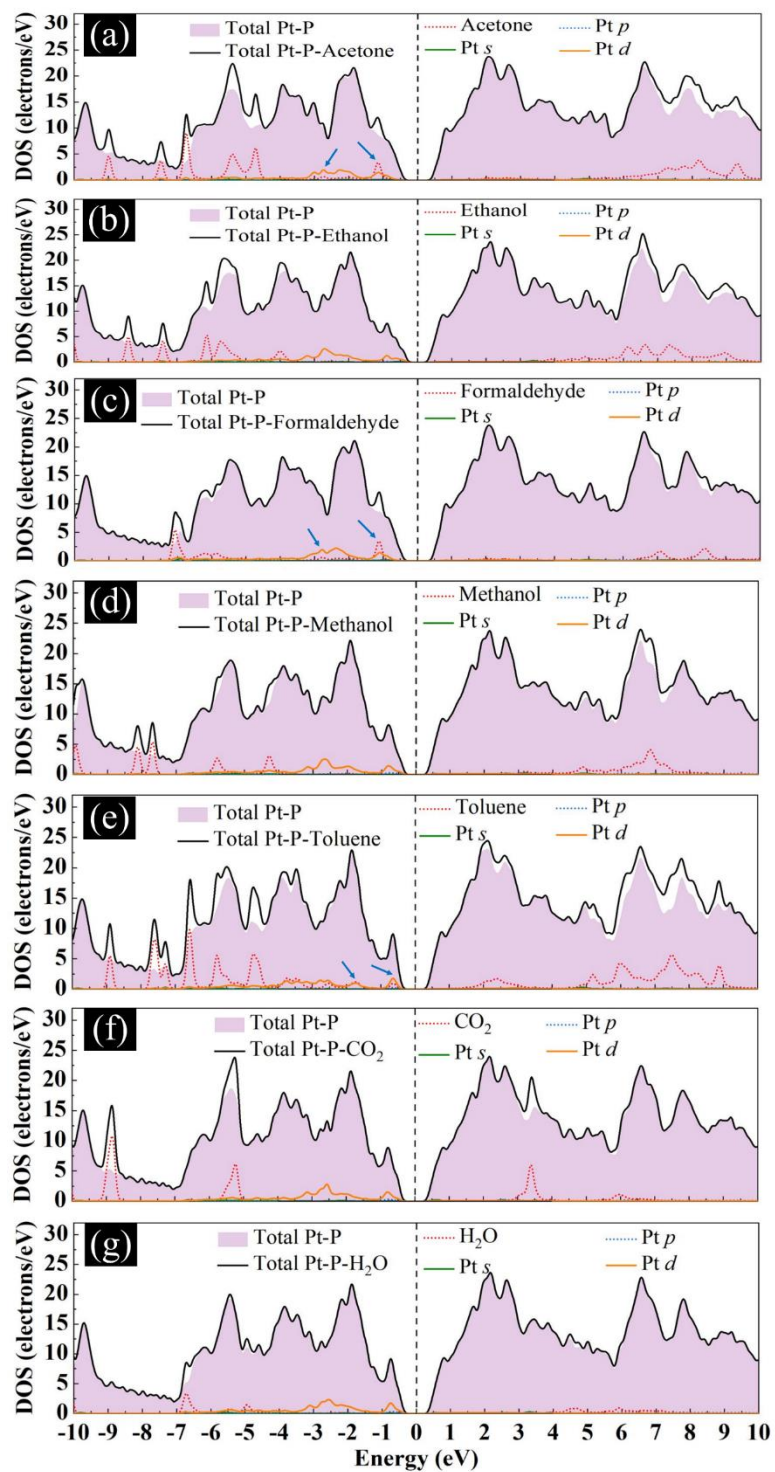


Figure 5-7. Total PDOS curves of gas molecules-Pt-decorated phosphorene (Pt-P) sheet. The dashed line means the Fermi level, which was set to be zero.

Next, the I - V characteristics were achieved for the sensors before and after molecules adsorption based on equation (2) to observe the conductance change. Due to the highly anisotropic structure of phosphorene, the electronic transport studied in both armchair, and zigzag directions (Figure 5-8) and both left and right electrodes were presumed to be periodic in x and y directions. A central region was seamlessly linked to the electrodes (left and right). The size of the central region and the electrodes for armchair direction was set to be $13.25 \text{ \AA} \times 4.37 \text{ \AA}$ and $13.25 \text{ \AA} \times 26.25 \text{ \AA}$, respectively. Also, these sizes were chosen for the zigzag direction to be $13.13 \text{ \AA} \times 26.5 \text{ \AA}$ and $13.13 \text{ \AA} \times 3.31 \text{ \AA}$, respectively. It was noticed that the amount of the current has a large difference between the armchair (scale of μA) and zigzag (scale of nA) directions. The anisotropic electronic band structure of monolayer phosphorene is the reason for the anisotropic transport properties of phosphorene. It was observed (in Figure 5-1 (b)) that both the bottom of the conduction band and the top of the valence band have many notable dispersions in the Γ - Y direction (reciprocal space) or armchair direction (real space). However, in the zigzag direction (real space) or Γ - X direction (reciprocal space), the bands are nearly flat. Therefore, the currents along the armchair have a much higher value compared with those along the zigzag direction.

Another important parameter to evaluate the performance of a gas device is sensitivity. Variations of the conductance for the nanosensors prior to and post-exposure to gases is the sensitivity (S), which can be obtained by:

$$S = \left| \frac{G_{\text{gas}} - G_{\text{pure}}}{G_{\text{pure}}} \right| \times 100 \quad (14)$$

where G_{pure} , and G_{gas} are the conductivity of the pristine or Pt-decorated phosphorene before and after exposure to VOCs, respectively. A comparative bar chart of the sensitivities for the pristine and Pt-decorated phosphorene sensors along with armchair and zigzag directions as shown in Figure 5-9.

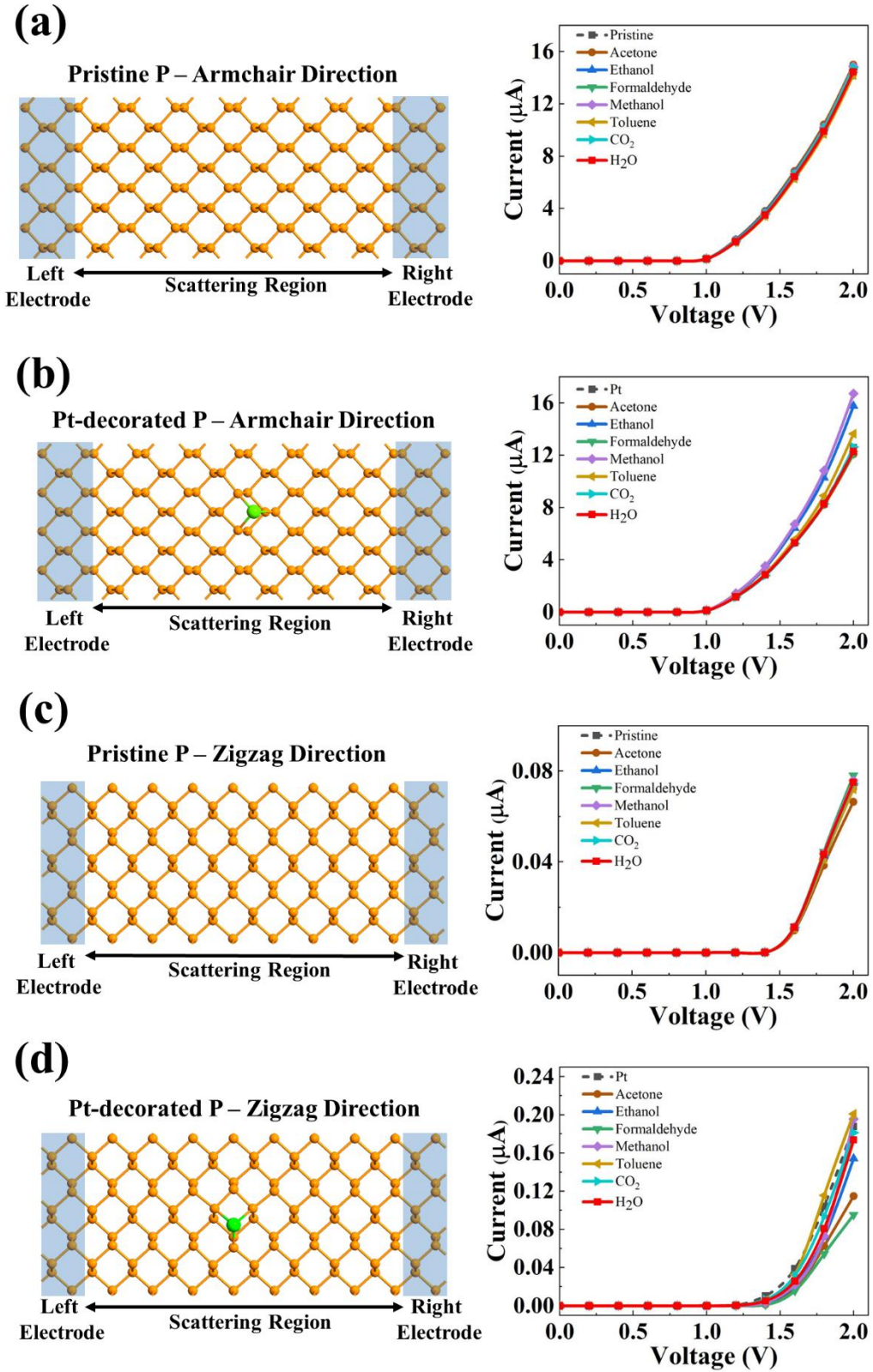


Figure 5-8. Illustrations of two probe devices, I-V characteristics calculations for pristine phosphorene (P), and Pt-decorated phosphorene (Pt-P) in a, b) armchair, and c, d) zigzag directions.

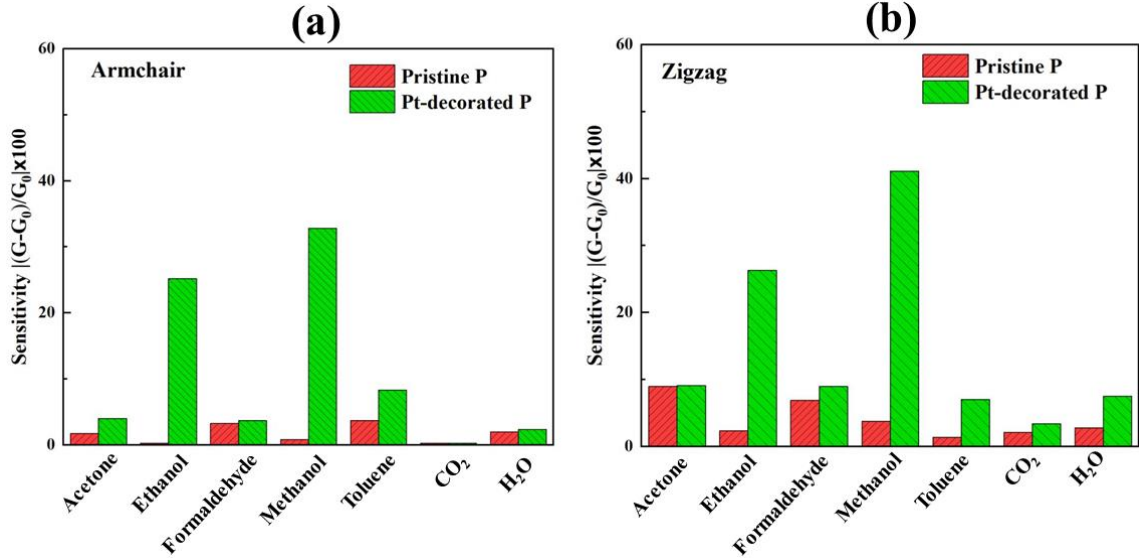


Figure 5-9. The sensitivity of adsorption of the studied gases for pristine (P) and Pt-decorated phosphorene (Pt-P) sheets for both (a) Armchair (b) Zigzag directions.

With a bias voltage exerted to the device, the Fermi level of the left electrode shifts upward, respecting the right electrode. Hence, the electrical current starts to flow right after the valence band maximum (VBM) of the left electrode meets the conduction band minimum (CBM) of the right electrode. It can be seen from Figure 8; no current is transmitted through the device in the armchair direction until the bias voltage exceeds 1.0 V, also in the zigzag direction, current flows when the bias voltage surpasses 1.4 V. Sensitivities were extracted at 2.0 V and presented in Figure 9. It was observed that the sensitivity of phosphorene toward ethanol and methanol was drastically improved by Pt decoration. The sensitivity of 25.2% (26.3%) and 32.8% (41.1%) were achieved in armchair (zigzag) direction for ethanol and methanol after decoration, respectively.

Another aspect of analyzing the device for VOCs is the selectivity of the sensor. In this regard, the ratios of the sensitivity of ethanol and methanol over other molecules in the armchair direction were obtained. It was noticed that the Pt-decorated phosphorene sensor showed high selectivity to methanol and ethanol. For example, for Pt-decorated phosphorene interaction with methanol (ethanol), they have sensitivity ratios of 8.16 (6.2), 1.3 (1), 8.9 (6.8), 1 (0.76), 3.9 (3), 113.1 (86.9), and 13.8 (10.5) for acetone, ethanol, formaldehyde, methanol, toluene, CO₂, and H₂O, respectively, meaning that methanol can be detected selectively.

A comparison between current work and other 2D materials for VOC gas sensing show that pristine and Pt-decorated phosphorene has superiority over other 2D materials. For example,

graphene with adsorption energy of -0.36 (acetone), -0.33 (ethanol), -0.21 (methanol), -0.091 (toluene) eV, ^[244, 245] C₂N with adsorption energies of -0.5 (acetone), -0.52 (ethanol), -0.5 (methanol), -0.4 (toluene) eV, ^[246] silicene with adsorption energies of -0.087 (formaldehyde), ^[247] MoS₂ with adsorption energies of -0.16 (acetone), -0.22 (ethanol), -0.11 (formaldehyde) eV, ^[248] MoSe₂ with adsorption energy of -0.732 (ethanol) and -0.522 (methanol) eV ^[249] have less adsorption energies in comparison with pristine and Pd-decorated phosphorene sheets for VOCs adsorption.

In a nutshell, our results manifest that the suspended Pt-decorated phosphorene device can be suitable for VOCs gas sensing application at room temperature. It is evident that Pt-decorated phosphorene-based sensor can be used to detect methanol with high sensitivity, high selectivity, and fast recovery time. Moreover, our results disclosed that even though acetone, formaldehyde, and toluene were adsorbed stronger than others based on the energy adsorption but other parameters such as charge transfer, recovery time, sensitivity, and selectivity also should be taken into account in order to make a correct judgment on a sensor's performance.

We also considered the impact of the change in size of the Pt nanoparticles on the stability of the Pt-Phosphorene structure. Our results (Figure 5-10 and Table 5-2) show that although the stability of the phosphorene decreases with increasing the size of the Pt nanoparticles, the structure remains very stable by increasing the size of the Pt nanoparticle.

Table 5-2. The adsorption energy of the different number of Platinum on the pristine Phosphorene surface.

Number of Pt	1	2	3	4
Adsorption energy (eV)	-5.84	-6.33	-8.93	-10.22

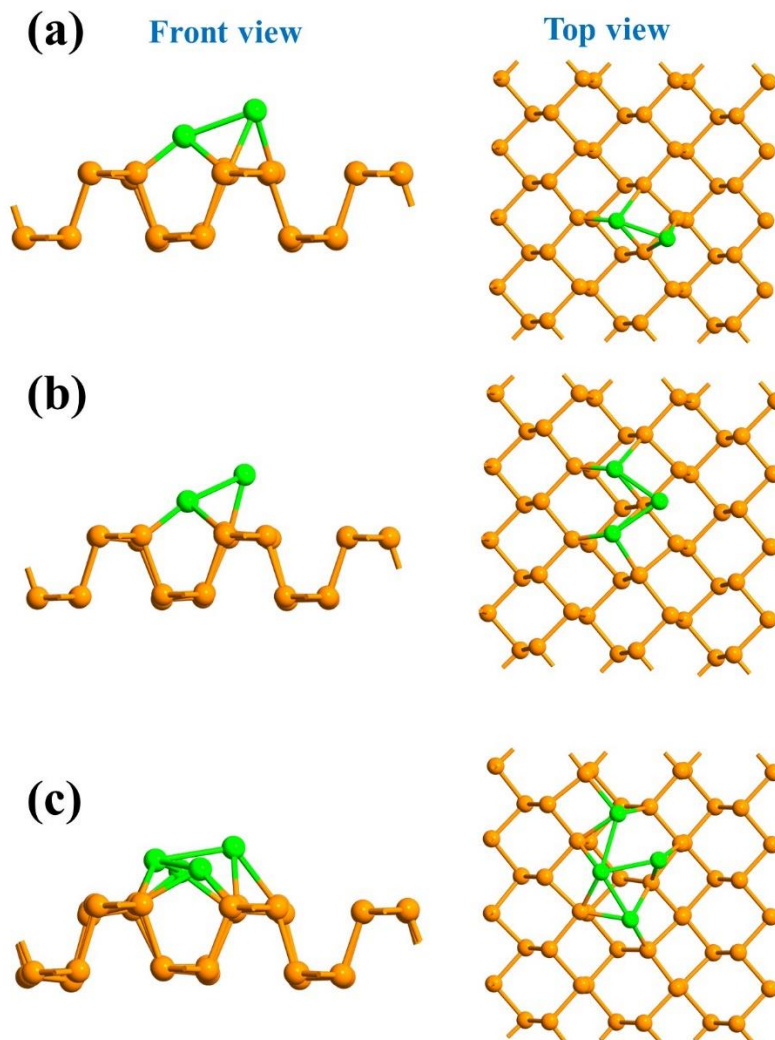


Figure 5-10. The most stable configuration of different number of Pt on the phosphorene. (a) 2 atoms of Pt. (b) 3 atoms of Pt. (c) 4 atoms of Pt.

We also studied the adsorption behavior of a single methanol on the phosphorene decorated with Pt nanoparticles with 1-4 atoms. As can be seen in Figure 5-11 and Table 5-3, the interaction between methanol and phosphorene decorated by a nanoparticle contained two Pt atoms is the strongest with adsorption energy of -2.43 eV. However, the optimal size is still a single Pt atom due to the optimal adsorption energy of -0.908 eV which ensures a fast recovery.

Table 5-3. The adsorption energy of Methanol on the the different number of Pt- decorated Phosphorene surface.

Number of Pt	1	2	3	4
--------------	---	---	---	---

Methanol adsorption energy (eV)	-0.908	-2.43	-0.96	-1.28
---------------------------------	--------	-------	-------	-------

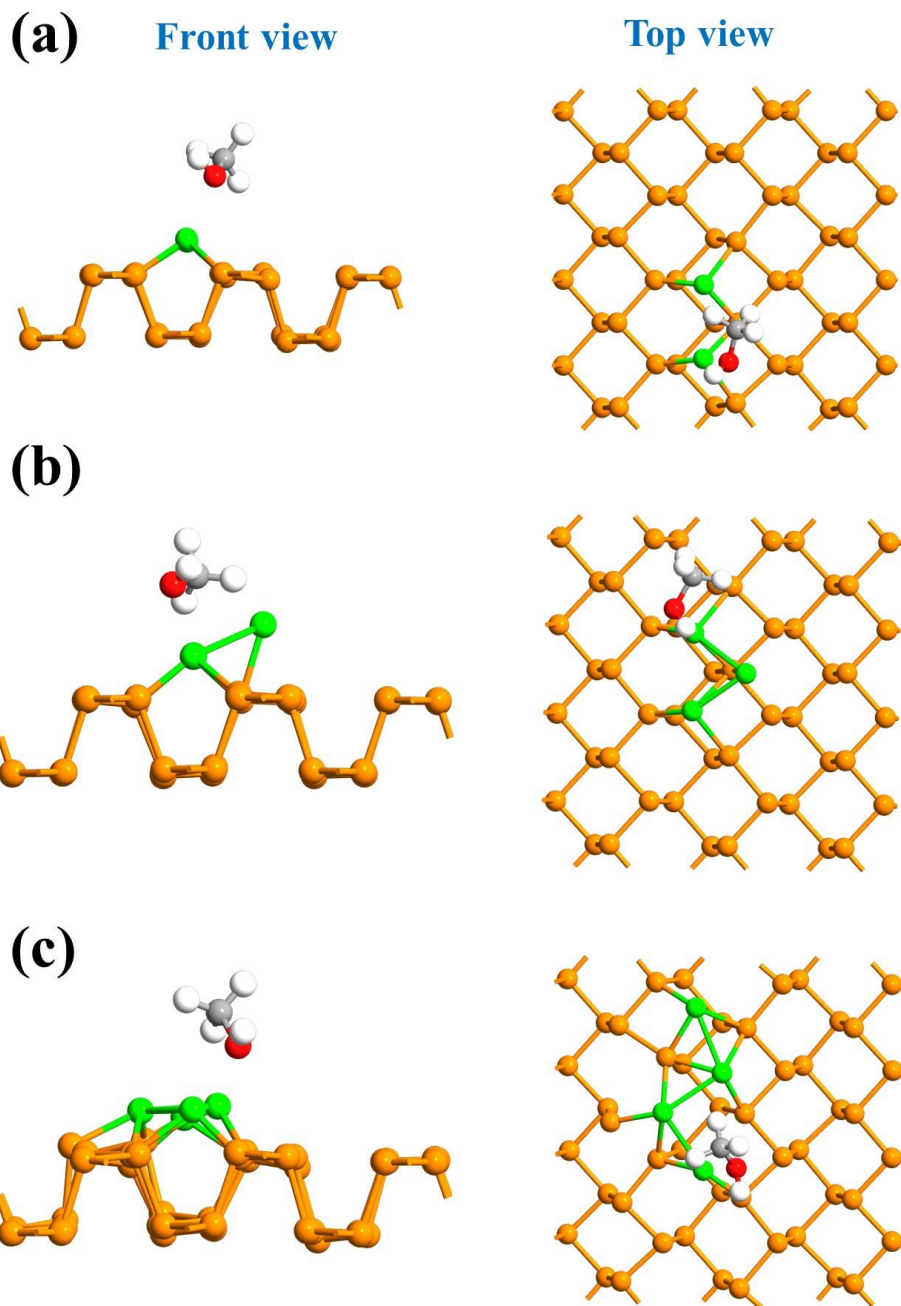


Figure 5-11. The most favorable adsorption of methanol upon different number of Pt- decorated phosphorene. (a) 2 atoms of Pt. (b) 3 atoms of Pt. (c) 4 atoms of Pt.

Summary

We scrutinized the geometric stability and adsorption behavior of pristine and Pt-decorated phosphorene with different VOCs (acetone, ethanol, formaldehyde, methanol, toluene) as well as CO₂ and H₂O using the first-principles based on the DFT method. For this purpose, the adsorption sites, adsorption energies, charge transfer, minimum distances, recovery time, sensitivity, and selectivity were calculated. We found that VOCs are only physisorbed on the pristine phosphorene and make no considerable electronic changes after the interaction with pristine phosphorene. However, after decorating the surface with Pt atom, the interactions between the VOCs and the phosphorene were enhanced, causing modifications in the electronic properties of the sensor upon gas exposure. The results reveal that the suspended Pt-decorated phosphorene system is capable of detecting methanol with high sensitivity, selectivity, and short recovery time at room temperature. Hence, our results give insight into the development of metal-decorated phosphorene-based gas sensors and deserve further experimental attention for future VOCs gas sensing applications.

6. Chapter 6

Theoretical Study on transition metal dichalcogenides (TMDs)

6.1 Detection of Colorectal cancer biomarkers- MoS₂

Early-stage disease and cancer diagnosis are of particular importance for effective patient identification as well as their treatment. Breath analysis is a promising method for this purpose which can help to detect disease biomarkers. Benzaldehyde, and Indole gas molecules as members of volatile organic compounds (VOCs) are composing a proportion of the exhaled breath and changes in the level of them from breath can be considered for colorectal cancer biomarkers. Due to these incentives, we scrutinized the sensing behavior of Molybdenum disulfide (MoS₂) toward Benzaldehyde, and Indole gas. We inspected the adsorption of the molecules on the pristine and Pd-, Pt-decorated MoS₂ by employing density functional non-equilibrium Green's function (DFT-NEGF). It was disclosed that the molecules were weakly adsorbed upon the pristine MoS₂. However, after the decoration of the surface, the adsorption energy and charge transfer of the molecules were improved greatly. On the other hand, the band gap was decreased after metal decoration. For example, adsorption energy of -2.37 eV, band gap of 1.32 eV was achieved with interaction of Indole with Pd-decorated MoS₂ and it can be desorbed under UV light and at temperature of 698 K with recovery time of 12.8 sec. Ergo, our analysis would help us better understand the adsorption mechanism of Pd-, and Pt-decorated MoS₂ based gas sensors. It may open a new route in early disease detection and colorectal cancer monitoring.

6.2 Overview

Colorectal cancer (CRC) or colon cancer is the second most deadly cancer worldwide, and amongst the third cause of cancer-related deaths in USA [250-254]. Nonetheless, it is a highly treatable and often curable disease if it is found at an early stage before it has spread [255]. Detection of CRC at the earliest possible stage is therefore of paramount importance for cancer treatment. Currently, the bulk of screening technologies such as colonoscopy is invasive, time-

consuming, and expensive, but breath analysis might be a particularly promising approach for fast, non-invasive, and cheap cancer screening [256]. Newer methods such as Cologuard which investigates specific DNA based markers are used for screening. Colonoscopy is done if the results come positive in Cologuard for men over 45 years of age. Noninvasive methods such as Cologuard can reduce the population of patients requiring tests such as colonoscopy that are expensive and invasive. Breath analysis is non-invasive and could potentially be useful for early detection of cancer.

Studies suggest that volatile organic compounds (VOCs) contained in exhaled breath can reflect the dysfunction or metabolic disorders [257, 258]. It has been reported that there are more than 870 kinds of VOCs in the human breath, which can provide vital information about the health status of the patient [231, 259-261]. It has been reported that specific exhaled VOCs are candidates for cancer diagnosis, including different types of cancers such as lung, stomach, liver, and breast cancers [262-265]. Several works highlighted the evidence of potential VOCs that might serve as biomarkers for CRC is accumulating [266-269]. Preliminary studies pointed out that organic analytes from exhaled breath like benzaldehyde and indole are associated with CRC cancer [87, 269, 270]. So, sensing of such compounds from exhaled breath seems indispensable for early detection of CRC.

Over the past years, 2D materials starting with graphene has attracted increased attention from various scientists and engineers because of its excellent properties such as mechanical stability, biocompatibility, high carrier mobility, and large surface area [71, 271-275]. Different materials such as graphene, black, and green phosphorene, and MoS₂ have been investigated for gas sensing applications [183, 276-278]. Among all 2D materials, MoS₂ has already exhibited emerging application specially for developing a gas sensor and become focal point of research due to its semiconducting nature, high surface-to-volume ratio, tunable band gap [279-282]. Bulk MoS₂ has an indirect band gap of ~1.29 eV and single layer has a band gap of 1.9 eV [283]. This suggests one can highly sensitive gas sensing devices based on number of layers and newer device configurations.

MoS₂ has been successfully synthesized by various methods such as chemical vapor deposition, and hydrothermal [284, 285] and it could be a feasible gas sensor at room temperature [286]. MoS₂ has progressively played a vital and versatile role in detecting flammable, toxic, and disease biomarker gases [287-289]. For instance, adsorption of formaldehyde as an air pollutant

has been investigated by Ma et al [289] and shown that formaldehyde is insensitive on pristine MoS₂. Moreover, several gases such as CO, CO₂, NH₃, NO, NO₂, CH₄ have been investigated theoretically by density functional theory (DFT) method on MoS₂ monolayer, and they found that NO, and NO₂ can bind strongly in comparison with the other molecules [290]. On the other hand, Zhang and Li [173] investigated the adsorption of three potential lung cancer biomarkers like isoprene, benzene, and 2-propenal from exhaled breath upon MoS₂ monolayer. They utilized the DFT method to explore these gas molecules and emphasized that to achieve higher performance, surface modification of MoS₂ is imperative.

The weak adsorption of pristine MoS₂ to gases necessitates to improve its sensitivity. In this regard, to modify the structure, and the sensitivity of MoS₂, the introduction of metals as decoration has been employed. For this motive, Qian et al [291] have revealed that H₂S and SO₂ were adsorbed stronger on the Pt-decorated MoS₂ compared to pristine MoS₂. In another study, Lakshmy et al [292] have investigated adsorption of catechol on pure and noble metal (Pd, Ti, and Ag) decorated MoS₂. They have found that the adsorption has been ameliorated after MoS₂ decoration [292].

Nonetheless, to the best of our knowledge, there has been no study so far has addressed the sensing mechanism of MoS₂ based gas sensor toward colorectal cancer biomarkers. Herein, we engaged first principle DFT to scrutinize comprehensively the adsorption behavior of benzaldehyde and indole molecules on pristine, Pt, and Pd-decorated MoS₂. Our results divulged that Pd-decorated MoS₂ has promising sensing toward indole and encourages further experimental investigation for gas sensor platform development, especially for early colorectal cancer detection.

6.3 Computational Method

All the first-principles calculations integrated with non-equilibrium Green's function (NEGF) were executed in Atomistix ToolKit (ATK) package [153, 154, 239]. Perdew-Burke-Ernzerhof (PBE) formalism with generalized gradient approximation (GGA) was adopted to address exchange-correlation functions [293].

The Fritz Haber Institute (FHI) pseudopotentials with double- ζ polarized basis sets were exploited with a density mesh cutoff of 75 Hartree. To account for the long-range van der Waals interactions more accurately, Grimme DFT-D3 van der Waals corrections were employed. The revised Perdew–Burke–Ernzerhof exchange– correlation functional was used to obtain a more accurate molecule to MoS₂ layer distance and binding energy. An adequate large vacuum space of

20 Å was examined to eliminate the image–image interactions. For adsorption of gas molecules upon pristine P or Pt, Pd-decorated MoS₂, the adsorption energy was obtained by:

$$E_{ad} = E_{P/Pt/Pd-MoS_2+ molecule} - (E_{P/Pt/Pd-MoS_2} + E_{molecule}) \quad (1)$$

Where, $E_{P/Pt/Pd-MoS_2+ molecule}$, $E_{P/Pt/Pd-MoS_2}$, and $E_{molecule}$ are the total energies for the pristine (P) or Pt, Pd-decorated MoS₂-molecule system, P or Pt, Pd-decorated MoS₂, and the single molecule, respectively. All the structures were permitted to be fully relaxed, before the calculations, till the force and stress acting on the atoms are converging 0.01 eV Å⁻¹ and 0.001 eV Å⁻³, accordingly.

Based on the Mulliken population analysis, the charge transfer (Q_T) between the pristine or decorated-MoS₂ surface and molecules was obtained. Worth to mention that a negative Q implicates that the MoS₂ sheet withdraws electrons from the molecule and contrarily a positive Q indicates that the sheet donates electrons to the molecule [72]. For the primitive Brillouin zones, sampling was performed with $3 \times 3 \times 1$ k-points for optimization and was then raised to $5 \times 5 \times 1$ k-points for electronic computations.

6.4 First-principles calculations using density functional theory:

First, the geometry, structural properties, and optimized structure of pristine MoS₂ monolayer are investigated. Fig. 1 (a) illustrates the top and side views of bare MoS₂ consisting of 32 S, and 16 Mo atoms after structural relaxation [294]. The electronic band structure of the relaxed monolayer was calculated and depicted in Fig. 1 (b). The calculations showed that MoS₂ has direct band gap of 1.66 eV, that is in good accordance with previous reports [77, 295].

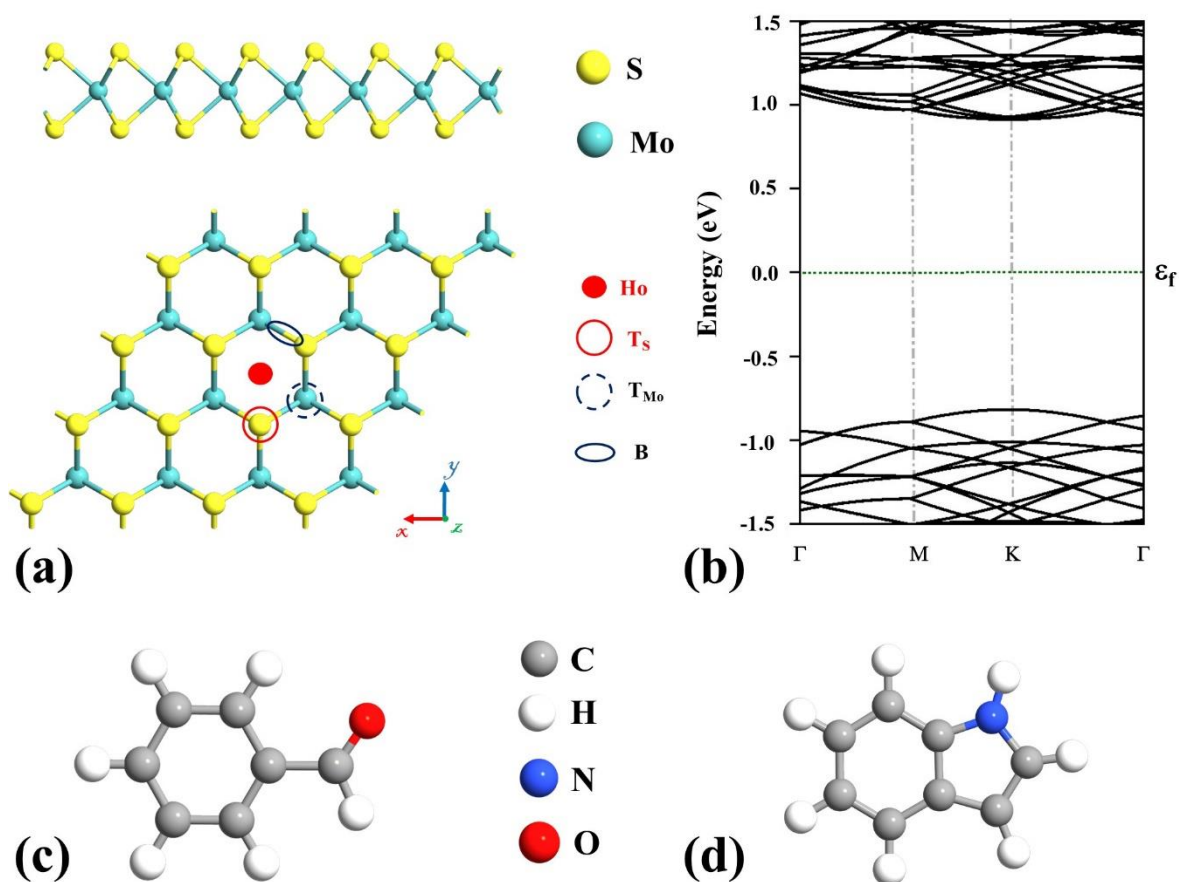


Figure. 1. (a) Optimized structure of a pristine MoS₂ (Two top and front views). Illustration of different possible adsorption sites on the surface (Ho, T_S, T_{Mo}, B). and (b) its corresponding energy band structure. The dotted green line designates the Fermi level, which is set to zero. (c) The relaxed molecular structures of Benzaldehyde, and (d) Indole.

Furthermore, to search for the most stable adsorption configurations of atoms, and molecules on MoS₂, four different positions labeled Ho, T_{Mo}, T_S, and B were considered which denote above the center of the hexagon, top of Mo, and S atoms, and the bridge site between two Mo, and S atoms, respectively (shown in Fig. 1(a)). Benzaldehyde and Indole molecules were also shown in Fig. 1 (c, d), respectively.

Next, adsorption of the molecules over MoS₂ with considering the possible adsorption sites were studied and exhibited in Fig. 2. The gas molecules were placed at a distance of 2 Å above the positions. From the most stable configuration upon adsorption of Benzaldehyde, it was found that it laid flat on MoS₂ with a minimum distance of 3.18 Å between the O atom of the molecule and the S atom of MoS₂. Indole had taken the same adsorption orientation upon the surface and there was a 3.23 Å minimum distance between the H atom of Indole and the S atom of MoS₂.

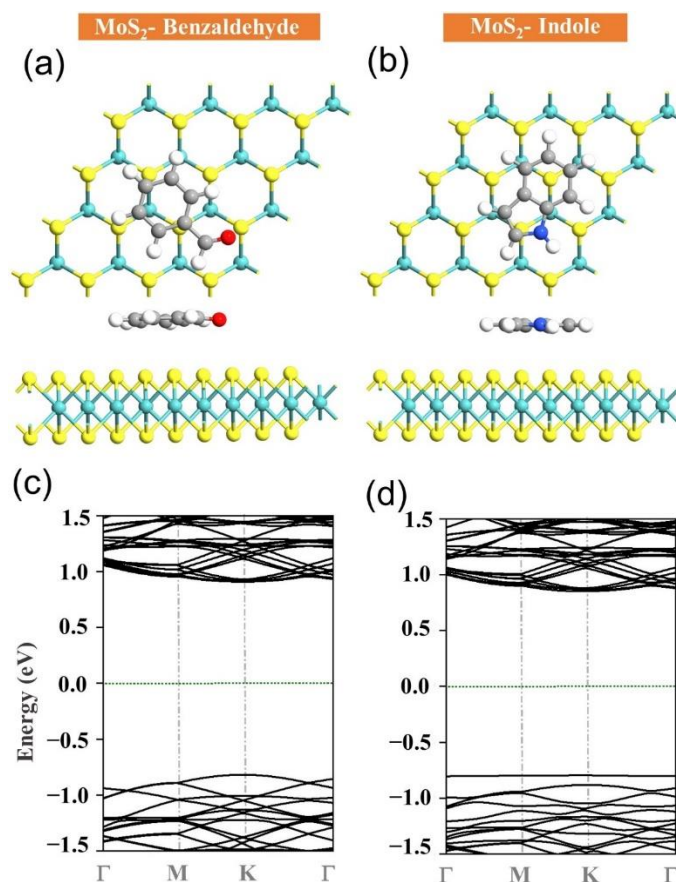


Figure. 2. The optimized structures of (a) Benzaldehyde, (b) Indole, adsorption upon bare MoS₂ along with their electronic band structures for (c) Benzaldehyde, and (d) Indole. The Fermi level was fixed to be zero (the dotted green line).

Moreover, the electronic band structures of the above configurations were obtained and displayed in Fig 2 (c, d). The amounts of adsorption energies for gas molecules upon interaction with pristine MoS₂ were obtained to be -1.33 , and -1.75 eV for Benzaldehyde, and Indole, respectively. The energy band gap of 1.658 , and 1.61 eV were found for Benzaldehyde, and Indole, respectively. Also, the adsorption energy of -1.33 , and -1.75 eV was obtained after the interaction of Benzaldehyde, and Indole upon bare MoS₂. It is worth mentioning that there is a small alteration in the energy band gap after molecule adsorption. For instance, there are 0.002 , and 0.05 eV changes after adsorption of Benzaldehyde, and Indole upon MoS₂, respectively.

To shed light on the electronic behavior of pristine MoS₂ with the molecules, the charge transfer was calculated and resulted in a slight electron transfer of $0.005 e$ from MoS₂ to

Benzaldehyde, and a charge transfer of 0.052 e from Indole to the MoS₂ sheet. All in all, it has been noticed that gases were weakly adsorbed on the pristine MoS₂ surface, and it seems necessary to improve the adsorption behavior of studied molecules. The results are described in Table. 1.

To improve the sensitivity of the gas molecules, the surface was decorated with Pd, and Pt atoms. Because the atoms tend to be adsorbed in various configurations, a number of input geometries were taken into account and the most optimized structures were obtained and shown in Fig. 3 (a, b). It appeared that they both tend to be adsorbed at top of the Mo atom (T_{Mo}) which are in good accordance with previous studies, and both exhibit nonmagnetic character [296-298].

It was observed that the Pd made three bonds with the S atoms of the surface with minimum distance of 2.37 Å. Besides, four bonds were created between the Pt and the MoS₂'s surface, in a way that three bonds are with S atoms and one bond with Mo atom. Also, there is minimum distance of 2.32 Å (Pt-S). Furthermore, the adsorption energy of -3.51, and -4.4 eV was calculated for Pd, and Pt atoms, respectively, and it can be an indication of strong adsorption.

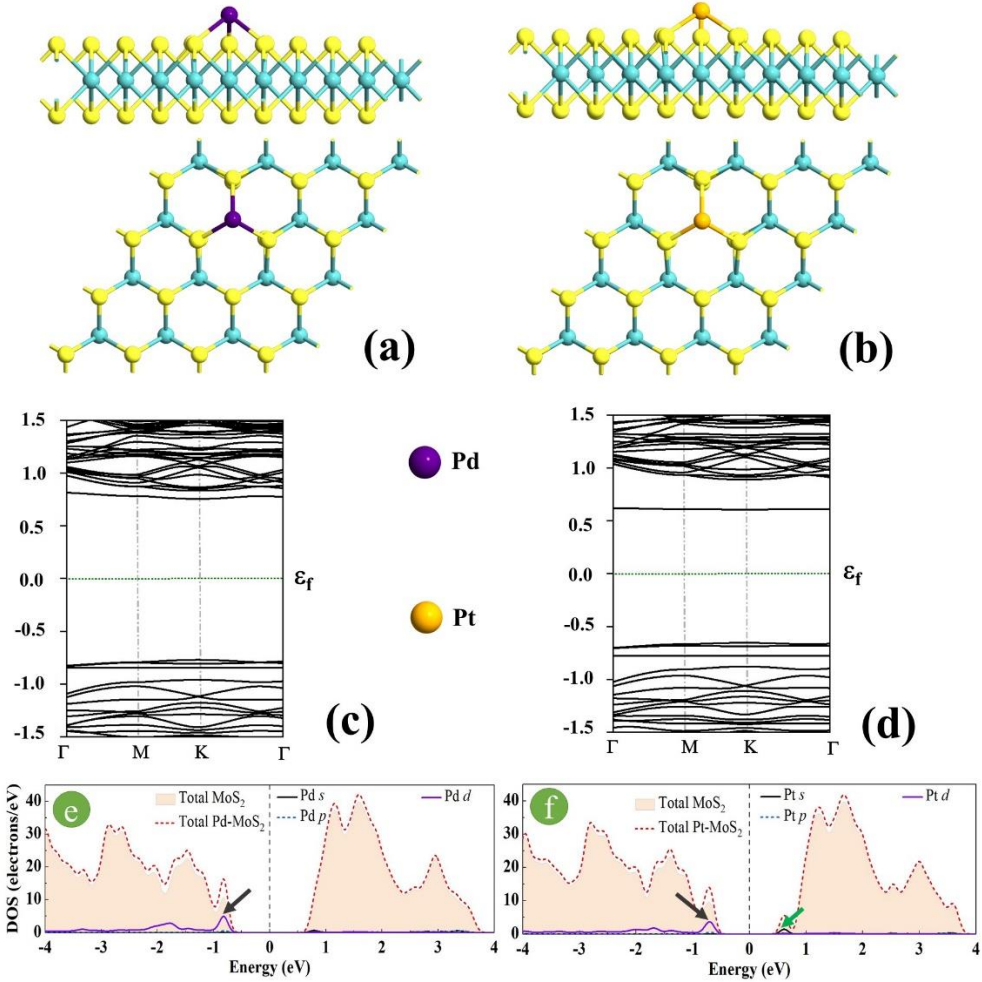


Figure 3. The relaxed structures of a single (a) Pd-, and (b) Pt- decorated MoS₂. Energy band structure for adsorption of (c) Pd, and (d) Pt, respectively. Total DOS curves for (a) Pd- MoS₂, and (b) Pt- MoS₂ systems.

Accordingly, the energy band structure and density of states (DOS) for these configurations were computed and exhibited in Fig. 3. It was divulged that energy band gap of 1.482, and 1.236 eV was obtained for Pd, and Pt adsorption. From the DOS distribution for both cases, one strong peak was noted in vicinity of the Fermi level among the *d*-orbital of the metal and the surface as highlighted by the black arrow. However, there is one small peak (green arrow) between the *s*-orbital of Pt and the surface of MoS₂.

Due to large adsorption energy, and the conspicuous changes in energy band gap, decreasing from 1.66 eV for pristine MoS₂, to 1.482, and 1.236 eV after Pd, and Pt adsorption, respectively, it can be concluded that they chemisorbed on the MoS₂'s sheet.

Moreover, the atomic radii for Pd, Pt, and S are 1.69, 1.77, and 0.88 Å, respectively [210]. So, the sum of the corresponding atomic radii for Pd-S, and Pt-S is 2.57, and 2.32 Å, respectively, which are less than the obtained minimum distances. This fact confirmed the strong adsorption of the metals upon MoS₂'s surface.

Next, adsorption of the molecules on Pd-, and Pt-decorated MoS₂ had been studied. To assess the adsorption of Benzaldehyde, and Indole upon Pd-, and Pt-MoS₂, they were placed at a distance of 2 Å above the metals with various molecular orientations. After the full relaxation of the structures, the most favorable configurations of the gas molecules on the Pd-, and Pt-decorated MoS₂ sheet were predicted and demonstrated in Fig. 4.

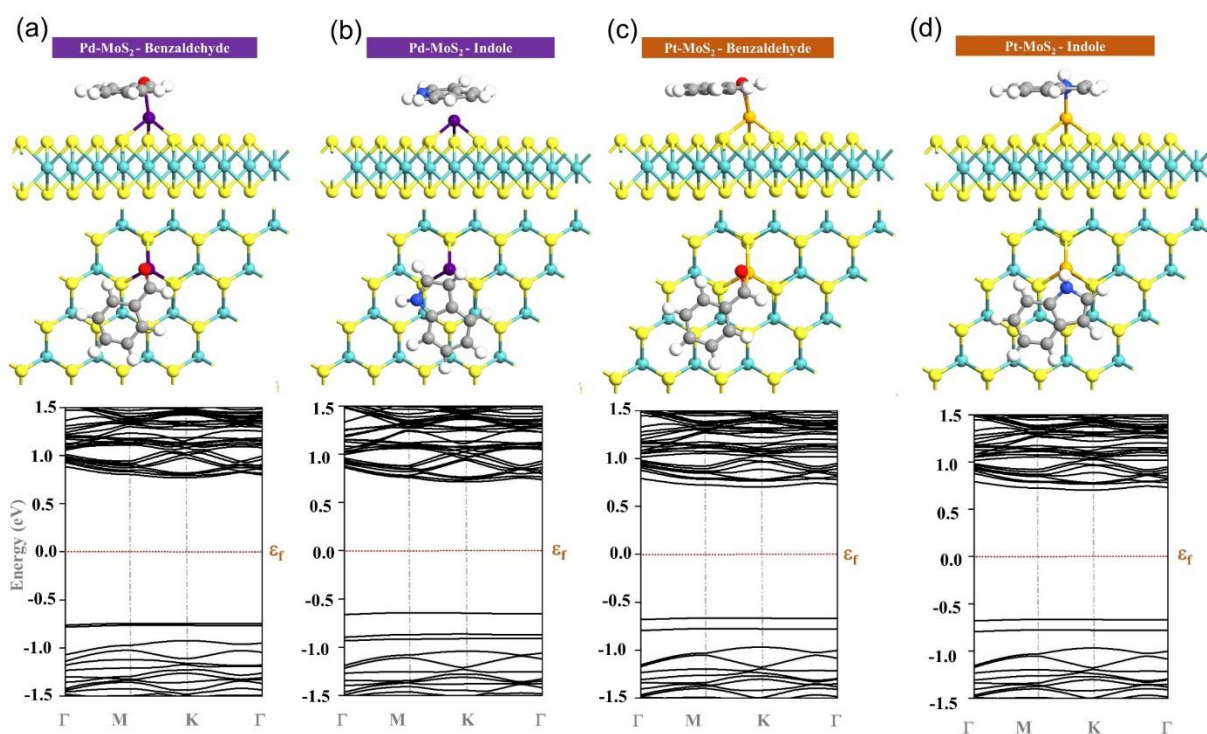


Figure. 4. The most stable adsorption configurations for (a) Benzaldehyde, and (b) Indole on Pd- MoS₂, as well as their electronic band gap, respectively. The most optimized structure for interaction of Pt-MoS₂ with (c) Benzaldehyde, and (d) Indole molecules with their electronic band gap, respectively.

In the quest for finding the most favorable configurations, the interaction strength was assessed by computing adsorption energies. The calculated adsorption energies for Pd-MoS₂ toward Benzaldehyde, and Indole were obtained to be -1.91, and -2.37 eV, respectively. It was noticed that the adsorption energy of the molecules was augmented after MoS₂ decoration compared to pristine MoS₂.

After considering and optimizing various structures, Benzaldehyde preferred to be adsorbed in parallel to the surface and made a bond between the O atom and Pd metal atom. The length of this bond as the minimum distance was measured to be 2.21 Å. Nevertheless, Indole did not create any bond with the Pd, and there is a minimum distance of 2.28 Å between the C atom and Pd. The atomic radii for O, C, and N are 0.73, 0.77, and 0.56 Å, respectively [210]. The calculated atomic distances among Pd-O (2.42 Å), and Pd-C (2.46 Å) are larger than the achieved minimum distances, affirming the strong adsorption.

Additionally, Pt-MoS₂ as a sensing platform was tested for Benzaldehyde, and Indole. The results divulged that after decoration, adsorption energy was enhanced significantly, for example, after adsorption of Benzaldehyde, and Indole on Pt-MoS₂, the energy of 2.53, and 2.2 eV was released, accordingly. Similarly, Benzaldehyde took the same parallel adsorption over the Pt atom as the Pd metal with the same bond Pt-O (minimum distance of 2.13 Å), which is much smaller than the atomic distance of 2.5 Å.

In the case of Indole adsorption on Pt-MoS₂, it was seen that it preferred to be adsorbed in a horizontal way with respect to MoS₂'s surface and made a bond with the Pt atom. There is a minimum distance between Pt and N atom of Indole with an amount of 2.25 Å which is again smaller than the atomic distance of 2.33 Å. Moreover, the adsorption behavior of decorated MoS₂ toward the molecules was further studied by calculating electronic band structures (Fig. 4).

Henceforth, the calculated energy band gap of Benzaldehyde over the Pd-, and Pt-MoS₂ was discovered to be 1.478, and 1.341 eV, respectively. In addition, the band gap of Indole adsorption over the Pd-, and Pt-MoS₂ was found to be 1.322, and 1.336 eV, accordingly. These outcomes indicate that the energy bandgap of Pd-, and Pt-MoS₂ was changed by more than 100 meV, after interaction with the associated molecules except Benzaldehyde with Pd- MoS₂.

To better grasp the interaction mechanism, the net total charge transfer (Q) was studied. Interestingly, it was found that Benzaldehyde acts as an electron acceptor and it withdraws 0.04, and 0.015 *e* from the Pd-, and Pt- MoS₂ sheets, respectively. While Indole plays as an electron donor, and it gives 0.094, and 0.185 *e* to the Pd-, and Pt- MoS₂ sheets, respectively. The whole calculations were displayed in Table 1.

Table 6-1. The calculated adsorption energy (E_{ad}), interaction distance (D), which is the distance between the molecule and the MoS₂ sheet, net charge transfer (Q), (the negative values of charge indicate a charge transfer from the molecule to the surface, and vice versa), energy bandgap (E_g), and recovery time (τ).

System	E_{ad} (eV)	D (Å)	Q (e)	E_g (eV)	τ (sec) @ T=298 K (Visible light)	τ (sec) @ T=698 K (Visible light)	τ (sec) @ T=298 K (UV light)	τ (sec) @ T=698 K (UV light)
Pristine MoS ₂	-	-	-	1.66	-	-	-	-
Pristine MoS ₂ -Benzaldehyde	-1.33	3.18	0.005	1.658	$3.06 \times 10^{+10}$	0.004	$3.06 \times 10^{+6}$	0.004×10^{-4}
Pristine MoS ₂ -Indole	-1.75	3.23	-0.052	1.61	$3.86 \times 10^{+17}$	4.28	$3.86 \times 10^{+13}$	4.28×10^{-4}
Pd-MoS ₂	-3.51	2.37	-	1.482	$2.2 \times 10^{+47}$	$2.16 \times 10^{+13}$	$2.2 \times 10^{+43}$	$2.16 \times 10^{+9}$
Pd- MoS ₂ -Benzaldehyde	-1.91	2.21	0.04	1.478	$1.96 \times 10^{+20}$	61.17	$1.96 \times 10^{+16}$	61.17×10^{-4}
Pd- MoS ₂ -Indole	-2.37	2.28	-0.094	1.322	$1.17 \times 10^{+28}$	$1.28 \times 10^{+5}$	$1.17 \times 10^{+24}$	12.8
Pt-MoS ₂	-4.4	2.32	-	1.236	$2.45 \times 10^{+62}$	$5.75 \times 10^{+19}$	$2.45 \times 10^{+58}$	$5.75 \times 10^{+15}$
Pt-MoS ₂ -Benzaldehyde	-2.53	2.13	0.015	1.341	$5.94 \times 10^{+30}$	$1.83 \times 10^{+6}$	$5.94 \times 10^{+26}$	183
Pt-MoS ₂ -Indole	-2.2	2.25	-0.185	1.336	$1.56 \times 10^{+25}$	$7.58 \times 10^{+3}$	$1.56 \times 10^{+21}$	0.75

To obtain more particular knowledge, the electronic DOS for the cases of the Benzaldehyde, and Indole adsorption over the Pd- or Pt-MoS₂ has been calculated and represented in Fig. 5.

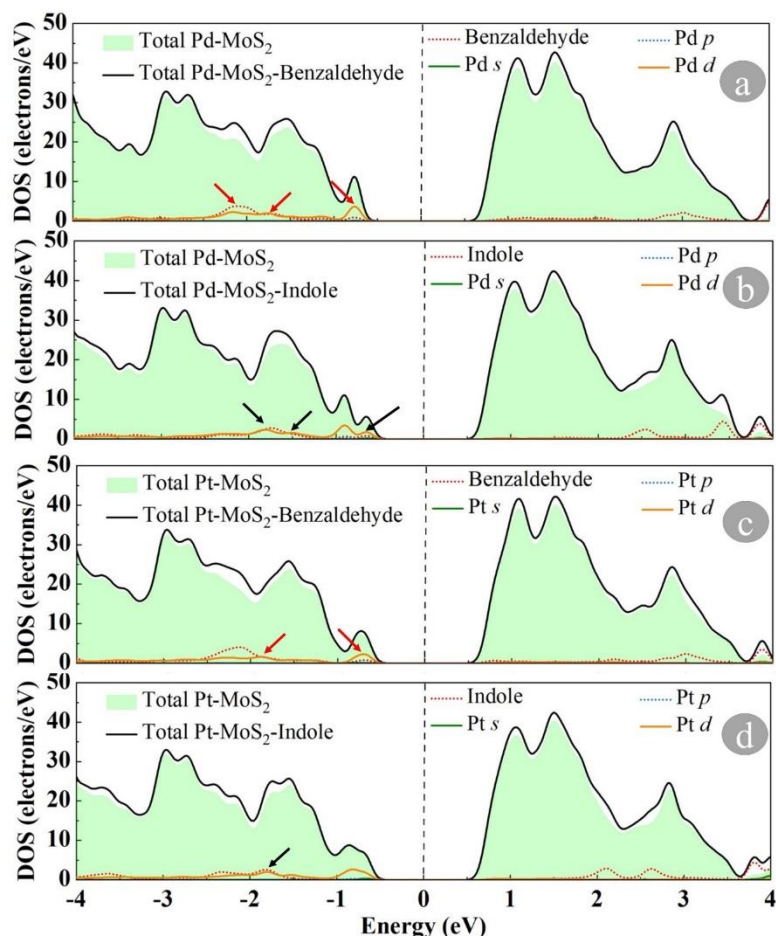


Figure. 5. Total DOS curves for Benzaldehyde adsorption on (a) Pd- MoS₂, (c) Pt- MoS₂, and Indole adsorption on (b) Pd- MoS₂, and (d) Pt- MoS₂ systems, respectively. The dashed line means the Fermi level, which was set to be zero.

It is apparent in Fig. 5, that a few peaks of the DOS of gas molecules happened around the Fermi level, confirming the strong interaction between the molecules and metal decorated MoS₂. The orbital hybridization between *d*-orbital of the metal atom and the gas has the main contribution to the total DOS of the complex system near the Fermi level. These agree well with the obtained large adsorption energies and can be seen that metal decorated MoS₂ is very sensitive toward the targets.

Finally, in order to further evaluate the performance of a gas sensor, recovery time as one of the key important indicators should be considered. A good gas sensor needs to be restored back fast to its primitive state after the desorption of the analyte, but it should be noted that a very short recovery time is not favorable for realizing detection in a real experiment [299]. The recovery time

(τ) is the time needed for the target gas to be desorbed from the sheet and from the transition state theory, it is defined [211].

$$\tau = \omega^{-1} \exp \left(-E_{ad} / K_B T \right) \quad (2)$$

where ω , k_B , and T represent attempt frequency, Boltzmann's constant (8.318×10^{-3} kJ/(mol·K)), and temperature, respectively. In visible light ($\omega = 10^{12}$ Hz) and at temperature of $T = 698$ K, the τ values for pristine, Pd-, and Pt-MoS₂ structures toward Benzaldehyde were achieved to be 0.004, 61.17, and $1.83 \times 10^{+6}$ s, respectively. In the same conditions Indole had τ values of 4.28, $1.28 \times 10^{+5}$, and $7.58 \times 10^{+3}$ s after adsorption on the pristine, Pd-, and Pt-MoS₂ structures, accordingly.

It has been reported that τ can be facilitated by exposure to UV light, because of the elimination of the desorption-barrier, [243] and the sensor can be applied in practical situations. To address this, the sensors were examined under UV light ($\omega = 10^{16}$ Hz), and it was seen that Benzaldehyde has a τ value of 183 s after interaction with Pt-MoS₂. Also, Indole showed that it has τ value of 12.8, and 0.75 s upon Pd-, and Pt-MoS₂, respectively. It should be mentioned that ambient temperature 298 K was also considered and presented in Table. 1 but it has not shown any promising recovery time.

To make it short, our results suggest that Pd-, and Pt-decorated MoS₂ show promises in gas molecule sensing applications. It was disclosed that the gases were weakly adsorbed on the pristine MoS₂, and the adsorption energy for Benzaldehyde, and Indole detection is ameliorated from -1.33 , and -1.75 eV to -1.91 (-2.53) eV, and -2.37 (-2.2) eV after decoration with Pd (Pt), respectively. Meanwhile the amount of charge transfer is also enlarged from 0.005, and $-0.052 e$ to 0.04 (0.015) e , and -0.094 (-0.185) e after decoration with Pd (Pt), accordingly. Moreover, for reusability of the sensor, the recovery time was studied, and it was revealed that Pd-MoS₂ has a recovery time of 61.17 *sec* under visible light and $T=698$ K after interaction with Benzaldehyde. However, Indole manifested that it can be desorbed from the Pd-MoS₂ with reasonable recovery time of 12.8 *sec* under UV light and $T=698$ K. Hence, it seems that decoration of the MoS₂ with the Pd, and Pt metal atoms could reinforce the detection of the target gases.

Summary

In summary, colon cancer is one of the leading causes of death worldwide. Early detection of cancer through non-invasive breath analysis is a strategy that could save lives. There is plenty of avenues here. First, gas adsorption can be tuned based on number of layers, device configuration and decoration with Nobel metals. We systematically investigated the adsorption energy, stable geometry, and electronic properties of the MoS₂ monolayer to gas molecules by first-principles calculations. Different adsorption locations and molecule orientations are included to distinguish the steadiest structures. We studied Benzaldehyde, and Indole as potential biomarkers for colorectal cancer as these two markers are present in breath of colon cancer patients. We find that Benzaldehyde, and Indole are physisorbed on pristine MoS₂ with slight charge transfer, and moderate adsorption energy. With the intention of enhancing the adsorption behavior, MoS₂ was decorated with the transition metals, Pd, and Pt atoms. The results evinced that the Pt, and Pd decoration are more favorable for the targets detection, because of the higher adsorption energy, charge transfer, and quick recovery time. The calculated results indicated that after decoration of MoS₂ with Pd, Pt, adsorption energy was increased 0.58, and 1.2 eV toward Benzaldehyde, respectively. Furthermore, energy band gap was also decreased 0.18, and 0.317 eV for Benzaldehyde adsorption upon Pd, Pt, respectively. Besides, the minimum distances were smaller than atomic distances for the targets over Pd-, Pt-MoS₂, supporting the strong adsorption. Moreover, it was discerned that Pt- MoS₂ could be reusable with recovery time of 183, 0.75 *sec* toward Benzaldehyde, and Indole at the temperature of 698 K, and under UV light, respectively. and its sensitivity has been improved after decoration. The findings suggest that the Pd-, and Pt-MoS₂ sensors could be an effective platform to detect Benzaldehyde and Indole. And it provides a new idea for the exploration of gas sensing technology, especially in medical applications. Pushing the frontiers of 2D nanomaterials for molecular sensing could yield devices for early detection of cancer.

7. Chapter 7

Theoretical Study on Novel 2D Materials

Graphene-like Borocarbonitride (BC₆N)- VOCs

In this work, we employ first-principles density functional theory calculations and non-equilibrium Green's function formalism to investigate the potential application of graphene-like borocarbonitride (BC₆N) for high-performance volatile organic compound (VOC) sensors used for human breath analysis. The adsorption behaviors of several VOCs (acetone, ethanol, methanol, formaldehyde, and toluene) and interfering gases in exhaled breath (carbon dioxide and water) are examined. The BC₆N monolayer is a semiconductor with a bandgap of 1.228 eV. It is discovered that all the above gas molecules are physisorbed on the pristine BC₆N sheet. The energy bandgap of pristine BC₆N is slightly altered after interaction with the gas molecules. It is revealed that introducing a single carbon vacancy in the BC₆N sheet can significantly increase the adsorption energies of the gas molecules. The modification of current-voltage responses due to VOC's disclose that the sensor shows high sensitivity and selectivity and short recovery toward ethanol. Our results suggest that defective BC₆N is a compelling and feasible candidate for chemiresistive sensors for applications in room temperature breath analysis of VOCs.

7.1 Overview

Breath analysis is a non-invasive strategy and a rapid method for disease diagnosis since ancient times. Volatile organic compounds (VOCs) in exhaled breath samples of patients are the targets of breath analyses [258, 300, 301]. More than 870 kinds of VOCs in the human breath provide vital information about dysfunction or metabolic disorders in the human body [231]. The detection of serious diseases such as various types of cancers, Parkinson's disease, diabetes, Alzheimer's disease, chronic kidney disease, and multiple sclerosis using breath analysis was reported [302]. Some VOCs in the breath, such as alcohols, ketones, aldehydes, and acids, are biomarkers for specific diseases. Hence, understating the level of VOCs leads us to differentiate healthy people from sick patients. The concentration of VOCs in the range of 1–5000 parts per billion (ppb) can be measured using gas chromatography-mass spectroscopy (GC-MS), which has

been used in clinical trials for the diagnosis of different disease through breath analyses [303-305]. However, using this technology as a screening tool needs bulky and expensive equipment, time-consuming preconcentration of samples, and highly trained personnel.

Room temperature gas sensors based on nanomaterials are promising candidates for breath analysis thanks to a high surface-to-volume ratio, band gap changes on gas adsorption, high sensitivity and selectivity, fast response time, quick recovery, low cost, low power consumption, controllable morphology, small size, and easy use [306]. Graphene, the first world's discovered two-dimensional (2D) material [307, 308], has been extensively investigated for gas sensing and biosensing applications. [39, 215, 309-319]. Since the first successful demonstration of graphene as a molecular gas sensor [215], the graphene-based VOC sensors have enticed interest in the detection of breath biomarkers [320]. Nevertheless, gas sensors based on pristine graphene show low sensitivity and selectivity toward diverse VOC molecules [320]. Functionalization with organic compounds, nanoparticles, conducting polymers, the introduction of dopants, and defect engineering are the effective methods to overcome the limitations associated with carbon based nanomaterials [20, 40, 41, 321-331].

Substitutional doping with Boron (B) and Nitrogen (N) atoms can enhance the sensing properties of graphene. Due to their similar atomic radius to the Carbon (C) atoms of the graphene, they have been widely employed as dopants for graphene [332-336]. The properties of monolayers BC_3 and C_3N , graphene analogs materials, have been extensively studied [337-341], and the potential use of them for gas sensing has been reported [342-352]. We investigated the adsorption behavior of different gas molecules on the BC_3 monolayer, reporting the high potential of the BC_3 -based gas sensor for NO detection and NO_2 dissociation [342]. Peyghan *et al.* reported BC_3 nanotubes as a possible gas sensor for various hazardous gases such as CO [345]. Beheshtian *et al.* studied the electronic sensitivity of pristine, Al-, and Si-doped BC_3 sheets toward formaldehyde [343]. They disclosed that although formaldehyde gas molecule is weakly adsorbed on the BC_3 sheet, both Al and Si doping enhance the reactivity of the sheet toward the molecule. Moreover, Chigo-Anota *et al.* [344] reported the adsorption behavior of H_2O on the BC_3 surface. Furthermore, the adsorption of gas molecules on the graphene-like C_3N has been studied by Ma *et al.* [346]. It was shown that C_3N has good sensitivity and selectivity for NO_2 and SO_2 adsorption [347]. Zhao

et al. showed that the adsorption capacity of C₃N toward H₂S and NH₃ can be enhanced by introducing monovacancy [352].

Recently, the BN-co-doped nanographene with a similar atomic arrangement was synthesized [353]. The graphene-like borocarbonitride (BC₆N) shows a semiconducting behavior and offers high carrier mobility comparable to that of black phosphorene [354]. Due to the acceptor and donor behavior of B and N atoms, respectively, BC₆N could be promising for sensing applications [355]. Babar *et al.* investigated the gas sensing performance of BC₆N for common gaseous pollutants (CO, CO₂, NO, NO₂, NH₃, H₂S, and SO₂) and discovered that the monovacancies in BC₆N enhance the sensitivity of the material toward the molecules [355].

Due to local charges induced by the presence of B and N atoms, one can expect that BC₆N show higher sensitivity toward VOCs compared to graphene. In addition to that, BC₆N might be a promising material for nanoelectronics applications due to high carrier mobility and a moderate direct bandgap. Hence, BC₆N is chosen as the channel material in an effort to realize a high-performance VOCs nanosensor. Here, we provide a comprehensive theoretical study on the adsorption behavior of different VOCs such as acetone ((CH₃)₂CO), ethanol (C₂H₅OH), methanol (CH₃OH), formaldehyde (CH₂O), and toluene (C₇H₈) molecules as common breath biomarkers on the graphene-like BC₆N monolayer. These selected VOCs represent different VOC categories of ketones, alcohols, aldehydes, and hydrocarbons. We also consider the water (H₂O) and carbon dioxide (CO₂) as interfering gases in exhaled breath that could be barriers for the detection of target biomarkers.

7.2 Computational Method

Calculations were performed using first-principles density functional theory (DFT) methods combined with nonequilibrium Green's function (NEGF) implemented in Atomistix ToolKit (ATK) packag [153, 154, 239]. The Generalized Gradient Approximation of Perdew–Burke–Ernzerhof (GGA-PBE) with a double- ζ polarized basis set was applied to solve Kohn–Sham equations and to expand electronic density. In addition, the long-range van der Waals (vdW) interactions was considered by employing the Grimme vdW correction (PBE-D2) [156, 157]. To avoid the image-image interactions, a vacuum space of 20 Å was considered in z direction in which the structures are not periodic. The electronic temperature and plane wave mesh cut-off energy were set to be 300 K and 60 Rydberg, respectively. All the structures were fully relaxed using

limited-memory Broyden-Fletcher-Goldfarb-Shanno (LBFGS) quasi-Newton method, until the force and the stress on each atom is less than 0.01 eV/Å and 0.001 eV/Å³, respectively. The Brillouin zones were sampled using a 3×3×1 Monkhorst-Pack k -point grid during geometry optimization. The k -point grid was then increased to 5×5×1 to achieve more accurate results for electronic structure calculations.

The adsorption energy provides quantitative data on the interaction strength between adsorbent and adsorbate. The vdW corrected energy of a single VOC molecule on the pristine and defective BC₆N sheet can be expressed by:

$$E_{ad} = E_{BC_6N+Molecule} - (E_{BC_6N} + E_{Molecule}) \quad (15)$$

where $E_{BC_6N+Molecule}$, E_{BC_6N} , and $E_{Molecule}$ are the total energies of the BC₆N-Molecule complex, pristine BC₆N sheet, and the isolated gas molecule, respectively. Furthermore, the co-adsorption energy of gas molecules on the pristine and defective BC₆N sheet is:

$$E_{co-ad} = [E_{BC_6N+Molecules} - (E_{BC_6N} + E_{Molecule_1} + \dots + E_{Molecule_n})] / n \quad (16)$$

where $E_{BC_6N+Molecules}$, $E_{Molecule_n}$, and n are the total energy of the BC₆N-molecules complex, the total energy of the n th isolated gas molecule, and the number of gas molecules that are co-adsorbed, respectively.

Moreover, the charge transfer (Q) upon adsorption of the gas molecule on the BC₆N sheet was obtained using Mulliken population analysis from counting the charge difference between the adsorbed and the isolated molecule. A negative Q indicates a charge transfer from the molecule to the monolayer sheet, whereas a positive Q shows that the molecule withdraws electrons from sheet.

The electron transport calculations were carried out using GGA-PBE combined with NEGF methods. A fast Fourier transform (FFT) solver is employed to solve Poisson's equation. The electrical current through the device with two metal electrodes under a finite bias voltage (V_b) can be calculated using the Landauer-Büttiker formula as follows [356-358]:

$$I = \frac{2e}{h} \int_{\mu_L}^{\mu_R} T(E, V_b) [f_R(E, V_b) - f_L(E, V_b)] dE \quad (17)$$

where f and T are Fermi-Dirac and transmission functions at energy E under the bias voltage V_b . Furthermore, μ_L and μ_R are the chemical potentials of the left and right electrodes. The bias energy window is $\mu_L = E_f - eV_b / 2$ and $\mu_R = E_f + eV_b / 2$. E_f is the Fermi energy, the average value of the left and right electrodes' chemical potentials, which is normally set to zero. The Brillouin zone of the device was sampled using $1 \times 3 \times 50$ Monkhorst-Pack k -point in the device calculator and $1 \times 3 \times 1$ in the transport calculations. Further, the plane wave mesh cut-off energy was set to be 150 Rydberg.

7.3 First-principles calculations using density functional theory:

Based on our calculations, the monolayer BC₆N has a 2D hexagonal lattice with eight atoms (six C atoms, one B atom, and one N atom) per unit cell, as shown in Figure 7-1 (a). The graphene-like atomic lattice of the pristine BC₆N was found to be fully planar, showing sp^2 hybridization of the atoms. One can consider BC₆N as a graphene lattice where two C atoms are replaced by one B atom and one N atom. The hexagonal lattice constant was measured to be 4.99 Å. Further, the C–C, C–N, and C–B bond lengths were found to be 1.42, 1.45, and 1.47 Å, respectively. It was discovered that BC₆N is a direct semiconductor with an energy bandgap of 1.228 eV at K-point, as shown in Figure 7-1 (b). Our findings are in good agreement with the literature data [354, 359, 360].

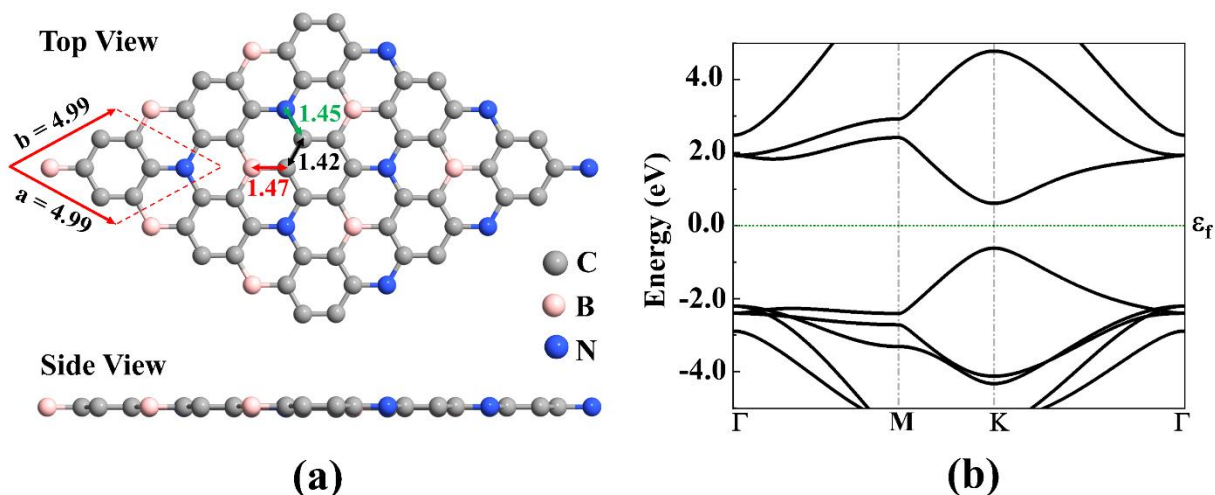


Figure 7-1. (a) Top and side view of the optimized structure of a pristine BC_6N sheet and its hexagonal unit cell containing six C atoms, one B atom, and one N atom. Bond lengths are given in the unit of \AA . (b) The corresponding band structure for a pristine BC_6N sheet semiconducting behavior with an energy bandgap of 1.228 eV at the K-point. The dotted green line indicates the Fermi level, which is set to zero.

In order to study the interactions between the gas molecules and the pristine BC_6N sheet, we assumed a 3×3 supercell of BC_6N that consists of 54 C atom, 9 B atoms, and 9 N atoms. Each gas molecule prefers to be adsorbed on the sheet with a special molecular orientation. The molecular axis of the molecules can be aligned in parallel or perpendicular with respect to the surface of the BC_6N sheet. Besides that, in the perpendicular orientation, various atoms can point down to the surface of the sheet. Moreover, different adsorption sites (top of B–C–N hexagon, top of C hexagon, top of C–C bond, top of C–B bond, top of C–N bond, top of C atom, top of B atom, and top of N atom) are available for the molecules to be adsorbed. Henceforth, several configurations can be considered as input geometries. In order to find the most stable adsorption configurations, all the possible structures were fully relaxed, and their adsorption energies were calculated. Based on Equation (1), the more negative energy adsorption is, the stronger the interaction between gas molecules the BC_6N sheet would be. The most stable adsorption configurations with the most negative adsorption energies were chosen for further studies and provided in Figure 7-2. Furthermore, adsorption energies, the minimum interaction distances, the net charge transfer, and the energy bandgap of the selected configurations were tabulated in Table 7-1.

As can be seen in Figure 7-2, the acetone and ethanol gas molecules prefer to be adsorbed in a vertical orientation, where the O atom of the molecules is pointing to the B atom of the BC₆N sheet. Upon interaction of methanol with BC₆N sheet, the molecule adopts a tilted vertical orientation with respect to the BC₆N surface with its O atom pointed to the C–N bond of the sheet. The formaldehyde molecule is adsorbed in a vertical orientation, respecting the BC₆N sheet with H atom pointed toward the C–C bond and the O atom oriented to the center of B–C–N hexagon. Toluene prefers to be adsorbed in a parallel orientation with respect to the BC₆N sheet with its carbon hexagon aligned to the B–C–N hexagon of the BC₆N sheet. For the case of carbon dioxide, it is tilted with the O atom oriented toward BC₆N. Additionally, the C atom of the molecule is placed on top of the C atom of the BC₆N. Finally, the water molecule is adsorbed in a parallel orientation with respect to the BC₆N surface, while its O atom is slightly tilted toward the N atom of BC₆N.

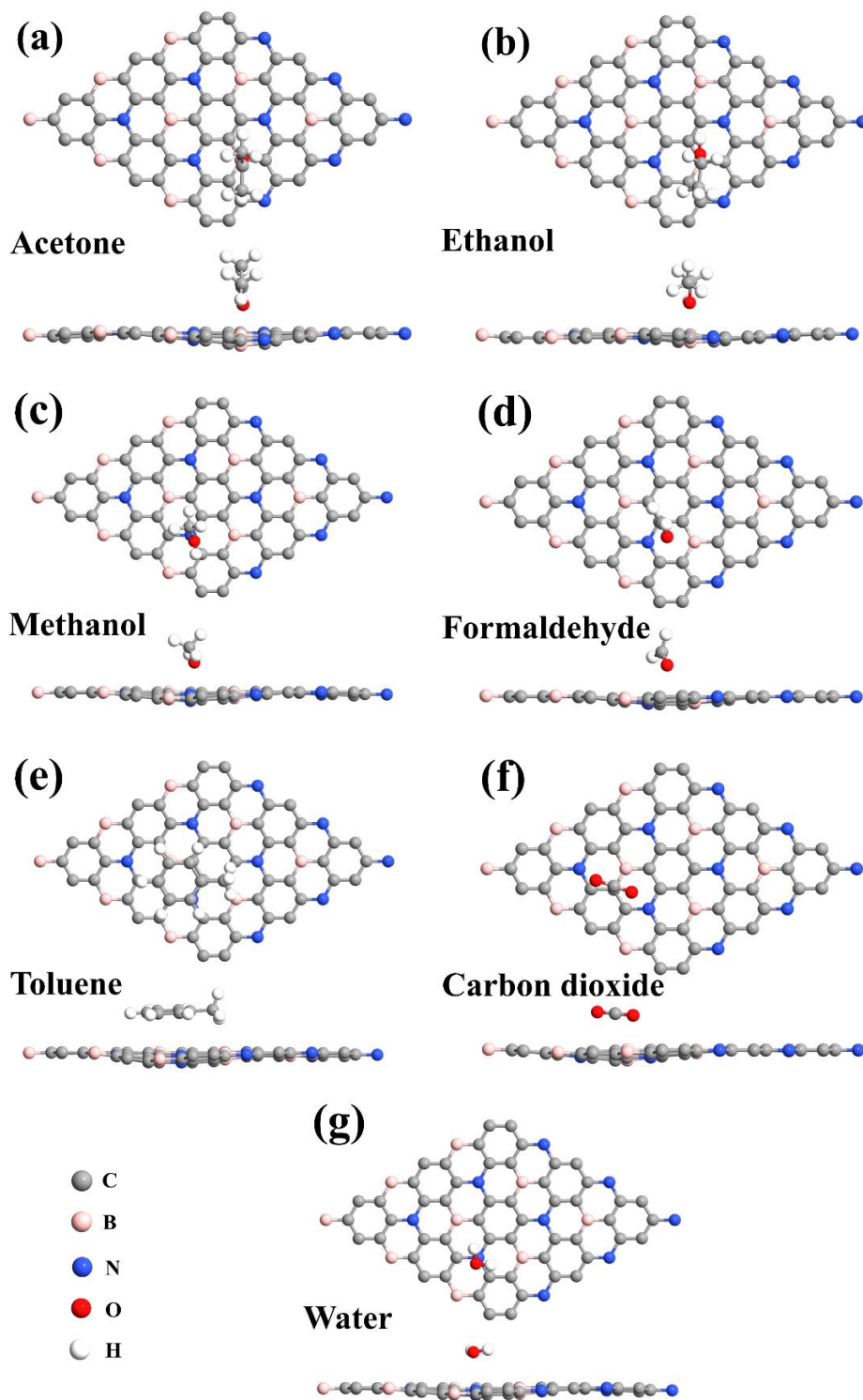


Figure 7-2. The most stable adsorption configurations (top and side view) for (a) acetone, (b) ethanol, (c) methanol, (d) formaldehyde, (e) toluene, (f) carbon dioxide, and (f) water molecules on pristine BC₆N sheet.

In order to develop a sensor with an efficient sensing mechanism, the adsorbent-adsorbate interactions should be strong enough to retain the gas molecule on the sensor and should be weak enough to let the gas molecule be removed from the sensor without damaging the properties of sensor's material. The obtained adsorption energies of acetone-, ethanol-, methanol-, formaldehyde-, toluene-, carbon dioxide-, and water-adsorbed pristine BC₆N sheet were found to be -0.381, -0.378, -0.316, -0.228, -0.910, -0.253, and -0.263 eV, respectively. These values suggest that all gas molecules were weakly physisorbed on the pristine BC₆N sheet, while only toluene molecule was strongly physisorbed on the sheet. It should be mentioned that the obtained adsorption energies for VOCs are adequately large to tolerate thermal disturbance at room temperature ($K_B T \cong 25 \text{ meV}$). Because of the fewer number of total atoms in the O-functionalized VOCs, the O-based VOCs show smaller adsorption energies in comparison with toluene (an aromatic hydrocarbon) that lacks O group. The obtained adsorption energies for VOCs on pristine BC₆N are greater than those reported for acetone (-0.36 eV) [244], ethanol (-0.33 eV) [244], methanol (-0.21 eV) [361], formaldehyde (-0.091 eV) [245], toluene (-0.52 eV) [244], carbon dioxide (-0.03 eV) [362], and water (-0.05 eV) [362] on pristine graphene sheet. The interactions between VOCs and BC₆N are also stronger than those found for acetone (-0.16 eV) and ethanol (-0.22 eV) with pristine MoS₂ sheet [248]. Also, the adsorption energies of acetone, ethanol, and toluene on monolayer black phosphorus were found to be -0.320 eV, -0.214 eV, and -0.432 eV, respectively, which are less than those achieved for pristine BC₆N [235]. Similarly, the interaction between ethanol (-0.20 eV) and acetone (-0.26 eV) with blue phosphorene is weaker than those with BC₆N [363]. It can be concluded that BC₆N sheet potentially may offer better performance toward VOCs among 2D materials. Besides adsorption energy, the coverage (the quantities of adsorption density) is an important factor that defines the sensitivity of a material. More VOC molecules adsorbed on the surface of the sensor results in an enhanced sensitivity. Therefore, the effect of the VOCs concentration and the co-adsorption of various species on the sensor performance was studied. For example, the co-adsorption of one acetone and one ethanol molecule and the co-adsorption of two and three acetone molecules were considered. The most stable co-adsorption configurations of gas molecules on pristine BC₆N sheet are presented in Figure 7-3. As can be seen in Figure 7-4, with increasing the quantity of VOCs from same species and with co-adsorption of VOCs from different species on the pristine BC₆N sheet, the absolute value of co-adsorption energies increase, indicating an enhancement in the sensitivity of the sensor.

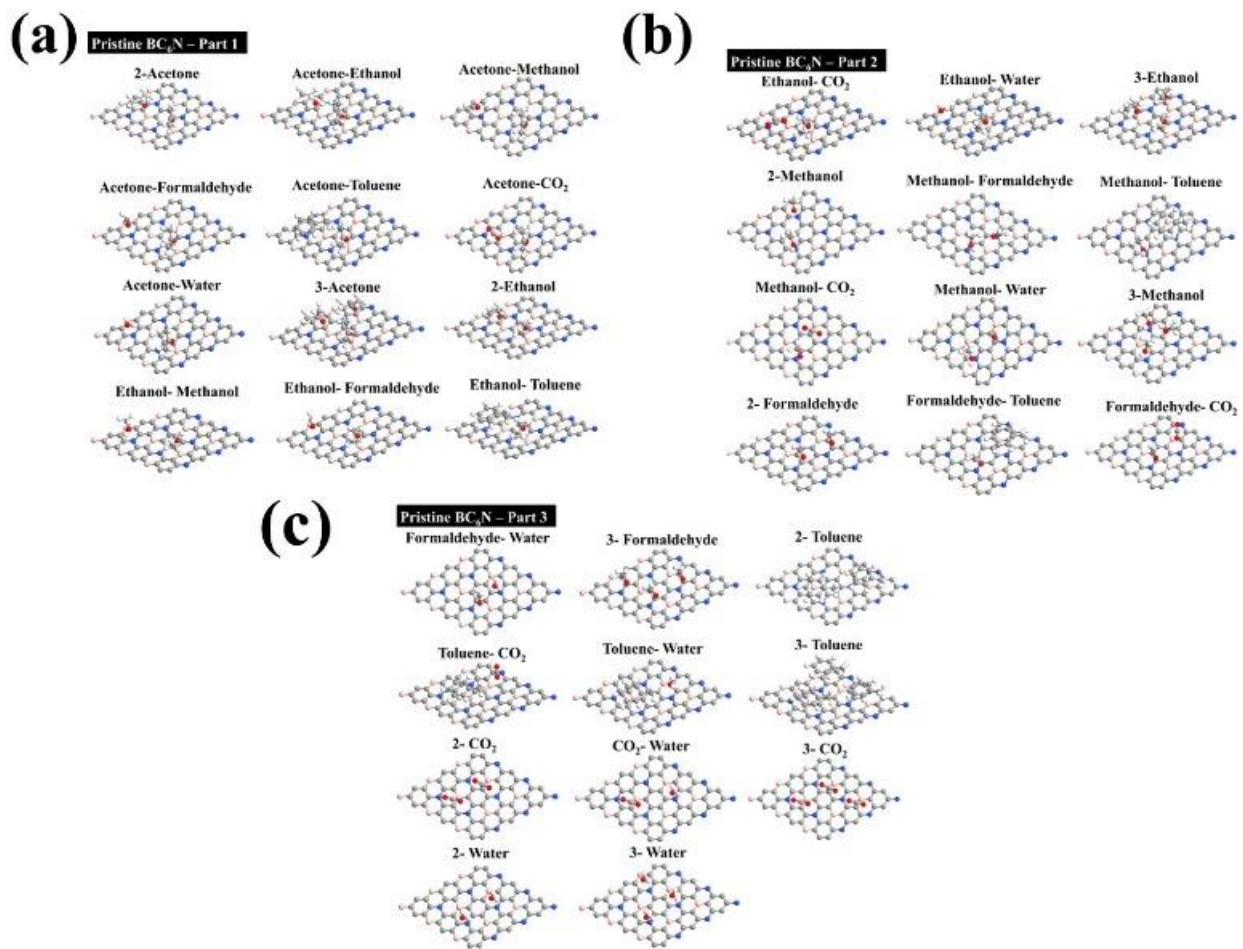


Figure 7-3. The relaxed structures of co-adsorbed gas molecules on pristine BC₆N sheet.

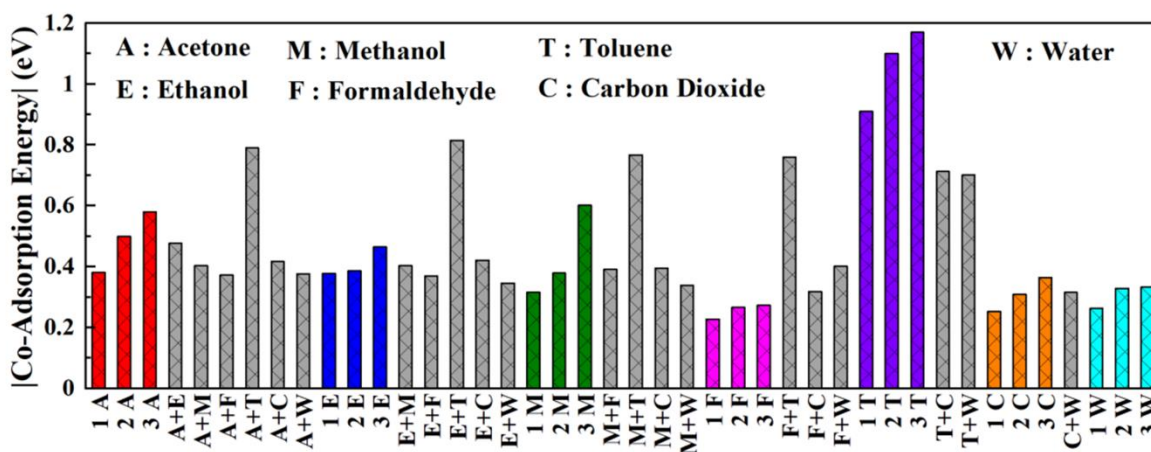


Figure 7-4. The co-adsorption energies of gas molecules on pristine BC₆N sheet.

The recovery time of a sensor after gas exposure (τ) can be estimated using the conventional transition state theory as follows [211]:

$$\tau = \nu_0^{-1} \exp(-E_{ad} / k_B T) \quad (18)$$

Here ν_0 is the attempt frequency, T is the temperature, and k_B is the Boltzmann constant. It is expected that at a constant temperature, small adsorption energies result in a fast desorption process of the gas molecules. To capture the gases reversibly, the adsorption energies suggest being between -0.60 eV to -1.0 eV. Table 7-1 lists the recovery time of the above systems. The obtained recovery times for desorption of acetone, ethanol, methanol, formaldehyde, toluene, carbon dioxide, and water from pristine BC₆N sheet at room temperature in visible light ($\nu_0 = 10^{12}$ Hz) were 2.6×10^{-6} , 2.3×10^{-6} , 2.1×10^{-7} , 6.8×10^{-9} , 2.0×10^{-3} , 1.8×10^{-8} , 2.6×10^{-8} sec, respectively. The longer recovery time of an individual toluene molecule from pristine BC₆N can be decreased to 0.28 sec by increasing the temperature to 400 K.

The physisorption of the gas molecules on the pristine BC₆N sheet resulted in large interaction distances. The interaction distances between acetone, ethanol, methanol, formaldehyde, toluene, carbon dioxide, and water molecules and BC₆N sheet were 2.51 (O–B), 2.49 (O–B), 2.58 (O–C), 2.63 (O–N), 2.69 (H–C), 2.84 (O–C), and 2.88 (O–N) Å, respectively. The covalent radii are 0.82, 0.77, 0.75, 0.73, 0.37 Å for B, C, N, O, H atoms, respectively [364]. Since the interaction distances are less than the sum of corresponding covalent radii of the atoms, it can be deduced that all gas molecules are physically adsorbed on the surface of the BC₆N sheet. Due to the physisorption behavior, a small net charge was transferred between the gas molecules and the pristine BC₆N sheet. The total charge transfer for acetone-, ethanol-, methanol-, formaldehyde-, toluene-, carbon dioxide-, and water-adsorbed pristine BC₆N sheet were measured to be 0.056, 0.054, 0.029, 0.043, 0.036, 0.014, and 0.015 e , respectively. Except for toluene that withdraws electrons from the sheet, other gas molecules act as charge donors.

In addition to satisfactory adsorption energy for a gas molecule-sensor system, the electrical properties of the sensor need to change upon the exposure of gas molecules in order to develop a reliable sensor. Electronic band structures of the above configurations are provided in Figure 7-5. One can see that upon adsorption of the molecules with the BC₆N, the electronic band structures of the pristine BC₆N remained almost unchanged near the Fermi level. This is in

agreement with the obtained small values of adsorption energy. The energy bandgap of pristine BC₆N (1.228 eV) was slightly (<8 meV) altered after interaction with the gas molecules. The obtained energy bandgaps for of acetone-, ethanol-, methanol-, formaldehyde-, toluene-, carbon dioxide-, and water-adsorbed pristine BC₆N sheet were found to be 1.225, 1.220, 1.223, 1.220, 1.220, 1.224, and 1.224 eV, respectively. The electrical conductivity (σ) of a semiconductor material can be determined by the energy bandgap (E_g) [165]:

$$\sigma \propto \exp(-E_g / 2k_B T) \quad (19)$$

The sensitivity (S) which is the variation of the σ for the nanosensors with and without gas, can be expressed as [165]:

$$S = \left| \frac{\sigma_{gas} - \sigma_{pure}}{\sigma_{pure}} \right| \times 100 \quad (20)$$

Here σ_{gas} and σ_{pure} are the conductivity of an isolated BC₆N sheet and the conductivity of gas molecule adsorbed-BC₆N sheet, respectively. Using Equations (4) and (5), pristine BC₆N showed 6.1%, 14.7%, 9.5%, 14.7%, 14.7%, 7.6%, and 7.6% sensitivity toward acetone, ethanol, methanol, formaldehyde, toluene, carbon dioxide, and water molecules, respectively.

Table 7-1. The calculated adsorption energy (E_{ad}), interaction distance (D), which is the distance between the molecule and BC_6N sheet, charge transfer (Q), energy bandgap (E_g), and recovery time (τ). The negative values of charge indicate a charge transfer from the molecule to the nanotube.

System	E_{ad} (eV)	D (Å)	Q (e)	E_g (eV)	τ (sec)
Pristine BC_6N	-	-	-	1.228	-
Acetone-Pristine BC_6N	-0.381	2.51	-0.056	1.225	2.6×10^{-6}
Ethanol-Pristine BC_6N	-0.378	2.49	-0.054	1.220	2.3×10^{-6}
Methanol-Pristine BC_6N	-0.316	2.58	-0.029	1.223	2.1×10^{-7}
Formaldehyde-Pristine BC_6N	-0.228	2.63	-0.043	1.220	6.8×10^{-9}
Toluene-Pristine BC_6N	-0.910	2.69	+0.036	1.220	$2.0 \times 10^{+3}$
Carbon dioxide-Pristine BC_6N	-0.253	2.84	-0.014	1.224	1.8×10^{-8}
Water-Pristine BC_6N	-0.263	2.88	-0.015	1.224	2.6×10^{-8}
Defective BC_6N	-	-	-	0	-
Acetone-Defective BC_6N	-0.527	2.60	-0.067	0	7.4×10^{-4}
Ethanol-Defective BC_6N	-0.754	2.45	-0.071	0	4.9
Methanol-Defective BC_6N	-0.750	2.58	-0.077	0	4.2
Formaldehyde-Defective BC_6N	-0.647	2.51	-0.082	0	7.7×10^{-2}
Toluene-Defective BC_6N	-1.00	2.66	-0.063	0	$6.8 \times 10^{+4}$
Carbon dioxide-Defective BC_6N	-0.315	2.82	-0.039	0	2.0×10^{-7}
Water-Defective BC_6N	-0.458	2.77	+0.026	0	5.1×10^{-5}

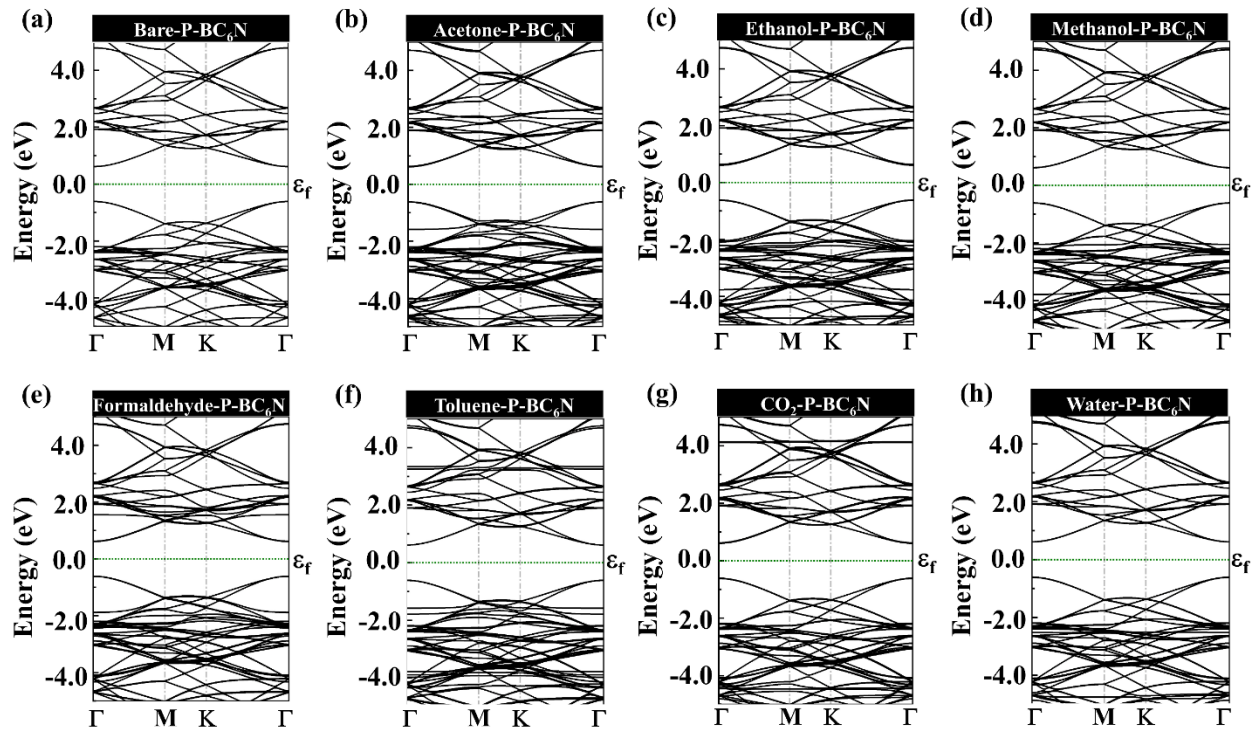


Figure 7-5. Energy band structures of (a) acetone, (b) ethanol, (c) methanol, (d) formaldehyde, (e) toluene, (f) carbon dioxide, and (f) water molecules on pristine BC_6N sheet. The dotted green line indicates the Fermi level, which is set to zero.

Similar to graphene, defects in the BC_6N sheet are inevitably generated during the fabrication process due to the imperfect growth conditions [365]. They can also be formed during the harsh treatments of the film, such as plasma oxidation [366, 367], ion and electron irradiation [368], or chemical treatments [369]. Vacancy defects with different sizes can be formed by knocking atoms out of BC_6N lattice. The electronic and transport properties of the BC_6N lattice can be affected by these unavoidable defects. Hence, it is necessary to investigate the impacts of vacancy defects on the electronic and gas sensing properties of the BC_6N sheet. Here, we considered a single atom vacancy defect in the graphene-like BC_6N sheet. The single vacancies can be created if a single B, C, or N atom is missing in the BC_6N lattice. As can be understood from the unit cell of the BC_6N lattice in Fig. 1(a), four different defective BC_6N structures can be considered: 1) removing C atom next to N atom from the lattice (D_{C-N-BC_6N}), 2) removing C atom next to B atom from the lattice (D_{C-B-BC_6N}), 3) removing N atom from the lattice (D_{N-BC_6N}), and 4) removing B atom from the lattice (D_{B-BC_6N}). The optimized defective BC_6N

structures are shown in Fig. 5. The structural stability can be studied regarding the defect formation energy as follow:

$$E_{D-form} = E_{D-BC_6N} - (E_{P-BC_6N} - \mu_{atom}) \quad (21)$$

where E_{D-BC_6N} , E_{P-BC_6N} , and μ_{atom} are the total energy of the defective BC_6N , the total energy of the pristine BC_6N , and the chemical potential of the missing atom. To calculate the chemical potentials of B, C, and N atoms, our reference systems were β -rhombohedral boron, graphite, and N_2 in the gas phase. The defect formation energies were calculated to be 4.27, 8.64, 8.15, and 6.22 for D_{C-N-BC_6N} , D_{C-B-BC_6N} , D_{N-BC_6N} , and D_{B-BC_6N} , respectively, signifying that the formation of single C atom vacancy adjacent to N atom is experimentally more likely to occur. Interestingly, the formation energy of the D_{C-N} in the BC_6N sheet is less than the formation energy of a single C vacancy in the graphene sheet (7.5 eV) [365], suggesting that D_{C-N} can be easily formed in the BC_6N . Therefore, we selected the D_{C-N-BC_6N} structure for further studies. It should be added that similar to graphene [370, 371], a single C atom adjacent to N atom vacancy in the BC_6N sheet undergoes a Jahn-Teller distortion, leading to two saturation C bonds and one N dangling bond toward the missing C atom. This results in the formation of a five-membered and a nine-membered ring, as shown in Figure 7-6 (a). Our observations correspond well with the previous report [355].

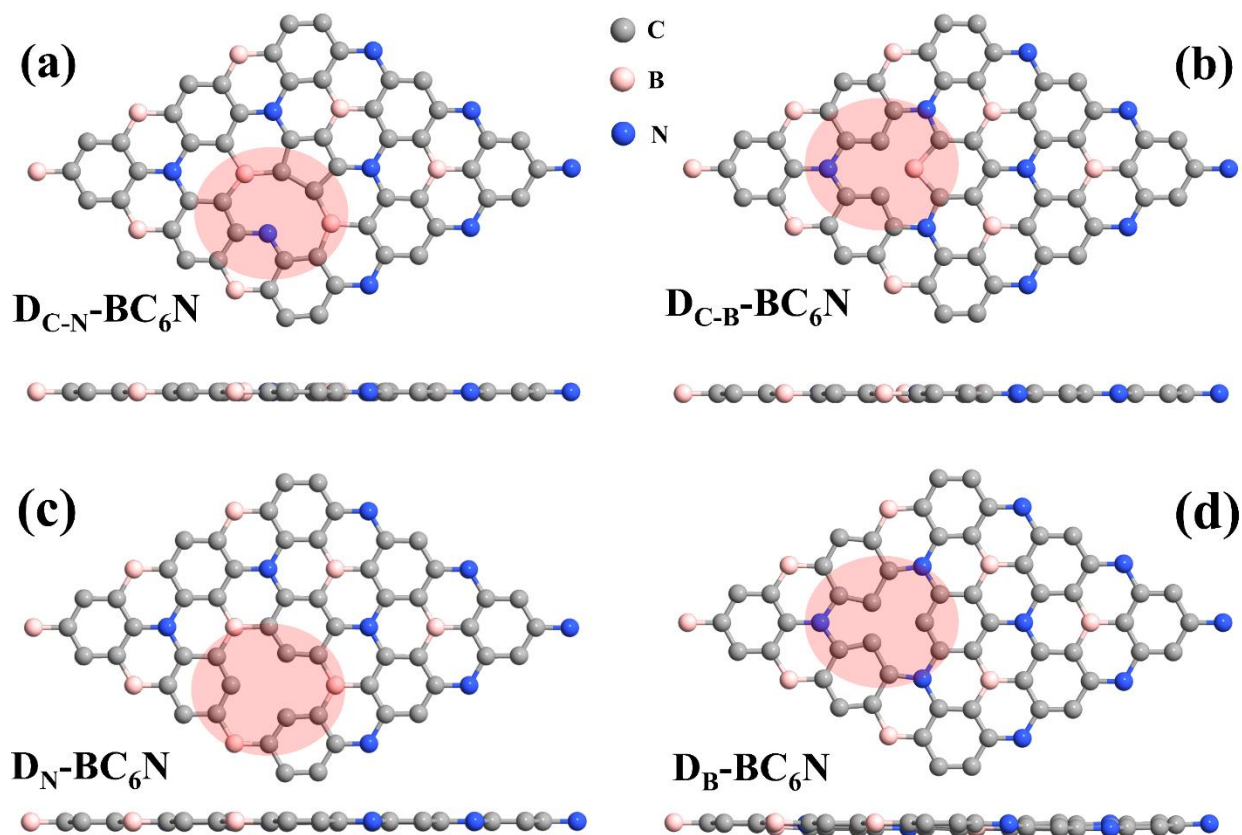


Figure 7-6. The most stable adsorption configurations (top and side view) for defective BC₆N sheet with one (a) C vacant adjacent to N atom, (b) C vacant adjacent to B atom, (c) N vacant, and (d) B vacant.

To focus on the effects of single vacancy defect on the sensing capability of the BC₆N sheet, the gas molecules were placed at the center of the defects with various orientations, and the structures were fully relaxed. The most stable configurations of adsorbed gas molecules on the D_{C-N}-BC₆N sheet are depicted in Figure 7-7.

The adsorption of gas molecules induces significant bending and buckling in the defective BC₆N around the defect area in comparison with a pristine sheet that almost retains its planarity after interaction with the molecules. This buckling is occurred due to the gas molecules which push the N atom with dangling bond in the defective BC₆N sheet out of the plane in the opposite direction where the molecule is located. It was discovered that upon exposure acetone to the defective BC₆N sheet, the molecule adopts a vertical orientation with respect to the plane of the sheet with O atom of acetone pointing to the N atom of the defective BC₆N. The minimum atom-atom distance between the acetone and defective BC₆N (O–N) was found to be 2.60 Å. The

ethanol adsorption mechanism on the defective BC₆N sheet shows similar behavior to acetone with the minimum atom-atom distance between the molecule and sheet of (O–N) 2.45 Å. Upon interaction of methanol and formaldehyde molecules with defective BC₆N sheet, the molecules adopt a tilted vertical orientation with respect to the surface of the sheet with the minimum atom-atom distance between the methanol/formaldehyde molecule and defective BC₆N (O–N) was found to be 2.58/2.51 Å. In the case of toluene, the molecule prefers to be adsorbed in a parallel orientation with respect to the plane of the defective BC₆N. The minimum interaction distance between the toluene and defective BC₆N (H–C) was found to be 2.66 Å. The carbon dioxide and water molecules were also aligned parallel to the defective BC₆N surface with C and O atom pointing toward N atom of the sheet, respectively. The minimum atom-atom distance between the carbon dioxide and defective BC₆N (C–N) and between the water and defective BC₆N (O–N) were calculated to be 2.85 and 2.77 Å, accordingly. It was discovered that the single vacancy defect in the BC₆N increases the adsorption energies of the gas molecules. The adsorption energies of acetone-, ethanol-, methanol-, formaldehyde-, toluene-, carbon dioxide-, and water-adsorbed defective BC₆N sheet were calculated to be –0.527, –0.754, –0.750, –0.647, –1.0, –0.315, and –0.458 eV, respectively. In comparison with pristine BC₆N sheet, the adsorption energies of acetone, ethanol, methanol, formaldehyde, toluene, carbon dioxide, and water molecules were increased 1.38, 1.99, 2.37, 2.83, 1.11, 1.24, and 1.73 times, respectively, after introducing a single vacancy in the sheet. Based on the obtained adsorption energies, it can be assumed that toluene was strongly physisorbed on the defective BC₆N sheet. Furthermore, ethanol, methanol, and formaldehyde molecules were moderately physisorbed on the D_{C-N}-BC₆N, while acetone, carbon dioxide, and water were weakly physisorbed. The total charge transfer for acetone-, ethanol-, methanol-, formaldehyde-, toluene-, carbon dioxide-, and water-adsorbed defective BC₆N sheet was found to be 0.067, 0.071, 0.077, 0.082, 0.063, 0.039, and 0.026 *e*, respectively, showing an increase in charge transfer between molecules and the BC₆N after formation the D_{C-N}. All gas molecules donate electrons to the sheet, except for water molecule that acts as an electron acceptor. From Equation (3), the recovery times for desorption of acetone, ethanol, methanol, formaldehyde, toluene, carbon dioxide, and water from defective BC₆N sheet at room temperature in visible light ($\nu_0 = 10^{12}$ Hz) were calculated to be 7.4×10^{-4} , 4.9, 4.2, 7.7×10^{-2} , 6.8×10^4 , 2.0×10^{-7} , 5.1×10^{-5} sec, respectively. In addition, the recovery time of toluene can be decreased to 3.9 sec by heating the sensor at 400 K. The obtained values for adsorption energies, charge transfer, and recovery times

suggest that defective BC₆N has the potential to capture ethanol, methanol, formaldehyde, and toluene reversibly. However, electronic transport properties change of the material by gas sensing should be evaluated in order to develop a reliable sensor.

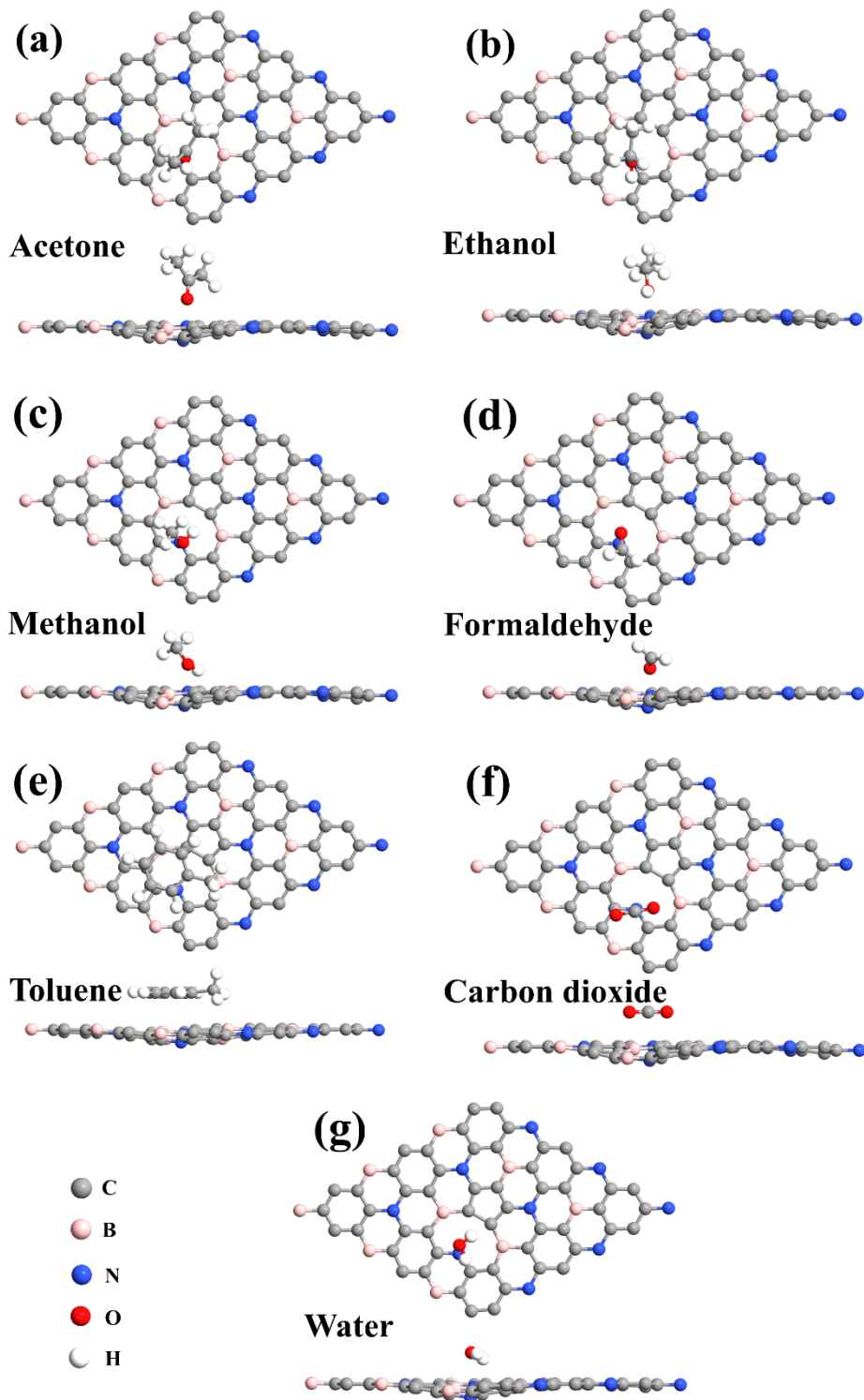


Figure 7-7. The most stable adsorption configurations (top and side view) for (a) acetone, (b) ethanol, (c) methanol, (d) formaldehyde, (e) toluene, (f) carbon dioxide, and (f) water molecules on defective BC₆N sheet.

Similar to the pristine BC₆N sheet, with increasing the coverage of VOCs from the same species and with co-adsorption of VOCs from various species on the defective BC₆N sheet, the absolute value of co-adsorption energies increase, implying that the sensitivity of the sensor is improved (see Figure 7-8). The most stable adsorption configurations of VOCs on the defective BC₆N sheets are provided in Figure 7-9.

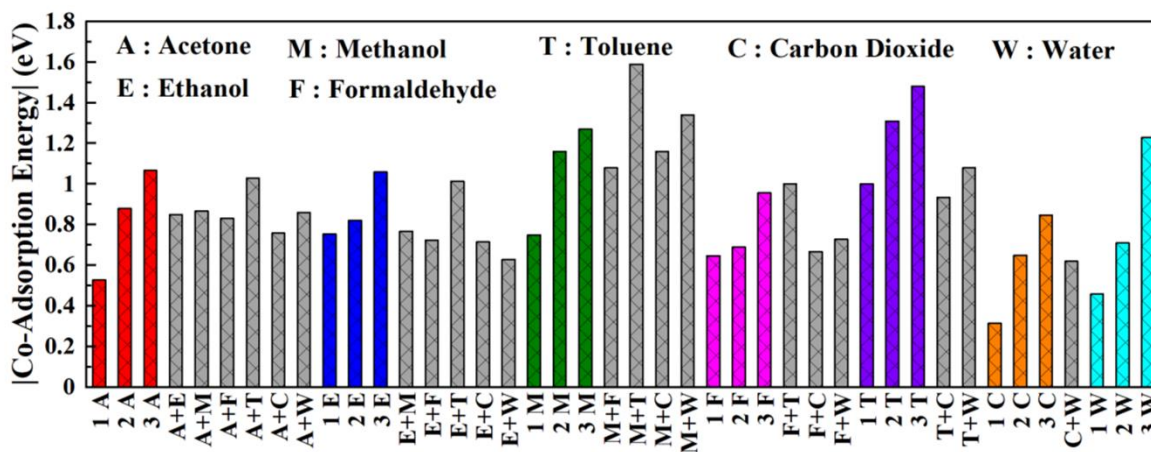


Figure 7-8. The co-adsorption energies of gas molecules on defective BC₆N sheet.

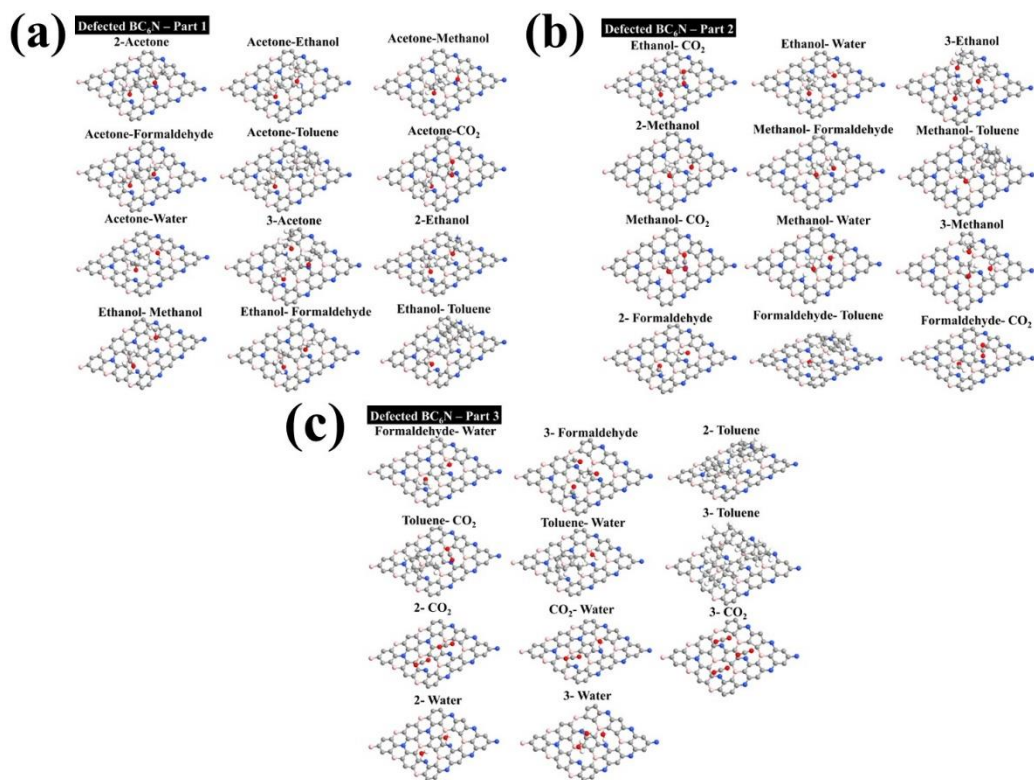


Figure 7-9. The relaxed structures of co-adsorbed gas molecules on defected BC_6N sheet.

To gain insight into the physisorption of gas molecules on the defective BC_6N , the electronic band structures and density of states (DOS) of all aforementioned configurations were calculated, see Figure 7-10 and Figure 7-11. In contrast to semiconducting pristine BC_6N , the defective BC_6N shows metallic behavior. Because of the increase in the local DOS at the Fermi energy level, which is spatially localized on the N dangling bond, the semiconductor to metal transition occurred. It should be noted that gas molecule's adsorption has almost no change in the energy bandgap of the defective BC_6N sheet. As can be seen in Figure 7-11, few or disappearance of the DOS of gas molecules around the Fermi level, confirming the weak interaction between them and defective BC_6N sheet through the physisorption process. However, the adsorbed VOCs contribute deeply to valence and conduction bands; hence, the gas molecules have no relevant influence on the electronic properties of the defective BC_6N around the Fermi level. This agrees well with the obtained small adsorption energies. Although the electronic properties of the semiconducting pristine BC_6N sheet and the metallic defective BC_6N sheet are not much impacted by the adsorption of VOCs, the charge transfer between the sheets and the VOCs during adsorption process could change the resistance of the system which can be experimentally measured.

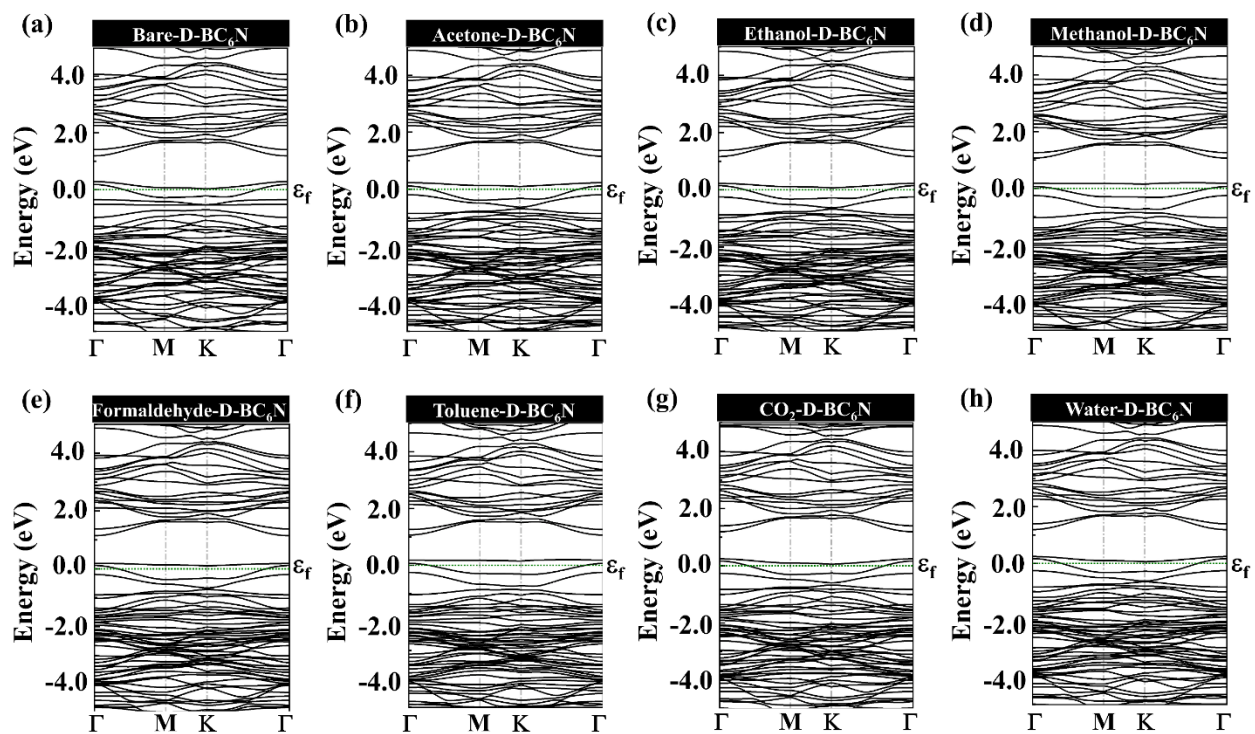


Figure 7-10. Energy band structures of (a) acetone, (b) ethanol, (c) methanol, (d) formaldehyde, (e) toluene, (f) carbon dioxide, and (f) water molecules on defective BC_6N sheet. The dotted green line indicates the Fermi level, which is set to zero.

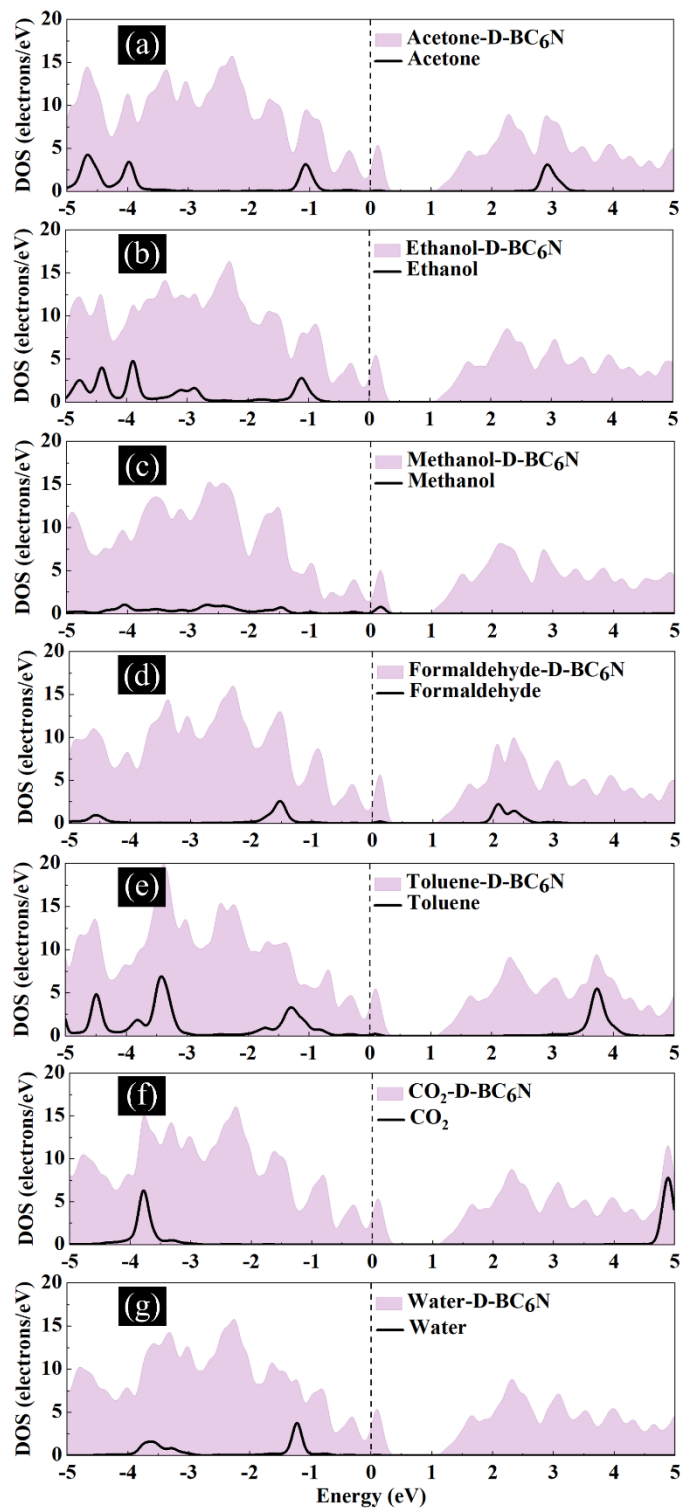


Figure 7-11. Total DOS curves for (a) acetone, (b) ethanol, (c) methanol, (d) formaldehyde, (e) toluene, (f) carbon dioxide, and (f) water molecules on defective BC_6N sheet. The dotted green line indicates the Fermi level, which is set to zero. The dashed lines indicate the Fermi level, which are set to zero.

To monitor the resistivity change of the metallic defective BC₆N, the transport transmission, and the corresponding $I-V$ characteristics of the sheet before and after gas molecules adsorption were calculated using Equation (2). Figure 7-12 (a) shows the geometry of the device configuration with two probes. The right and left electrodes are periodic in the transport direction (z -direction). The central region is seamlessly connected to the right and left electrodes. To screen out the perturbation inside the device in the sensing region, the electrode regions are extended into the central region, called screening regions. The size of the electrodes and central region were chosen to be $14.76 \text{ \AA} \times 8.52 \text{ \AA}$ and $14.76 \text{ \AA} \times 34.10 \text{ \AA}$, respectively. The $I-V$ curves of defective BC₆N device with and without the gas adsorption are presented in Figure 7-12 (b)-(h). By applying a bias to the device, the Fermi level of the left electrode shifts upward with respect to that of the right electrode. When the bias voltage surmounts the threshold voltage at which the conduction band minimum of the right electrode reaches the valence band maximum of the left electrode, the current starts to flow. As can be seen in Figure 7-12 (b), when the bias voltage is less than 0.6 V, no current passes through the bare defective BC₆N device. This value attributes to the energy bandgap of the confined defective BC₆N nanosheet with a width of 14.76 \AA . With increasing the bias voltage, the $I-V$ curve of the bare device presents a parabolic growth trend. The current passing through the bare defective BC₆N was $20 \mu\text{A}$ at 2 V. Introduction of gas molecules in the center of the scattering region caused little impact on the current tunneling through the energy band gaps, keeping the threshold voltage of the bare device almost unchanged after interaction with the gas molecules. The $I-V$ of the bare defective BC₆N slightly changed upon adsorption of acetone, indicating low sensitivity of the sensor for detection of the molecule. Despite the large adsorption energy for the toluene molecule, the conductivity of the sensor was hardly altered after interaction with toluene, proving that the evaluation of the sensor based on the adsorption energy is not enough for selecting a high-performance sensor. However, adsorption of ethanol, methanol, and formaldehyde gas molecules on the defective BC₆N bring about significant changes in the resistivity of the sensor for bias window between 0.8 to 1.6 V. The sensor sensitivity $(G_{TG} - G_B)/G_B \times 100$ was calculated, where G_B is the conductance of the bare defective BC₆N device, and G_{TG} is the conductance of defective BC₆N device in the presence of the target gas molecules. Table 7-2 lists the sensitivity (%) of the sensor toward various gas molecules at bias voltages of 1.0, 1.2, and 1.4 V. When 1.2 V bias voltage was applied to the sensor, 48.8%, 49.1%, and 47.0% sensitivities

were achieved for sensing ethanol, methanol, and formaldehyde, respectively. Interestingly, at 1.0 and 1.4 V, the sensor showed high sensitivities of 84.3% and 61.0%, respectively, toward ethanol along with low sensitivities toward other gas molecules, indicating that the sensor can selectively detect ethanol. Figure 7-13 (a) presents the sensitivities of defective BC₆N sheet (at a bias voltage of 1.4 V) and pristine BC₆N sheet toward various VOCs. The obtained sensitivities for defective BC₆N sheet toward ethanol are 4.15 times greater than those found for the pristine BC₆N sheet. To quantify the selectivity of the sensor for ethanol detection, the ratios of the sensitivity of ethanol to the sensitivity of other VOCs were calculated and presented in Figure 7-13 (b). The sensitivity ratios of ethanol to acetone, methanol, formaldehyde, toluene, CO₂, and water for defective BC₆N sheet as channel material are 35.8, 33.8, 3.9, 6.9, 23.4, and 25.4, respectively, suggesting that excellent selective detection of ethanol can be achieved. Although the adsorption energies of ethanol (−0.754 eV) and methanol (−0.750 eV) on defective BC₆N sheet are very close, one can see that the sensor with the defective BC₆N as channel material can detect ethanol with high sensitivity (61.0%) and selectivity ($S_{Ethanol}/S_{Methanol} = 33.8$). As a result, adsorption energy alone might not be a good predictor for the performance of the resistive gas sensor.

Table 7-3 compares the performance of the VOCs sensors based on various 2D materials. As can be seen, the interactions between VOCs and defective BC₆N sheet are stronger than those with other 2D materials such as graphene [244, 245], MoS₂ [248, 372], defected MoS₂ [248], MoSe₂ [249], phosphorene [235, 363, 373], defected phosphorene [235], germanane [374], silicene [247], and so on. However, the values of adsorption energies for VOCs on some materials like borophene [375], TiO₂ [376], and MXene (Ti₃C₂(OH)₂) [377] are higher than those on BC₆N sheets. Although ethanol binds to graphyne with an adsorption energy of −0.354 eV, the sensor experiences 222.2% energy bandgap changes after interaction with the molecule, proving that low adsorption energy does not necessarily lead to a low response [378]. Moreover, while ethanol is strongly chemisorbed on the borophene with an adsorption energy of −1.75 eV and causes 276.19% energy bandgap variation, the sensor suffers a very long recovery (~10¹⁷ sec at room temperature under UV), which hinders its application to be used as a reusable gas sensor. It is worth mentioning that the bandgap variation (%) in Table 3 was defined as $(E_{gG} - E_{gB})/E_{gG} \times 100$, where E_{gG} is the bandgap of the bare 2D material, and E_{gB} is the bandgap of the 2D material in presence of the target gas molecules [378]. Hence, the bandgap variation does not represent the sensitivity as we calculated in this work. Our proposed sensor based on the defective BC₆N sheet

indicates higher sensitivity toward ethanol in comparison with the black phosphorene-based sensor (9%) [235]. It should be added that the sensor exhibited low sensitivities toward carbon dioxide and water molecules, although the changes in current are more pronounced for the former molecule. This suggests that H₂O and CO₂ gas molecules, as interfering gases in exhaled breath cannot limit the detection of the target biomarkers. Overall, our findings suggest that defective BC₆N can be a compelling 2D material to achieve highly sensitive and selective chemiresistive VOC sensors with fast recovery for breath analysis applications.

Table 7-2. The sensitivity (%) of the sensor based on defective BC₆N with two electrodes toward acetone, ethanol, methanol, formaldehyde, toluene, carbon dioxide, and water molecules at bias voltages of 1.0, 1.2, and 1.4 V. Negative (positive) sensitivity means that the current of the sensor dropped (enhanced) after interaction with the gas molecule.

Target Gases Bias Voltage	Target Gases						
	Acetone	Ethanol	Methanol	Formaldehyde	Toluene	Carbon dioxide	Water
1.0 V	-10.6	-84.3	+5.0	+5.3	-9.0	-26.9	-9.5
1.2 V	-13.4	-48.8	-49.1	-47.0	-10.3	-19.9	-16.8
1.4 V	+1.7	-61.0	+1.8	-15.4	-8.8	-2.6	+2.4

Table 7-3. Theoretically reviewed 2D materials for VOCs sensing.

2D Sensing Materials	Analytes	Adsorption Energy (eV)	Sensor's Performance	Refs.
Graphene	Acetone, Ethanol, Methanol, Toluene	-0.36, -0.33, -0.21, -0.091	NR	[244, 245]
Graphdiyne	Acetone, Ethanol, Propanol, Toluene	-0.50, -0.52, -0.50, -0.40	NR	[379]
C ₂ N	Acetone, Ethanol, Propanol, Toluene	-0.25, -0.23, -0.28, -0.34	NR	[379]
Graphyne	Methanol, Ethanol	-0.345, -0.354	52.63%, 222.2% Bandgap variations	[378]
MoS ₂	Acetone, Ethanol, Propanol, Formaldehyde	-0.16, -0.22, -0.22, -0.11	NR	[248, 372]
SV-MoS ₂	Acetone, Ethanol, Propanol	-0.56, -0.66, -0.60	NR	[248]
MoSe ₂	Methanol, Ethanol	-0.522, -0.732	21.29%, 0% Bandgap variations	[249]
Black Phosphorene	Acetone, Ethanol, Toluene	-0.320, -0.214, -0.320	9% sensitivity for ethanol and 12.34 ns recovery time	[235]
Blue Phosphorene	Acetone, Ethanol, Propanol	-0.26, -0.20, -0.26	NR	[363]
SV-Blue Phosphorene	Acetone, Ethanol, Propanol	-0.53, -0.45, -0.51	NR	[363]
Green Phosphorene	Methanol, Ethanol	-0.393, -0.686	4.93%, 19.06% Bandgap variations	[373]
Borophene	Ethanol	-1.75	276.19% Bandgap variations	[375]
Germanane	Methanol	-0.703	0.52% Bandgap variations	[374]
Silicene	Formaldehyde	-0.087	NR	[247]
GeS	Acetone, Ethanol, Methanol	-0.509, -0.450, -0.379	NR	[380]
Ti ₃ C ₂ (OH) ₂	Acetone	-0.774	0.97% response at 100 ppm	[377]
TiO ₂	Acetone	-0.86	NR	[376]
BC ₆ N	Acetone, Ethanol, Methanol, Formaldehyde, Toluene	-0.381, -0.378, -0.316, -0.228, -0.910	6.1%, 14.7%, 9.5%, 14.7%, 14.7% Sensitivities	This work

D-BC ₆ N	Acetone, Ethanol, Methanol, Formaldehyde, Toluene	-0.527, -0.754, -0.750, -0.647, -1.00	1.7%, 61.0%, 1.8%, 15.4%, 8.8% Sensitivities Highly selective to Ethanol 740 μs, 4.9 s, 4.2 s, 77 ms, 6800 s recovery time	This work
---------------------	---	---	--	--------------

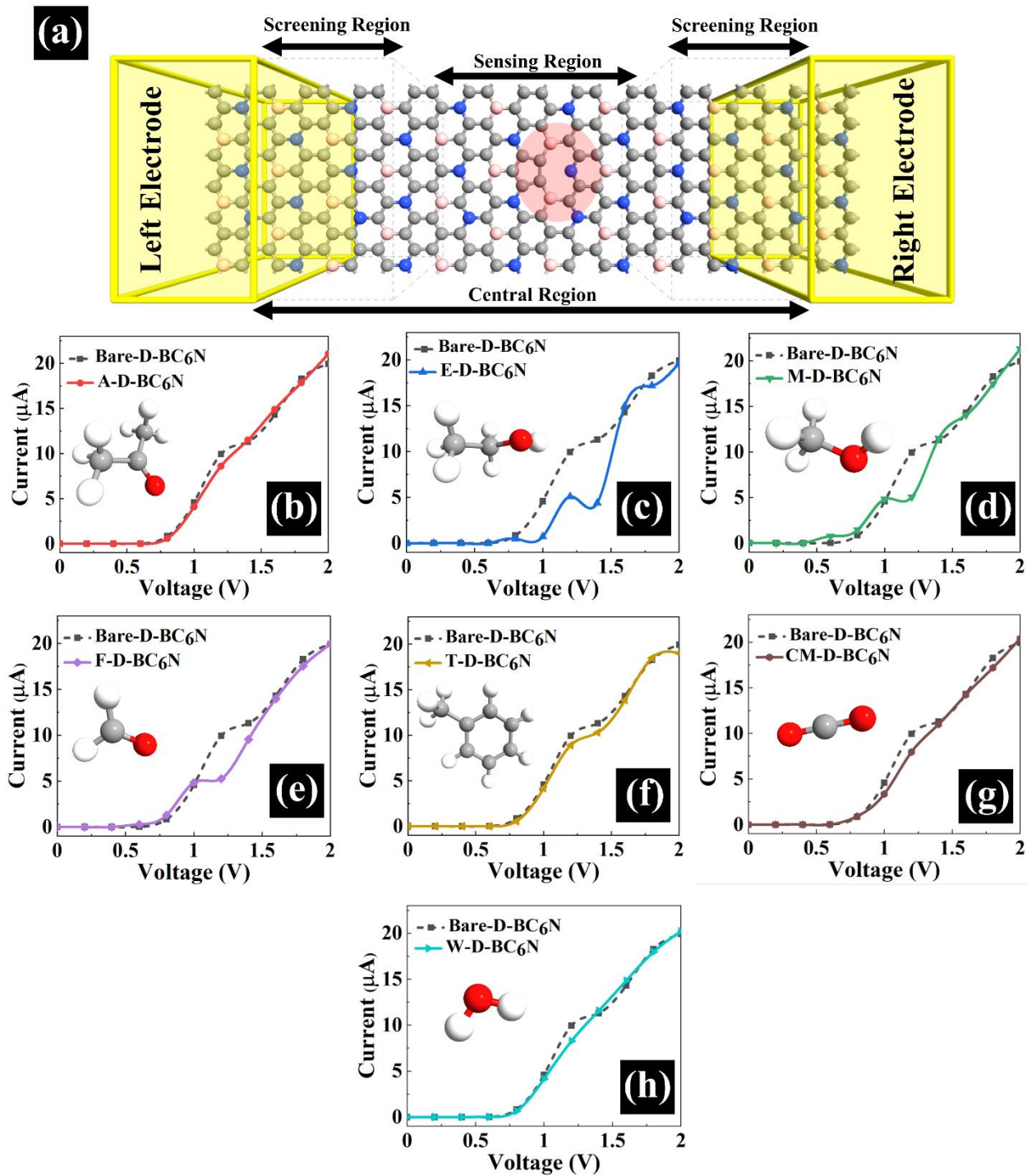


Figure 7-12. (a) Schematic structural model of a gas sensor based on defective BC₆N with two electrodes. I-V characteristics of BC₆N sensor after (b) acetone, (c) ethanol, (d) methanol, (e) formaldehyde, (f) toluene, (g) carbon dioxide, and (h) water molecules adsorption.

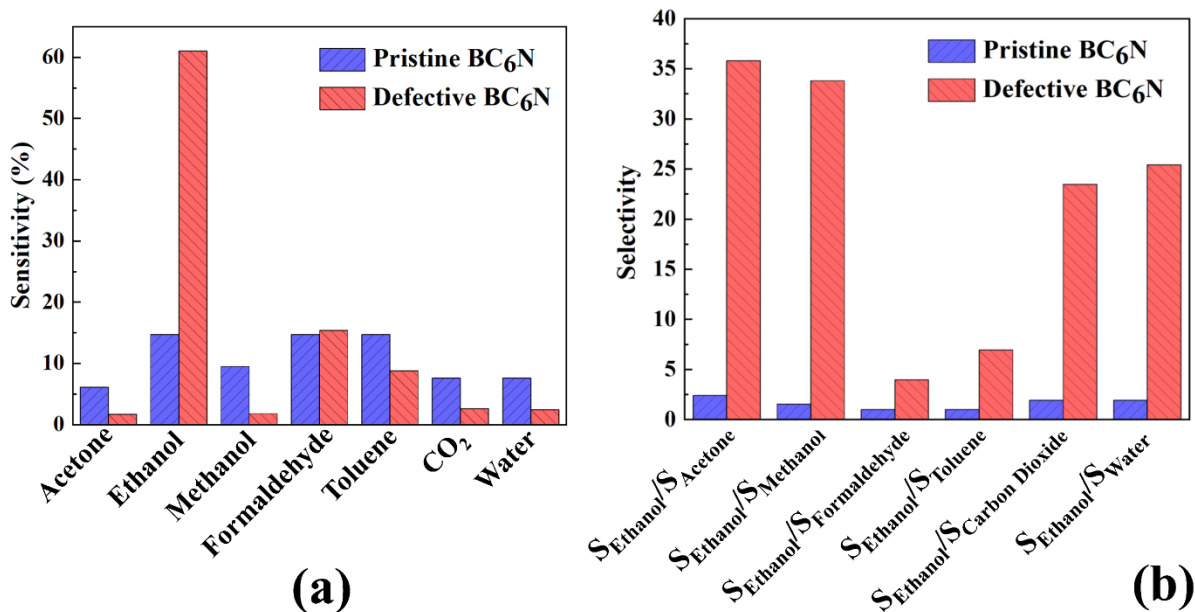


Figure 7-13. (a) Sensitivity of pristine and defective BC₆N sensor toward acetone, ethanol, methanol, formaldehyde, toluene, carbon dioxide, and water gas molecules. (b) The selectivity of pristine and defective BC₆N sensor for ethanol detection.

Summary

We investigated the adsorption of various gas molecules (acetone, ethanol, methanol, formaldehyde, toluene, carbon dioxide, and water) on the monolayer BC₆N sheet using first principles DFT calculations and inspected its potential for application in VOC sensors used in breath analysis. To this end, the adsorption sites, adsorption energies, charge transfer, and interaction distances were determined. We discovered that defective BC₆N exhibits considerable sensitivity toward the considered gas molecules. No noticeable changes were observed in the electronic properties of the pristine BC₆N after interaction with the gas molecules. It was disclosed that single vacancies, could appreciably enhance the adsorption energies of the gas molecules and the values of charge transfer. The $I-V$ characteristics of the defective BC₆N sheet were calculated before and after gas adsorption using the NEGF formalism. It was discovered that the sensor based on defective BC₆N shows high sensitivity and selectivity to ethanol in the presence of water

making it suitable for breath analysis of alcohols. The sensitivity of the sensor was not restricted by the interfering gases, such as H₂O and CO₂ gas molecules in exhaled breath. The recovery time of the VOC sensor was found to be very short. Therefore, our findings suggest that defective BC₆N is a potential material for detection of different biomarkers in human breath.

8. Chapter 8

Theoretical Study on Novel 2D Materials

Phosphochalcogenide, (PdPSe, and PdPS)-Inorganic Gas

Molecules

In recent years there exist considerable and ongoing demands for tracing gas molecules for the purpose of environmental monitoring, public health, and early disease diagnosis. Two-dimensional (2D) materials, owing to their large active area and appealing electrical, optical, and mechanical characteristics, are highly promising candidates for designing advanced next-generation gas sensors. Motivated by the latest experimental advance in the fabrication of palladium phosphide selenium (PdPSe), in this work we explore PdPS and PdPSe monolayers as novel platforms for the detection of harmful gas molecules including CO, CO₂, NH₃, NO, and NO₂. Herein, we utilized first-principles density functional theory calculations to investigate the adsorption behavior of hazardous gases on the PdPS/PdPSe-based sensor. We firstly found that the PdPS and PdPSe monolayers are semiconductors with appealing bandgaps. Next, we systematically assessed the most favorable adsorption configurations and examined the electronic properties of gas-adsorbed PdPS/PdPSe monolayers. It was manifested that CO, CO₂, and NH₃ gas molecules are physisorbed on the PdPS, and PdPSe, while upon adsorption of NO, and NO₂, the band gap changed significantly, especially for NO₂, the PdPS/PdPSe sensor undergoes a semiconductor to metal transition. It was moreover realized that after adsorption of NO, and NO₂, respectively, over PdPS energies of 0.98, 1.01 eV are released, and over PdPSe energies of 1.12, and 1.21 eV are emitted. According to calculated recovery time, the PdPS platform yields a quick recovery after exposure to NO, and NO₂ with times of 4.33 and 11.9 s, respectively, at room temperature and under UV light. PdPSe nonetheless exhibits a recovery time of 1.74 s at 498 K and under visible light after interaction with NO₂. Our study results suggest PdPS, and PdPSe platforms are eminently promising for detecting NO₂ molecule.

8.1 Overview

In recent years, the environment, global biological ecosystems, and human health have been threatened by the continuous production of air pollutants [381-384]. The typical gaseous pollutants are carbon dioxide, ammonia, and nitrogen dioxide arising from fossil fuel burning and industrial activities [385]. Among main pollutant gases, nitrogen oxides, such as NO and NO₂, carbon oxides such as CO, and CO₂ along with NH₃ are important [240, 386-388]. Additionally, they can cause severe damage to the respiratory system, for example, NO₂, and CO is considered as one of the suffocating agents for humans and can decrease lung function [389, 390]. Hence, the monitoring, detection, and elimination of these harmful gases are of great interest due to their environmental, public health, and economic relevance. Since the emergence of graphene as the first two-dimensional (2D) nanomaterials, they have been increasingly receiving interest toward 2D materials due to their exceptional properties, such as high surface area, strong surface activities, low cost, and fascinating transport properties [215, 391, 392]. Moreover, because of outstanding structural and electrical properties, 2D materials are highly appealing for numerous advanced and critical applications, such as nanoelectronics, optoelectronics, catalysis and gas sensors [393]. In this regard, various 2D nanomaterials have been studied so far for gas sensing applications, such as graphene [39, 394], silicene [395], germanene [396, 397], black phosphorene [182], green phosphorene, boron nitride [398], and borocarbonitride (BC₆N) [222, 232].

To date, extensive researches have been conducted on the gas sensing application of 2D materials, like using graphene towards toxic gaseous species (such as CO₂, CO, NO₂, NH₃) [39], nonetheless, bare graphene shows low sensitivity toward the studied toxic gases. In addition, sensing performance of transition-metal dichalcogenides like MoSe₂ and MoTe₂ toward NO, NO₂, and NH₃ gas molecules have been investigated [399], but it was reported aforementioned pristine sheets are not sensitive to the small gas molecules and they were weakly adsorbed. Furthermore, silicene was used as a platform for the detection of NO, NO₂, NH₃, and CO gases [395]. Based on density functional theory (DFT) and nonequilibrium Green's function method, the structural configurations, adsorption sites, adsorption energies, and charge transfer of all studied gas molecules on the silicene nanosensors were systematically discussed. However, it was seen that pristine silicene is not sensitive enough to the considered gases. By the same token, the adsorption behavior of common gases such as CO, CO₂, NH₃, NO, and NO₂ molecules on germanene was investigated by the density functional theory method [397], and it was found that they were weakly

adsorbed on the germanene. In another study, the adsorption of NO, NO₂, CO, and NH₃ molecules on black phosphorene have been investigated [227]. It was found that the adsorption was improved but there are still not sufficient practical values, and CO, and NH₃ molecules were weakly adsorbed. The physisorption of common gas molecules on the studied materials limits their immediate potential for gas sensing.

Following the latest advances in the synthesis of phosphochalcogenides PdPX (X = S, Se) [400, 401] nanosheets, they have attracted enormous attentions and they have been used as a semiconductor for photocatalysts water splitting [402, 403]. The stability of the palladium phosphide sulfide (PdPS) monolayer was confirmed by calculating phonon band dispersions [403] and it yields multiple active sites for hydrogen evolution reaction. Very recently, penta-PdPSe, a novel 2D pentagonal material with a novel low-symmetry orthorhombic structure, was introduced to the 2D family [404], it is also exhibited high anisotropic optical, electronic, and optoelectronic properties. Moreover, noble PdPS was synthesized lately by the method of chemical vapor transition (CVT) and used for polarized detection application [405] and it showed superior optoelectrical properties. As novel experimentally realized 2D systems, it is an important question, whether these nanosheets can be employed as efficient nanosensors for common harmful gas molecules, such as CO, CO₂, NH₃, NO, and NO₂, which are all of great practical interest for medical, and environmental applications, on the PdPS and PdPSe nanosheets. Therefore, the objective of the present is to conduct a systematic and comprehensive investigation gas sensing performance of PdPS and PdPSe monolayers for the above-mentioned gases by employing first-principles DFT calculations.

8.2 Computational Method

All first-principles calculations were performed employing Atomistix ToolKit (ATK) package, using DFT method [153, 154]. The generalized gradient approximation (GGA) with the Perdew-Burke-Ernzerhof (PBE) exchange–correlation functional was also employed. In order to describe the long-range vdW interactions, the Grimme van der Waals (vdW) correction (PBE-D3) was adopted [157]. For the purpose of evaluation of the adsorption stability and interaction between the gas molecules and the PdPS/PdPSe sheet, their adsorption energy (E_{ad}) was defined as:

$$E_{ad} = E_{PdPS/PdPSe+X} - (E_X + E_{PdPS/PdPSe}) \quad (22)$$

where $E_{(PdPS/PdPSe+X)}$ is the total energy of the molecule adsorbed on the PdPS/PdPSe surface, and $E_{(X)}$ and $E_{(PdPS/PdPSe)}$ are the energies of the corresponding molecule and single PdPS/PdPSe monolayer. In this calculation, negative adsorption energy represents that the interaction is exothermic and energetically favorable. Furthermore, the electronic temperature and the energy mesh cut-off to be 300°K and 45 Hartree were set, respectively. The Fritz Haber Institute (FHI) pseudopotentials with a double-zeta basis set were used. The primitive Brillouin zone was sampled using $5 \times 5 \times 1$ special k -points under the Monkhorst-Pack scheme for optimization and $6 \times 6 \times 1$ k -points for electronic calculations. To eradicate the interaction between adjacent periodic sections a sufficiently large vacuum space of 20 Å in the z direction was considered. Moreover, in optimization, the convergence tolerances of force and stress on each atom were selected to be less than 0.01, and 0.001 eV/Å, respectively. Charge transfer (Q) upon adsorption of the gas molecule on the PdPS/PdPSe sheets was analyzed employing Hartwigsen–Goedecker–Hutter (HGH) pseudopotentials with Tier 5 basis set. It is worth mentioning that the negative values of charge specify a charge transfer from molecule to the PdPS/PdPSe sheets. Dynamical stability was also investigated using phonon band structure calculations.

Generally, a gas detection device can be divided into three regions to explore its transport properties, the central (scattering) region, left, and right leads (electrodes), as depicted in Figure 8-1 (b, e). The conductance of the sensor is related to the transmission coefficient at the Fermi level and can be defined as:

$$C(\epsilon) = G_0 T(\epsilon) \quad (23)$$

Here, $G_0 = 2e^2/h$ is the quantum conductance, $T(\epsilon)$, e , and h is the electron transmission coefficient, electron charge and Planck's constant, respectively. $T(\epsilon)$ can be defined as below from the Green's function:

$$T(\epsilon) = \Gamma_L(\epsilon) G(\epsilon) \Gamma_R(\epsilon) G^\dagger(\epsilon) \quad (24)$$

In this equation, $\Gamma_{L,R}(\epsilon) = (\sum_{L(R)}(\epsilon) - (\sum_{L(R)}(\epsilon))^\dagger) / i$, in which $\Gamma_{L,R}$ is the broadening function of left (right) lead. $\sum_{L(R)}(\epsilon)$ is the lead self-energy of the left (right) lead.

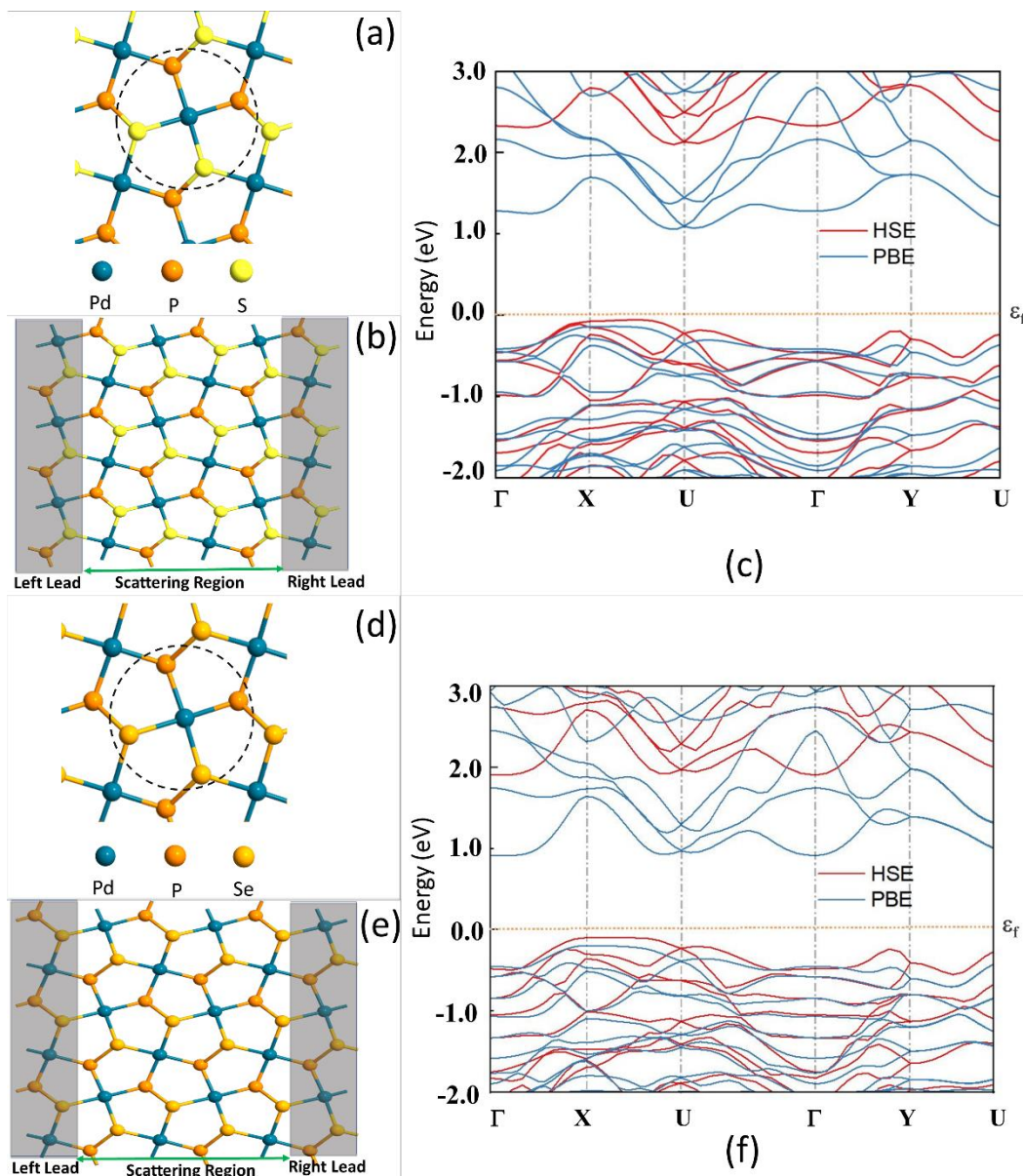


Figure 8-1. (a) Bonds between Pd, P, and S atoms. (b) Schematic of PdPS-based gas device (c) Electronic Band structure of PdPS unit cell by PBE, and HSE calculations. (d) Bonds between Pd, P, and Se atoms. (e) Schematic of PdPSe-based gas device (f) Electronic Band structure of PdPSe unit cell by PBE, and HSE calculations.

8.3 First-principles calculations using density functional theory:

PdPS, and PdPSe monolayers exhibit orthorhombic configurations and each Pd atom is in square-planar coordination, surrounded by two sulfur (two selenium for PdPSe) and two phosphorus atoms (Figure 8-1 (a, d)). The rectangular in-plane lattice parameters were found to be 5.65, and 5.69 Å and 5.84, and 5.89 Å for PdPS and PdPSe monolayers, respectively, in close agreement with previous experimental and theoretical reports [403, 404]. It needs to be mentioned that the sizes of $17.07 \times 17.16 \times 20$ Å, and $17.52 \times 17.69 \times 20$ Å were selected for PdPS, and PdPSe sheets, respectively. Moreover, as shown in Fig. 1 for the unit cells of PdPS, and PdPSe monolayers the electronic band structures were calculated, and the energy band gap of 1.196, and 1.107 eV (by the PBE approach) was achieved, respectively. Additionally, the energy band gap of 2.15, and 2 eV was found by the Heyd-Scuseria-Ernzerhof (HSE) approach for PdPS, and PdPSe, respectively, which the band gaps are in good agreement with literature data [402, 406]. It is worth mentioning that the dynamic stability of both structures (PdPS, and PdPSe) was examined using phonon spectrum calculation (Figure 8-2), and it was found that they both have dynamic stability.

The side and top views of the optimized PdPS, and PdPSe monolayers are illustrated in Figure 8-3 (a, c). The partial density of states (DOS) was calculated for PdPS, and PdPSe monolayers as shown in Figure 8-3. As it was shown in Figure 8-3 (b, d), the *d* orbital of Pd atom overlapped with *p* orbital of S (Se), and *s* orbital of P atoms, which indicates that there are strong bonds between the atoms within the monolayer and the *d* orbital of Pd is the main contribution to conduction band minimum (CBM) and valence band maximum (VBM).

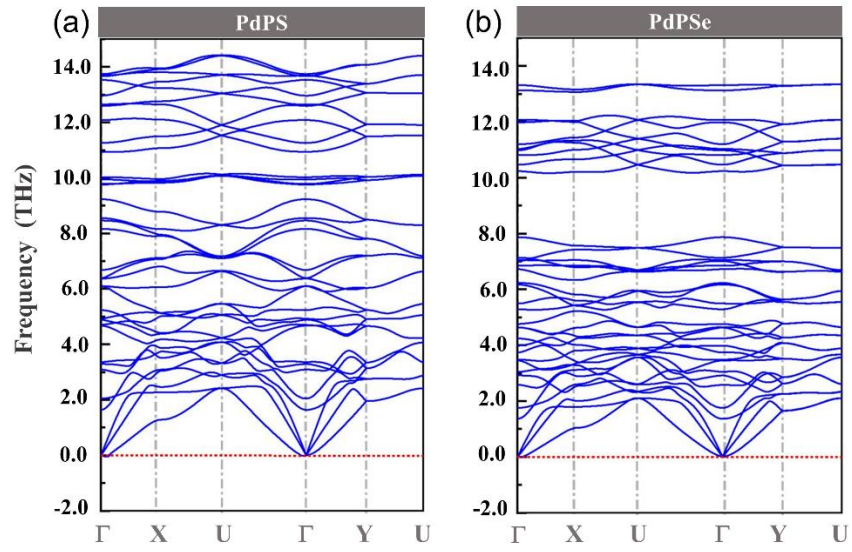


Figure 8-2. Phonon band structure for (a) PdPS, and (b) PdPSe monolayers

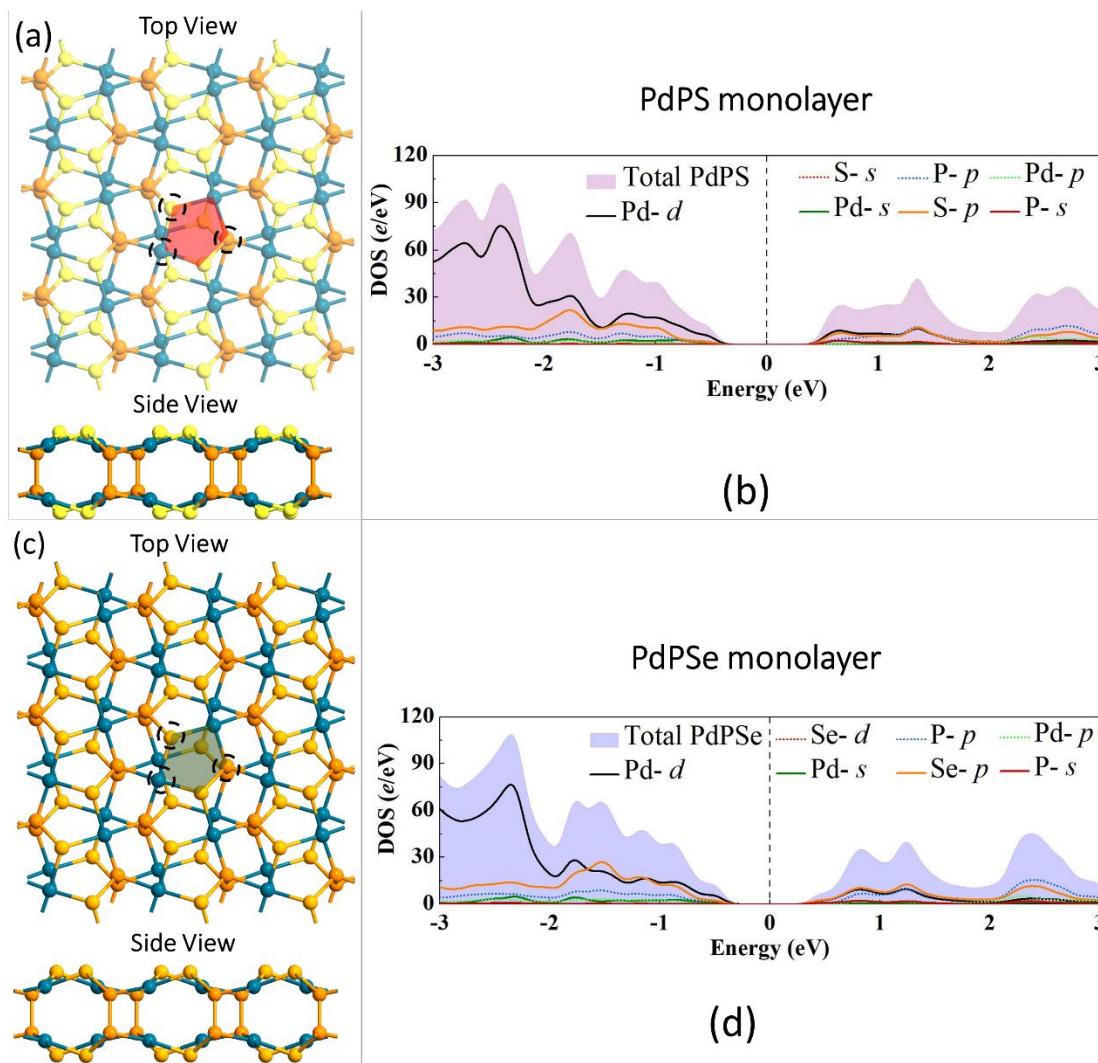


Figure 8-3. (a) Optimized structure of PdPS-based gas device in both view (side and top) along with possible adsorption sites on the surface (b) DOS of the PdPS monolayer (c) Optimized structure of PdPSe-based gas device in both view (side and top) along with possible adsorption sites on the surface (d) DOS of the PdPSe monolayer.

Next, we shift our attention to study the adsorption of CO, CO₂, NH₃, NO, and NO₂ gas molecules over PdPS, and PdPSe monolayers. Due to fact that the molecules tend to be adsorbed in various configurations, different sites on the PdPS/PdPSe should be taken into account. Different possible sites for adsorption were considered as highlighted in Figure 8-3 (a, c) including the top of Pd, P, and S (Se) atoms and the center of the Pd-P-S (Pd-P-Se) ring. Thus, the gas molecules were placed at a distance of 2 Å over the assumed sites with several molecular

orientations. For CO and NO diatomic molecules, they can be placed in perpendicular directions with respect to the surface, in which both N/C, and O atoms can be pointed toward the surface of PdPS, and PdPSe. Moreover, CO₂, and NO₂ as triatomic molecules, and NH₃ as the tetraatomic molecules can be placed in a way that the O atoms of CO₂, and NO₂, and H atom of NH₃ pointed down or up with respect to the PdPS, and PdPSe surfaces. Accordingly, the most relaxed configurations of the gas molecules on the PdPS, and PdPSe sheets were predicted and are also illustrated in Figure 8-4, and Figure 8-5, respectively. All the structures were allowed to reach energy minimized configuration based on their original configurations, and the lowest adsorption energy configurations were defined. The adsorption energy of -0.769 , -0.639 , -0.863 , -0.984 , and -1.01 eV was achieved for CO, CO₂, NH₃, NO, and NO₂ gas molecules upon PdPS monolayer, respectively. In case of CO, and NO molecules, they both tilted a little from vertical orientation with respect to the PdPS surface. CO adsorbed with its C atom pointed to the Pd atom of the sheet with a minimum distance of 2.52 \AA (C-Pd), also NO adsorbed in the same orientation, its N atom pointed to the Pd atom with a minimum distance of 2.51 \AA (N-Pd). CO₂ molecule however adsorbed approximately horizontally with respect to the surface of the PdPS monolayer, in which there is a minimum distance of 3.16 \AA between the O atom and S atom (O-S) of the substrate. The NH₃ molecule nonetheless presents a more complicated adsorption mechanism than the previous molecules, in a way that it prefers to adsorb horizontally in a way that N atom is pointed toward the surface. In this case, it was found that there is a minimum distance of 2.66 \AA between the H atom and S atom (H-S) of the monolayer. Last but not least we examine the adsorption of NO₂ molecule. After the energy minimization, it was observed that the N atom pointed down toward the substrate surface, with a 2.5 \AA between N, and Pd atoms (N-Pd). Additionally, the adsorption energies of -0.57 , -0.53 , -0.54 , -1.12 , and -1.21 eV were measured for CO, CO₂, NH₃, NO, and NO₂ gas molecules over PdPSe surface, respectively. Herein, for CO, and NO molecules, they adopt the same adsorption behavior as adsorption upon PdPS, there is a minimum distance of 3.20 \AA (C-Se), and 2.30 \AA (N-Pd) for CO, and NO, respectively.

In case of CO₂, and NO₂, they both showed similar adsorption expression and there are minimum distances between O atom of CO₂, and Se atom (O-Se) with an amount of 3.40 \AA , and for NO₂, there is 2.37 \AA minimum distance between N, and Pd atoms (N-Pd). Nonetheless, the NH₃ molecule adsorbed horizontally in a way that its N atom pointed up, it was found that there is a minimum distance of 2.97 \AA between the H atom and Se atom (H-Se) of the sheet. Additionally,

atomic radii for S, Se, Pd, P, O, C, N, and H atoms are 0.88, 1.03, 1.69, 1.07, 0.48, 0.67, 0.56, and 0.53 Å, respectively [210]. So, the sums of the atomic radii for C-Pd, N-Pd, O-S, and H-S, are 2.36, 2.25, 1.36, and 1.41 Å, respectively for PdPS adsorption with the molecules. Also, for PdPSe monolayer, there are sums of the atomic radii of 1.7, 2.25, 1.51, and 1.56 Å for C-Se, N-Pd, O-Se, and H-Se, respectively. Henceforth, it is evident that for CO, CO₂, and NH₃ the sums of corresponding atomic radii are much less than the corresponding obtained minimum distance between atoms, offering that they were physisorbed. However, the sums of corresponding atomic radii for NO, and NO₂ are indeed close to the corresponding calculated minimum distances, recommending that the adsorption between NO, and NO₂ could be considered as chemisorption.

To enhance the understanding of the effects of gas molecules adsorption, the electronic band structure and band gaps for the configurations were explored as illustrated in Figure 8-4 and Figure 8-5 for each considered gas over PdPS and PdPSe monolayers, respectively. The energy band gap of PdPS (1.196 eV) decreases to 1.082, 1.057, and 1.055 eV upon interaction with CO, CO₂, and NH₃, respectively, equivalent with only 9.5, 11.6, and 11.7% band gap alteration (ΔE_g) after the interaction. For the cases of NO, and NO₂ molecules adsorption on the PdPS sheet, the band gap alteration becomes interestingly considerable. From Figure 8-4 (i) can be noticed that there is a drastic band gap change after NO adsorption (with an amount of 0.02 eV), and it can be perceived that the Fermi level shifted to the conduction band, and it shows n-type semiconducting behavior. Furthermore, from Figure 8-4 (j) can be seen that there is a flat band on the Fermi level, suggesting that NO₂-PdPS complex has metallic behavior.

In general, because of close atomic and electronic properties the adsorption of the considered gas molecules over PdPSe monolayer show similar behavior as PdPS counterpart. In this case, changes of 24.8, 25.4, and 25.8 % occur in band gap for the adsorption of CO, CO₂, and NH₃, respectively. Moreover, we predicted the same drastic decrease in band gap alteration in PdPSe monolayer (1.107 eV) after NO adsorption (0.06 eV). Analogous to PdPS, after NO₂ adsorption on PdPSe, the energy band gap decreased noticeably to 0 eV as it is obvious from Figure 8-5 (j), suggesting that NO₂-PdPSe shows the metallic behavior. To shed light on the adsorption process of the gases upon the PdPS-/PdPSe-based sensor, the net total charge transfer was studied and calculated. Based on the calculations, CO, CO₂, NH₃, and NO gas molecules donate a net charge of 0.158, 0.036, 0.102, 0.196 *e* to the PdPS sheet, respectively. In contrast, after the adsorption of NO₂, it withdraws a net charge of 0.015 *e* from the PdPS sheet. Regarding the PdPSe sheet, CO₂, NH₃,

and NO molecules give electrons to the surface with a net charge of 0.004, 0.103, 0.121 e , but, for CO molecule, it acts as an electron acceptor with a negligible net charge of 0.001 e . When it comes to NO₂ adsorption, there is a large charge transferring with an amount of 0.145 e that is transmitted from the PdPSe surface to the molecule.

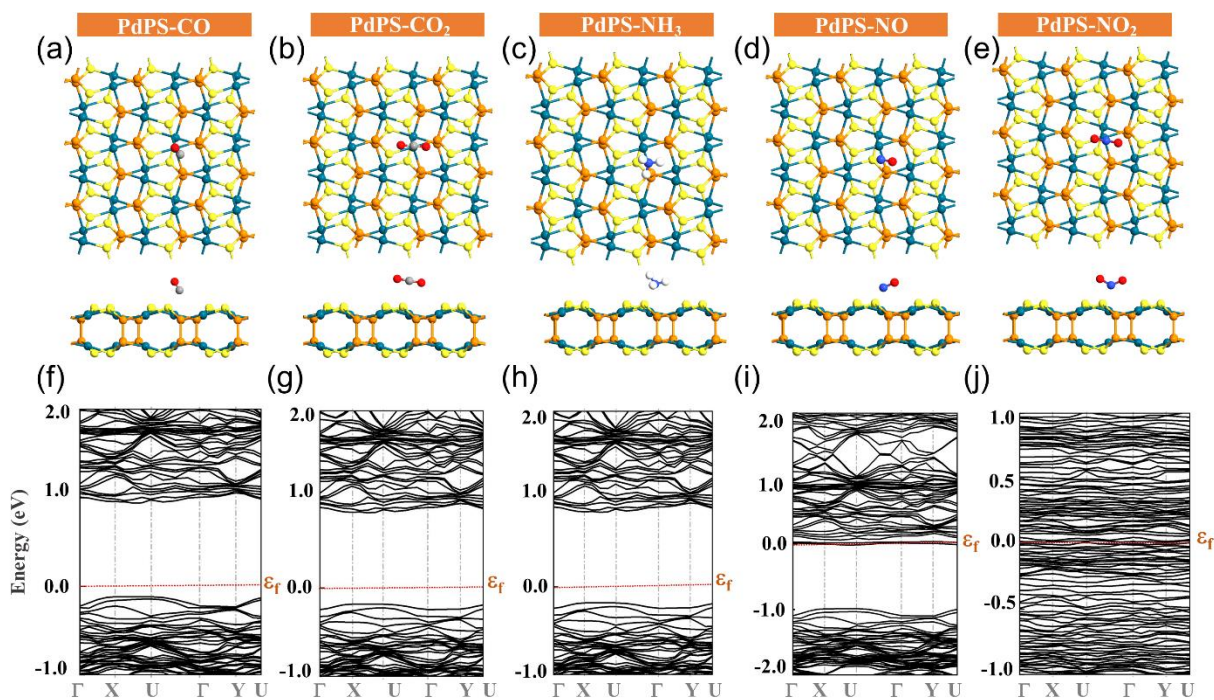


Figure 8-4. The most stable adsorption configurations (top and side view) for CO, CO₂, NH₃, NO, and NO₂ gas molecules adsorption on the PdPS along with their corresponding electronic band structure.

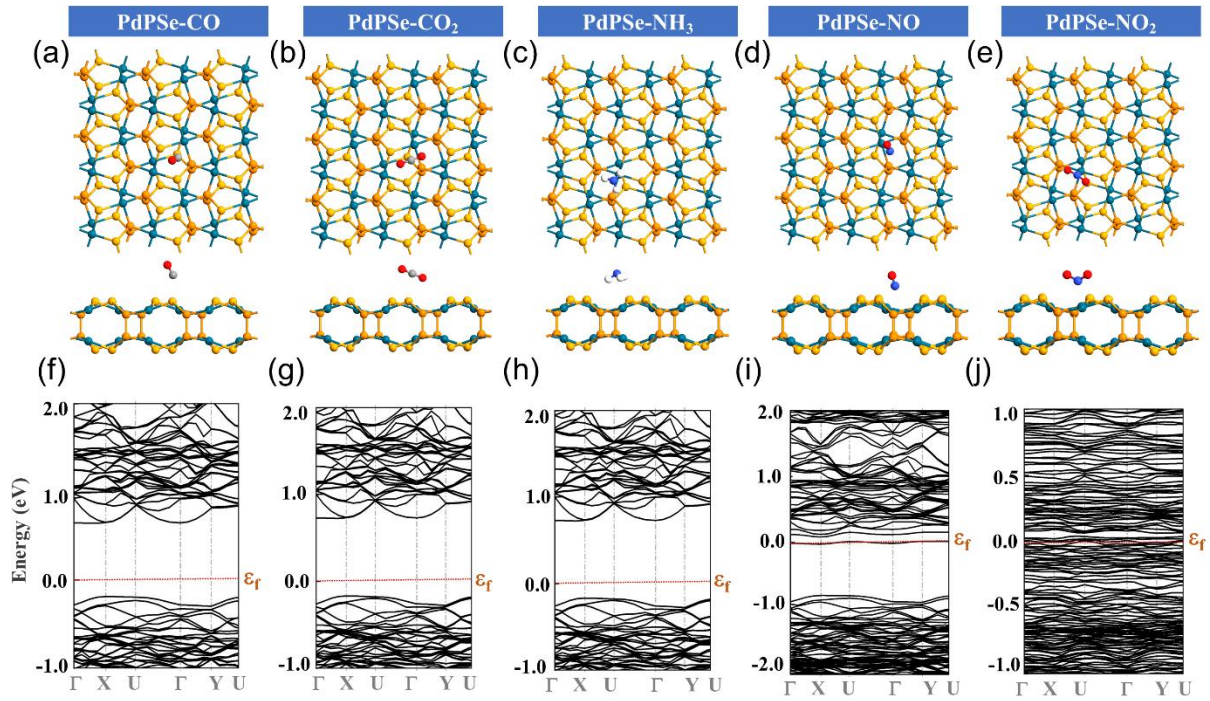


Figure 8-5. The most stable adsorption configurations (top and side view) for CO, CO₂, NH₃, NO, and NO₂ gas molecules adsorption on the PdPSe along with their corresponding electronic band structure.

One critical parameter for the assessment of the gas sensors is their ability to rapidly recover after exposure to the gas molecule. According to the conventional transition state theory and Van't-Hoff-Arrhenius expression [211], recovery time (τ) is an important factor for performance evaluation as defined follow:

$$\tau = A^{-1} e^{(-E_{ad}/KBT)} \quad (4)$$

Here A is the attempt frequency, T is temperature and K_B is the constant of Boltzmann (8.318×10^{-3} kJ/(mol·K)). It is noteworthy that attempt frequency (A) is 10^{12} , and 10^{16} Hz for visible and UV light conditions, respectively. and Two different temperatures (298, and 498 K) and lights (visible and UV) [232] were opted to calculate τ of the PdPS, and PdPSe monolayers for the gas molecules as detailed in Table 8-1. Regarding the equation, the τ of gas desorption is proportional to adsorption energy and inversely proportional to temperature. Nevertheless, for the case of PdPS monolayer, it was found that at 298 k and under visible light, CO was desorbed from the surface with the recovery time of 10.3 s, and the τ for NH₃ detection was obtained 389.53 s, but for other gas molecules, the recovery time is either short or long (0.0636 , $4.33 \times 10^{+4}$, and $1.19 \times 10^{+5}$ s for

CO₂, NO, and NO₂). It was noticed that with the same condition (298 k and visible light), PdPSe exhibits recovery time, τ of 0.0043, 9.13×10^{-4} , 0.0013, $8.62 \times 10^{+6}$, and $2.86 \times 10^{+8}$ s for CO, NH₃, CO₂, NO, and NO₂ molecules, respectively. It is worth mentioning that gas sensors in real experiments should hold and detect the gas within a reasonable time, not too short, or long [5, 243, 407]. Interestingly, the recovery time for NO, and NO₂ adsorption were found to be 4.33, and 11.9 s under UV light and at 298 k, which are acceptably short. Besides, the τ of 0.21, and 1.74 s were calculated for NO, and NO₂ gases at 498 k, respectively, under the visible light. These results highlight that PdPS and PdPSe nanosheets are appealing gas sensors with quick recovery times, particularly for sensing of NO, and NO₂ molecules.

Table 8-1. The calculated adsorption energy (E_{ad}), interaction distance (D), which is the distance between the molecule and the PdPS/ PdPSe sheets, charge transfer (Q), the negative values of charge indicate a charge transfer from the molecule to the nanotube, energy bandgap (E_g), and recovery time (τ).

System	E_{ad} (eV)	D (Å)	Q (e)	E_g (eV)	τ @ T=298 K (visible light)	τ @ T=498 K (visible light)	τ @ T=298 K (UV light)
PdPS	-	-	-	1.196	-	-	-
PdPS- CO	-0.769	2.52	-0.158	1.082	10.3	6.02×10^{-5}	0.001
PdPS- CO ₂	-0.639	3.16	-0.036	1.057	0.0636	2.91×10^{-6}	6.3×10^{-6}
PdPS- NH ₃	-0.863	2.66	-0.102	1.055	389.5356	5.38×10^{-4}	0.039
PdPS- NO	-0.984	2.51	-0.196	0.02	$4.33 \times 10^{+4}$	0.009	4.33
PdPS- NO ₂	-1.01	2.5	0.015	0	$1.19 \times 10^{+5}$	0.016	11.9
PdPSe	-	-	-	1.107	-	-	-
PdPSe -CO	-0.57	3.20	0.001	0.832	0.0043	5.84×10^{-7}	4.33×10^{-7}
PdPSe -CO ₂	-0.53	3.40	-0.004	0.825	9.13×10^{-4}	2.3×10^{-7}	9.13×10^{-8}
PdPSe- NH ₃	-0.54	2.97	-0.103	0.821	0.0013	2.9×10^{-7}	1.34×10^{-7}
PdPSe- NO	-1.12	2.30	-0.121	0.06	$8.62 \times 10^{+6}$	0.21	862.16
PdPSe- NO ₂	-1.21	2.37	0.145	0	$2.86 \times 10^{+8}$	1.74	$2.86 \times 10^{+4}$

In order to track the adsorption mechanism, the projected DOS (PDOS) of the gases on the PdPS, and PdPSe surfaces was studied and displayed in Figure 8-6, and Figure 8-7. It was revealed that after adsorption of CO, CO₂, and NH₃, no orbital hybridization happened between the molecule and the surface, which means that there is no strong adsorption. Nonetheless, after adsorption of NO, and NO₂ on both PdPS, and PdPSe, there is a peak in the vicinity of the Fermi level, indicating that electronic properties of the PdPS, and PdPSe sensor have been changed as spotted with red, and green arrows, respectively. Specifically, after adsorption of NO₂, a peak at Fermi level appeared meaning that there is a considerable alteration in electronic properties of the device, and the sensor transformed from semiconductor to metallic. These discoveries justified the results from the band structure calculation for the gas molecules.

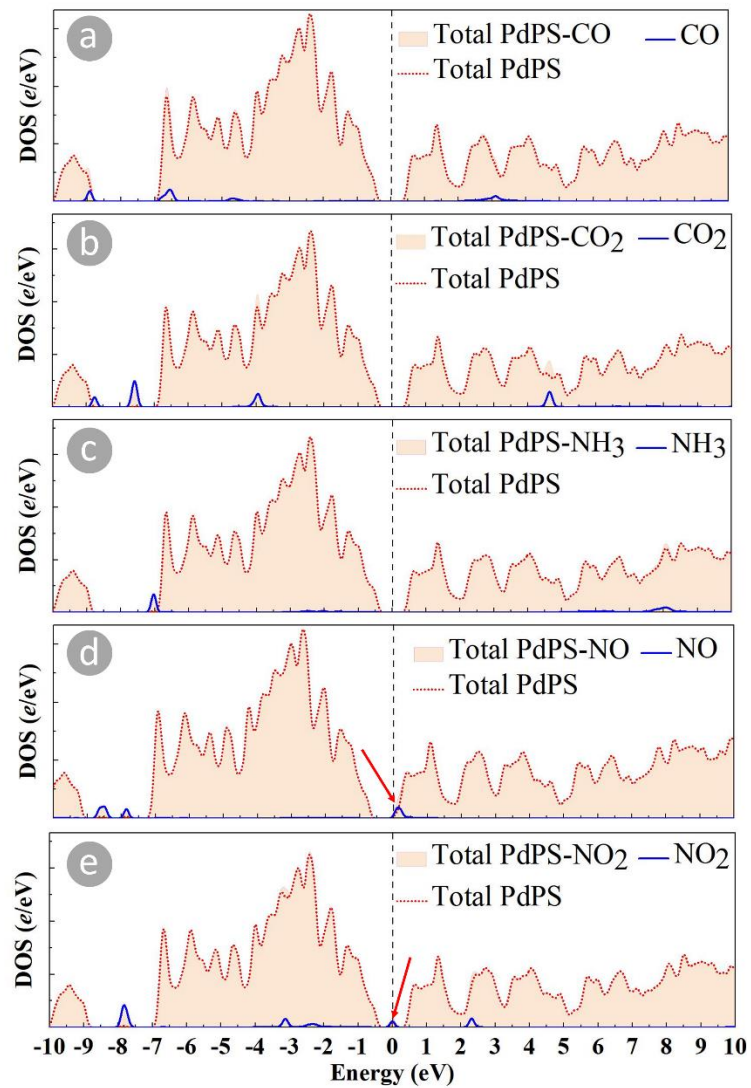


Figure 8-6. Density of states (DOS) for adsorption of (a) CO, (b) CO₂, (c) NH₃, (d) NO, and (e) NO₂ gas molecules upon PdPS monolayer.

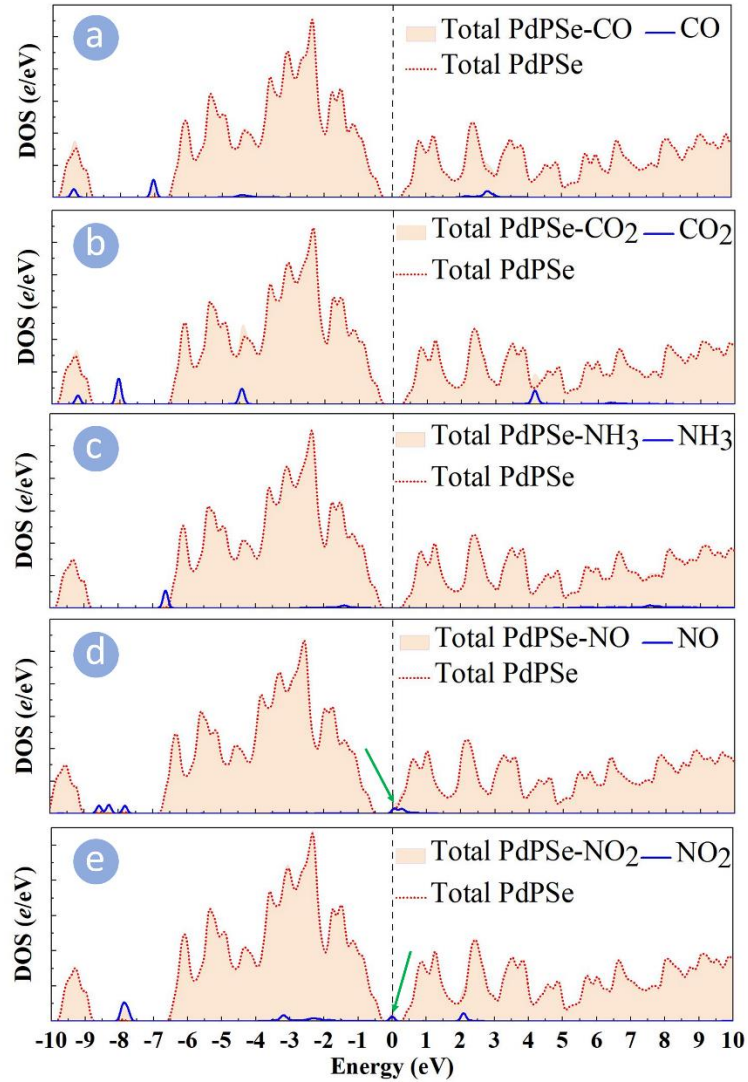


Figure 8-7. Density of states (DOS) for adsorption of (a) CO, (b) CO₂, (c) NH₃, (d) NO, and (e) NO₂ gas molecules upon PdPSe monolayer.

Eventually, to investigate the adsorption of gases on the conductance of the PdPS, and PdPSe the quantum conductance of the PdPS/PdPSe-based sensor prior to and post gas adsorption has been studied as demonstrated in Figure 8-8. Based on the two-point probe sensor as was shown in Figure 8-1 (b, e) and described earlier in equations 2, and 3, the changes of conductance have been inspected. It is apparent that after adsorption of CO, CO₂, and NH₃ on the PdPS, and PdPSe, the conductance decreases and increases slightly at low energies but on the other hand the change of conductance for NO-, and NO₂-PdPS/PdPSe systems is more obvious at low energies.

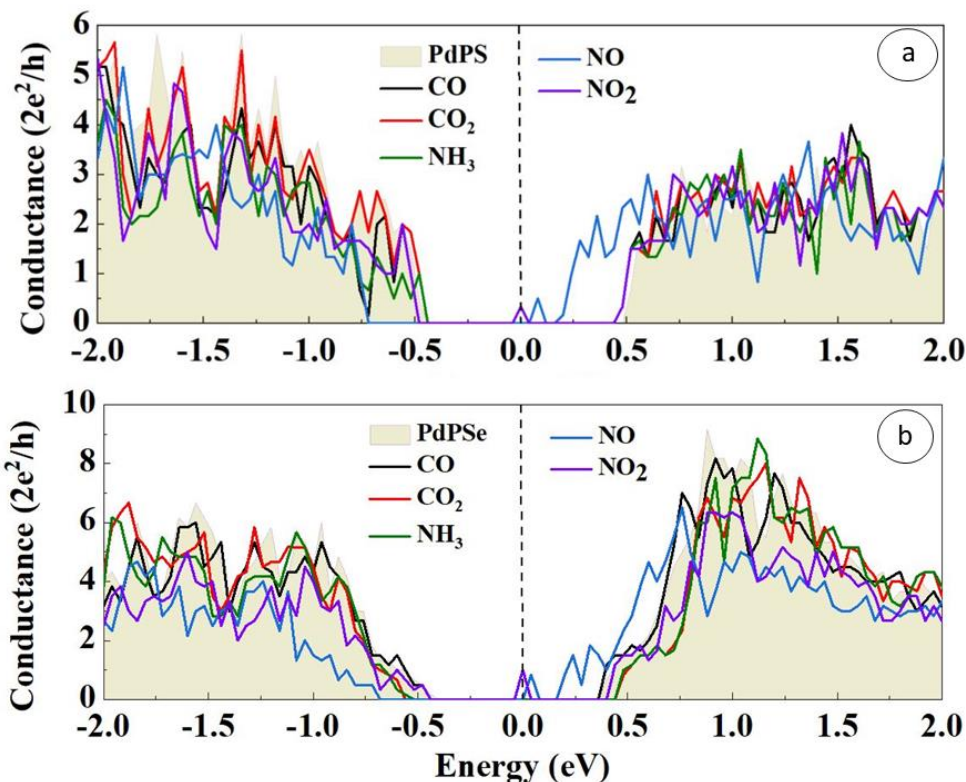


Figure 8-8. Quantum conductance of (a) PdPS-, (b) PdPSe-based device prior to and post adsorption of the gas molecules.

So, these findings are in great accordance with the preceding results, and the peak around the Fermi level for the NO approves the semiconducting behavior of it, and for the NO₂ adsorption, affirms its metallic behavior. Additionally, the adsorption of H₂ molecule upon PdPS/PdPSe structures was studied, and the adsorption energy of -0.35, and -0.12 eV was achieved for H₂ molecule adsorption on PdPS and PdPSe monolayers, respectively, which is indicative of weak adsorption.

Overall, it can be deduced that PdPS/PdPSe-based gas sensor has wonderful potential for detection of NO₂, and NO, on account of the fact that there are considerable conductance changes after adsorption, along with fairly large adsorption energy and short recovery time.

Summary

In summary, based on the density functional theory calculations, we have examined the adsorption of some small gas molecules (NO_2 , NO , CO_2 , CO , and NH_3) on the novel PdPS, and PdPSe monolayers. Various adsorption locations of gas molecules on the PdPS, and PdPSe monolayer were tested and the most stable configurations have been selected for further investigation. We have noted that the CO , CO_2 , and NH_3 gases adsorption on the PdPS, and PdPSe sheets involved physisorption due to the small adsorption energies and small band gap variation, for example, there are band gap changes of 9.5, 11.6, and 11.7% from the band gap of PdPS for the corresponding molecules. Significant band gap change happened for NO_2 , and NO , respectively, in which that band gap changed from 1.196 (for PdPS) to 0.02 eV after NO adsorption, but in the case of NO_2 , on both PdPS, and PdPSe, band gap suddenly decreased to 0, which is indicative of metallic behavior. The results have divulged that PdPS-, and PdPSe-based gas sensor can be used as potential candidates in NO , NO_2 detection, especially for NO_2 with reasonable adsorption energy (-1.01 , and -1.21 eV for PdPS, and PdPSe, respectively) and recovery time of 11.9 s at room temperature for PdPS, and recovery time of 1.74 s at 498k for PdPSe. Thus, the PdPS-, and PdPSe-based gas sensors may provide novel sensing platforms and they require further experimental investigation.

9. Chapter 9

Experimental Study on CNT Sensor- Lung Cancer

The detection of low concentration formaldehyde as a potential breath marker for lung cancer is a technical challenge in the current gas sensor field due to its weak electrical signal and its susceptibility to humidity. Here, we report on a combination of density functional theory (DFT) and experimental data to establish that aldehydes in super-saturated water vapor (80% humidity) can be detected using nanotubes molecular field-effect transistors. A thin film of high-purity semiconducting single-wall carbon nanotubes (SWCNTs) network and a catalytic metal were used as the sensing material. The fabricated back-gated Pt-decorated SWCNT FET sensors showed a response of 26.99% to 300 ppm formaldehyde at room temperature and humidity of 80% which is 11.58 times greater than that obtained for its detection using back gated bare SWCNT FET. DFT calculation also confirmed that the sensitivity of Pt-decorated SWCNT toward methanediol (formaldehyde in humidity) detection is 7.29 greater than that obtained for methanediol detection using pristine SWCNT. Moreover, the fabricated back-gated Pt-decorated SWCNT FET sensors exhibited a good recovery of 115 sec towards 300 ppm formaldehyde at 70 °C with sub-ppb theoretical calculation limit-of-detection (LOD). Hence, back-gated Pt-decorated SWCNT FET sensor is a promising candidate for easy screening of lung cancer patients.

9.1 Overview

The ability to use human breath non-invasively to diagnose various disease states has been attempted since antiquity. Ancient physicians have used the smell of breath and urine, the color

of stools to determine a person's physiological state. These are a small molecule volatile organic compounds (VOCs) as a result of changes in body's metabolism, indicating a pathophysiological process occurring inside the body. For example, a sweet and fruity odor of breath can be a sign of uncontrolled diabetic ketoacidosis, a sewer smell of breath can be an indication of lung disease and bacterial proliferation, and a fishy smell can be indications of liver ailments [21]. VOCs are mainly endogenous, produced due to body's normal metabolic processes, but exogenous VOCs exist in abundant quantities due to human activity.

A variety of VOCs are found in the indoor air that can be hazardous and can significantly put the health of populations in danger if not checked on a regular basis. Aldehydes and other volatile organic compounds (VOCs) are chemicals categorized with low boiling points from 50–260 °C; therefore, they can be found indoors in the gaseous phase and poses a considerable risk for human health [408, 409]. Typically, the indoor concentration of VOCs in winter is higher (at least 3 times) than that during the summer, although summer-oxidant episodes can make select VOCs go many times higher, especially in large and industrialized cities [410-412]. Formaldehyde, acetaldehyde, pentanal, and hexanal are dominant aldehydes found indoors in bedrooms, living rooms, kitchens, and newly manufactured homes and furniture can pose a risk to human health over long exposures [413-423]. Because of its known hazardous properties for humans, there are guidelines to prevent health risks established by the World Health Organization (WHO) [424]. Studies have shown a positive association between high levels of aldehydes and other VOCs indoors and sick building syndrome occurrences, respiratory problems of which include asthma and wheezing, nasal cancer, gastric cancer, oral cancer, lung cancer and leukemia [20, 182, 183, 425-433]. Formaldehyde continues to receive substantial publicity due to its elevated presence (77 ppb) in the air of Federal Emergency Management

Agency (FEMA) trailers after the hurricane Katrina disaster [434, 435]. Inhaled formaldehyde at sufficient concentrations has been established as a carcinogen for nasal tumors and leukemia in rodents [425]. Other non-cancerous endpoints associated with formaldehyde exposure includes reproductive problems, developmental problems in children, neurological problems, and immune system problems [425]. The threshold of formaldehyde for developing nasal tumors is between 6 ppm and 15 ppm [425]. Exposures at 6 ppm and above for sufficient duration produce substantial genomic and histopathological derangements directly associated with the development of nasal tumors [425]. Similarly, sufficient evidence exists for acetaldehyde as a carcinogen for hamsters and rats, causing lung and nasal cancers [436].

The use of nanomaterials such as quantum dots, nanotubes, nanosheets, nanoflowers, etc. whose size ranges between 1-10 nm is attractive for chemo molecular sensing due to a number of benefits such as room temperature operation, significant modulation of conductance with exposure to hazardous VOCs, modulation of selectivity with different catalytic metals and ability to be integrated with electronics. Nanotechnology-based approaches can be highly transformative, potentially enabling the integration of sensor arrays into smartphones, smart thermostats, smart fire-alarms, sensors in the cooking range to monitor VOCs in kitchen, sensor arrays in the bedroom to monitor VOCs while asleep and even in personal clothing. These sensors could be connected to a central network that can continuously analyze the presence of VOCs inside homes, office buildings, and hospitals during all times of the year. Recent approaches using nano-sensor arrays and classifiers were able to diagnose and classify 17 diseases from 1404 subjects via pattern analysis of exhaled molecules [437, 438]. However, in both these studies, significant molecular modification was needed of the nanotubes/nanowires

with organic molecules for VOC detection and multiple VOC's had affinity to the same sensors, needing classification.

Among all available materials, carbon nanotubes (CNTs) have exhibited emerging advances especially for fabricating field-effect transistor (FET)-type gas sensors for VOCs detection [439, 440]. Similarly, single-wall carbon nanotubes (SWCNT) molecular sensors have been reported to detect lung cancer biomarkers from exhaled breath by coating the sensors with a variety of thin (0.5–1.0 μm in thickness) organic films [441]. The sensors array showed discrimination between the volatile organic compounds (VOCs) found in the breath of patients with lung cancer, relative to healthy controls when exposed to breath for 10 minutes, especially if the sensors array is preceded with either water extractor and/or pre-concentrator of VOCs [441]. While sensitive, such thick organic films may have a lower shelf-life and can enable drift in the sensors over long periods of time. An ideal chemical sensor for breath print analysis should be sensitive at very low VOC concentrations in the presence of water vapor because the headspace of clinical samples is fully humidified [437, 438]. This is a significant challenge for nanomaterial-based sensors as a nonspecific binding of water vapor competes with trace concentrations of target analyte for adsorption sites. For certain VOC sensing, hydrophobic receptors, such as stacks of polycyclic aromatic hydrocarbons (PAHs), have good discrimination of VOC and water signal [442]. Yet, for most trace breath biomarkers, removal or separation of humidity is necessary for large and reproducible sensor responses. However, a combination of fundamental and experimental studies has been lacking for aldehyde (VOC) detection from/mimicking human breath.

Here in this work, we report on a combination of an experimental data and first-principle calculations based on density functional theory (DFT) to establish that aldehydes at ppb level in

super-saturated water vapor (mimicking human breath) can be detected using nanotube molecular FETs. It is worth mentioning that due to the attractive features of FET-based gas sensors such as small size, easy integration, mass-production capability, and low-cost manufacturing, we developed a FET-type SWCNT. We establish that SWCNT FETs ‘decorated’ with metal atoms and clusters have high selectivity in preferring low energy adsorption sites for aldehydes in the presence of water vapor that enables the detection of trace amounts of formaldehyde in super-saturated water vapor (80% humidity). The metal decoration is also much more stable compared to organic functionalization methods and can potentially enable a longer operational and shelf lives. These combined theoretical and experimental results have important implications both for the fundamental understanding of SWNT/molecular interactions in the presence of water vapors and for the development of large sensor arrays for the detection of human volatolomes and environmental exposure.

9.2 Experimental Method

Back-gated CNFET sensors were fabricated on a 4-inch heavily n-doped Si wafer, which also works as the back-gate electrode with a 100 nm thick SiO₂ layer on top of it as the gate dielectric. Standard photolithography was done to pattern source/drain interdigitated electrodes (IDEs). Then, 10 nm Cr and 90 nm Au layers were deposited using e-beam evaporation, followed by an ultrasonic vibration-assisted lift-off process to form source/drain IDEs. 10 pairs of IDEs (5/5 μm, electrode/gap) were defined. Next, 100 μl of the 99% Iso-semiconducting SWNTs suspension was mixed with 85 ml of DI water and 15 ml of 1% w/v SDS, for a final concentration of 1 μg/100 ml. After 1 hr ultrasonication at room temperature, the uniform solution was vacuum filtered over the cellulose membrane with 0.05 μm pore size. The filter was then rinsed by isopropanol and DI water to remove the excess nanotubes. In the next step, the CNT film network was pressed onto

the SiO₂ surface for 30 min, followed by transferring to an acetone vapor bath to dissolve the overlying filter membrane. The wafer was then annealed at 250 °C to decrease the resistance of the devices. Finally, the 200×200 μm² CNT channel regions were created by photolithography, followed by oxygen plasma etching to remove the extra CNTs. 147 sensors with 3.5×7.2 cm² size chips were obtained after dicing the 4-inch silicon wafer. For decoration of SWCNTs with Pt, Pd, or Ni nanoparticles, a 5 Å-thick metal film was deposited onto the networked SWCNTs using an e-beam evaporation technique with a low evaporation rate of 0.1 Å/s. For decoration ITO nanoparticles on SWCNTs, a 5 Å-thick ITO film was deposited onto the networked SWCNTs using a sputtering technique.

Structural Characterization

SEM and AFM images of the CNT film were obtained using JEOL JSM-7000F and Park Systems XE-70 instruments, respectively. Raman spectroscopy measurements were performed using a Horiba XploRa Raman microspectrometer.

Materials

The Iso-semiconducting SWNTs (diameter: 1.2–1.7 nm, length: 100 nm–5μm, purity: >99%, concentration: 1 mg CNT in 100 ml surfactant solution) were supplied by Nanointegris LLC. A 4-inch heavily n-doped Si wafer (crystal direction: <100>, dopant/type: As/N, sheet resistance: <0.005 ohm-cm, thickness: 525±25 μm) with a thermally grown 100 nm thick SiO₂ layer on the polished side was purchased from WaferPro. Sodium dodecyl sulfate (SDS) was purchased from Sigma-Aldrich. The membrane filter with 0.05 μm pore size was supplied by Millipore Sigma. Formaldehyde solution 37 wt. % in H₂O was purchased from Fisher Scientific. Deionized water (DI) used in this experiment was obtained by using a Milli-Q water system.

Construction of Nanotube Molecular Sensors

Figure 9-1 (a) presents the schematic of the back-gated nanotube molecular sensors for breath analysis. The schematic flow of the fabrication process is shown in Figure 9-1 (b). The details of the fabrication process can be seen in the Methods section. Figure 9-1 (c) illustrates a photograph of an entire Si wafer consisting of 147 sensors. Moreover, a photograph of a single device with $3.5 \times 7.2 \text{ cm}^2$ size and optical microscopy image of its interdigitated electrodes are presented in Figure 9-1 (d). The interdigitated electrodes have a total finger area of $5 \mu\text{m} \times 175 \mu\text{m}$ and gap size of $5 \mu\text{m}$. The Iso-semiconducting SWNTs (diameter: 1.2–1.7 nm, length: 100 nm– $5 \mu\text{m}$, purity: >99%) were used in this study. Figure 9-1 (e) shows the Raman spectroscopy of CNT films suggesting a Radial breathing mode (RBM) mode (174 cm^{-1}), a small D band (1340 cm^{-1}), a very large G band (1590 cm^{-1}), and a pronounced 2D band or G' band (2673 cm^{-1}). The large G/D band ratios (~ 30) suggest extremely low levels of amorphous carbon and damaged nanotubes. Figure 9-1 (f) presents the scanning electron micrograph (SEM) of SWCNTs and the atomic force microscopy (AFM) image of the nanotubes is presented in the inset, indicating a uniform network density of the nanotubes in a random arrangement.

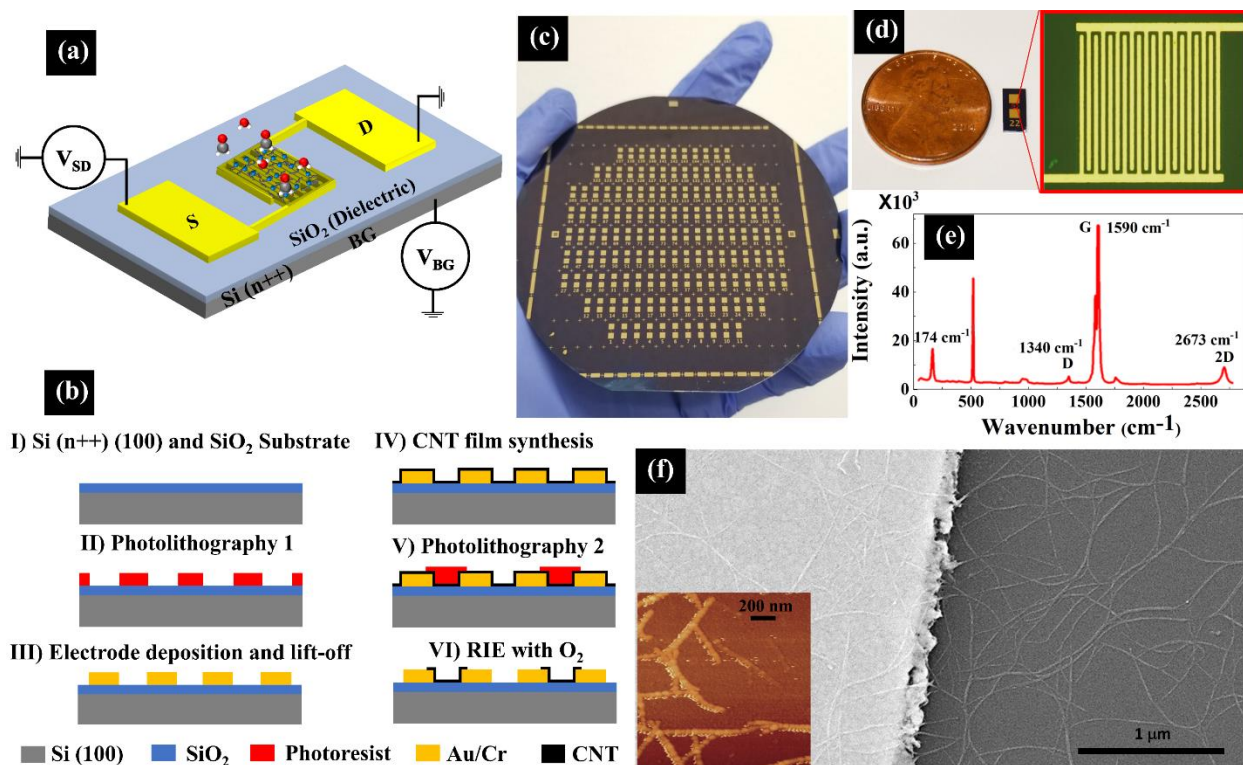


Figure 9-1. (a) Conceptual illustration of a back-gated metal-decorated CNT FET. (b) Flowchart of device fabrication. (c) Photograph of an entire wafer consisting of 147 sensors. (d) Photograph of a single device and optical microscopy image of its interdigitated electrodes. (e) Raman spectroscopy of carbon nanotubes; a small D band, large G band and pronounced 2D band suggest the carbon nanotube structure. (f) SEM image of nanotubes; the inset is an AFM image of a nanotube film.

Gas Sensing System

The response of back-gated CNT-FET sensors to humidity and formaldehyde was measured using a home-made sensing system. The clean dry air (CDA) was split into two separate lines, each controlled by a mass flow controller (MFC) (Alicat Basis-BC-L0020). The lines were connected to two bubblers. Injected formaldehyde was generated by blowing air through the first bubbler containing diluted formaldehyde in DI water. The second bubbler containing DI water was used to dilute the formaldehyde and adjust the humidity level. After bubblers, the gas lines were

combined and introduced to the gas sensing chamber. Purging of the chamber was performed in N₂. The humidity and the temperature of the chamber were monitored with a humidity sensor (Honeywell HIH-4000-001) and a temperature sensor (Thorlabs-TSP01). During the experiments, the temperature of the air mixture was ~23 °C, and relative humidity was ~80%. A resistive foil heater (ThorLab-TLK-H) and a heater controller (ThorLab-TC200) were employed to heat up the sensors. The formaldehyde concentration was measured by placing detector tubes in the gas sensing chamber (Gastec 91M, 91L, 91PL). All MFCs, solenoid valves, heaters, sensors were operated by a LabView program. An Agilent 4156C semiconductor parameter analyzer equipped with a custom LabVIEW interface was used for monitoring the sensors and data collection. Figure 9-2 schematically shows the sensor device and gas sensing system. The details are presented in the Methods section.

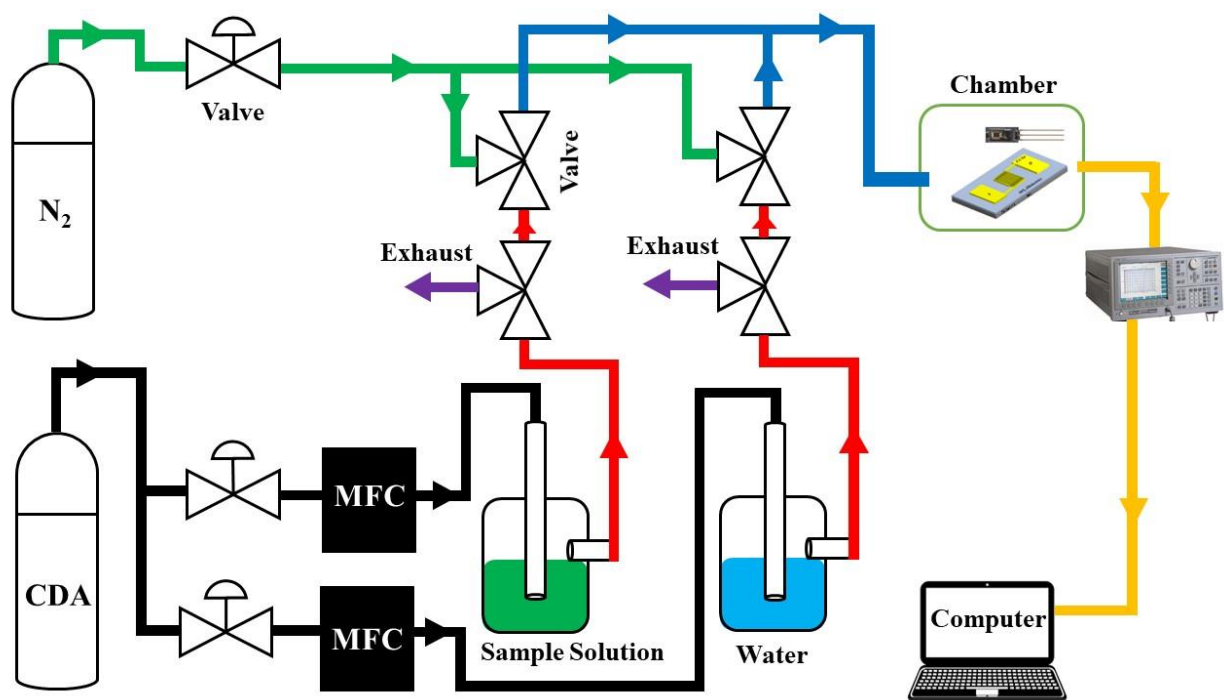


Figure 9-2. Schematic diagram of gas sensing setup.

9.3 Computational Method

The theoretical investigations based on first-principle density functional theory (DFT) calculations were carried out to predict the adsorption behavior of formaldehyde (CH_2O), water (H_2O), and methanediol ($\text{CH}_2(\text{OH})_2$) molecules on the pristine SWCNT and Pt-decorated SWCNT using Atomistix ToolKit (ATK) package [153, 154, 443]. The Generalized Gradient Approximation of Perdew-Burke-Ernzerhof (GGA-PBE) exchange-correlation functional with a double- ζ basis set was used to relax the structures. In order to describe long-range vdW interactions [156], the Grimme van der Waals (vdW) correction (PBE-D2) [157] was also included. The electron temperature was 300°K, and the energy mesh cut-off was set to 150 Ry. To avoid the interactions between the nanotube and its periodic images, a vacuum space of 20 Å was considered in x and y directions in which the nanotube is not periodic. The geometry optimizations are performed until the force on each atom is less than 0.01 eV/Å. The Brillouin zones were sampled by $1 \times 1 \times 11$ k -point using the Monkhorst Pack scheme during structure relaxation. In order to obtain more accurate results for electronic structure calculations, the k -point was increased to $1 \times 1 \times 111$. The charge transfer (Q) upon adsorption of the gas molecules on the nanotube was obtained using Mulliken population analysis from counting the charge difference between the adsorbed gas molecule and the isolated gas molecule.

9.4 Experimental Results

The impact of concentration of the CNT's solution on the electrical properties of the nanotubes were first investigated by fabricating back-gated CNT FETs with CNT films at different concentrations. The on (off) currents were found to be 3.97 mA (440 μA), 1.71 mA (15.20 μA),

1.11 mA (8.34 μ A) for back-gated CNT FETs with 6, 2, and 1 μ g CNT mass, respectively. Besides that, the on/off current ratios are 9.02 for 6 μ g CNT mass, 112.5 for 2 μ g CNT mass, and 133.09 for 1 μ g CNT mass, suggesting that decreasing CNT mass reduces the off current and consequently enhance the on/off current ratio. Hence, ultra-thin CNT film at 1 μ g level was elected for this study, and the SEM and AFM images were shown in Figure 9-1 (f).

We first analyzed the effect of humidity on the electronic properties of back-gated pristine CNT FETs. All Experiments were done at $V_g = -5$ V and $V_{ds} = 1$ V when the device is in the linear region. The source-drain current of the sensor as a function of gate voltage was measured before and after exposure to humid air and during the recovery and plotted in Figure 9-3 (a). To gain a better understanding of the humidity impacts on the sensor, we also plotted the difference of $I_{sd} - V_g$ of the sensor before (the reference) and after exposure and during recovery, as shown in Figure 9-3 (b). The sensor was first exposed to air with humid relativity of 80% (generated from water bubbler in Figure 9-2) for 5 min, resulting in a significant reduction of the current in the on the region. After turning the bubbler off, the chamber was then purged with N_2 flow for 10 min to allow the sensor to recover. However, the sensor was not fully recovered due to the strong adsorption of the water molecules to the possible defects of the nanotubes. The nanotubes were annealed at 150 $^{\circ}$ C for a total time of 7.5 min for a full recovery. We then tested the humidity response of our sensors at different gate voltages to comprehend how fast the device responds to humidity in different operating regions (See Figure 9-3 (c)). The sensor was first exposed to N_2 flow for 1 min. Then, the humidity was introduced into the chamber for 5 min. The currents of the sensor were normalized with respect to the current of the sensor under N_2 , as shown in Figure 9-3 (c). It was reported that upon exposure to humidity, the water molecules donate electrons to the pristine SWCNTs [444, 445]. These electrons can neutralize the majority carrier of the p-type

SWCNT (free holes). When a negative (positive) gate voltage is applied to the sensor, the positive (negative) charge carriers gets trapped in the dielectric layer. These charges are localized at the dielectric and nanotube surface and accumulate with increasing the gate voltage. Hence, the interaction of SWCNT and humidity can be affected by holes neutralization and trapped charges.

When $V_G = -5V$ (on state), the positive charge traps formed at the surface of the nanotubes act as a positive electric potential, leading to the reduction of the effective gate voltage. Thus, the depletion region is widened, and consequently, the I_{sd} decreases. As expected, a larger reduction in I_{sd} was observed when $V_G = -10V$ due to the fact that more traps were created in comparison with $V_G = -5V$. Furthermore, the neutralization of the free holes by electrons donated by water molecules leads to a decrease in I_{sd} , which is more pronounced at higher gate voltages. Hence, a sharper decrease was observed at $V_G = -10 V$.

The known formaldehyde concentrations were created using the bubbler system in Figure 9-2. For example, to achieve 300 ppm formaldehyde vapor, 10 mL formaldehyde was mixed with 90 mL DI water to create a 10% formaldehyde solution. Out of two lines connected to clean dry air, one line was bubbled through formaldehyde solution, and the other one was bubbled through DI water. By controlling the flow rate of the two lines using two mass flow controllers (MFCs), the known concentration of formaldehyde and relative humidity of the air were created and then delivered to the gas chamber. The sensor was exposed to 300 ppm formaldehyde in the presence of humid air with a relative humidity of 80% to mimic human breath. The chamber was purged with N_2 for 2 min, then was exposed to humidity for 1 min, and finally was exposed to 300 ppm formaldehyde in humid air for 1 min. The sensor was then allowed to recover in the presence of humid air. Figure 9-3 (a) shows the response and recovery curves for seven cycles when the gas sensor alternately changes between humid air and 300 ppm formaldehyde in the humid air. The

drift in the background current can be correlated to the trapped charges in the dielectric layer. One can see that the sensor is able to detect formaldehyde in the presence of super-saturated water vapor. The sensor sensitivity $|(G_{HF} - G_H)/G_H| \times 100$ was calculated, where G_H is the conductance in the presence of humidity, and G_{HF} is the conductance in the presence of formaldehyde and humidity. The sensitivity of the back gated pristine SWCNT FET to 300 ppm formaldehyde in the humid air was found to be 2.33%. Ergo, pristine SWCNT cannot be a good choice to detect formaldehyde with a very low concentration. For this reason, SWNTs were decorated with metal nanoparticles in order to enhance the sensor's response to low concentration formaldehyde. It is worth mentioning that the conductivity of pristine SWCNT increases after interaction with water molecules as simulation results suggested. This difference between theoretical and experimental results can be attributed to the fact that the nanotubes can contain defects. In the presence of defects, the oxygen molecules can be chemisorbed, shifting the p-type behavior of pristine SWCNT to n-type [446].

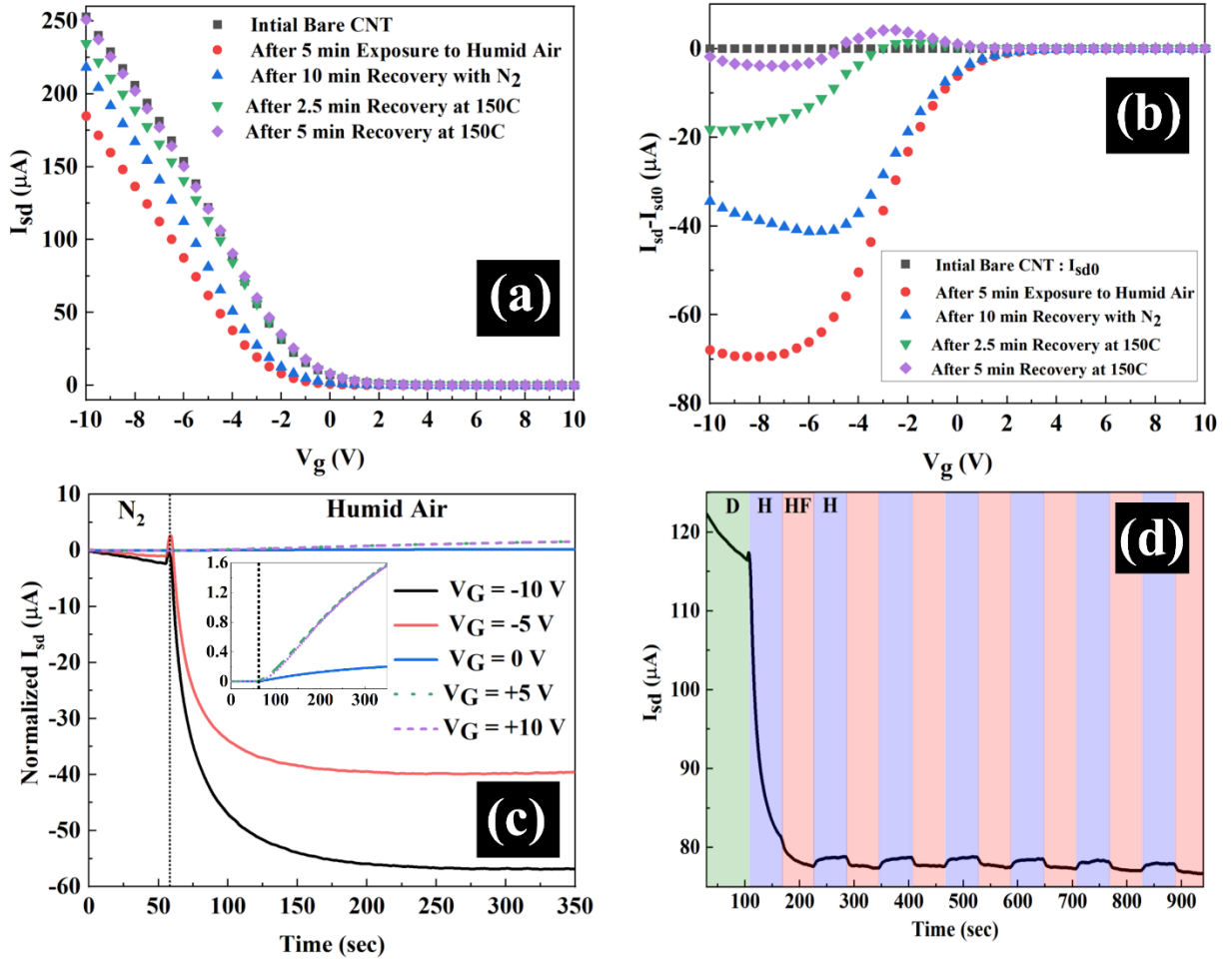


Figure 9-3. (a) Source-drain current of a back-gated CNT FET as a function of gate voltage measured in dry air (initial), after exposure in 80% humid air for 5 min, recovery with N_2 for 10 min, recovery in dry air at $150^\circ C$ for 2.5 min, and recovery in dry air at $150^\circ C$ for 5 min. (b) The difference between source-drain current presented in (a) and the source-drain current measured in dry air (initial) versus gate voltage. (c) The normalized source-drain current change of the back-gated CNT FET in N_2 and humid air (RH = 80%) at different gate voltages. The inset shows source-drain current change at $V_G = 0, -5,$ and -10 V. (d)

Dynamic sensing transient of a back-gated CNT FET for 300 ppm formaldehyde in DI water at room temperate. D, H, and HF represent drift, humid air, and formaldehyde in humid air, respectively. The V_d s were set to 1 V.

The back-gated CNT FETs were decorated with different nanoparticles such as Ni, Pd, Pt, and ITO using electron-beam evaporation or the sputtering method. The indicated thickness of the deposited layer was 5 \AA , thin enough to avoid electrical shorting of the devices (*i.e.* this will form single atom and nanocluster decoration). To make sure the current passes through the nanotube

network, a control device (with no SWCNT) was covered by nanoparticles. No conductivity was observed, confirming that the metal layer is not continuous. Figure 9-4 (a)-(e) show the $I_{sd}-V_G$ characteristics for a back-gated bare and metal-decorated CNT FETs at $V_{sd} = 1V$. Although the bare CNT devices showed a p-type semiconducting behavior with a gate dependency, devices are less sensitive to the gate voltages after coating with Pt and Pd nanoparticles. This phenomenon can be correlated to the screening induced by metal nanoparticles [447]. Coating the devices with Ni and ITO nanoparticles preserve the sensitivity to the gate voltages. One possible reason that Ni as a metal does not experience the loss of gate dependence can be the metal oxidation after coating. Decoration of the SCWNT with nanoparticles also causes a decrease in the on current and an increase in the off current, leading to a reduction in the on-off current ratio. For bare, Ni-, Pd, Pt-, and ITO-decorated back-gated CNT FETs, the on-off current ratios were 22000, 445, 1.7, 2.2, and 112, respectively. The decrease in on-current after coating nanoparticles can be attributed to the electron transfer between pristine SWCNTs and nanoparticles. For example, ITO, which is an n-type semiconductor, transfers a large number of electrons to the nanotubes, leading to a significant drop in the on-current. The C atoms of SWCNT are more electronegative compared to Pt, Pd, and Ni. Therefore, the nanotubes withdraw electrons from metal nanoparticles, reducing the number of holes and consequently, the current of the device. Figure 9-4 (d) presents the magnitude of the hysteresis ($V_{Hysteresis}$) and the area of hysteresis loop for the bare and metal decorated CNT FETs. $V_{Hysteresis}$ is defined as the difference between gate voltages to achieve $(I_{SD,max} + I_{SD,min})/2$ for the forward and reverse sweep directions. The magnitude of hysteresis for bare CNT FET (4.96 V) was decreased to 3.7 V and 2.8 V after coating Ni and ITO nanoparticles and was almost depressed by introducing Pd (0.17 V) and Pt (0.29 V) nanoparticles.

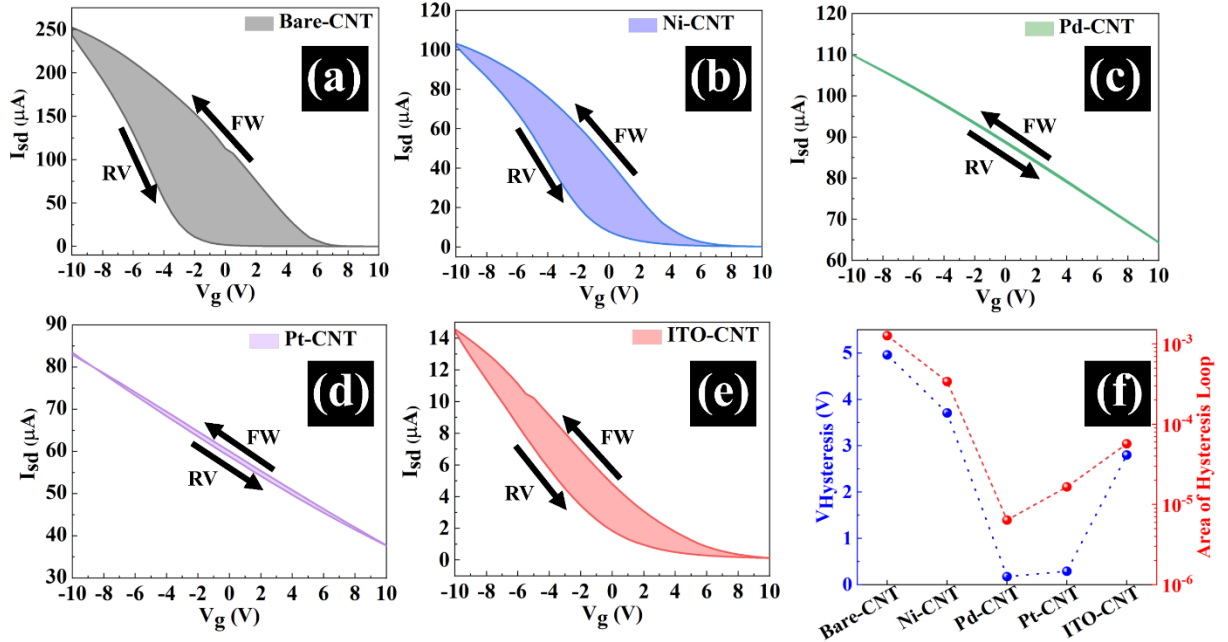


Figure 9-4. The I_{sd} – V_G characteristics for a back-gated (a) bare, (b) Ni-decorated, (c) Pd-decorated, (d) Pt-decorated, and (e) ITO-decorated CNT FETs at $V_{sd} = 1\text{V}$. Hysteresis ($V_{\text{Hysteresis}}$) was measured at $(I_{sd,\text{max}} + I_{sd,\text{min}})/2$ between the forward (FW) and reverse (RV) sweeps. (f) Hysteresis and area of hysteresis loop for different back-gated CNT FETs.

Next, back-gated metal-decorated CNT devices tested with 300 ppm formaldehyde in humid air with a relative humidity of 80% and their conductance changes as well as the sensitivity histograms are presented in Figure 9-5 (a) and (b). The sensitivity of the bare CNT device (2.33%) was changed to 3.66%, 12.48%, 26.99%, and 0.63% after coating Ni, Pd, Pt, and ITO nanoparticles. The functionalization of CNTs with catalytic metals such as Pt and Pd can significantly enhance their responses to the formaldehyde in the humid air. Interestingly, the sensitivity of back gated Pt-SWCNT FET toward 300 ppm formaldehyde in the humid air is 11.58 times greater than that obtained for its detection using back gated bare SWCNT FET, in a reasonable agreement with those obtained in the theoretical section for detection of a single molecule methanediol (7.29). The drop in conductivity of Pt-SWCNT FET upon interaction with

formaldehyde matches with DFT findings, suggesting that formaldehyde molecules donate electrons to the Pt-decorated nanotubes. Hence, back gated SWCNT FET decorated by Pt nanoparticles were selected for further studies.

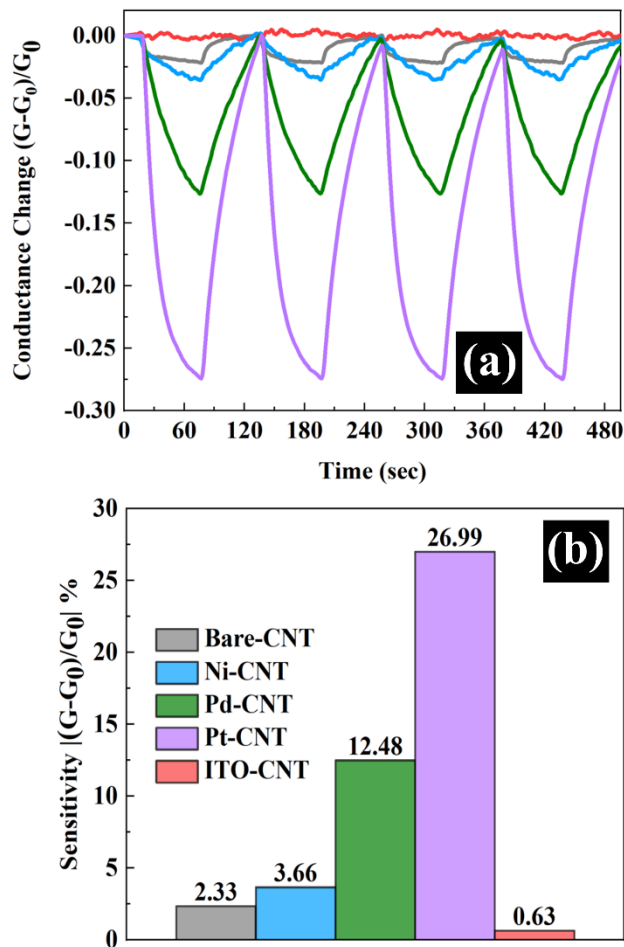


Figure 9-5. (a) Conductance change and (b) sensitivity of back-gated Bare, Ni-, Pd-, Pt-, ITO-decorated CNT FETs to 300 ppm formaldehyde at RH=80% and room temperature. Experiments were done at $V_g = -5$ V and $V_{ds} = 1$ V.

Sensing experiments for formaldehyde concentrations ranging from 3 ppb to 300 ppm at RH=80% were performed for back-gated Pt-decorated SWCNT FETs, and their dynamic sensing transients were plotted in Figure 9-6. Four sensing cycle experiments were performed for each concentration. The sensor showed a highly sensitive and reversible response to formaldehyde

down to 3 ppb. It should be mentioned that 3 ppb (100 nL formaldehyde diluted in 100 mL DI water) was the lowest concentration that we could reliably create using a high precision micropipette.

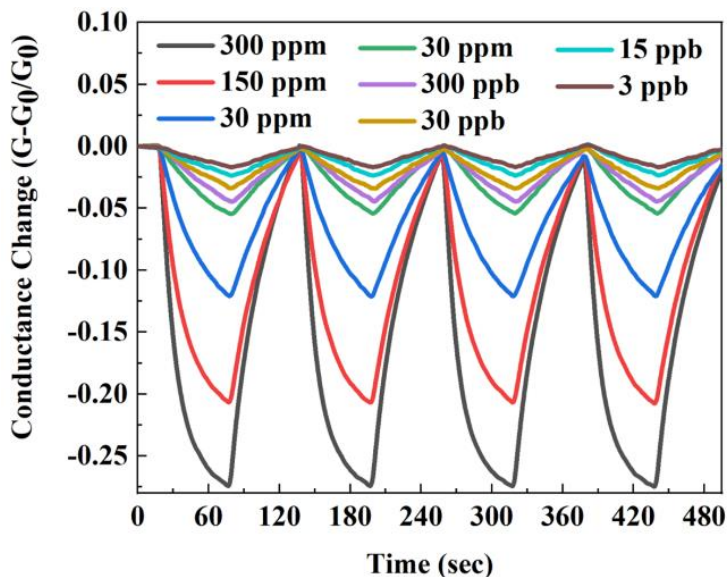


Figure 9-6. Dynamic sensing transients of back-gated Pt-decorated CNT FET for 3 ppb - 300 ppm formaldehyde at RH=80% and room temperature. Experiments were done at $V_g = -5$ V and $V_{ds} = 1$ V.

To describe the relationship between sensitivity and formaldehyde concentration, the Freundlich isotherm model could be applied, see Figure 9-7 (a). A regressed equation of $Sensitivity = 4.46346 \times Concentration^{0.30988}$ can be used to fit with a good coefficient of $R^2 = 0.98154$. Although the response of the sensor tends to saturate at high concentrations of formaldehyde, three different regions with linear dependency between the response and the concentration of formaldehyde were found, showing that our sensor is capable of detecting formaldehyde in humid air with wide dynamic range. As shown in Figure 9-7 (a), the sensor's response with respect to the concentration of formaldehyde is linear in region 1 (3 ppb – 30 ppb), region 2 (0.3 ppm-30 ppm), and region 3 (30 ppm-300 ppm). The slopes of linear regression for different regions were presented in Figure 9-7 (a) insets. As mentioned above, the lowest detectable concentration is

limited to our lab equipment. The limit of detection (LOD) suggested by the International Union of Pure and Applied Chemistry (IUPAC) is [448]:

$$\text{LOD (ppm)} = 3 \frac{\text{RMS}_{\text{Noise}}}{\text{Slope}} \quad (25)$$

The $\text{RMS}_{\text{Noise}}$ of the sensor can be obtained using the conductance variations in the baseline via the root-mean-square error [449].

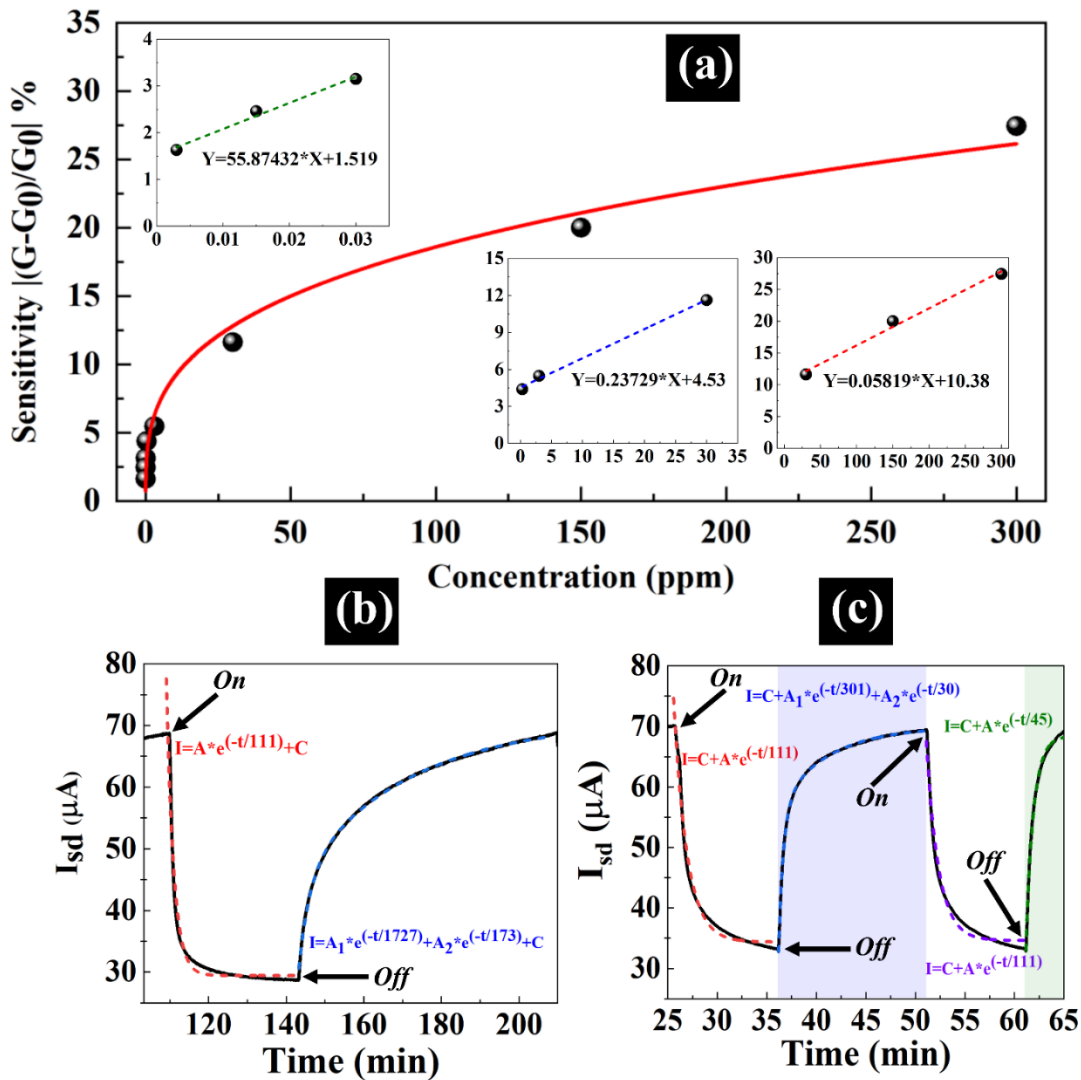


Figure 9-7. (a) The sensitivity of the back-gated Pt-decorated CNT FET as a function of formaldehyde concentration at RH=80% and room temperature. The insets show a zoom on 0.003 – 0.03 ppm, 0.3 – 30 ppm, and 30 – 300 ppm regions. (b) The dynamic response-recovery curve of the back-gated Pt-decorated

for 300 ppm formaldehyde at RH=80% and room temperature. The response and recovery curves were modeled by an exponential fit (dashed lines) (c) Dynamic response-recovery curve of the back-gated Pt-decorated for 300 ppm formaldehyde. The first recovery (blue region) was done at RH=80% and T = 70°C. The second recovery (green region) was made in a dry atmosphere at T = 70°C. The response and recovery curves were modeled by an exponential fit (dashed lines). Experiments were done at $V_g = -5$ V and $V_{ds} = 1$ V.

Then, a fifth-order polynomial curve-fitting was performed. Hence, RMS_{Noise} can be defined as:

$$RMS_{Noise} = \sqrt{\frac{V_{\chi^2}}{N}} \quad (26)$$

where N is the number of data point and V_{χ^2} is:

$$V_{\chi^2} = \sum (y_i - y)^2 \quad (27)$$

Here, y_i and y are measured and fitted data points, respectively. The RMS_{Noise} was calculated to be 0.000828 for the back-gated Pt-SWCNT FET. Using Equation 5, we calculated LOD for three different regions. The formaldehyde detection limit in humidity was calculated to be 42.72 ppb for region 3, 10.47 ppb for region 2, and 44.49 ppt for region 1. Ergo, our sensor can detect sub-ppb formaldehyde in humid air at room temperature and RH=80%.

The response time is the time needed for the sensor to reach 90% of the initial conductance after introducing formaldehyde to the chamber. Conversely, the time taken for the sensor to reach 10% of its initial conductance after the stoppage of the formaldehyde is recovery time. In our measurements, the formaldehyde exposure and recovery time intervals were chosen to be 60 sec to demonstrate the potential application of the sensor for being employed in real-time breath analysis systems. However, the sensor response was not fully saturated (ON phase), and the sensor was not fully recovered to its original conductance (OFF phase) during 60 sec intervals at room temperature. Therefore, it is critical to consider long time intervals of our sensors to specific concentrations of formaldehyde to extract response and recovery time. Figure 9-7 (b) presents the

dynamic response-recovery curve of the back-gated Pt-decorated for 300 ppm formaldehyde at RH=80% and room temperature with ON time interval of 2000 sec and OFF time interval of 4000 sec. The response and recovery times for the Pt-SWCNT sensor in response to 300 ppm formaldehyde in the presence of humidity were found to be 280 sec and 2500 sec, respectively. However, for pristine SWCNT, the response time was 28 sec and recovery time was 42 sec in response to 300 ppm formaldehyde in humidity based on DFT suggested, while formaldehyde and methanediol molecules are only physisorbed on pristine SWCNT, they are strongly chemisorbed on the Pt-SWCNT. Interestingly, the response and recovery times for the sensor in response to 3 ppb formaldehyde in the presence of 80% humidity were found to be 1170 sec and 1700 sec, respectively (See Figure 9-8).

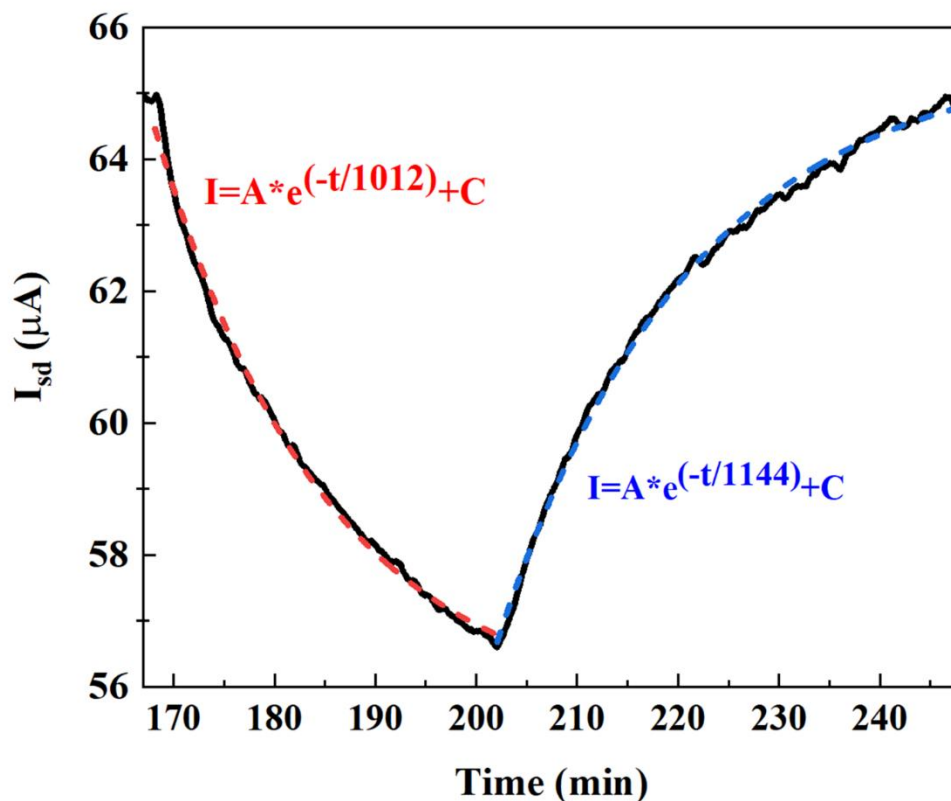


Figure 9-8. The dynamic response-recovery curve of the back-gated Pt-decorated for 3 ppb formaldehyde at RH=80% and room temperature. The response and recovery curves were modeled by an exponential fit (dashed lines).

The response curve was modeled by an exponential decay fit, while the recovery curve was modeled by two exponential decay modes (dashed lines in Figure 9-7 (b)). The time constant for the response curve was 111 sec. Further, the time constants for two modes of exponential decays were found to be 1727 and 173 sec. The strong interaction between formaldehyde and water molecules with Pt nanoparticles is the main reason for the longer recovery of Pt-SWCNT compared to that pristine SWCNT as theory suggested. A slight heat at high temperatures is a possible way to achieve a faster recovery. To this goal, the sensor was heated at 70 °C. The Dynamic response-recovery curve of the back-gated Pt-decorated for 300 ppm formaldehyde with

ON time interval of 600 sec and OFF time interval of 900 sec was presented in Figure 9-7 (c). The blue region shows the recovery curve at RH=80% and $T = 70^{\circ}\text{C}$. The recovery time was found to be 330 sec. Since during recovery, the humidity was still introducing to the chamber, the sensor recovery in a dry atmosphere at $T = 70^{\circ}\text{C}$ was performed (the green region in Figure 9-7 (c)). Excitingly, the sensor recovery time was decreased to 115 sec. The response curves were also modeled by an exponential fit. Similar to recovery at room temperature and RH=80%, the recovery curve at $T = 70^{\circ}\text{C}$ and RH=80% can be fitted via two exponential decay modes with time constants of 301 and 30 sec. However, the recovery curve in a dry atmosphere at $T = 70^{\circ}\text{C}$ can be modeled via exponential decay with a time constant of 45 sec. It can be deduced that humidity is responsible for the second exponential decay mode in the recovery curve.

9.5 First-principles calculations using density functional theory:

A zigzag (8,0) SWCNT was considered in a periodically repeating supercell with lattice constants of $a = b = 20 \text{ \AA}$, large enough to avoid the interactions of adjacent cells, and $c = 12.82 \text{ \AA}$. The diameter of the nanotube is 6.37 \AA and the average C—C bond length is 1.42 \AA . The SWCNT supercell modelled was composed of 96 carbon atoms. Our theoretical calculations showed that the pristine (8,0) SWCNT is a semiconductor with a bandgap of 0.648 eV, in good agreement with the literature [143]. This fact confirmed the accuracy of our computational method. To assess the chemical sensing of the nanotubes, single gas molecules (CH_2O , H_2O , and $\text{CH}_2(\text{OH})_2$) were placed at a distance of 2 \AA above a C atom, a C—C bond, and the center of a C hexagon. At these locations, the molecular axis could be aligned in parallel or perpendicular with respect to the surface of the nanotube. Moreover, the O atom in the molecules can point to the

nanotube or point away from it. After full relaxation of the structures, their structural stabilities were appraised by calculating their adsorption energies. The adsorption energy of a molecule on the SWCNT or Pt-SWCNT is defined as:

$$E_{\text{ad}} = E_{\text{Molecule+X}} - (E_{\text{Molecule}} + E_{\text{X}}) \quad (28)$$

where X is SWCNT or Pt-SWCNT. $E_{\text{Molecule+X}}$, E_{X} , and E_{Molecule} are the total energies of the nanotube-molecule complex, nanotube, and the isolated molecule, respectively. The more negative the adsorption energy is, the stronger the adsorption of the molecule on the nanotube would be. The most stable adsorption configurations of gas molecules on the pristine nanotube were chosen for this study and presented in Figure 9-9 (a). The adsorption energies of the structures, the net charge transfer from the molecule to the nanotube using Mulliken population analysis, the energy bandgap of the structures, and the binding distances between molecules and the nanotubes are listed in Table 9-1. Upon exposure CH₂O to the pristine SWCNT, the O atom was pointing to the nanotube. Our results showed that the formaldehyde molecule is physically adsorbed on the pristine nanotube with a small adsorption energy of -0.282 eV and the minimum O—C interaction distance of 3.09 Å. The adsorption energy of an H₂O molecule on pristine SWCNT and the minimum H—C interaction distance were -0.247 eV and 2.31 Å, respectively, showing that the interactions between the water molecule and pristine nanotubes are also weak. A small charge of -0.003 *e* (-0.002 *e*) is transferred between CH₂O (H₂O) and nanotube, agreeing well with its corresponding adsorption energy. Methanediol (CH₂(OH)₂) is the hydrated form of formaldehyde (CH₂O). The adsorption energy of CH₂(OH)₂ on pristine SWCNT was -0.179 eV, which is higher than that corresponds to CH₂O (-0.282 eV), showing that the hydration of formaldehyde has a negative impact on its adsorption on pristine SWCNT. Methanediol was

physically adsorbed on the pristine SWCNT due to the weak van der Waals interaction between the molecule and the nanotube. The interaction distance of the nanotube from the molecule was 2.70 Å (O–C). Upon adsorption of the CH₂(OH)₂, the nanotube gained 0.003 *e*. This small charge transfer corresponded well with the obtained adsorption energy.

According to Figure 9-9 (B), there was a little reduction in the energy bandgap of pristine SWNT (0.648 eV) after interaction with formaldehyde (0.646 eV), water (0.645 eV), and methanediol (0.645 eV) which were consistent with very small charge transfer between the molecules and the nanotube.

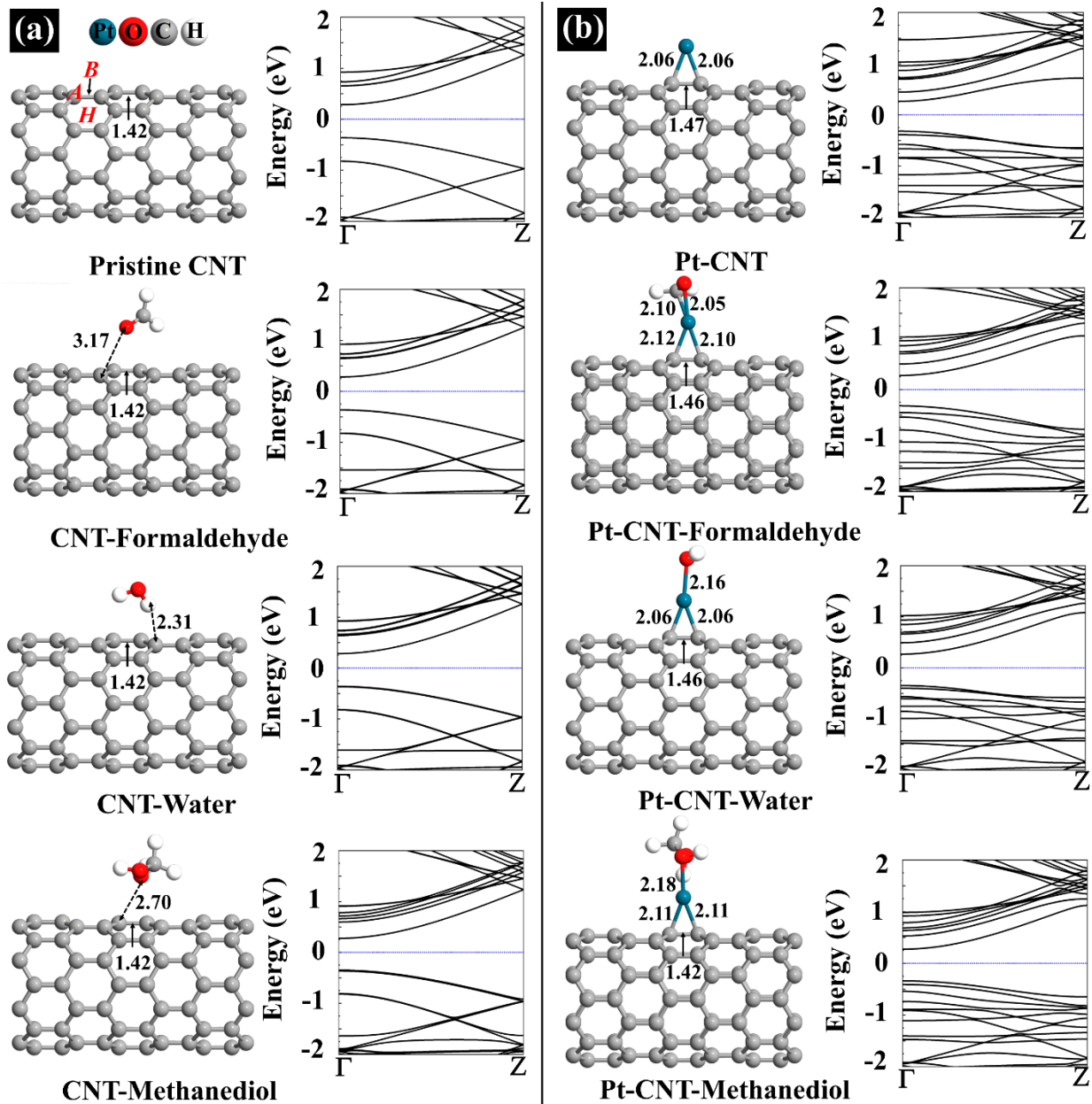


Figure 9-9. (a) The optimized structures of pristine CNT, CNT-formaldehyde, CNT-water, CNT-methanediol and their corresponding energy band structures. (b) The optimized structures of Pt- CNT, Pt-CNT-formaldehyde, Pt-CNT-water, Pt-CNT-methanediol and their corresponding energy band structures. The bond lengths and the binding distances are also given in the unit of Å. The sticks between atoms are only for visualization. The dotted blue line indicates the Fermi level, which is set to zero.

A platinum atom decorated on the surface of the SWCNT is expected to modify its electronic properties and enhance its reactivity toward formaldehyde adsorption. A single Pt atom

can adsorb on an SWCNT at different locations, including A site (above a C atom), B site (above a C–C bond), and H site (center of a C–C hexagon), as seen in Figure 9-9 (a). Based on our calculations, a Pt atom preferred to locate above the middle of the C–C bond, see **Error! Reference source not found.** (b), and form a Pt–C–C isosceles triangle with Pt–C and C–C side lengths of 2.06 and 1.47 Å, respectively. The C–C bond length near the Pt atom (1.47 Å) was longer than those in other areas of the tube (1.42 Å) because the formation of the Pt–C bond deteriorates the strength of the C–C bond in the nanotube. Furthermore, the C atoms connected to the Pt atom were protruded, showing the presence of sp^3 hybridization rather than sp^2 . As a result, the diameter of the pristine SWCNT (6.37 Å) was enlarged globally after decoration with a Pt atom (6.47 Å) in the decoration orientation. This conspicuous deformation in SWCNT after complexation with a Pt atom can be related to the strong adsorption energy (–2.572 eV) and a large charge transfer (0.101 e) between Pt and C atoms, in agreement with the literature [139, 143, 160, 212]. The C atoms with an electronegativity of 2.55 surrounding the Pt atom with an electronegativity of 2.28 draw electrons from the metal, resulting in the accumulation of positive charges on the metal atom. The energy bandgap of SWCNT (0.648 eV) became 0.582 eV after its decoration with Pt. This drop in the bandgap can be associated with the redistribution of the total charges after charge transfer from Pt atom to the SWCNT. One can conclude that Pt atom can act as a binding center for the molecules that cannot be trapped by the C atom in the pristine SWCNT.

Next, we addressed the adsorption mechanisms of the CH_2O , H_2O , and $\text{CH}_2(\text{OH})_2$ molecules onto a Pt-SWCNT. The most stable adsorption configurations are presented in Fig. 1 (b). The adsorption energies, binding distances, and the total charge transfer are tabulated in Table 9-1. The O and C atoms in the CH_2O molecule were trapped by Pt atom with distances of 2.05 Å and 2.10 Å, respectively. The strong chemical interactions between the formaldehyde and Pt atom

depress the Pt atom and SWCNT interactions, causing the Pt–C bond elongated from 2.06 Å to 2.12 and 2.10 Å during the adsorption process. Besides, the C–C bond of Pt-SWCNT in the interaction area (1.47 Å) was slightly reinforced after interaction with formaldehyde (1.46 Å) as a result of strength deterioration of Pt–C bonds. While CH₂O retained its molecular form, the H–C and O–C bond lengths, which were 1.09 Å and 1.20 Å in the isolated molecule, were elongated to 1.11 (1.10) Å and 1.32 Å, respectively, after interaction with the Pt decorated nanotube. The adsorption energy of the Pt-SWCNT-formaldehyde system was –2.067 eV, which is 7.33 times lower compared to that obtained for SWCNT-Formaldehyde system. A significant number of electrons (0.253 *e*) was transferred to the nanotube, confirming the strong interaction between the formaldehyde molecule and Pt coated SWCNT. Unlike the weak adsorption on pristine SWCNT, the water molecule can be chemisorbed on Pt-SWCNT, forming an O–Pt bond (2.16 Å) with an adsorption energy of –1.345 eV. Furthermore, a large amount of charge (0.156 *e*) was transferred to the nanotube upon the interaction between water and Pt-SWCNT. The Pt-SWCNT structure remained almost unchanged during the water adsorption.

Finally, the adsorption mechanism of methanediol on the Pt-SWCNT was investigated. The CH₂(OH)₂ molecule was chemically adsorbed on the Pt atom to form an O–Pt bond (2.18 Å). The Pt–C bond in Pt-SWCNT-methanediol became relatively weak (was elongated to 2.11 Å) due to strong interactions between methanediol and Pt atom. The adsorption energy (–1.550 eV) and charge transfer (0.170 *e*) confirmed the chemisorption of methanediol after interaction with the Pt-SWCNT; however, it was less stable compared to Pt-SWCNT-formaldehyde system. The adsorption of methanediol on Pt-SWCNT was 8.65 greater than that obtained for methanediol on pristine SWCNT.

The charge transfer from molecules to Pt-SWCNT brought about significant changes to the electronic properties of the nanotube. According to Figure 9-9 (b), the energy bandgap of Pt-SWCNT increased from 0.582 eV to 0.596, 0.613, and 0.612 eV after interaction with formaldehyde, water, and methanediol, respectively, suggesting that the conductivity of the system would drop.

Table 9-1. The calculated adsorption energy (E_{ad}), binding distance which is the shortest atom to atom distance between molecule and the nanotube (D), the charge transfer (Q) on the molecule or Pt, energy bandgap (E_g), and sensitivity (S). The negative values of charge indicate a charge transfer from the molecule to the nanotube.

System	E_{ad} (eV)	D (Å)	Q (e)	E_g (eV)	$ S $ (%)
Pristine SWCNT	-	-	-	0.648	-
SWCNT-Formaldehyde	- 0.282	3.09 (O-C)	- 0.003	0.646	4.08
SWCNT-Water	- 0.247	2.31 (H-C)	- 0.002	0.645	2.02
SWCNT-Methanediol	- 0.179	2.70 (O-C)	- 0.003	0.645	6.18
Pt-SWCNT	- 2.572	2.06 (C-Pt)	- 0.101	0.582	-
Pt-SWCNT-Formaldehyde	- 2.067	2.05 (O-Pt) and 2.10 (C-Pt)	- 0.253	0.596	24.44
Pt/SWCNT-Water	- 1.345	2.16 (O-Pt)	- 0.156	0.613	46.20
Pt-SWCNT-Methanediol	- 1.550	2.18 (O-Pt)	- 0.170	0.612	45.11

The density of states (DOS) of SWCNT and Pt-SWCNT are shown in Figure 9-10 (a). After adsorption of Pt atom, the electronic properties of SWCNT experienced significant changes. A Pt atom with an electron configuration of $[Xe] 4f^{14} 5d^9 6s^1$ has ten valence electrons. The orbital hybridization between the d -orbital of the Pt atom and π electron cloud of C atoms has the main contribution to the total DOS of the Pt-SWCNT system around the Fermi level. For Pt-SWCNT-molecule systems, the hybridization between Pt $5d$ and C $2p$ or O $2p$ orbitals of the molecule plays a vital role. An orbital hybridization exists if the DOS of two orbitals lie in the same energy range. To evaluate the metal-molecule interaction strengths, the number of overlapping peaks between d orbital of Pt and p orbital of C or O atom of the molecules were counted. In the case of Pt-SWCNT-

Formaldehyde, 22 overlapping peaks between d orbital of Pt atom and p orbitals of O and C atoms of formaldehyde were found in the valence and conduction bands, as seen in Figure 9-10 (b). The PDOS of the Pt-CNT-Water system demonstrated 13 overlapping peaks in the conduction band between d orbital of Pt and p orbital of O atom of water, see Figure 9-10 (c). Further, the hybridization of d orbital of Pt atom and s orbital of H atom and p orbital of O atom of water can be seen deep in the conduction band. In the case of Pt-SWCNT-Methanediol, 8 overlapping peaks between d orbital of Pt and p orbital of C atom of the methanediol were observed, check Figure 9-10 (d). The orbitals were also overlapped deep in the conduction band. It should be mentioned that although the number of overlapping peaks was higher in the case of Pt-SWCNT-Water compared to Pt-SWCNT-Methanediol, the intensity of p orbital of O atom of the molecule was much weaker in the former case, suggesting that the interaction of Pt-SWCNT with methanediol was more substantial than that with water.

To gain a deeper insight into the adsorption process of the gas molecules, the electronic total charge densities of the systems are provided in Figure 9-10 (e). Although there was no orbital overlap between pristine SWCNT and CH_2O , H_2O , and $\text{CH}_2(\text{OH})_2$ molecules, a strong (moderate) orbital overlap was observed between CH_2O (H_2O and $\text{CH}_2(\text{OH})_2$) molecules and Pt atom in Pt/SWCNT system, confirming the chemisorption of the molecules on the system. These results were in agreement with obtained adsorption energies, charge transfer, and binding distances.

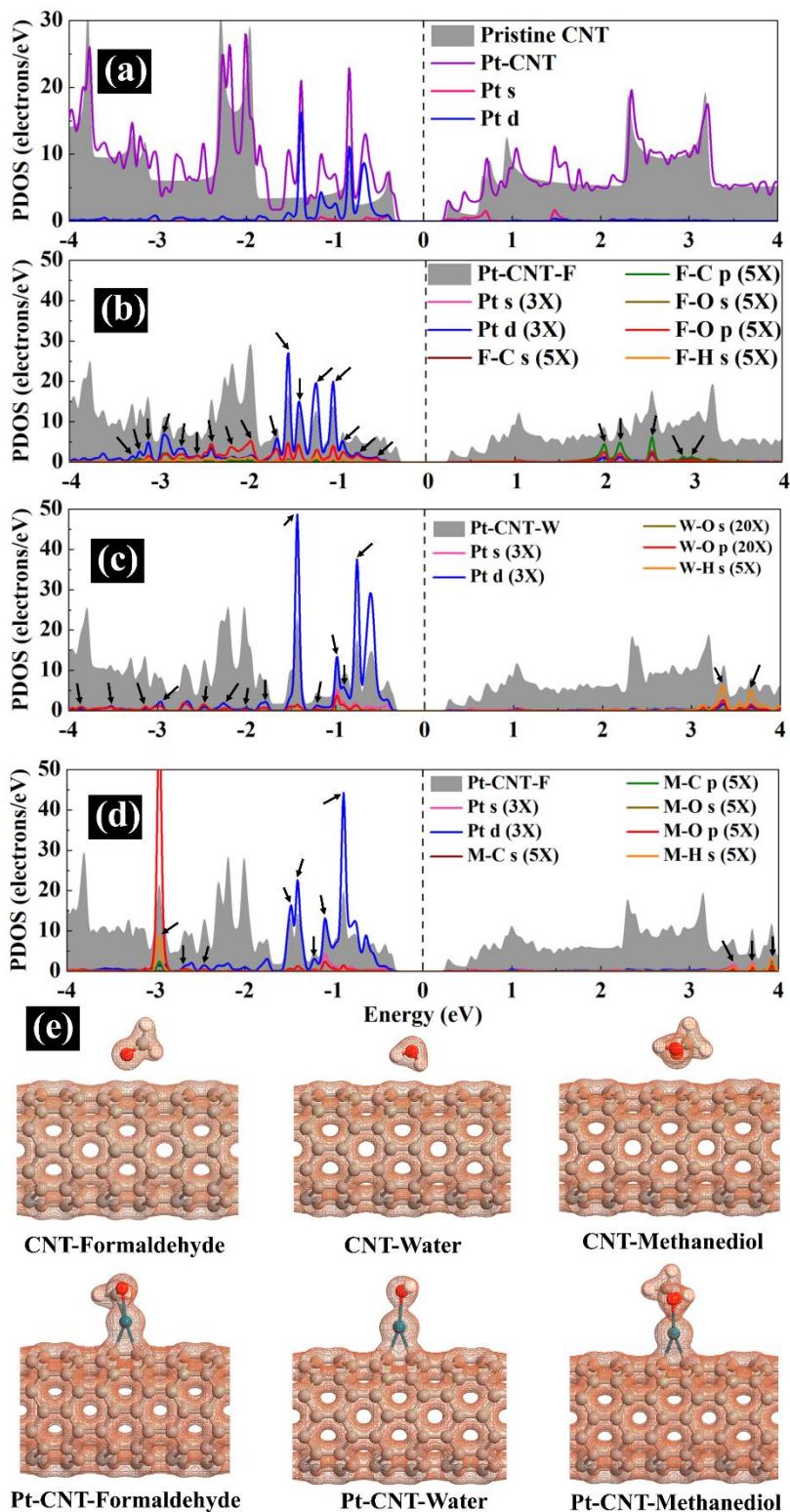


Figure 9-10. Total DOS curves for (a) pristine CNT, (b) Pt-CNT-formaldehyde (F), (c) Pt-CNT-water (W), and (d) Pt-CNT-methanediol (M). The dashed lines indicate the Fermi level, which are set to zero.

Sensitivity (S) is the variation of the conductivity (σ) for the sensors with and without gas is expressed as [165]:

$$S = \frac{\sigma_{\text{gas}} - \sigma_{\text{pure}}}{\sigma_{\text{pure}}} \times 100 \quad (29)$$

Here σ_{gas} and σ_{pure} are the conductivity of the toluene adsorbed system and isolated system, respectively. The electrical conductivity of a system can be evaluated using its bandgap (E_g) [165]:

$$\sigma = \sigma_0 \exp(-E_g / 2k_B T) \quad (30)$$

Here T is the temperature, and k_B is the Boltzmann constant. After the interaction of CH_2O , H_2O , and $\text{CH}_2(\text{OH})_2$ with pristine the SWCNT, the energy bandgaps were slightly decreased (the conductivities were increased), as can be seen in Table 9-1. These small changes agreed well with the small number of electrons exchanged between the molecules and the pristine SWCNT. Pristine SWCNT showed 4.08 %, 6.18 %, and 6.18 % sensitivity toward formaldehyde, water, and methanediol adsorption. As a result, the pristine SWCNT is not a suitable sensor for formaldehyde and methanediol detection. Pt decoration of the nanotubes boosted its sensing capability toward formaldehyde. The bandgap of Pt-SWCNT was widened 14, 31, and 30 meV upon interaction with CH_2O , H_2O , and $\text{CH}_2(\text{OH})_2$, respectively. An increase in the bandgap resulted in a significant drop in the conductivity of the system, making Pt-SWCNT an ideal platform for formaldehyde detection. Interestingly, although the Pt-SWCNT-formaldehyde had the highest adsorption energy, the Pt-SWCNT experienced more changes in its bandgap while interacting with methanediol and water. It was found that the sensitivities of Pt-SWCNT systems for formaldehyde, water, and methanediol detection are 24.44 %, 46.20 %, and 45.11 %, respectively. The sensitivity of Pt-SWCNT toward methanediol detection was 7.29 greater than that obtained for methanediol detection using pristine SWCNT.

The sensor recovery time (τ) can be expressed using the conventional transition state theory as follows [211]:

$$\tau \propto \exp(-E_{ad} / k_B T) \quad (31)$$

The smaller the adsorption energy is, the faster the desorption process would be. Since the chemisorption of the molecules on the Pt-SWCNT happened with high adsorption energies, therefore long recovery time was expected for the sensor to be completely recovered. Heating the nanotubes can accelerate the desorption process.

Summary

Figure 9-11 shows the experimental and theoretical sensitivities of the Pt-SWCNT sensor to formaldehyde, water, and methanediol. One can notice that there is a perfect match between results obtained in theory and the experiment for humidity (water) and formaldehyde in humidity (methanediol).

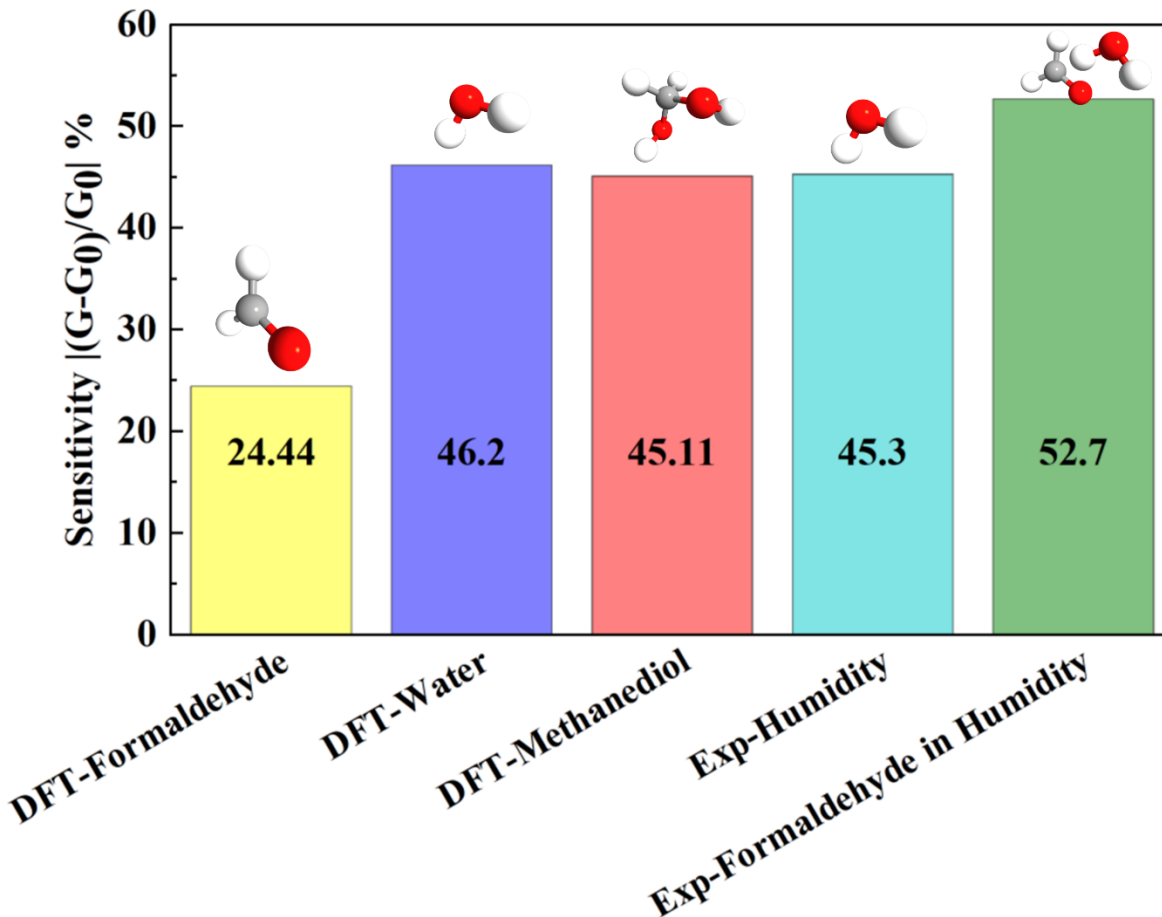


Figure 9-11. The experimental sensitivities of the back-gated Pt-decorated SWCNT FET to 80% humidity and formaldehyde in 80% humidity vs the DFT sensitivities of the Pt-decorated SWCNT to individual formaldehyde, water, and methanediol molecule.

In conclusion, combining experimental data with DFT calculations, we showed that aldehydes at a sub-ppb level in super-saturated water vapor (mimicking human breath) can be detected using nanotube molecular FETs. Our DFT results showed that the Pt-SWCNT is 7.29 times more sensitive than pristine SWCNT to methanediol (formaldehyde in humidity). Inspired by theoretical calculations, back-gated FETs with a thin film of high-purity semiconducting SWCNTs as the sensing material were fabricated. The on/off current ratios of the FETs were significantly enhanced from 10^2 to 10^6 using an electrical breakdown technique based on removing metallic paths between source and drain. The high-performance back gated pristine

SWCNT FET showed a small sensitivity of 2.33% to 300 ppm formaldehyde in 80% humidity. The sensitivity of the back gated pristine SWCNT FET was improved to 26.99% by decorating the sensing material with Pt nanoparticles. Back-gated Pt-decorated SWCNT FETs showed a highly sensitive and reversible response to formaldehyde down to 3 ppb in humid air at room temperature and RH=80%. A theoretical LOD of sub-ppb revealed the significant potential of our sensors for the detection of very low concentrations of formaldehyde in lung cancer patients' breath. The sensor recovery time was found to 330 sec and 115 sec in a dry atmosphere and at RH=80%, respectively, at $T = 70^{\circ}\text{C}$.

10. Chapter 10

Conclusion and Future Directions

The discovery and development of disease biomarkers has revolutionized the diagnosis and treatment of many diseases. Biomarkers can be classified into several categories based on their characteristics and functions. The ability to identify diseases using human breath has been made possible by modern nanotechnology, which has allowed the development of gas sensors that can detect and monitor a variety of diseases from human breath. Gas-sensing detection of human breath provides early diagnosis that is quick, affordable, and non-invasive. Semiconductor gas sensors are among the best components for sensor integration, as they can achieve simultaneous recognition for many analytes, improving the accuracy of diagnosis when used in conjunction with pattern-recognition technology. The analysis of volatile organic compounds in exhaled breath samples provides a new frontier in medical diagnostics due to their noninvasive nature and possible cost-effectiveness.

Today, advanced materials and technologies, such as using trained canines or nanotube molecular FETs, can be utilized for the detection of volatile organic compounds (VOCs) in human breath. By utilizing metal-decorated SWCNTs, it is possible to significantly improve the adsorption energy of toluene, an important lung cancer biomarker in exhaled breath of patients. Metal-decorated SWCNTs offer promising results for the early screening of lung cancer from human breath or for sensors used in personal safety monitoring in various environments. Toluene (C_7H_8) and formaldehyde (CH_2O) organic aromatic compounds are considered essential lung cancer biomarkers.

In our recent study, first-principle calculations were used to investigate the interaction between toluene, an important lung cancer biomarker, and pristine and metal-decorated SWCNTs. The results showed that utilizing transition metals like Pt, Pd, Rh, or Ru on SWCNT systems as the adsorbent significantly improved the adsorption energy of toluene, leading to stronger chemisorption. Metal-decorated SWCNTs offer promising potential for the early screening of lung cancer from human breath, with Rh- and Ru-SWCNT systems offering outstanding responses to toluene. In another study, nanotube molecular FETs were used to detect formaldehyde in supersaturated water vapor mimicking human breath. By decorating the sensing material with Pt nanoparticles, the back-gated Pt-decorated SWCNT FETs showed highly sensitive and reversible responses to formaldehyde down to 3 ppb, with a theoretical limit of detection (LOD) of sub-ppb. These sensors have significant potential for detecting very low concentrations of formaldehyde in lung cancer patients' breath. Moreover, we used the SWCNT based gas sensor for the detection of liver cancer biomarkers in exhaled breath. We found that Pt-decorated SWCNT has a higher capability for detecting octenol, decane, and hexanal (as liver cancer biomarkers) compared to pristine SWCNT, resulting in chemisorption.

Next, we shifted our attention to phosphorene as a 2D subfamily and scrutinized the adsorption behavior of pristine and Pt-decorated phosphorene with various VOCs, CO₂ and H₂O. The results indicated that only physisorption occurred on the pristine phosphorene with no significant electronic changes, while the interactions were enhanced after decorating the surface with Pt. The Pt-decorated phosphorene system showed high sensitivity, selectivity, and short recovery time for detecting methanol at room temperature. The findings suggest the potential of metal-decorated phosphorene-based gas sensors for VOCs gas sensing applications.

Furthermore, we investigated the adsorption of potential biomarkers for colorectal and breast cancer on TMD 2D nanomaterials using first-principles calculations based on density functional theory. We find that the adsorption of Benzaldehyde and Indole (colorectal cancer biomarkers) on pristine MoS₂ is physisorption, with slight charge transfer and moderate adsorption energy. However, after decorating MoS₂ with Pt and Pd atoms, the adsorption energy, charge transfer, and recovery time are significantly improved, making Pt- and Pd-MoS₂ sensors effective platforms for detecting these biomarkers. Similarly, we studied the adsorption of nonanal and octanal (breast cancer biomarkers) on pristine WS₂ and WS₂ decorated with Ni and Pt. We find that the adsorption of these biomarkers on pristine WS₂ is physisorption, but after decoration with Ni and Pt, the adsorption energy and sensitivity towards octanal are significantly improved, making Ni- and Pt-WS₂ prominent adsorbing substrates for this biomarker.

In another survey, novel graphene like BC₆N monolayer was selected to be investigated. The study explored the potential of defective BC₆N as a sensitive and selective material for VOC sensors used in breath analysis. The investigation included the adsorption of various gas molecules and their effects on the electronic properties of the material. It was found that defective BC₆N showed high sensitivity and selectivity to ethanol in the presence of water, and the recovery time of the VOC sensor was very short. These findings suggest that defective BC₆N could be a promising material for the detection of different biomarkers in human breath.

In seeking for new materials, we have investigated the adsorption of small inorganic gas molecules on PdPS and PdPSe monolayers (as novel material) using density functional theory calculations. The results revealed that PdPS and PdPSe-based gas sensors have potential for NO and NO₂ detection due to their reasonable adsorption energy and recovery time. Additionally, the study found that CO, CO₂, and NH₃ gas adsorption on the PdPS and PdPSe sheets involved

physisorption, while NO₂ and NO adsorption led to significant band gap changes. These findings suggest that PdPS and PdPSe-based gas sensors could provide a promising sensing platform, but further experimental investigation is needed.

All in all, the use of nanosensors for the detection of diseases like cancer through exhaled breath shows great potential as a non-invasive and cost-effective diagnostic tool. Various types of Point-of-care (POC) devices based on nanosensors have been developed and tested for the detection of specific biomarkers in exhaled breath, and promising results have been obtained in some cases. However, there are still several challenges that need to be addressed, including the analysis procedures, the optimization of sensor sensitivity and selectivity, and the validation of results through large-scale clinical trials, the exploration of new biomarkers for different types of cancers and further research is needed to improve the performance of nanosensors. Overall, the use of nanosensors for in-vitro diagnostics (IVD) and especially for disease detection in exhaled breath holds great promise for improving healthcare outcomes and saving lives and capital, and continued research in this area is crucial for realizing this potential.

References

- [1] S. Bayda, M. Adeel, T. Tuccinardi, M. Cordani, and F. Rizzolio, "The history of nanoscience and nanotechnology: from chemical–physical applications to nanomedicine," *Molecules*, vol. 25, no. 1, p. 112, 2019.

- [2] M. C. Roco, "The long view of nanotechnology development: the National Nanotechnology Initiative at 10 years," in *Nanotechnology research directions for societal needs in 2020*: Springer, 2011, pp. 1-28.
- [3] U. Yaqoob and M. I. Younis, "Chemical gas sensors: Recent developments, challenges, and the potential of machine learning—A review," *Sensors*, vol. 21, no. 8, p. 2877, 2021.
- [4] B. Saruhan, R. Lontio Fomekong, and S. Nahirniak, "Influences of semiconductor metal oxide properties on gas sensing characteristics," *Frontiers in Sensors*, vol. 2, p. 657931, 2021.
- [5] S. Mehdi Aghaei, A. Aasi, and B. Panchapakesan, "Experimental and Theoretical Advances in MXene-Based Gas Sensors," *ACS Omega*, 2021/01/20 2021, doi: 10.1021/acsomega.0c05766.
- [6] M. Kiani, M. U. Rehman, X. Tian, and B. Yakobson, "Two-Dimensional Nanomaterials for the Development of Efficient Gas Sensors: Recent Advances, Challenges, and Future Perspectives," *Advanced Materials Technologies*, vol. 7, no. 7, p. 2101252, 2022.
- [7] S. M. Sze, Y. Li, and K. K. Ng, *Physics of semiconductor devices*. John wiley & sons, 2021.
- [8] G. E. Moore, "Cramming more components onto integrated circuits," *Proceedings of the IEEE*, vol. 86, no. 1, pp. 82-85, 1998.
- [9] M. Lundstrom, "Moore's law forever?," *Science*, vol. 299, no. 5604, pp. 210-211, 2003.
- [10] Y.-F. Sun *et al.*, "Metal oxide nanostructures and their gas sensing properties: a review," *Sensors*, vol. 12, no. 3, pp. 2610-2631, 2012.
- [11] C. Dincer *et al.*, "Disposable sensors in diagnostics, food, and environmental monitoring," *Advanced Materials*, vol. 31, no. 30, p. 1806739, 2019.
- [12] Z. Ni *et al.*, "Tunable bandgap in silicene and germanene," *Nano letters*, vol. 12, no. 1, pp. 113-118, 2012.
- [13] Y. Yoon, K. Ganapathi, and S. Salahuddin, "How good can monolayer MoS₂ transistors be?," *Nano letters*, vol. 11, no. 9, pp. 3768-3773, 2011.
- [14] V. Nagarajan, B. Vishnuja, and R. Chandiramouli, "Adsorption studies of SF₆ and decomposed constituents on 4–8 arsenene nanotubes—A first-principles study," *Computational and Theoretical Chemistry*, vol. 1211, p. 113663, 2022.
- [15] J. Cao, J. Zhou, J. Chen, W. Wang, Y. Zhang, and X. Liu, "Effects of phase selection on gas-sensing performance of MoS₂ and WS₂ substrates," *ACS omega*, vol. 5, no. 44, pp. 28823-28830, 2020.
- [16] Q. H. Wang, K. Kalantar-Zadeh, A. Kis, J. N. Coleman, and M. S. Strano, "Electronics and optoelectronics of two-dimensional transition metal dichalcogenides," *Nature nanotechnology*, vol. 7, no. 11, pp. 699-712, 2012.
- [17] G. Fiori *et al.*, "Electronics based on two-dimensional materials," *Nature nanotechnology*, vol. 9, no. 10, pp. 768-779, 2014.
- [18] F. Schwierz, J. Pezoldt, and R. Granzner, "Two-dimensional materials and their prospects in transistor electronics," *Nanoscale*, vol. 7, no. 18, pp. 8261-8283, 2015.
- [19] C. Tan *et al.*, "Recent advances in ultrathin two-dimensional nanomaterials," *Chemical reviews*, vol. 117, no. 9, pp. 6225-6331, 2017.
- [20] A. Aasi, S. M. Aghaei, and B. Panchapakesan, "A density functional theory study on the interaction of toluene with transition metal decorated carbon nanotubes: a promising platform for early detection of lung cancer from human breath," *Nanotechnology*, vol. 31, no. 41, p. 415707, 2020.
- [21] J. Pereira *et al.*, "Breath analysis as a potential and non-invasive frontier in disease diagnosis: an overview," *Metabolites*, vol. 5, no. 1, pp. 3-55, 2015.
- [22] M. Kaloumenou, E. Skotadis, N. Lagopati, E. Efstathopoulos, and D. Tsoukalas, "Breath Analysis: A Promising Tool for Disease Diagnosis—The Role of Sensors," *Sensors*, vol. 22, no. 3, p. 1238, 2022.

- [23] I. Sayago *et al.*, "Carbon nanotube networks as gas sensors for NO₂ detection," *Talanta*, vol. 77, no. 2, pp. 758-764, 2008/12/15/ 2008, doi: <https://doi.org/10.1016/j.talanta.2008.07.025>.
- [24] A. Goldoni, L. Petaccia, S. Lizzit, and R. Larciprete, "Sensing gases with carbon nanotubes: a review of the actual situation," *Journal of Physics: Condensed Matter*, vol. 22, no. 1, p. 013001, 2009/12/02 2010, doi: 10.1088/0953-8984/22/1/013001.
- [25] E. Lee, Y. S. Yoon, and D.-J. Kim, "Two-dimensional transition metal dichalcogenides and metal oxide hybrids for gas sensing," *ACS sensors*, vol. 3, no. 10, pp. 2045-2060, 2018.
- [26] C.-C. Liu, W. Feng, and Y. Yao, "Quantum spin Hall effect in silicene and two-dimensional germanium," *Physical review letters*, vol. 107, no. 7, p. 076802, 2011.
- [27] M. Gmitra, S. Konschuh, C. Ertler, C. Ambrosch-Draxl, and J. Fabian, "Band-structure topologies of graphene: Spin-orbit coupling effects from first principles," *Physical Review B*, vol. 80, no. 23, p. 235431, 2009.
- [28] Y. Cai, G. Zhang, and Y.-W. Zhang, "Layer-dependent band alignment and work function of few-layer phosphorene," *Scientific reports*, vol. 4, p. 6677, 2014.
- [29] A. Aaryashree, P. Shinde, A. Kumar, D. J. Late, and C. S. Rout, "Recent advances in 2D black phosphorus based materials for gas sensing applications," *Journal of Materials Chemistry C*, 2021.
- [30] M. Akhtar *et al.*, "Recent advances in synthesis, properties, and applications of phosphorene," *npj 2D Materials and Applications*, vol. 1, no. 1, pp. 1-13, 2017.
- [31] S. Joseph *et al.*, "Theoretical study on tuning band gap and electronic properties of atomically thin nanostructured MoS₂/metal cluster heterostructures," *ACS omega*, vol. 6, no. 10, pp. 6623-6628, 2021.
- [32] H.-P. Komsa and A. V. Krasheninnikov, "Two-dimensional transition metal dichalcogenide alloys: stability and electronic properties," *The journal of physical chemistry letters*, vol. 3, no. 23, pp. 3652-3656, 2012.
- [33] S. Mouri, Y. Miyauchi, and K. Matsuda, "Tunable photoluminescence of monolayer MoS₂ via chemical doping," *Nano letters*, vol. 13, no. 12, pp. 5944-5948, 2013.
- [34] H. Zou, Q. Zeng, M. Peng, W. Zhou, X. Dai, and F. Ouyang, "Electronic structures and optical properties of P and Cl atoms adsorbed/substitutionally doped monolayer MoS₂," *Solid State Communications*, vol. 280, pp. 6-12, 2018.
- [35] P. Xiao *et al.*, "Solution-processed 3D RGO–MoS₂/pyramid Si heterojunction for ultrahigh detectivity and ultra-broadband photodetection," *Advanced Materials*, vol. 30, no. 31, p. 1801729, 2018.
- [36] A. Li, J. Pan, Z. Yang, L. Zhou, X. Xiong, and F. Ouyang, "Charge and strain induced magnetism in monolayer MoS₂ with S vacancy," *Journal of Magnetism and Magnetic Materials*, vol. 451, pp. 520-525, 2018.
- [37] J. Zhang *et al.*, "Reversible and selective ion intercalation through the top surface of few-layer MoS₂," *Nature communications*, vol. 9, no. 1, pp. 1-9, 2018.
- [38] W. Liao, Y. Huang, H. Wang, and H. Zhang, "Van der Waals heterostructures for optoelectronics: progress and prospects," *Applied Materials Today*, vol. 16, pp. 435-455, 2019.
- [39] O. Leenaerts, B. Partoens, and F. Peeters, "Adsorption of H₂O, N₂, CO, and NO on graphene: A first-principles study," *Physical Review B*, vol. 77, no. 12, p. 125416, 2008.
- [40] Y.-H. Zhang *et al.*, "Improving gas sensing properties of graphene by introducing dopants and defects: a first-principles study," *Nanotechnology*, vol. 20, no. 18, p. 185504, 2009.
- [41] J. Dai, J. Yuan, and P. Giannozzi, "Gas adsorption on graphene doped with B, N, Al, and S: A theoretical study," *Applied Physics Letters*, vol. 95, no. 23, p. 232105, 2009.
- [42] J. Dai and J. Yuan, "Adsorption of molecular oxygen on doped graphene: Atomic, electronic, and magnetic properties," *Physical Review B*, vol. 81, no. 16, p. 165414, 2010.

- [43] S. J. Ray, "First-principles study of MoS₂, phosphorene and graphene based single electron transistor for gas sensing applications," *Sensors and Actuators B: Chemical*, vol. 222, pp. 492-498, 2016/01/01/ 2016, doi: <https://doi.org/10.1016/j.snb.2015.08.039>.
- [44] L. Kou, T. Frauenheim, and C. Chen, "Phosphorene as a superior gas sensor: selective adsorption and distinct I–V response," *The Journal of Physical Chemistry Letters*, vol. 5, no. 15, pp. 2675-2681, 2014.
- [45] M. Xu, T. Liang, M. Shi, and H. Chen, "Graphene-Like Two-Dimensional Materials," *Chemical Reviews*, vol. 113, no. 5, pp. 3766-3798, 2013/05/08 2013, doi: 10.1021/cr300263a.
- [46] T. Kuila, S. Bose, A. K. Mishra, P. Khanra, N. H. Kim, and J. H. Lee, "Chemical functionalization of graphene and its applications," *Progress in Materials Science*, vol. 57, no. 7, pp. 1061-1105, 2012/09/01/ 2012, doi: <https://doi.org/10.1016/j.pmatsci.2012.03.002>.
- [47] A. K. Geim and K. S. Novoselov, "The rise of graphene," *Nature materials*, vol. 6, no. 3, pp. 183-191, 2007.
- [48] S. Iijima, "Helical microtubules of graphitic carbon," *nature*, vol. 354, no. 6348, pp. 56-58, 1991.
- [49] Y. Tian *et al.*, "Analysis of the size distribution of single-walled carbon nanotubes using optical absorption spectroscopy," *The Journal of Physical Chemistry Letters*, vol. 1, no. 7, pp. 1143-1148, 2010.
- [50] H. Zhu, C. Xu, D. Wu, B. Wei, R. Vajtai, and P. Ajayan, "Direct synthesis of long single-walled carbon nanotube strands," *Science*, vol. 296, no. 5569, pp. 884-886, 2002.
- [51] O. V. Kharissova and B. I. Kharisov, "Variations of interlayer spacing in carbon nanotubes," *Rsc Advances*, vol. 4, no. 58, pp. 30807-30815, 2014.
- [52] H. Dai, "Carbon nanotubes: opportunities and challenges," *Surface science*, vol. 500, no. 1-3, pp. 218-241, 2002.
- [53] J. Hass, W. De Heer, and E. Conrad, "The growth and morphology of epitaxial multilayer graphene," *Journal of Physics: Condensed Matter*, vol. 20, no. 32, p. 323202, 2008.
- [54] A. Krishnan, E. Dujardin, T. Ebbesen, P. Yianilos, and M. Treacy, "Young's modulus of single-walled nanotubes," *Physical review B*, vol. 58, no. 20, p. 14013, 1998.
- [55] M.-F. Yu, O. Lourie, M. J. Dyer, K. Moloni, T. F. Kelly, and R. S. Ruoff, "Strength and breaking mechanism of multiwalled carbon nanotubes under tensile load," *Science*, vol. 287, no. 5453, pp. 637-640, 2000.
- [56] D. V. Smitherman Jr, "Technology Development and Demonstration Concepts for the Space Elevator," in *55th International Astronautical Congress of the International Astronautical Federation, the International Academy of Astronautics, and the International Institute of Space Law*, 2004, p. IAA. 3.8. 3.02.
- [57] A. M. Cassell, J. A. Raymakers, J. Kong, and H. Dai, "Large scale CVD synthesis of single-walled carbon nanotubes," *The Journal of Physical Chemistry B*, vol. 103, no. 31, pp. 6484-6492, 1999.
- [58] Y. Zhan, Z. Liu, S. Najmaei, P. M. Ajayan, and J. Lou, "Large-area vapor-phase growth and characterization of MoS₂ atomic layers on a SiO₂ substrate," *Small*, vol. 8, no. 7, pp. 966-971, 2012.
- [59] J. W. Suk *et al.*, "Transfer of CVD-grown monolayer graphene onto arbitrary substrates," *ACS nano*, vol. 5, no. 9, pp. 6916-6924, 2011.
- [60] K. Novoselov, o. A. Mishchenko, o. A. Carvalho, and A. Castro Neto, "2D materials and van der Waals heterostructures," *Science*, vol. 353, no. 6298, p. aac9439, 2016.
- [61] Q. Cao and J. A. Rogers, "Ultrathin films of single-walled carbon nanotubes for electronics and sensors: a review of fundamental and applied aspects," *Advanced Materials*, vol. 21, no. 1, pp. 29-53, 2009.

- [62] K. Hata, D. N. Futaba, K. Mizuno, T. Namai, M. Yumura, and S. Iijima, "Water-assisted highly efficient synthesis of impurity-free single-walled carbon nanotubes," *Science*, vol. 306, no. 5700, pp. 1362-1364, 2004.
- [63] T. Hiraoka *et al.*, "Synthesis of single- and double-walled carbon nanotube forests on conducting metal foils," *Journal of the American Chemical Society*, vol. 128, no. 41, pp. 13338-13339, 2006.
- [64] C. L. Cheung, J. H. Hafner, and C. M. Lieber, "Carbon nanotube atomic force microscopy tips: Direct growth by chemical vapor deposition and application to high-resolution imaging," *Proceedings of the National Academy of Sciences*, vol. 97, no. 8, pp. 3809-3813, 2000.
- [65] D.-m. Sun *et al.*, "Flexible high-performance carbon nanotube integrated circuits," *Nature nanotechnology*, vol. 6, no. 3, pp. 156-161, 2011.
- [66] G. Kalita and M. Tanemura, "Fundamentals of chemical vapor deposited graphene and emerging applications," *Graphene Materials-Advanced Applications*, pp. 30-35, 2017.
- [67] I. Dube, *Mechanism of gas sensing in carbon nanotube field effect transistors*. Georgetown University, 2014.
- [68] C. Thomsen and S. Reich, "Raman scattering in carbon nanotubes," *Light Scattering in Solid IX*, pp. 115-234, 2007.
- [69] R. Gusmao, Z. Sofer, and M. Pumera, "Black phosphorus rediscovered: from bulk material to monolayers," *Angewandte Chemie International Edition*, vol. 56, no. 28, pp. 8052-8072, 2017.
- [70] T. Kaewmaraya *et al.*, "Novel green phosphorene as a superior chemical gas sensing material," *Journal of Hazardous Materials*, vol. 401, p. 123340, 2021.
- [71] A. Aasi, R. Javahersaz, S. Mehdi Aghaei, and B. Panchapakesan, "Novel green phosphorene as a superior gas sensor for dissolved gas analysis in oil transformers: using DFT method," *Molecular Simulation*, pp. 1-10, 2022.
- [72] A. Aasi, E. Aasi, S. Mehdi Aghaei, and B. Panchapakesan, "Green Phosphorene as a Promising Biosensor for Detection of Furan and p-Xylene as Biomarkers of Disease: A DFT Study," *Sensors*, vol. 22, no. 9, p. 3178, 2022. [Online]. Available: <https://www.mdpi.com/1424-8220/22/9/3178>.
- [73] L. Li *et al.*, "Black phosphorus field-effect transistors," *Nature nanotechnology*, vol. 9, no. 5, p. 372, 2014.
- [74] H. Liu *et al.*, "Phosphorene: an unexplored 2D semiconductor with a high hole mobility," *ACS nano*, vol. 8, no. 4, pp. 4033-4041, 2014.
- [75] A. Jain and A. J. McGaughey, "Strongly anisotropic in-plane thermal transport in single-layer black phosphorene," *Scientific reports*, vol. 5, no. 1, pp. 1-5, 2015.
- [76] R. Kumar, N. Goel, M. Hojamberdiev, and M. Kumar, "Transition metal dichalcogenides-based flexible gas sensors," *Sensors and Actuators A: Physical*, vol. 303, p. 111875, 2020.
- [77] D. J. Late *et al.*, "Sensing behavior of atomically thin-layered MoS₂ transistors," *ACS nano*, vol. 7, no. 6, pp. 4879-4891, 2013.
- [78] H. Tao, Y. Zhang, Y. Gao, Z. Sun, C. Yan, and J. Texter, "Scalable exfoliation and dispersion of two-dimensional materials—an update," *Physical Chemistry Chemical Physics*, vol. 19, no. 2, pp. 921-960, 2017.
- [79] B. Cho *et al.*, "Charge-transfer-based gas sensing using atomic-layer MoS₂," *Scientific reports*, vol. 5, no. 1, pp. 1-6, 2015.
- [80] T. Pham, G. Li, E. Bekyarova, M. E. Itkis, and A. Mulchandani, "MoS₂-based optoelectronic gas sensor with sub-parts-per-billion limit of NO₂ gas detection," *ACS nano*, vol. 13, no. 3, pp. 3196-3205, 2019.
- [81] B. Liu, L. Chen, G. Liu, A. N. Abbas, M. Fathi, and C. Zhou, "High-performance chemical sensing using Schottky-contacted chemical vapor deposition grown monolayer MoS₂ transistors," *ACS nano*, vol. 8, no. 5, pp. 5304-5314, 2014.

- [82] N. Nasiri and C. Clarke, "Nanostructured gas sensors for medical and health applications: low to high dimensional materials," *Biosensors*, vol. 9, no. 1, p. 43, 2019.
- [83] Z. Jia, A. Patra, V. K. Kutty, and T. Venkatesan, "Critical review of volatile organic compound analysis in breath and in vitro cell culture for detection of lung cancer," *Metabolites*, vol. 9, no. 3, p. 52, 2019.
- [84] A. Krilaviciute, J. A. Heiss, M. Leja, J. Kupcinskas, H. Haick, and H. Brenner, "Detection of cancer through exhaled breath: a systematic review," *Oncotarget*, vol. 6, no. 36, p. 38643, 2015.
- [85] M. Phillips *et al.*, "Volatile markers of breast cancer in the breath," *The breast journal*, vol. 9, no. 3, pp. 184-191, 2003.
- [86] N. Alkhouri *et al.*, "Isoprene in the exhaled breath is a novel biomarker for advanced fibrosis in patients with chronic liver disease: a pilot study," *Clinical and translational gastroenterology*, vol. 6, no. 9, p. e112, 2015.
- [87] N. De Vietro *et al.*, "Relationship between cancer tissue derived and exhaled volatile organic compound from colorectal cancer patients. Preliminary results," *Journal of Pharmaceutical and Biomedical Analysis*, vol. 180, p. 113055, 2020.
- [88] P. A. Russo *et al.*, "Room-temperature hydrogen sensing with heteronanostructures based on reduced graphene oxide and tin oxide," *Angewandte Chemie International Edition*, vol. 51, no. 44, pp. 11053-11057, 2012.
- [89] W. Yang, P. Wan, X. Zhou, J. Hu, Y. Guan, and L. Feng, "Additive-free synthesis of In₂O₃ cubes embedded into graphene sheets and their enhanced NO₂ sensing performance at room temperature," *ACS Applied Materials & Interfaces*, vol. 6, no. 23, pp. 21093-21100, 2014.
- [90] L. Li, S. He, M. Liu, C. Zhang, and W. Chen, "Three-dimensional mesoporous graphene aerogel-supported SnO₂ nanocrystals for high-performance NO₂ gas sensing at low temperature," *Analytical chemistry*, vol. 87, no. 3, pp. 1638-1645, 2015.
- [91] H. Zhang, J. Feng, T. Fei, S. Liu, and T. Zhang, "SnO₂ nanoparticles-reduced graphene oxide nanocomposites for NO₂ sensing at low operating temperature," *Sensors and Actuators B: Chemical*, vol. 190, pp. 472-478, 2014.
- [92] D. Jariwala, V. K. Sangwan, L. J. Lauhon, T. J. Marks, and M. C. Hersam, "Emerging device applications for semiconducting two-dimensional transition metal dichalcogenides," *ACS nano*, vol. 8, no. 2, pp. 1102-1120, 2014.
- [93] Z. Zhang *et al.*, "Hydrogen gas sensor based on metal oxide nanoparticles decorated graphene transistor," *Nanoscale*, vol. 7, no. 22, pp. 10078-10084, 2015.
- [94] Y. H. Kim *et al.*, "Self-activated transparent all-graphene gas sensor with endurance to humidity and mechanical bending," *ACS nano*, vol. 9, no. 10, pp. 10453-10460, 2015.
- [95] S. Kumar, S. Kaushik, R. Pratap, and S. Raghavan, "Graphene on paper: A simple, low-cost chemical sensing platform," *ACS applied materials & interfaces*, vol. 7, no. 4, pp. 2189-2194, 2015.
- [96] D. Sarkar *et al.*, "Functionalization of transition metal dichalcogenides with metallic nanoparticles: implications for doping and gas-sensing," *Nano letters*, vol. 15, no. 5, pp. 2852-2862, 2015.
- [97] S. Cui, Z. Wen, X. Huang, J. Chang, and J. Chen, "Stabilizing MoS₂ nanosheets through SnO₂ nanocrystal decoration for high-performance gas sensing in air," *Small*, vol. 11, no. 19, pp. 2305-2313, 2015.
- [98] J. Pereira *et al.*, "Breath Analysis as a Potential and Non-Invasive Frontier in Disease Diagnosis: An Overview," (in English), *Metabolites*, vol. 5, no. 1, pp. 3-55, Mar 2015, doi: 10.3390/metabo5010003.
- [99] T. Thomas and T. J. Thomas, "Polyamine metabolism and cancer," (in English), *J Cell Mol Med*, vol. 7, no. 2, pp. 113-126, Apr-Jun 2003, doi: DOI 10.1111/j.1582-4934.2003.tb00210.x.

- [100] G. F. Kessler, L. M. Sheehan, and A. Lipton, "Urinary Polyamine Levels in Cancer-Patients," (in English), *P Am Assoc Canc Res*, vol. 15, no. Mar, pp. 41-41, 1974. [Online]. Available: <Go to ISI>://WOS:A1974S269500161.
- [101] M. McCulloch, T. Jezierski, M. Broffman, A. Hubbard, K. Turner, and T. Janecki, "Diagnostic accuracy of canine scent detection in early- and late-stage lung and breast cancers," (in English), *Integr Cancer Ther*, vol. 5, no. 1, pp. 30-39, Mar 2006, doi: 10.1177/1534735405285096.
- [102] T. R. Murray-Stewart, P. M. Woster, and R. A. Casero, "Targeting polyamine metabolism for cancer therapy and prevention," (in English), *Biochem J*, vol. 473, pp. 2937-2953, Oct 2016, doi: 10.1042/Bcj20160383.
- [103] F. R. Saunders and H. M. Wallace, "Polyamine metabolism and cancer prevention," (in English), *Biochem Soc T*, vol. 35, pp. 364-368, Apr 2007, doi: Doi 10.1042/Bst0350364.
- [104] G. Horvath, G. A. Jarverud, S. Jarverud, and I. Horvath, "Human ovarian carcinomas detected by specific odor," (in English), *Integr Cancer Ther*, vol. 7, no. 2, pp. 76-80, Jun 2008, doi: 10.1177/1534735408319058.
- [105] I. E. Tothill, "Biosensors for cancer markers diagnosis," in *Seminars in cell & developmental biology*, 2009, vol. 20, no. 1: Elsevier, pp. 55-62.
- [106] K. Schmidt and I. Podmore, "Current challenges in volatile organic compounds analysis as potential biomarkers of cancer," *Journal of biomarkers*, vol. 2015, 2015.
- [107] M. Ligor *et al.*, "Determination of volatile organic compounds in exhaled breath of patients with lung cancer using solid phase microextraction and gas chromatography mass spectrometry," (in English), *Clin Chem Lab Med*, vol. 47, no. 5, pp. 550-560, May 2009, doi: 10.1515/Cclm.2009.133.
- [108] A. L. Association, "Lung Cancer Fact Sheet," 2019. [Online]. Available: <https://www.lung.org/lung-health-diseases/lung-disease-lookup/lung-cancer/resource-library/lung-cancer-fact-sheet>.
- [109] A. Bajtarevic *et al.*, "Noninvasive detection of lung cancer by analysis of exhaled breath," *BMC cancer*, vol. 9, no. 1, p. 348, 2009.
- [110] K. D. Van de Kant, L. J. van der Sande, Q. Jöbsis, O. C. van Schayck, and E. Dompeling, "Clinical use of exhaled volatile organic compounds in pulmonary diseases: a systematic review," *Respiratory research*, vol. 13, no. 1, p. 117, 2012.
- [111] G. Gregis *et al.*, "Characterization of materials toward toluene traces detection for air quality monitoring and lung cancer diagnosis," *Materials Chemistry and Physics*, vol. 192, pp. 374-382, 2017.
- [112] H. Pyta, "BTX Air Pollution in Zabrze, Poland," *Polish Journal of Environmental Studies*, vol. 15, no. 5, 2006.
- [113] J. J. Shah and H. B. Singh, "Distribution of volatile organic chemicals in outdoor and indoor air: A national VOCs data base," *Environmental science & technology*, vol. 22, no. 12, pp. 1381-1388, 1988.
- [114] L. Sui *et al.*, "Au-loaded hierarchical MoO₃ hollow spheres with enhanced gas-sensing performance for the detection of BTX (benzene, toluene, and xylene) and the sensing mechanism," *ACS applied materials & interfaces*, vol. 9, no. 2, pp. 1661-1670, 2017.
- [115] K.-S. Kim *et al.*, "A nanopore structured high performance toluene gas sensor made by nanoimprinting method," *Sensors*, vol. 10, no. 1, pp. 765-774, 2010.
- [116] K. Suematsu *et al.*, "Nanoparticle cluster gas sensor: controlled clustering of SnO₂ nanoparticles for highly sensitive toluene detection," *ACS applied materials & interfaces*, vol. 6, no. 7, pp. 5319-5326, 2014.
- [117] B. Panchapakesan, D. L. DeVoe, M. R. Widmaier, R. Cavicchi, and S. Semancik, "Nanoparticle engineering and control of tin oxide microstructures for chemical microsensor applications," (in

- English), *Nanotechnology*, vol. 12, no. 3, pp. 336-349, Sep 2001, doi: Doi 10.1088/0957-4484/12/3/323.
- [118] L. Deng, X. Ding, D. Zeng, S. Zhang, and C. Xie, "High Sensitivity and Selectivity of C-Doped WO_3 Gas Sensors Toward Toluene and Xylene," *IEEE Sensors Journal*, vol. 12, no. 6, pp. 2209-2214, 2011.
- [119] S. Wang, Y. Wang, H. Zhang, X. Gao, J. Yang, and Y. Wang, "Fabrication of porous $\alpha\text{-Fe}_2\text{O}_3$ nanoshuttles and their application for toluene sensors," *RSC advances*, vol. 4, no. 58, pp. 30840-30849, 2014.
- [120] J. Kong *et al.*, "Nanotube molecular wires as chemical sensors," *science*, vol. 287, no. 5453, pp. 622-625, 2000.
- [121] P. G. Collins, K. Bradley, M. Ishigami, and d. A. Zettl, "Extreme oxygen sensitivity of electronic properties of carbon nanotubes," *science*, vol. 287, no. 5459, pp. 1801-1804, 2000.
- [122] O. Varghese, P. Kichambre, D. Gong, K. Ong, E. Dickey, and C. Grimes, "Gas sensing characteristics of multi-wall carbon nanotubes," *Sensors and Actuators B: Chemical*, vol. 81, no. 1, pp. 32-41, 2001.
- [123] A. Modi, N. Koratkar, E. Lass, B. Wei, and P. M. Ajayan, "Miniaturized gas ionization sensors using carbon nanotubes," *Nature*, vol. 424, no. 6945, pp. 171-174, 2003.
- [124] N. Peng, Q. Zhang, C. L. Chow, O. K. Tan, and N. Marzari, "Sensing mechanisms for carbon nanotube based NH_3 gas detection," *Nano letters*, vol. 9, no. 4, pp. 1626-1630, 2009.
- [125] Y. Wang and J. T. Yeow, "A review of carbon nanotubes-based gas sensors," *Journal of sensors*, vol. 2009, 2009.
- [126] M. M. Rana, D. S. Ibrahim, M. M. Asyraf, S. Jarin, and A. Tomal, "A review on recent advances of CNTs as gas sensors," *Sensor Review*, 2017.
- [127] T. Han, A. Nag, S. C. Mukhopadhyay, and Y. Xu, "Carbon Nanotubes and its gas-sensing applications: A Review," *Sensors and Actuators A: Physical*, 2019.
- [128] A. Abdelhalim, A. Abdellah, G. Scarpa, and P. Lugli, "Metallic nanoparticles functionalizing carbon nanotube networks for gas sensing applications," *Nanotechnology*, vol. 25, no. 5, p. 055208, 2014.
- [129] V. Schroeder, S. Savagatrup, M. He, S. Lin, and T. M. Swager, "Carbon nanotube chemical sensors," *Chemical reviews*, vol. 119, no. 1, pp. 599-663, 2018.
- [130] L. Woods, Ş. Bădescu, and T. Reinecke, "Adsorption of simple benzene derivatives on carbon nanotubes," *Physical Review B*, vol. 75, no. 15, p. 155415, 2007.
- [131] Y. Liu, J. Zhang, X. Chen, J. Zheng, G. Wang, and G. Liang, "Insights into the adsorption of simple benzene derivatives on carbon nanotubes," *RSC Advances*, vol. 4, no. 101, pp. 58036-58046, 2014.
- [132] B. Satishkumar, E. M. Vogl, A. Govindaraj, and C. Rao, "The decoration of carbon nanotubes by metal nanoparticles," *Journal of physics D: Applied physics*, vol. 29, no. 12, p. 3173, 1996.
- [133] J. Kong, M. G. Chapline, and H. Dai, "Functionalized carbon nanotubes for molecular hydrogen sensors," *Advanced Materials*, vol. 13, no. 18, pp. 1384-1386, 2001.
- [134] Q. Zhao, M. Buongiorno Nardelli, W. Lu, and J. Bernholc, "Carbon nanotube– metal cluster composites: a new road to chemical sensors?," *Nano Letters*, vol. 5, no. 5, pp. 847-851, 2005.
- [135] E. Espinosa *et al.*, "Metal-decorated multi-wall carbon nanotubes for low temperature gas sensing," *Thin Solid Films*, vol. 515, no. 23, pp. 8322-8327, 2007.
- [136] D. R. Kauffman, D. C. Sorescu, D. P. Schofield, B. L. Allen, K. D. Jordan, and A. Star, "Understanding the sensor response of metal-decorated carbon nanotubes," *Nano letters*, vol. 10, no. 3, pp. 958-963, 2010.

- [137] R. Leghrib, A. Felten, F. Demoisson, F. Reniers, J.-J. Pireaux, and E. Llobet, "Room-temperature, selective detection of benzene at trace levels using plasma-treated metal-decorated multiwalled carbon nanotubes," *Carbon*, vol. 48, no. 12, pp. 3477-3484, 2010.
- [138] Z. Zanolli, R. Leghrib, A. Felten, J.-J. Pireaux, E. Llobet, and J.-C. Charlier, "Gas sensing with Au-decorated carbon nanotubes," *ACS nano*, vol. 5, no. 6, pp. 4592-4599, 2011.
- [139] K. Li, W. Wang, and D. Cao, "Metal (Pd, Pt)-decorated carbon nanotubes for CO and NO sensing," *Sensors and Actuators B: chemical*, vol. 159, no. 1, pp. 171-177, 2011.
- [140] R. Leghrib, T. Dufour, F. Demoisson, N. Claessens, F. Reniers, and E. Llobet, "Gas sensing properties of multiwall carbon nanotubes decorated with rhodium nanoparticles," *Sensors and actuators B: Chemical*, vol. 160, no. 1, pp. 974-980, 2011.
- [141] Y. J. Kwon, H. G. Na, S. Y. Kang, S.-W. Choi, S. S. Kim, and H. W. Kim, "Selective detection of low concentration toluene gas using Pt-decorated carbon nanotubes sensors," *Sensors and Actuators B: Chemical*, vol. 227, pp. 157-168, 2016.
- [142] X. Zhang, H. Cui, X. Dong, D. Chen, and J. Tang, "Adsorption performance of Rh decorated SWCNT upon SF6 decomposed components based on DFT method," *Applied Surface Science*, vol. 420, pp. 825-832, 2017.
- [143] H. Cui, X. Zhang, D. Chen, and J. Tang, "Pt & Pd decorated CNT as a workable media for SOF2 sensing: A DFT study," *Applied Surface Science*, vol. 471, pp. 335-341, 2019.
- [144] N. Bohli, M. Belkilani, J. Casanova-Chafer, E. Llobet, and A. Abdelghani, "Multiwalled carbon nanotube based aromatic volatile organic compound sensor: sensitivity enhancement through 1-hexadecanethiol functionalisation," *Beilstein Journal of Nanotechnology*, vol. 10, no. 1, pp. 2364-2373, 2019.
- [145] Q. Wan, Y. Xu, X. Chen, and H. Xiao, "Exhaled gas detection by a novel Rh-doped CNT biosensor for prediagnosis of lung cancer: a DFT study," *Molecular Physics*, vol. 116, no. 17, pp. 2205-2212, 2018.
- [146] S.-L. Yau, Y.-G. Kim, and K. Itaya, "In situ scanning tunneling microscopy of benzene adsorbed on Rh (111) and Pt (111) in HF solution," *Journal of the American Chemical Society*, vol. 118, no. 33, pp. 7795-7803, 1996.
- [147] M. Saeys, M.-F. Reyniers, G. B. Marin, and M. Neurock, "Density functional study of benzene adsorption on Pt (111)," *The Journal of Physical Chemistry B*, vol. 106, no. 30, pp. 7489-7498, 2002.
- [148] P. De Souza, D. Aranda, J. De M. Carneiro, C. Da SB De Oliveira, O. Antunes, and F. Passos, "Theoretical study on the adsorption of aromatic compounds on platinum clusters," *International journal of quantum chemistry*, vol. 92, no. 4, pp. 400-411, 2003.
- [149] C. Morin, D. Simon, and P. Sautet, "Chemisorption of benzene on Pt (111), Pd (111), and Rh (111) metal surfaces: a structural and vibrational comparison from first principles," *The Journal of Physical Chemistry B*, vol. 108, no. 18, pp. 5653-5665, 2004.
- [150] S. Jenkins, "Aromatic adsorption on metals via first-principles density functional theory," *Proceedings of the Royal Society A: Mathematical, Physical and Engineering Sciences*, vol. 465, no. 2110, pp. 2949-2976, 2009.
- [151] W. Liu, J. Carrasco, B. Santra, A. Michaelides, M. Scheffler, and A. Tkatchenko, "Benzene adsorbed on metals: Concerted effect of covalency and van der Waals bonding," *Physical Review B*, vol. 86, no. 24, p. 245405, 2012.
- [152] J. A. G. Torres, B. Ramberger, H. A. Früchtl, R. Schaub, and G. Kresse, "Adsorption energies of benzene on close packed transition metal surfaces using the random phase approximation," *Physical Review Materials*, vol. 1, no. 6, p. 060803, 2017.
- [153] J. Taylor, H. Guo, and J. Wang, "Ab initio modeling of quantum transport properties of molecular electronic devices," *Physical Review B*, vol. 63, no. 24, p. 245407, 2001.

- [154] M. Brandbyge, J.-L. Mozos, P. Ordejón, J. Taylor, and K. Stokbro, "Density-functional method for nonequilibrium electron transport," *Physical Review B*, vol. 65, no. 16, p. 165401, 2002.
- [155] Atomistix ToolKit (ATK) QuantumWise Simulator [Online] Available: <http://www.quantumwise.com>
- [156] S. Grimme, C. Mück-Lichtenfeld, and J. Antony, "Noncovalent interactions between graphene sheets and in multishell (hyper) fullerenes," *The Journal of Physical Chemistry C*, vol. 111, no. 30, pp. 11199-11207, 2007.
- [157] S. Grimme, "Semiempirical GGA-type density functional constructed with a long-range dispersion correction," *Journal of computational chemistry*, vol. 27, no. 15, pp. 1787-1799, 2006.
- [158] V. Amir-Ebrahimi, A. Choplin, J. Demaison, and G. Roussy, "Microwave spectrum of the ¹³C-ring-monosubstituted toluenes and structure of toluene," *Journal of Molecular Spectroscopy*, vol. 89, no. 1, pp. 42-52, 1981.
- [159] V. Verdinelli, E. German, C. R. Luna, J. M. Marchetti, M. A. Volpe, and A. Juan, "Theoretical study of hydrogen adsorption on Ru-decorated (8, 0) single-walled carbon nanotube," *The Journal of Physical Chemistry C*, vol. 118, no. 48, pp. 27672-27680, 2014.
- [160] E. Durgun, S. Dag, V. Bagci, O. Gülseren, T. Yildirim, and S. Ciraci, "Systematic study of adsorption of single atoms on a carbon nanotube," *Physical Review B*, vol. 67, no. 20, p. 201401, 2003.
- [161] C. R. Luna *et al.*, "Hydrogen adsorption and associated electronic and magnetic properties of Rh-decorated (8, 0) carbon nanotubes using density functional theory," *The Journal of Physical Chemistry C*, vol. 119, no. 23, pp. 13238-13247, 2015.
- [162] L. Brewer, "Bonding and structures of transition metals," *Science*, vol. 161, no. 3837, pp. 115-122, 1968.
- [163] V. H. Grassian and E. Muettterties, "Vibrational electron energy loss spectroscopic study of benzene, toluene, and pyridine adsorbed on palladium (111) at 180 K," *Journal of Physical Chemistry*, vol. 91, no. 2, pp. 389-396, 1987.
- [164] G.-K. Liu *et al.*, "Effect of intrinsic properties of metals on the adsorption behavior of molecules: Benzene adsorption on Pt group metals," *The Journal of Physical Chemistry B*, vol. 110, no. 35, pp. 17498-17506, 2006.
- [165] X. Zhang, L. Yu, X. Wu, and W. Hu, "Experimental sensing and density functional theory study of H₂S and SOF₂ adsorption on Au-modified graphene," *Advanced Science*, vol. 2, no. 11, p. 1500101, 2015.
- [166] H. Sung *et al.*, "Global cancer statistics 2020: GLOBOCAN estimates of incidence and mortality worldwide for 36 cancers in 185 countries," *CA: a cancer journal for clinicians*, vol. 71, no. 3, pp. 209-249, 2021.
- [167] P. S. Pinheiro *et al.*, "Liver cancer: a leading cause of cancer death in the United States and the role of the 1945–1965 birth cohort by ethnicity," *JHEP Reports*, vol. 1, no. 3, pp. 162-169, 2019.
- [168] Z. Altintas and I. Tohill, "Biomarkers and biosensors for the early diagnosis of lung cancer," *Sensors and Actuators B: Chemical*, vol. 188, pp. 988-998, 2013.
- [169] R. Majidi and M. Nadafan, "Detection of exhaled gas by γ -graphyne and twin-graphene for early diagnosis of lung cancer: A density functional theory study," *Physics Letters A*, vol. 384, no. 1, p. 126036, 2020.
- [170] A. Banerjee, P. Rabbitts, and J. George, "Lung cancer• 3: fluorescence bronchoscopy: clinical dilemmas and research opportunities," *Thorax*, vol. 58, no. 3, p. 266, 2003.
- [171] T. H. Risby and F. K. Tittel, "Current status of midinfrared quantum and interband cascade lasers for clinical breath analysis," *Optical Engineering*, vol. 49, no. 11, p. 111123, 2010.
- [172] V. Nagarajan and R. Chandiramouli, "Novel method to detect the lung cancer biomarker volatiles using hydrogen vacant silicane nanosheets: a DFT investigation," *Computational and Theoretical Chemistry*, vol. 1138, pp. 107-116, 2018.

- [173] G. Zhao and M. Li, "Ni-doped MoS₂ biosensor: a promising candidate for early diagnosis of lung cancer by exhaled breathe analysis," *Applied Physics A*, vol. 124, no. 11, pp. 1-9, 2018.
- [174] T. A. Popov, "Human exhaled breath analysis," *Annals of Allergy, Asthma & Immunology*, vol. 106, no. 6, pp. 451-456, 2011.
- [175] K.-H. Kim, S. A. Jahan, and E. Kabir, "A review of breath analysis for diagnosis of human health," *TrAC Trends in Analytical Chemistry*, vol. 33, pp. 1-8, 2012.
- [176] Z. Wang and C. Wang, "Is breath acetone a biomarker of diabetes? A historical review on breath acetone measurements," *Journal of breath research*, vol. 7, no. 3, p. 037109, 2013.
- [177] S. Kaghazkonani and S. Afshari, "Sensing C₃–C₁₀ Straight Chain Aldehydes Biomarker Gas Molecules: Density Functional Theory," *Russian Journal of Physical Chemistry B*, vol. 15, no. 6, pp. 1095-1101, 2021.
- [178] B. Behera, R. Joshi, G. A. Vishnu, S. Bhalerao, and H. J. Pandya, "Electronic nose: A non-invasive technology for breath analysis of diabetes and lung cancer patients," *Journal of breath research*, vol. 13, no. 2, p. 024001, 2019.
- [179] W. Zhang, H. Yan, and C. He, "g-C₆N₆ monolayer: A highly sensitive molecule sensor for biomarker volatiles of liver cirrhosis," *Applied Surface Science*, vol. 566, p. 150716, 2021.
- [180] F. Liu, P. Xiao, H. Fang, H. Dai, L. Qiao, and Y. Zhang, "Single-walled carbon nanotube-based biosensors for the detection of volatile organic compounds of lung cancer," *Physica E: Low-dimensional Systems and Nanostructures*, vol. 44, no. 2, pp. 367-372, 2011.
- [181] S. Das, S. Pal, and M. Mitra, "Significance of exhaled breath test in clinical diagnosis: a special focus on the detection of diabetes mellitus," *Journal of medical and biological engineering*, vol. 36, no. 5, pp. 605-624, 2016.
- [182] A. Aasi, S. M. Aghaei, and B. Panchapakesan, "Pt-decorated Phosphorene as a Propitious Room Temperature VOCs Gas Sensor for Sensitive and Selective Detection of Alcohols," *Journal of Materials Chemistry C*, 2021.
- [183] A. Aasi, S. M. Aghaei, S. E. Bajgani, and B. Panchapakesan, "Computational Study on Sensing Properties of Pd-Decorated Phosphorene for Detecting Acetone, Ethanol, Methanol, and Toluene—A Density Functional Theory Investigation," *Advanced Theory and Simulations*, vol. 4, no. 10, p. 2100256, 2021.
- [184] S. Wang, J. Wang, Y. Zhu, J. Yang, and F. Yang, "A new device for liver cancer biomarker detection with high accuracy," *Sensing and Bio-Sensing Research*, vol. 4, pp. 40-45, 2015.
- [185] V. Nagarajan, N. Srividya, and R. Chandiramouli, "Interaction studies of liver cancer biomarkers on black phosphorene sheets—A DFT outlook," *FlatChem*, vol. 30, p. 100293, 2021.
- [186] S. C. Dhanabalan, J. S. Ponraj, Z. Guo, S. Li, Q. Bao, and H. Zhang, "Emerging trends in phosphorene fabrication towards next generation devices," *Advanced Science*, vol. 4, no. 6, p. 1600305, 2017.
- [187] J. Li, C. Wan, C. Wang, H. Zhang, and X. Chen, "2D material chemistry: graphdiyne-based biochemical sensing," *Chemical Research in Chinese Universities*, vol. 36, no. 4, pp. 622-630, 2020.
- [188] D. Tyagi *et al.*, "Recent advances in two-dimensional-material-based sensing technology toward health and environmental monitoring applications," *Nanoscale*, vol. 12, no. 6, pp. 3535-3559, 2020.
- [189] V. Nagarajan and R. Chandiramouli, "Sorption studies of sulfadimethoxine and tetracycline molecules on β -antimonene nanotube-A first-principles insight," *Journal of Molecular Graphics and Modelling*, vol. 108, p. 107988, 2021.
- [190] R. Bhuvaneswari, V. Nagarajan, and R. Chandiramouli, "Molecular interaction studies of styrene on single and double-walled square-octagon phosphorene nanotubes—First-principles investigation," *Chemical Physics Letters*, vol. 785, p. 139149, 2021.

- [191] R. Bhuvaneswari, V. Nagarajan, and R. Chandiramouli, "DFT study on the adsorption properties of aldrin and dieldrin molecules on blue phosphorene nanotubes," *Physica B: Condensed Matter*, vol. 626, p. 413545, 2022.
- [192] X. Zhang, H. Cui, Y. Gui, and J. Tang, "Mechanism and application of carbon nanotube sensors in SF 6 decomposed production detection: a review," *Nanoscale research letters*, vol. 12, no. 1, p. 177, 2017.
- [193] N. Anzar, R. Hasan, M. Tyagi, N. Yadav, and J. Narang, "Carbon nanotube-A review on Synthesis, Properties and plethora of applications in the field of biomedical science," *Sensors International*, vol. 1, p. 100003, 2020.
- [194] H. Hashemzadeh and H. Raissi, "The functionalization of carbon nanotubes to enhance the efficacy of the anticancer drug paclitaxel: a molecular dynamics simulation study," *Journal of Molecular Modeling*, vol. 23, no. 8, pp. 1-10, 2017.
- [195] E. Dilonardo *et al.*, "Electrophoretic deposition of Au NPs on MWCNT-based gas sensor for tailored gas detection with enhanced sensing properties," *Sensors and Actuators B: Chemical*, vol. 223, pp. 417-428, 2016.
- [196] T. Kokabu, K. Takashima, S. Inoue, Y. Matsumura, and T. Yamamoto, "Transport phenomena of electrons at the carbon nanotube interface with molecular adsorption," *Journal of Applied Physics*, vol. 122, no. 1, p. 015308, 2017.
- [197] Y. Xu, Z. Gan, and S.-C. Zhang, "Enhanced thermoelectric performance and anomalous Seebeck effects in topological insulators," *Physical review letters*, vol. 112, no. 22, p. 226801, 2014.
- [198] M. Yoosefian, Z. Barzgari, and J. Yoosefian, "Ab initio study of Pd-decorated single-walled carbon nanotube with C-vacancy as CO sensor," *Structural Chemistry*, vol. 25, no. 1, pp. 9-19, 2014.
- [199] S. Demir and M. F. Fellah, "Carbon nanotubes doped with Ni, Pd and Pt: A density functional theory study of adsorption and sensing NO," *Surface Science*, vol. 701, p. 121689, 2020.
- [200] P. Buasaeng, W. Rakrai, B. Wannoo, and C. Tabtimsai, "DFT investigation of NH₃, PH₃, and AsH₃ adsorptions on Sc-, Ti-, V-, and Cr-doped single-walled carbon nanotubes," *Applied Surface Science*, vol. 400, pp. 506-514, 2017.
- [201] I. M. Sharafeldin and N. K. Allam, "DFT insights into the electronic properties and adsorption of NO₂ on metal-doped carbon nanotubes for gas sensing applications," *New Journal of Chemistry*, vol. 41, no. 24, pp. 14936-14944, 2017.
- [202] K. T. Philemon and K. K. Korir, "Carbon dioxide gas sensing, capture, and storage potential of calcium oxide surface and single walled carbon nanotube: insights from ab initio simulation," *Journal of Physics: Condensed Matter*, vol. 32, no. 24, p. 245901, 2020.
- [203] X. Zhang, Z. Dai, Q. Chen, and J. Tang, "A DFT study of SO₂ and H₂S gas adsorption on Au-doped single-walled carbon nanotubes," *Physica Scripta*, vol. 89, no. 6, p. 065803, 2014.
- [204] F. K. Fotooh and M. Nayeri, "Methane adsorption on the surface of metal (Fe, Ni, Pd) decorated SWCNT: A density functional theory (DFT) study," *Surface Science*, vol. 713, p. 121913, 2021.
- [205] A. Aasi, B. Mortazavi, and B. Panchapakesan, "Two-dimensional PdPS and PdPSe nanosheets: Novel promising sensing platforms for harmful gas molecules," *Applied Surface Science*, p. 152115, 2021.
- [206] M. Sun, Y. Luo, Y. Yan, and U. Schwingenschlogl, "Ultrahigh carrier mobility in the two-dimensional semiconductors B₈Si₄, B₈Ge₄, and B₈Sn₄," *Chemistry of Materials*, vol. 33, no. 16, pp. 6475-6483, 2021.
- [207] M. Jyothi, V. Nagarajan, and R. Chandiramouli, "Chemisorption of atrazine and diuron molecules on γ -arsenene nanosheet-a first-principles study," *Chemical Physics Letters*, vol. 794, p. 139484, 2022.

- [208] V. Nagarajan and R. Chandiramouli, "Twisted bilayer arsenene sheets as a chemical sensor for toluene and M-xylene vapours—A DFT investigation," *Journal of Molecular Graphics and Modelling*, vol. 109, p. 108034, 2021.
- [209] J.-X. Zhao and Y.-H. Ding, "Theoretical study of the interactions of carbon monoxide with Rh-decorated (8, 0) single-walled carbon nanotubes," *Materials Chemistry and Physics*, vol. 110, no. 2-3, pp. 411-416, 2008.
- [210] E. t. Clementi and D.-L. Raimondi, "Atomic screening constants from SCF functions," *The Journal of Chemical Physics*, vol. 38, no. 11, pp. 2686-2689, 1963.
- [211] I. G. Pitt, R. G. Gilbert, and K. R. Ryan, "Application of transition-state theory to gas-surface reactions: barrierless adsorption on clean surfaces," *The Journal of Physical Chemistry*, vol. 98, no. 49, pp. 13001-13010, 1994.
- [212] P. Pannopard, P. Khongpracha, M. Probst, and J. Limtrakul, "Gas sensing properties of platinum derivatives of single-walled carbon nanotubes: A DFT analysis," *Journal of Molecular Graphics and Modelling*, vol. 28, no. 1, pp. 62-69, 2009.
- [213] K. Xu *et al.*, "Nanomaterial-based gas sensors: A review," *Instrumentation Science & Technology*, vol. 46, no. 2, pp. 115-145, 2018.
- [214] K. S. Novoselov *et al.*, "Two-dimensional gas of massless Dirac fermions in graphene," *nature*, vol. 438, no. 7065, pp. 197-200, 2005.
- [215] F. Schedin *et al.*, "Detection of individual gas molecules adsorbed on graphene," *Nature materials*, vol. 6, no. 9, pp. 652-655, 2007.
- [216] K. Toda, R. Furue, and S. Hayami, "Recent progress in applications of graphene oxide for gas sensing: A review," *Analytica chimica acta*, vol. 878, pp. 43-53, 2015.
- [217] T. Wang *et al.*, "A review on graphene-based gas/vapor sensors with unique properties and potential applications," *Nano-Micro Letters*, vol. 8, no. 2, pp. 95-119, 2016.
- [218] I. Osica *et al.*, "Highly networked capsular silica–porphyrin hybrid nanostructures as efficient materials for acetone vapor sensing," *ACS applied materials & interfaces*, vol. 9, no. 11, pp. 9945-9954, 2017.
- [219] A. V. Singhal, H. Charaya, and I. Lahiri, "Noble metal decorated graphene-based gas sensors and their fabrication: A review," *Critical Reviews in Solid State and Materials Sciences*, vol. 42, no. 6, pp. 499-526, 2017.
- [220] Z. Bo, X. Guo, X. Wei, H. Yang, J. Yan, and K. Cen, "Density functional theory calculations of NO₂ and H₂S adsorption on the group 10 transition metal (Ni, Pd and Pt) decorated graphene," *Physica E: Low-dimensional Systems and Nanostructures*, vol. 109, pp. 156-163, 2019.
- [221] W. Y. Chen, C.-C. Yen, S. Xue, H. Wang, and L. A. Stanciu, "Surface functionalization of layered molybdenum disulfide for the selective detection of volatile organic compounds at room temperature," *ACS applied materials & interfaces*, vol. 11, no. 37, pp. 34135-34143, 2019.
- [222] S. Aghaei, A. Aasi, S. Farhangdoust, and B. Panchapakesan, "Graphene-like BC₆N nanosheets are potential candidates for detection of volatile organic compounds (VOCs) in human breath: A DFT study," *Applied Surface Science*, vol. 536, p. 147756, 2021.
- [223] S. S. Varghese, S. H. Varghese, S. Swaminathan, K. K. Singh, and V. Mittal, "Two-dimensional materials for sensing: graphene and beyond," *Electronics*, vol. 4, no. 3, pp. 651-687, 2015.
- [224] W. Yang, L. Gan, H. Li, and T. Zhai, "Two-dimensional layered nanomaterials for gas-sensing applications," *Inorganic Chemistry Frontiers*, vol. 3, no. 4, pp. 433-451, 2016.
- [225] J. Li, X. Chen, Z. Yang, X. Liu, and X. Zhang, "Highly anisotropic gas sensing of atom-thin borophene: a first-principles study," *Journal of Materials Chemistry C*, vol. 9, no. 3, pp. 1069-1076, 2021.
- [226] E. S. Reich, "Phosphorene excites materials scientists," *Nature*, vol. 506, no. 7486, p. 19, 2014.
- [227] A. N. Abbas *et al.*, "Black phosphorus gas sensors," *ACS nano*, vol. 9, no. 5, pp. 5618-5624, 2015.

- [228] S. Y. Cho *et al.*, "Superior chemical sensing performance of black phosphorus: comparison with MoS₂ and graphene," *Advanced Materials*, vol. 28, no. 32, pp. 7020-7028, 2016.
- [229] H. Guo, S. Lee, L. Chan, and W. Li, "Risk assessment of exposure to volatile organic compounds in different indoor environments," *Environmental Research*, vol. 94, no. 1, pp. 57-66, 2004.
- [230] J. Bartzis *et al.*, "On organic emissions testing from indoor consumer products' use," *Journal of hazardous materials*, vol. 285, pp. 37-45, 2015.
- [231] B. de Lacy Costello *et al.*, "A review of the volatiles from the healthy human body," *Journal of breath research*, vol. 8, no. 1, p. 014001, 2014.
- [232] A. Aasi, S. Mehdi Aghaei, and B. Panchapakesan, "Outstanding Performance of Transition-Metal-Decorated Single-Layer Graphene-like BC₆N Nanosheets for Disease Biomarker Detection in Human Breath," *ACS Omega*, 2021.
- [233] A. A. o. C. T. A. H. C. o. t. T. G. f. M. Poisoning, D. G. Barceloux, G. Randall Bond, E. P. Krenzelok, H. Cooper, and J. Allister Vale, "American Academy of Clinical Toxicology practice guidelines on the treatment of methanol poisoning," *Journal of toxicology: Clinical toxicology*, vol. 40, no. 4, pp. 415-446, 2002.
- [234] S. Young and Z. Lin, "Ethanol gas sensors based on multi-wall carbon nanotubes on oxidized Si substrate," *Microsystem Technologies*, vol. 24, no. 1, pp. 55-58, 2018.
- [235] P. Ou, P. Song, X. Liu, and J. Song, "Superior Sensing Properties of Black Phosphorus as Gas Sensors: A Case Study on the Volatile Organic Compounds," *Advanced Theory and Simulations*, vol. 2, no. 1, p. 1800103, 2019.
- [236] G. Lee, S. Kim, S. Jung, S. Jang, and J. Kim, "Suspended black phosphorus nanosheet gas sensors," *Sensors and Actuators B: Chemical*, vol. 250, pp. 569-573, 2017.
- [237] T. Kaewmaraya, L. Ngamwongwan, P. Moontragoon, A. Karton, and T. Hussain, "Drastic improvement in gas-sensing characteristics of phosphorene nanosheets under vacancy defects and elemental functionalization," *The Journal of Physical Chemistry C*, vol. 122, no. 35, pp. 20186-20193, 2018.
- [238] S. Lei *et al.*, "Nitrogen-based gas molecule adsorption of monolayer phosphorene under metal functionalization," *Scientific reports*, vol. 9, no. 1, pp. 1-13, 2019.
- [239] Q. Simulator, "Atomistix ToolKit (ATK)," ed, 2012.
- [240] S. Y. Lei, Z. Y. Yu, H. Y. Shen, X. L. Sun, N. Wan, and H. Yu, "CO adsorption on metal-decorated phosphorene," *ACS omega*, vol. 3, no. 4, pp. 3957-3965, 2018.
- [241] A. Kuang *et al.*, "Adsorption and decomposition of metal decorated phosphorene toward H₂S, HCN and NH₃ molecules," *Applied Surface Science*, vol. 473, pp. 242-250, 2019.
- [242] V. V. Kulish, O. I. Malyi, C. Persson, and P. Wu, "Adsorption of metal adatoms on single-layer phosphorene," *Physical Chemistry Chemical Physics*, vol. 17, no. 2, pp. 992-1000, 2015.
- [243] R. J. Chen *et al.*, "Molecular photodesorption from single-walled carbon nanotubes," *Applied Physics Letters*, vol. 79, no. 14, pp. 2258-2260, 2001.
- [244] P. Lazar *et al.*, "Adsorption of small organic molecules on graphene," *Journal of the American Chemical Society*, vol. 135, no. 16, pp. 6372-6377, 2013.
- [245] Q. Zhou *et al.*, "DFT study of formaldehyde adsorption on vacancy defected graphene doped with B, N, and S," *Chemical Physics*, vol. 440, pp. 80-86, 2014.
- [246] T. Hussain *et al.*, "Sensing of volatile organic compounds on two-dimensional nitrogenated holey graphene, graphdiyne, and their heterostructure," *Carbon*, vol. 163, pp. 213-223, 2020.
- [247] X. Wang, H. Liu, and S.-T. Tu, "Study of formaldehyde adsorption on silicene with point defects by DFT method," *RSC advances*, vol. 5, no. 80, pp. 65255-65263, 2015.
- [248] X.-Q. Tian *et al.*, "Engineering of the interactions of volatile organic compounds with MoS₂," *Journal of Materials Chemistry C*, vol. 5, no. 6, pp. 1463-1470, 2017.

- [249] V. Nagarajan and R. Chandiramouli, "MoSe₂ nanosheets for detection of methanol and ethanol vapors: a DFT study," *Journal of Molecular Graphics and Modelling*, vol. 81, pp. 97-105, 2018.
- [250] R. Siegel, D. Naishadham, and A. Jemal, "Cancer statistics for hispanics/latinos, 2012," *CA: a cancer journal for clinicians*, vol. 62, no. 5, pp. 283-298, 2012.
- [251] J. Ferlay, D. Parkin, and E. Steliarova-Foucher, "Estimates of cancer incidence and mortality in Europe in 2008," *European journal of cancer*, vol. 46, no. 4, pp. 765-781, 2010.
- [252] S. Bingham and E. Riboli, "Diet and cancer—the European prospective investigation into cancer and nutrition," *Nature Reviews Cancer*, vol. 4, no. 3, pp. 206-215, 2004.
- [253] R. Siegel *et al.*, "Cancer treatment and survivorship statistics, 2012," *CA: a cancer journal for clinicians*, vol. 62, no. 4, pp. 220-241, 2012.
- [254] S. Bastaminejad, M. Taherikalani, R. Ghanbari, A. Akbari, N. Shabab, and M. Saidijam, "Investigation of microRNA-21 expression levels in serum and stool as a potential non-invasive biomarker for diagnosis of colorectal cancer," *Iranian biomedical journal*, vol. 21, no. 2, p. 106, 2017.
- [255] M. G. Keane and G. J. Johnson, "Early diagnosis improves survival in colorectal cancer," *The Practitioner*, vol. 256, no. 1753, pp. 15-19, 2012.
- [256] G. Russo *et al.*, "Highly sensitive, non-invasive detection of colorectal cancer mutations using single molecule, third generation sequencing," *Applied & translational genomics*, vol. 7, pp. 32-39, 2015.
- [257] W. Miekisch, J. K. Schubert, and G. F. Noeldge-Schomburg, "Diagnostic potential of breath analysis—focus on volatile organic compounds," *Clinica chimica acta*, vol. 347, no. 1-2, pp. 25-39, 2004.
- [258] A. W. Boots, J. J. van Berkel, J. W. Dallinga, A. Smolinska, E. F. Wouters, and F. J. van Schooten, "The versatile use of exhaled volatile organic compounds in human health and disease," *Journal of breath research*, vol. 6, no. 2, p. 027108, 2012.
- [259] R. A. Sola Martinez, J. M. Pastor Hernandez, O. Yanes Torrado, M. Canovas Diaz, T. de Diego Puente, and M. Vinaixa Crevillent, "Exhaled volatile organic compounds analysis in clinical pediatrics: a systematic review," *Pediatric Research*, vol. 89, no. 6, pp. 1352-1363, 2021.
- [260] M. Khoubnasabjafari, M. R. A. Mogaddam, E. Rahimpour, J. Soleymani, A. A. Saei, and A. Jouyban, "Breathomics: review of sample collection and analysis, data modeling and clinical applications," *Critical Reviews in Analytical Chemistry*, pp. 1-27, 2021.
- [261] B. Ray, S. Parmar, V. Vijayan, S. Vishwakarma, and S. Datar, "Detection of trace volatile organic compounds in spiked breath samples: A leap towards Breathomics," *Nanotechnology*, vol. 33, no. 20, p. 205505, 2022.
- [262] M. Phillips *et al.*, "Prediction of breast cancer using volatile biomarkers in the breath," *Breast cancer research and treatment*, vol. 99, no. 1, pp. 19-21, 2006.
- [263] S. Kumar *et al.*, "Mass spectrometric analysis of exhaled breath for the identification of volatile organic compound biomarkers in esophageal and gastric adenocarcinoma," *Annals of surgery*, vol. 262, no. 6, pp. 981-990, 2015.
- [264] S. Kort *et al.*, "Multi-centre prospective study on diagnosing subtypes of lung cancer by exhaled-breath analysis," *Lung Cancer*, vol. 125, pp. 223-229, 2018.
- [265] D. Marzorati, L. Mainardi, G. Sedda, R. Gasparri, L. Spaggiari, and P. Cerveri, "A review of exhaled breath: a key role in lung cancer diagnosis," *Journal of breath research*, vol. 13, no. 3, p. 034001, 2019.
- [266] D. Altomare *et al.*, "Exhaled volatile organic compounds identify patients with colorectal cancer," *Journal of British Surgery*, vol. 100, no. 1, pp. 144-150, 2013.

- [267] H. Haick, Y. Y. Broza, P. Mochalski, V. Ruzsanyi, and A. Amann, "Assessment, origin, and implementation of breath volatile cancer markers," *Chemical Society Reviews*, vol. 43, no. 5, pp. 1423-1449, 2014.
- [268] C. Wang *et al.*, "Noninvasive detection of colorectal cancer by analysis of exhaled breath," *Analytical and bioanalytical chemistry*, vol. 406, no. 19, pp. 4757-4763, 2014.
- [269] H. Amal *et al.*, "Breath testing as potential colorectal cancer screening tool," *International journal of cancer*, vol. 138, no. 1, pp. 229-236, 2016.
- [270] T. G. de Meij *et al.*, "Electronic nose can discriminate colorectal carcinoma and advanced adenomas by fecal volatile biomarker analysis: proof of principle study," *International Journal of Cancer*, vol. 134, no. 5, pp. 1132-1138, 2014.
- [271] F. Akbar, M. Kolahdouz, S. Larimian, B. Radfar, and H. Radamson, "Graphene synthesis, characterization and its applications in nanophotonics, nanoelectronics, and nanosensing," *Journal of Materials Science: Materials in Electronics*, vol. 26, no. 7, pp. 4347-4379, 2015.
- [272] M. Donarelli and L. Ottaviano, "2D materials for gas sensing applications: a review on graphene oxide, MoS₂, WS₂ and phosphorene," *Sensors*, vol. 18, no. 11, p. 3638, 2018.
- [273] A. Aasi, R. Javahersaz, S. M. Aghaei, and B. Panchapakesan, "First-principles insight into two-dimensional palladium phosphide tellurium (PdP₂Te) monolayer as a promising scavenger for detecting SF₆ decompositions," *Journal of Materials Science*, 2022/03/01 2022, doi: 10.1007/s10853-022-07033-x.
- [274] V. Nagarajan, K. Deepika, B. Swetha, K. M. Reddy, and R. Chandiramouli, "δ-antimonene nanosheet as a sensing element for ethyl acetate and butyl acetate—a first-principles study," *Molecular Physics*, p. e2103469, 2022.
- [275] V. Nagarajan and R. Chandiramouli, "Sensing response of novel ε-antimonene nanosheet towards ethyl acetate and isopropyl acetate—a DFT insight," *Chemical Physics*, p. 111632, 2022.
- [276] Q. He *et al.*, "Fabrication of flexible MoS₂ thin-film transistor arrays for practical gas-sensing applications," *Small*, vol. 8, no. 19, pp. 2994-2999, 2012.
- [277] Y. Zhou, C. Gao, and Y. Guo, "UV assisted ultrasensitive trace NO₂ gas sensing based on few-layer MoS₂ nanosheet–ZnO nanowire heterojunctions at room temperature," *Journal of Materials Chemistry A*, vol. 6, no. 22, pp. 10286-10296, 2018.
- [278] A. Aasi, S. M. Aghaei, and B. Panchapakesan, "Noble Metal (Pt or Pd)-Decorated Atomically Thin MoS₂ as a Promising Material for Sensing Colorectal Cancer Biomarkers Through Exhaled Breath," *International Journal of Computational Materials Science and Engineering*, 2023.
- [279] W. Zhang, P. Zhang, Z. Su, and G. Wei, "Synthesis and sensor applications of MoS₂-based nanocomposites," *Nanoscale*, vol. 7, no. 44, pp. 18364-18378, 2015.
- [280] C. Rao, K. Gopalakrishnan, and U. Maitra, "Comparative study of potential applications of graphene, MoS₂, and other two-dimensional materials in energy devices, sensors, and related areas," *ACS applied materials & interfaces*, vol. 7, no. 15, pp. 7809-7832, 2015.
- [281] P. K. Kannan, D. J. Late, H. Morgan, and C. S. Rout, "Recent developments in 2D layered inorganic nanomaterials for sensing," *Nanoscale*, vol. 7, no. 32, pp. 13293-13312, 2015.
- [282] A. Aasi, S. Ebrahimi Bajgani, and B. Panchapakesan, "A first-principles investigation on the adsorption of octanal and nonanal molecules with decorated monolayer WS₂ as promising gas sensing platform," *AIP Advances*, vol. 13, no. 2, p. 025157, 2023.
- [283] V. Rahneshin, F. Khosravi, D. A. Ziolkowska, J. B. Jasinski, and B. Panchapakesan, "Chromatic mechanical response in 2-D layered transition metal dichalcogenide (TMDs) based nanocomposites," *Scientific reports*, vol. 6, no. 1, pp. 1-14, 2016.
- [284] F. K. Perkins, A. L. Friedman, E. Cobas, P. Campbell, G. Jernigan, and B. T. Jonker, "Chemical vapor sensing with monolayer MoS₂," *Nano letters*, vol. 13, no. 2, pp. 668-673, 2013.

- [285] R. Lv *et al.*, "Transition metal dichalcogenides and beyond: synthesis, properties, and applications of single-and few-layer nanosheets," *Accounts of chemical research*, vol. 48, no. 1, pp. 56-64, 2015.
- [286] H. Li *et al.*, "Fabrication of single-and multilayer MoS₂ film-based field-effect transistors for sensing NO at room temperature," *small*, vol. 8, no. 1, pp. 63-67, 2012.
- [287] B. Radisavljevic, A. Radenovic, J. Brivio, V. Giacometti, and A. Kis, "Single-layer MoS₂ transistors," *Nature nanotechnology*, vol. 6, no. 3, pp. 147-150, 2011.
- [288] Z. Yin *et al.*, "Single-layer MoS₂ phototransistors," *ACS nano*, vol. 6, no. 1, pp. 74-80, 2012.
- [289] D. Ma *et al.*, "Formaldehyde molecule adsorption on the doped monolayer MoS₂: a first-principles study," *Applied Surface Science*, vol. 371, pp. 180-188, 2016.
- [290] S. Zhao, J. Xue, and W. Kang, "Gas adsorption on MoS₂ monolayer from first-principles calculations," *Chemical Physics Letters*, vol. 595, pp. 35-42, 2014.
- [291] H. Qian, W. Lu, X. Wei, W. Chen, and J. Deng, "H₂S and SO₂ adsorption on Pt-MoS₂ adsorbent for partial discharge elimination: A DFT study," *Results in Physics*, vol. 12, pp. 107-112, 2019.
- [292] S. Lakshmy, G. Sanyal, A. Vaidyanathan, S. Joseph, N. Kalarikkal, and B. Chakraborty, "Catechol detection in pure and transition metal decorated 2D MoS₂: Acumens from density functional theory approaches," *Applied Surface Science*, vol. 562, p. 150216, 2021.
- [293] H. Cui, X. Zhang, D. Chen, and J. Tang, "Adsorption mechanism of SF₆ decomposed species on pyridine-like PtN₃ embedded CNT: a DFT study," *Applied Surface Science*, vol. 447, pp. 594-598, 2018.
- [294] A. Shokri and N. Salami, "Gas sensor based on MoS₂ monolayer," *Sensors and Actuators B: Chemical*, vol. 236, pp. 378-385, 2016.
- [295] Y. Xu, Y. Li, X. Chen, C. Zhang, R. Zhang, and P. Lu, "First-principle study of hydrogenation on monolayer MoS₂," *Aip Advances*, vol. 6, no. 7, p. 075001, 2016.
- [296] P. Wu, N. Yin, P. Li, W. Cheng, and M. Huang, "The adsorption and diffusion behavior of noble metal adatoms (Pd, Pt, Cu, Ag and Au) on a MoS₂ monolayer: a first-principles study," *Physical Chemistry Chemical Physics*, vol. 19, no. 31, pp. 20713-20722, 2017.
- [297] D. Chen, X. Zhang, J. Tang, H. Cui, and Y. Li, "Noble metal (Pt or Au)-doped monolayer MoS₂ as a promising adsorbent and gas-sensing material to SO₂, SOF₂ and SO₂F₂: a DFT study," *Applied Physics A*, vol. 124, no. 2, pp. 1-12, 2018.
- [298] N. Aguilar, M. Atilhan, and S. Aparicio, "Single atom transition metals on MoS₂ monolayer and their use as catalysts for CO₂ activation," *Applied Surface Science*, vol. 534, p. 147611, 2020.
- [299] A. Aasi, E. Aasi, S. Mehdi Aghaei, and B. Panchapakesan, "CNT biodevices for early liver cancer diagnosis based on biomarkers detection- a promising platform," *Journal of Molecular Graphics and Modelling*, p. 108208, 2022/04/30/ 2022, doi: <https://doi.org/10.1016/j.jmgm.2022.108208>.
- [300] Y. Y. Broza and H. Haick, "Nanomaterial-based sensors for detection of disease by volatile organic compounds," *Nanomedicine*, vol. 8, no. 5, pp. 785-806, 2013.
- [301] X. Sun, K. Shao, and T. Wang, "Detection of volatile organic compounds (VOCs) from exhaled breath as noninvasive methods for cancer diagnosis," *Analytical and bioanalytical chemistry*, vol. 408, no. 11, pp. 2759-2780, 2016.
- [302] S. Das and M. Pal, "Non-invasive monitoring of human health by exhaled breath analysis: A comprehensive review," *Journal of The Electrochemical Society*, vol. 167, no. 3, p. 037562, 2020.
- [303] D. W. Potter and J. Pawliszyn, "Detection of substituted benzenes in water at the pg/ml level using solid-phase microextraction and gas chromatography—ion trap mass spectrometry," *Journal of Chromatography A*, vol. 625, no. 2, pp. 247-255, 1992.

- [304] S. E. Ebeler, A. J. Clifford, and T. Shibamoto, "Quantitative analysis by gas chromatography of volatile carbonyl compounds in expired air from mice and human," *Journal of Chromatography B: Biomedical Sciences and Applications*, vol. 702, no. 1-2, pp. 211-215, 1997.
- [305] S. Sethi, R. Nanda, and T. Chakraborty, "Clinical application of volatile organic compound analysis for detecting infectious diseases," *Clinical microbiology reviews*, vol. 26, no. 3, pp. 462-475, 2013.
- [306] X. Zhou *et al.*, "Nanomaterial-based gas sensors used for breath diagnosis," *Journal of Materials Chemistry B*, vol. 8, no. 16, pp. 3231-3248, 2020.
- [307] K. S. Novoselov *et al.*, "Electric field effect in atomically thin carbon films," *science*, vol. 306, no. 5696, pp. 666-669, 2004.
- [308] K. S. Novoselov *et al.*, "Two-dimensional gas of massless Dirac fermions in graphene," *Nature*, vol. 438, no. 7065, pp. 197-200, 2005.
- [309] J. T. Robinson, F. K. Perkins, E. S. Snow, Z. Wei, and P. E. Sheehan, "Reduced graphene oxide molecular sensors," *Nano letters*, vol. 8, no. 10, pp. 3137-3140, 2008.
- [310] J. D. Fowler, M. J. Allen, V. C. Tung, Y. Yang, R. B. Kaner, and B. H. Weiller, "Practical chemical sensors from chemically derived graphene," *ACS nano*, vol. 3, no. 2, pp. 301-306, 2009.
- [311] G. Lu, L. E. Ocola, and J. Chen, "Reduced graphene oxide for room-temperature gas sensors," *Nanotechnology*, vol. 20, no. 44, p. 445502, 2009.
- [312] G. Ko, H.-Y. Kim, J. Ahn, Y.-M. Park, K.-Y. Lee, and J. Kim, "Graphene-based nitrogen dioxide gas sensors," *Current Applied Physics*, vol. 10, no. 4, pp. 1002-1004, 2010.
- [313] M. Pumera, "Graphene in biosensing," *Materials today*, vol. 14, no. 7-8, pp. 308-315, 2011.
- [314] G. Chen, T. M. Paronyan, and A. R. Harutyunyan, "Sub-ppt gas detection with pristine graphene," *Applied Physics Letters*, vol. 101, no. 5, p. 053119, 2012.
- [315] S. Sabury, S. H. Kazemi, and F. Sharif, "Graphene-gold nanoparticle composite: application as a good scaffold for construction of glucose oxidase biosensor," *Materials Science and Engineering: C*, vol. 49, pp. 297-304, 2015.
- [316] K. Arora, "Recent Biosensing Applications of Graphene-Based Nanomaterials," *Handbook of Graphene, Volume 6: Biosensors and Advanced Sensors*, p. 297, 2019.
- [317] W. Wang, H. Su, Y. Wu, T. Zhou, and T. Li, "Biosensing and Biomedical Applications of Graphene: A Review of Current Progress and Future Prospect," *Journal of The Electrochemical Society*, vol. 166, no. 6, p. B505, 2019.
- [318] A. Nag, A. Mitra, and S. C. Mukhopadhyay, "Graphene and its sensor-based applications: A review," *Sensors and Actuators A: Physical*, vol. 270, pp. 177-194, 2018.
- [319] V. Kumar, Y.-S. Lee, J.-W. Shin, K.-H. Kim, D. Kukkar, and Y. F. Tsang, "Potential applications of graphene-based nanomaterials as adsorbent for removal of volatile organic compounds," *Environment International*, vol. 135, p. 105356, 2020.
- [320] K. M. Tripathi, T. Kim, D. Lasic, and T. T. Tung, "Recent advances in engineered graphene and composites for detection of volatile organic compounds (VOCs) and non-invasive diseases diagnosis," *Carbon*, vol. 110, pp. 97-129, 2016.
- [321] H. Yu, P. Xu, D.-W. Lee, and X. Li, "Porous-layered stack of functionalized AuNP-rGO (gold nanoparticles-reduced graphene oxide) nanosheets as a sensing material for the micro-gravimetric detection of chemical vapor," *Journal of Materials Chemistry A*, vol. 1, no. 14, pp. 4444-4450, 2013.
- [322] M. D. Shirsat *et al.*, "Porphyrin-functionalized single-walled carbon nanotube chemiresistive sensor arrays for VOCs," *The Journal of Physical Chemistry C*, vol. 116, no. 5, pp. 3845-3850, 2012.
- [323] S.-J. Choi, B.-H. Jang, S.-J. Lee, B. K. Min, A. Rothschild, and I.-D. Kim, "Selective detection of acetone and hydrogen sulfide for the diagnosis of diabetes and halitosis using SnO₂ nanofibers

- functionalized with reduced graphene oxide nanosheets," *ACS applied materials & interfaces*, vol. 6, no. 4, pp. 2588-2597, 2014.
- [324] S.-J. Choi *et al.*, "Fast responding exhaled-breath sensors using WO₃ hemitubes functionalized by graphene-based electronic sensitizers for diagnosis of diseases," *ACS applied materials & interfaces*, vol. 6, no. 12, pp. 9061-9070, 2014.
- [325] S. Nag *et al.*, "Ultrasensitive QRS made by supramolecular assembly of functionalized cyclodextrins and graphene for the detection of lung cancer VOC biomarkers," *Journal of Materials chemistry B*, vol. 2, no. 38, pp. 6571-6579, 2014.
- [326] S. Yoo, X. Li, Y. Wu, W. Liu, X. Wang, and W. Yi, "Ammonia gas detection by tannic acid functionalized and reduced graphene oxide at room temperature," *Journal of Nanomaterials*, vol. 2014, 2014.
- [327] W. Liu, Y. Liu, R. Wang, L. Hao, D. Song, and Z. Li, "DFT study of hydrogen adsorption on Eu-decorated single- and double-sided graphene," *physica status solidi (b)*, vol. 251, no. 1, pp. 229-234, 2014.
- [328] A. S. Rad, "First principles study of Al-doped graphene as nanostructure adsorbent for NO₂ and N₂O: DFT calculations," *Applied Surface Science*, vol. 357, pp. 1217-1224, 2015.
- [329] L. Ma, J.-M. Zhang, K.-W. Xu, and V. Ji, "A first-principles study on gas sensing properties of graphene and Pd-doped graphene," *Applied Surface Science*, vol. 343, pp. 121-127, 2015.
- [330] B. Wannan and C. Tabtimsai, "A DFT investigation of CO adsorption on VIII B transition metal-doped graphene sheets," *Superlattices and Microstructures*, vol. 67, pp. 110-117, 2014.
- [331] A. Aasi, S. M. Aghaei, M. D. Moore, and B. Panchapakesan, "Pt-, Rh-, Ru-, and Cu-Single-Wall Carbon Nanotubes Are Exceptional Candidates for Design of Anti-Viral Surfaces: A Theoretical Study," *International Journal of Molecular Sciences*, vol. 21, no. 15, p. 5211, 2020.
- [332] L. Panchakarla *et al.*, "Synthesis, structure, and properties of boron- and nitrogen-doped graphene," *Advanced Materials*, vol. 21, no. 46, pp. 4726-4730, 2009.
- [333] D. Geng *et al.*, "High oxygen-reduction activity and durability of nitrogen-doped graphene," *Energy & Environmental Science*, vol. 4, no. 3, pp. 760-764, 2011.
- [334] H. Wang, T. Maiyalagan, and X. Wang, "Review on recent progress in nitrogen-doped graphene: synthesis, characterization, and its potential applications," *Acs Catalysis*, vol. 2, no. 5, pp. 781-794, 2012.
- [335] Z. S. Wu *et al.*, "Three-dimensional nitrogen and boron co-doped graphene for high-performance all-solid-state supercapacitors," *Advanced Materials*, vol. 24, no. 37, pp. 5130-5135, 2012.
- [336] S. Agnoli and M. Favaro, "Doping graphene with boron: a review of synthesis methods, physicochemical characterization, and emerging applications," *Journal of Materials Chemistry A*, vol. 4, no. 14, pp. 5002-5025, 2016.
- [337] H. Tanaka *et al.*, "Novel macroscopic BC₃ honeycomb sheet," *Solid state communications*, vol. 136, no. 1, pp. 22-25, 2005.
- [338] S. Yang *et al.*, "C₃N—A 2D crystalline, hole-free, tunable-narrow-bandgap semiconductor with ferromagnetic properties," *Advanced Materials*, vol. 29, no. 16, p. 1605625, 2017.
- [339] J. Mahmood *et al.*, "Two-dimensional polyaniline (C₃N) from carbonized organic single crystals in solid state," *Proceedings of the National Academy of Sciences*, vol. 113, no. 27, pp. 7414-7419, 2016.
- [340] Y. Hong, J. Zhang, and X. C. Zeng, "Monolayer and bilayer polyaniline C₃N: two-dimensional semiconductors with high thermal conductivity," *Nanoscale*, vol. 10, no. 9, pp. 4301-4310, 2018.
- [341] S. Yang *et al.*, "C₃N—A 2D Crystalline, Hole-Free, Tunable-Narrow-Bandgap Semiconductor with Ferromagnetic Properties," *Advanced Materials*, vol. 29, no. 16, p. 1605625, 2017, doi: 10.1002/adma.201605625.

- [342] S. M. Aghaei, M. Monshi, I. Torres, S. Zeidi, and I. Calizo, "DFT study of adsorption behavior of NO, CO, NO₂, and NH₃ molecules on graphene-like BC₃: a search for highly sensitive molecular sensor," *Applied Surface Science*, vol. 427, pp. 326-333, 2018.
- [343] J. Beheshtian, A. A. Peyghan, and M. Noei, "Sensing behavior of Al and Si doped BC₃ graphenes to formaldehyde," *Sensors and Actuators B: Chemical*, vol. 181, pp. 829-834, 2013.
- [344] E. Chigo-Anota, M. A. Alejandro, A. B. Hernández, J. J. S. Torres, and M. Castro, "Long range corrected-wPBE based analysis of the H₂O adsorption on magnetic BC₃ nanosheets," *RSC Advances*, 10.1039/C5RA27231A vol. 6, no. 24, pp. 20409-20421, 2016, doi: 10.1039/C5RA27231A.
- [345] A. A. Peyghan, S. Yourdkhani, and M. Noei, "Working mechanism of a BC₃ nanotube carbon monoxide gas sensor," *Communications in Theoretical Physics*, vol. 60, no. 1, p. 113, 2013.
- [346] D. Ma *et al.*, "C₃N monolayers as promising candidates for NO₂ sensors," *Sensors and Actuators B: Chemical*, vol. 266, pp. 664-673, 2018.
- [347] H. Cui, C. Yan, P. Jia, and W. Cao, "Adsorption and sensing behaviors of SF₆ decomposed species on Ni-doped C₃N monolayer: A first-principles study," *Applied Surface Science*, vol. 512, p. 145759, 2020/05/15/ 2020, doi: <https://doi.org/10.1016/j.apsusc.2020.145759>.
- [348] Y. Tang, X. Cui, W. Chen, D. Zhu, H. Chai, and X. Dai, "A theoretical study on metal atom-modified BC₃ sheets for effects of gas molecule adsorptions," *Applied Physics A*, vol. 124, no. 6, p. 434, 2018.
- [349] Z. Zhao, Y. Yong, S. Hu, C. Li, and Y. Kuang, "Adsorption of gas molecules on a C₃N monolayer and the implications for NO₂ sensors," *AIP Advances*, vol. 9, no. 12, p. 125308, 2019.
- [350] V. Babar, S. Sharma, and U. Schwingenschlögl, "Highly sensitive sensing of NO and NO₂ gases by monolayer C₃N," *Advanced Theory and Simulations*, vol. 1, no. 6, p. 1700008, 2018.
- [351] M. D. Esrafil and S. Heydari, "Si-doped C₃N monolayers as efficient single-atom catalysts for the reduction of N₂O: a computational study," *Molecular Physics*, pp. 1-8, 2020.
- [352] O. Faye, U. Eduok, J. A. Szpunar, and A. C. Beye, "Two-dimensional carbon nitride (C₃N) nanosheets as promising materials for H₂S and NH₃ elimination: A computational approach," *Physica E: Low-dimensional Systems and Nanostructures*, vol. 117, p. 113794, 2020.
- [353] K. Matsui, S. Oda, K. Yoshiura, K. Nakajima, N. Yasuda, and T. Hatakeyama, "One-shot multiple boronation toward BN-doped nanographenes," *Journal of the American Chemical Society*, vol. 140, no. 4, pp. 1195-1198, 2018.
- [354] X. Liu *et al.*, "Valley-selective circular dichroism and high carrier mobility of graphene-like BC₆N," *Nanoscale*, vol. 10, no. 27, pp. 13179-13186, 2018.
- [355] V. Babar, S. Sharma, and U. Schwingenschlögl, "Gas Sensing Performance of Pristine and Monovacant C₆BN Monolayers Evaluated by Density Functional Theory and the Nonequilibrium Green's Function Formalism," *The Journal of Physical Chemistry C*, vol. 124, no. 10, pp. 5853-5860, 2020.
- [356] Y. Meir and N. S. Wingreen, "Landauer formula for the current through an interacting electron region," *Physical review letters*, vol. 68, no. 16, p. 2512, 1992.
- [357] M. Buttiker, "Coherent and sequential tunneling in series barriers," *IBM Journal of Research and Development*, vol. 32, no. 1, pp. 63-75, 1988.
- [358] R. Landauer, "Spatial variation of currents and fields due to localized scatterers in metallic conduction," *IBM Journal of research and development*, vol. 1, no. 3, pp. 223-231, 1957.
- [359] B. Mortazavi, M. Shahrokhi, M. Raeisi, X. Zhuang, L. F. C. Pereira, and T. Rabczuk, "Outstanding strength, optical characteristics and thermal conductivity of graphene-like BC₃ and BC₆N semiconductors," *Carbon*, vol. 149, pp. 733-742, 2019.

- [360] A. Bafekry, "Graphene-like BC₆N single-layer: Tunable electronic and magnetic properties via thickness, gating, topological defects, and adatom/molecule," *Physica E: Low-dimensional Systems and Nanostructures*, vol. 118, p. 113850, 2020.
- [361] E. Schröder, "Methanol adsorption on graphene," *Journal of Nanomaterials*, vol. 2013, 2013.
- [362] A. S. Rad and V. P. Foukolaei, "Density functional study of Al-doped graphene nanostructure towards adsorption of CO, CO₂ and H₂O," *Synthetic Metals*, vol. 210, pp. 171-178, 2015.
- [363] S. Sun, T. Hussain, W. Zhang, and A. Karton, "Blue phosphorene monolayers as potential nano sensors for volatile organic compounds under point defects," *Applied Surface Science*, vol. 486, pp. 52-57, 2019.
- [364] E. Clementi and D.-L. Raimondi, "Atomic screening constants from SCF functions," *The Journal of Chemical Physics*, vol. 38, no. 11, pp. 2686-2689, 1963.
- [365] F. Banhart, J. Kotakoski, and A. V. Krasheninnikov, "Structural defects in graphene," *ACS nano*, vol. 5, no. 1, pp. 26-41, 2011.
- [366] K. Choi *et al.*, "Terahertz and optical study of monolayer graphene processed by plasma oxidation," *Applied Physics Letters*, vol. 102, no. 13, p. 131901, 2013.
- [367] J. Wu, W. Shi, and N. Chopra, "Plasma oxidation kinetics of gold nanoparticles and their encapsulation in graphene shells by chemical vapor deposition growth," *The Journal of Physical Chemistry C*, vol. 116, no. 23, pp. 12861-12874, 2012.
- [368] A. W. Robertson *et al.*, "Spatial control of defect creation in graphene at the nanoscale," *Nature communications*, vol. 3, no. 1, pp. 1-7, 2012.
- [369] A. Bagri, C. Mattevi, M. Acik, Y. J. Chabal, M. Chhowalla, and V. B. Shenoy, "Structural evolution during the reduction of chemically derived graphene oxide," *Nature chemistry*, vol. 2, no. 7, pp. 581-587, 2010.
- [370] J. C. Meyer, C. Kisielowski, R. Erni, M. D. Rossell, M. Crommie, and A. Zettl, "Direct imaging of lattice atoms and topological defects in graphene membranes," *Nano letters*, vol. 8, no. 11, pp. 3582-3586, 2008.
- [371] Z. Wang, Y. Zhou, J. Bang, M. P. Prange, S. Zhang, and F. Gao, "Modification of defect structures in graphene by electron irradiation: Ab initio molecular dynamics simulations," *The Journal of Physical Chemistry C*, vol. 116, no. 30, pp. 16070-16079, 2012.
- [372] X. Deng, X. Liang, S.-P. Ng, and C.-M. L. Wu, "Adsorption of formaldehyde on transition metal doped monolayer MoS₂: A DFT study," *Applied Surface Science*, vol. 484, pp. 1244-1252, 2019.
- [373] B. Swetha, V. Nagarajan, and R. Chandiramouli, "Interaction Studies of Methanol and Ethanol Vapors on Green Phosphorene Sheets: A First-Principles Study," *ChemistrySelect*, vol. 4, no. 48, pp. 14237-14243, 2019.
- [374] U. Srimathi, V. Nagarajan, and R. Chandiramouli, "Germanane nanosheet as a novel biosensor for liver cirrhosis based on adsorption of biomarker volatiles—a DFT study," *Applied Surface Science*, vol. 475, pp. 990-998, 2019.
- [375] V. Nagarajan and R. Chandiramouli, "Borophene nanosheet molecular device for detection of ethanol—a first-principles study," *Computational and Theoretical Chemistry*, vol. 1105, pp. 52-60, 2017.
- [376] M. Yao, Y. Ji, H. Wang, Z. Ao, G. Li, and T. An, "Adsorption mechanisms of typical carbonyl-containing volatile organic compounds on anatase TiO₂ (001) surface: a DFT investigation," *The Journal of Physical Chemistry C*, vol. 121, no. 25, pp. 13717-13722, 2017.
- [377] S. J. Kim *et al.*, "Metallic Ti₃C₂T_x MXene gas sensors with ultrahigh signal-to-noise ratio," *ACS nano*, vol. 12, no. 2, pp. 986-993, 2018.
- [378] V. Nagarajan, S. Dharani, and R. Chandiramouli, "Density functional studies on the binding of methanol and ethanol molecules to graphyne nanosheet," *Computational and Theoretical Chemistry*, vol. 1125, pp. 86-94, 2018.

- [379] T. Hussain *et al.*, "Sensing of volatile organic compounds on two-dimensional nitrogenated holey graphene, graphdiyne, and their heterostructure," *Carbon*, 2020.
- [380] K. Pu *et al.*, "Al-doped GeS nanosheet as a promising sensing material for O-contained volatile organic compounds detection," *Applied Surface Science*, p. 146797, 2020.
- [381] H. Rodhe, "A comparison of the contribution of various gases to the greenhouse effect," *Science*, vol. 248, no. 4960, pp. 1217-1219, 1990.
- [382] T. Boningari and P. G. Smirniotis, "Impact of nitrogen oxides on the environment and human health: Mn-based materials for the NO_x abatement," *Current Opinion in Chemical Engineering*, vol. 13, pp. 133-141, 2016.
- [383] Z. Mao, S. Dong, J. Li, X. Lin, X. Jian, and P. Wu, "Applied biaxial strain induced tunable sensing performance of green phosphorene monolayer towards small molecules: A DFT study," *Applied Surface Science*, vol. 536, p. 147759, 2021.
- [384] C. R. Usher, A. E. Michel, and V. H. Grassian, "Reactions on mineral dust," *Chemical reviews*, vol. 103, no. 12, pp. 4883-4940, 2003.
- [385] O. I. Joensuu, "Fossil fuels as a source of mercury pollution," *Science*, vol. 172, no. 3987, pp. 1027-1028, 1971.
- [386] R. J. Levy, "Carbon monoxide pollution and neurodevelopment: a public health concern," *Neurotoxicology and teratology*, vol. 49, pp. 31-40, 2015.
- [387] T. R. Anderson, E. Hawkins, and P. D. Jones, "CO₂, the greenhouse effect and global warming: from the pioneering work of Arrhenius and Callendar to today's Earth System Models," *Endeavour*, vol. 40, no. 3, pp. 178-187, 2016.
- [388] D. Cortés-Arriagada, N. Villegas-Escobar, and D. E. Ortega, "Fe-doped graphene nanosheet as an adsorption platform of harmful gas molecules (CO, CO₂, SO₂ and H₂S), and the co-adsorption in O₂ environments," *Applied Surface Science*, vol. 427, pp. 227-236, 2018.
- [389] R. Ehrlich, "Effect of nitrogen dioxide on resistance to respiratory infection," *Bacteriological reviews*, vol. 30, no. 3, pp. 604-614, 1966.
- [390] M. A. Bauer, M. J. Utell, P. E. Morrow, D. M. Speers, and F. R. Gibb, "Inhalation of 0.30 ppm nitrogen dioxide potentiates exercise-induced bronchospasm in asthmatics," *American review of respiratory disease*, vol. 134, no. 5, pp. 1203-1208, 1986.
- [391] A. S. Rad and E. Abedini, "Chemisorption of NO on Pt-decorated graphene as modified nanostructure media: a first principles study," *Applied Surface Science*, vol. 360, pp. 1041-1046, 2016.
- [392] B. Mortazavi, "Ultrahigh thermal conductivity and strength in direct-gap semiconducting graphene-like BC₆N: A first-principles and classical investigation," *Carbon*, 2021.
- [393] I. Barbolina *et al.*, "Submicron sensors of local electric field with single-electron resolution at room temperature," *Applied physics letters*, vol. 88, no. 1, p. 013901, 2006.
- [394] W. Yuan and G. Shi, "Graphene-based gas sensors," *Journal of Materials Chemistry A*, vol. 1, no. 35, pp. 10078-10091, 2013.
- [395] J. Prasongkit, R. G. Amorim, S. Chakraborty, R. Ahuja, R. H. Scheicher, and V. Amornkitbamrung, "Highly sensitive and selective gas detection based on silicene," *The Journal of Physical Chemistry C*, vol. 119, no. 29, pp. 16934-16940, 2015.
- [396] V. Nagarajan and R. Chandiramouli, "NO₂ adsorption behaviour on germanene nanosheet—a first-principles investigation," *Superlattices and Microstructures*, vol. 101, pp. 160-171, 2017.
- [397] W. Xia, W. Hu, Z. Li, and J. Yang, "A first-principles study of gas adsorption on germanene," *Physical Chemistry Chemical Physics*, vol. 16, no. 41, pp. 22495-22498, 2014.
- [398] K. Zhang, Y. Feng, F. Wang, Z. Yang, and J. Wang, "Two dimensional hexagonal boron nitride (2D-hBN): synthesis, properties and applications," *Journal of Materials Chemistry C*, vol. 5, no. 46, pp. 11992-12022, 2017.

- [399] P. Panigrahi, T. Hussain, A. Karton, and R. Ahuja, "Elemental substitution of two-dimensional transition metal dichalcogenides (MoSe₂ and MoTe₂): implications for enhanced gas sensing," *ACS sensors*, vol. 4, no. 10, pp. 2646-2653, 2019.
- [400] W. Jeitschko, "The structure of PdPS and the crystal chemistry of late transition-metal dipnictides and dichalcogenides," *Acta Crystallographica Section B: Structural Crystallography and Crystal Chemistry*, vol. 30, no. 11, pp. 2565-2572, 1974.
- [401] J. Folmer, J. Turner, and B. Parkinson, "Photoelectrochemical characterization of several semiconducting compounds of palladium with sulfur and/or phosphorus," *Journal of Solid State Chemistry*, vol. 68, no. 1, pp. 28-37, 1987.
- [402] Y. Jing, Y. Ma, Y. Wang, Y. Li, and T. Heine, "Ultrathin layers of PdPX (X= S, Se): two dimensional semiconductors for photocatalytic water splitting," *Chem.–Eur. J.*, vol. 23, pp. 13612-13616, 2017.
- [403] Y. Jiao *et al.*, "Ab initio study of two-dimensional PdPS as an ideal light harvester and promising catalyst for hydrogen evolution reaction," *Materials today energy*, vol. 7, pp. 136-140, 2018.
- [404] P. Li *et al.*, "Penta-PdPSe: A New 2D Pentagonal Material with Highly In-Plane Optical, Electronic, and Optoelectronic Anisotropy," *Advanced Materials*, p. 2102541, 2021.
- [405] X. Wang *et al.*, "Polarimetric Image Sensor and Fermi Level Shifting Induced Multi-Channel Transition Based on Two-dimensional PdPS," *Advanced Materials*, p. 2107206.
- [406] R. Kempt, A. Kuc, and T. Heine, "Two-Dimensional Noble-Metal Chalcogenides and Phosphochalcogenides," *Angewandte Chemie International Edition*, vol. 59, no. 24, pp. 9242-9254, 2020.
- [407] S. Feng *et al.*, "Review on smart gas sensing technology," *Sensors*, vol. 19, no. 17, p. 3760, 2019.
- [408] A. Araki, R. Ketema, Y. A. Bamai, and R. Kishi, *Aldehydes, Volatile Organic Compounds and Health (Indoor Environmental Quality and Health Risk toward Healthier Environment for All)*. Springer, 2020.
- [409] V. Feron, H. Til, F. De Vrijer, R. Woutersen, F. Cassee, and P. Van Bladeren, "Aldehydes: occurrence, carcinogenic potential, mechanism of action and risk assessment," *Mutation Research/Genetic Toxicology*, vol. 259, no. 3-4, pp. 363-385, 1991.
- [410] R. Harkov, B. Kebbekus, J. W. Bozzelli, P. J. Liroy, and J. Daisey, "Comparison of selected volatile organic compounds during the summer and winter at urban sites in New Jersey," 1984.
- [411] S. L. Forbes, K. A. Perrault, P.-H. Stefanuto, K. D. Nizio, and J.-F. Focant, "Comparison of the decomposition VOC profile during winter and summer in a moist, mid-latitude (Cfb) climate," *PLoS One*, vol. 9, no. 11, 2014.
- [412] M. Rehwagen, U. Schlink, and O. Herbarth, "Seasonal cycle of VOCs in apartments," *Indoor air*, vol. 13, no. 3, pp. 283-291, 2003.
- [413] B. Clarisse, A. Laurent, N. Seta, Y. Le Moullec, A. El Hasnaoui, and I. Momas, "Indoor aldehydes: measurement of contamination levels and identification of their determinants in Paris dwellings," *Environmental Research*, vol. 92, no. 3, pp. 245-253, 2003.
- [414] H. Wang and G. C. Morrison, "Ozone-initiated secondary emission rates of aldehydes from indoor surfaces in four homes," *Environmental Science & Technology*, vol. 40, no. 17, pp. 5263-5268, 2006.
- [415] S. H. Shin and W. K. Jo, "Volatile organic compound concentrations, emission rates, and source apportionment in newly-built apartments at pre-occupancy stage," *Chemosphere*, vol. 89, no. 5, pp. 569-578, 2012.
- [416] A. T. Hodgson, A. F. Rudd, D. Beal, and S. Chandra, "Volatile organic compound concentrations and emission rates in new manufactured and site-built houses," *Indoor Air*, vol. 10, no. 3, pp. 178-92, Sep 2000, doi: 10.1034/j.1600-0668.2000.010003178.x.

- [417] C. Chen, T. Lo, Y. Tsay, C. Lee, and K. Liu, "Application of a novel formaldehyde sensor with MEMS (Micro Electro Mechanical Systems) in indoor air quality test and improvement in medical spaces," *Applied Ecology and Environmental Research*, vol. 15, no. 2, pp. 81-89, 2017.
- [418] C. Patko, I. Patko, and Z. Pasztory, "Indoor Air Quality Testing in Low-Energy Wooden Houses: Measurement of Formaldehyde and VOC-s," (in English), *Acta Polytechnica Hungarica*, vol. 10, no. 8, pp. 105-116, 2013. [Online]. Available: <Go to ISI>://WOS:000331663700006.
- [419] K. Miyajima *et al.*, "Gas-phase biosensor with high sensitive & selective for formaldehyde vapor: Monitoring of residential air quality for indoor public health," in *2013 Seventh International Conference on Sensing Technology (ICST)*, 2013: IEEE, pp. 447-450.
- [420] Y. M. Su and C. H. Lin, "A Study to Formaldehyde Adsorption on Bird's-Nest Fern Green-wall to the Effect of the Indoor Air Quality (IAQ)," (in Chinese), *2012 International Conference in Humanities, Social Sciences and Global Business Management (Issgbm 20120)*, Vol 8, vol. 8, pp. 98-104, 2012. [Online]. Available: <Go to ISI>://WOS:000322284400018.
- [421] Y. Y. Maruo and J. Nakamura, "Portable formaldehyde monitoring device using porous glass sensor and its applications in indoor air quality studies," *Analytica chimica acta*, vol. 702, no. 2, pp. 247-253, 2011.
- [422] G. Xiao *et al.*, "Trace amount formaldehyde gas detection for indoor air quality monitoring," in *2011 IEEE International Instrumentation and Measurement Technology Conference*, 2011: IEEE, pp. 1-4.
- [423] T. Salthammer, "The formaldehyde dilemma," *International journal of hygiene and environmental health*, vol. 218, no. 4, pp. 433-436, 2015.
- [424] G. D. Nielsen, S. T. Larsen, and P. Wolkoff, "Re-evaluation of the WHO (2010) formaldehyde indoor air quality guideline for cancer risk assessment," *Archives of toxicology*, vol. 91, no. 1, pp. 35-61, 2017.
- [425] R. Golden, "Identifying an indoor air exposure limit for formaldehyde considering both irritation and cancer hazards," *Critical reviews in toxicology*, vol. 41, no. 8, pp. 672-721, 2011.
- [426] L. Zhang, C. Steinmaus, D. A. Eastmond, X. K. Xin, and M. T. Smith, "Formaldehyde exposure and leukemia: a new meta-analysis and potential mechanisms," *Mutation Research/Reviews in Mutation Research*, vol. 681, no. 2-3, pp. 150-168, 2009.
- [427] M. Salaspuro, "Acetaldehyde and gastric cancer," *Journal of digestive diseases*, vol. 12, no. 2, pp. 51-59, 2011.
- [428] K. Salmela, R. Roine, P. Sipponen, J. HOOKNIKANNE, and M. Salaspuro, "HIGH GASTRIC-JUICE ACETALDEHYDE-LEVELS IN ATROPHIC GASTRITIS-A POSSIBLE RISK FOR GASTRIC-CANCER," in *Gastroenterology*, 1993, vol. 104, no. 4: WB SAUNDERS CO INDEPENDENCE SQUARE WEST CURTIS CENTER, STE 300, PHILADELPHIA ..., pp. A446-A446.
- [429] N. Homann, J. Tillonen, H. Rintamaki, M. Salaspuro, C. Lindqvist, and J. H. Meurman, "Poor dental status increases acetaldehyde production from ethanol in saliva: a possible link to increased oral cancer risk among heavy drinkers," (in English), *Oral Oncology*, vol. 37, no. 2, pp. 153-158, Feb 2001, doi: Doi 10.1016/S1368-8375(00)00076-2.
- [430] M. P. Salaspuro, "Acetaldehyde, microbes, and cancer of the digestive tract," *Critical reviews in clinical laboratory sciences*, vol. 40, no. 2, pp. 183-208, 2003.
- [431] D. Smith, T. Wang, J. Sulé-Suso, P. Španěl, and A. E. Haj, "Quantification of acetaldehyde released by lung cancer cells in vitro using selected ion flow tube mass spectrometry," *Rapid communications in mass spectrometry*, vol. 17, no. 8, pp. 845-850, 2003.
- [432] G. McGwin Jr, J. Lienert, and J. I. Kennedy Jr, "Formaldehyde exposure and asthma in children: a systematic review," *Environmental health perspectives*, vol. 118, no. 3, pp. 313-317, 2010.

- [433] P. F. G. Gannon, P. Bright, M. Campbell, S. P. Ohickey, and P. S. Burge, "Occupational Asthma Due to Glutaraldehyde and Formaldehyde in Endoscopy and X-Ray Departments," (in English), *Thorax*, vol. 50, no. 2, pp. 156-159, Feb 1995, doi: DOI 10.1136/thx.50.2.156.
- [434] R. Maddalena, M. Russell, D. P. Sullivan, and M. G. Apte, "Formaldehyde and other volatile organic chemical emissions in four FEMA temporary housing units," *Environmental science & technology*, vol. 43, no. 15, pp. 5626-5632, 2009.
- [435] M. W. Murphy *et al.*, "Formaldehyde levels in FEMA-supplied travel trailers, park models, and mobile homes in Louisiana and Mississippi," (in English), *Indoor Air*, vol. 23, no. 2, pp. 134-141, Apr 2013, doi: 10.1111/j.1600-0668.2012.00800.x.
- [436] A. Mizumoto, S. Ohashi, K. Hirohashi, Y. Amanuma, T. Matsuda, and M. Muto, "Molecular mechanisms of acetaldehyde-mediated carcinogenesis in squamous epithelium," *International journal of molecular sciences*, vol. 18, no. 9, p. 1943, 2017.
- [437] M. K. Nakhleh *et al.*, "Diagnosis and Classification of 17 Diseases from 1404 Subjects via Pattern Analysis of Exhaled Molecules," (in English), *Acs Nano*, vol. 11, no. 1, pp. 112-125, Jan 2017, doi: 10.1021/acsnano.6b04930.
- [438] N. Shehada *et al.*, "Silicon nanowire sensors enable diagnosis of patients via exhaled breath," *ACS nano*, vol. 10, no. 7, pp. 7047-7057, 2016.
- [439] L. Liu *et al.*, "Aligned, high-density semiconducting carbon nanotube arrays for high-performance electronics," *Science*, vol. 368, no. 6493, pp. 850-856, 2020.
- [440] C. Liu, J. Hu, G. Wu, J. Cao, Z. Zhang, and Y. Zhang, "Carbon Nanotube-Based Field-Effect Transistor-Type Sensor with a Sensing Gate for Ppb-Level Formaldehyde Detection," *ACS Applied Materials & Interfaces*, vol. 13, no. 47, pp. 56309-56319, 2021.
- [441] G. Peng, E. Trock, and H. Haick, "Detecting simulated patterns of lung cancer biomarkers by random network of single-walled carbon nanotubes coated with nonpolymeric organic materials," *Nano letters*, vol. 8, no. 11, pp. 3631-3635, 2008.
- [442] N. Bachar, L. Liberman, F. Muallem, X. Feng, K. Müllen, and H. Haick, "Sensor arrays based on polycyclic aromatic hydrocarbons: chemiresistors versus quartz-crystal microbalance," *ACS applied materials & interfaces*, vol. 5, no. 22, pp. 11641-11653, 2013.
- [443] D. Lee, Y. Chander, S. M. Goyal, and T. Cui, "Carbon nanotube electric immunoassay for the detection of swine influenza virus H1N1," *Biosensors and Bioelectronics*, vol. 26, no. 8, pp. 3482-3487, 2011.
- [444] P. S. Na *et al.*, "Investigation of the humidity effect on the electrical properties of single-walled carbon nanotube transistors," *Applied Physics Letters*, vol. 87, no. 9, p. 093101, 2005.
- [445] A. Zahab, L. Spina, P. Poncharal, and C. Marliere, "Water-vapor effect on the electrical conductivity of a single-walled carbon nanotube mat," *Physical Review B*, vol. 62, no. 15, p. 10000, 2000.
- [446] L. Valentini, I. Armentano, L. Lozzi, S. Santucci, and J. Kenny, "Interaction of methane with carbon nanotube thin films: role of defects and oxygen adsorption," *Materials Science and Engineering: C*, vol. 24, no. 4, pp. 527-533, 2004.
- [447] B.-K. Kim *et al.*, "The effect of metal cluster coatings on carbon nanotubes," *Nanotechnology*, vol. 17, no. 2, p. 496, 2005.
- [448] L. A. Currie, "Nomenclature in evaluation of analytical methods including detection and quantification capabilities (IUPAC Recommendations 1995)," *Pure and applied chemistry*, vol. 67, no. 10, pp. 1699-1723, 1995.
- [449] H. Martens and T. Naes, *Multivariate calibration*. John Wiley & Sons, 1992.